Universidade de Lisboa
Faculdade de Ciências
Departamento de Física

Dynamics and interactions of nuclear proteins revealed by quantitative photobleaching microscopy

José Miguel Rino Henriques

Tese orientada pela Prof. Doutora Maria Carmo-Fonseca
Instituto de Medicina Molecular, Faculdade de Medicina
e pelo Prof. Doutor Eduardo Ducla-Soares
Instituto de Biofísica e Engenharia Biomédica, Faculdade de Ciências
Universidade de Lisboa

Doutoramento em Biofísica
Lisboa, 2007

Table of Contents

Acknowledgements

First and foremost, I would like to thank my advisor Prof. Maria Carmo-Fonseca for giving a young physicist the opportunity to learn and work in a cell biology group, and for teaching him how to strive for excellence in research and clarity in scientific speech. I would also like to thank Prof. Eduardo Ducla-Soares for the enduring support and motivation over the years.

Financial support was generously granted by fellowships from Fundação para a Ciência e Tecnologia (BD/21518/99) and the European Commission ("RNOMICS" QLG2-CT-2001-01554 and "Integrated Technologies for *in vivo* Molecular Imaging" LSHG-CT-2003-503259), for which I am most grateful.

I am sincerely grateful to my colleague and fellow physicist José Braga, with whom it has been a pleasure and a privilege to work with over the years. This work greatly benefited from the close collaboration, discussion of ideas and invaluable friendship he has given me. I am also deeply grateful to Joana Desterro, who was always keen on answering my many questions and doubts on Biology and lab techniques and is undoubtedly an inspiration with her optimistic dedication to work and life. Grazie mille Maria Vivo, per tutto il supporto, incoraggiamento e grande amicizia and also many thanks to Sandra Caldeira, Tiago Carneiro, João Paulo Tavanez, Isabel Roque, Sofia Rebelo, Marta Agostinho, Noélia Custódio and Anita Gomes for their everyday support, rewarding friendship and outstanding lab atmosphere. Also, great thanks to Teresa Carvalho, Patrícia Carvalho, Margarida Gama-Carvalho, Célia Carvalho, Teresa Pacheco, João Ferreira and Inês Condado for their friendly assistance and collaboration in my work. A special thanks to Catarina Henriques, for the extensive bibliography I was given access to, and also the insightful comments and affectionate support in so many parts of this work. I also thank all the remaining past and present members of the Cell Biology unit and of the IMM for making it so enjoyable to work here.

This work would not have been the same without all of its collaborations. I am grateful to Elisa Izaurralde for having welcomed me in a short-term visit to her lab at the EMBL. Also, Vielen Dank an Daniel Forler, for teaching me how to keep cells alive in a culture dish and making my stay in Heidelberg a very pleasant one. I would also like to thank Dorus Gadella (Swammerdam Institute for Life Sciences, University of Amsterdam) for the extremely fruitful short-term visits to his lab and discussion of ideas and Erik van Munster for all the support and assistance with the FLIM technique.

My sincere gratitude to all my friends, who contributed dearly to this work by always being there when I needed them.

Finally, I would like to thank my family and especially my parents and sister for the unconditional support, comprehension and dedication with which they have lovingly taught me the most valuable things in life. This work is dedicated to them.

Palavras-chave:	**Keywords:**
Microscopia confocal	Confocal microscopy
FRET	FRET
FLIP	FLIP
Difusão	Diffusion
Núcleo celular	Cell nucleus
mRNA	mRNA
Splicing	Splicing

Sumário

O núcleo celular é um organito complexo, dotado de um elevado grau de organização mas também uma natureza extremamente dinâmica. A utilização de proteínas fluorescentes como marcadores moleculares para visualização em células vivas, bem como as técnicas de *photobleaching*, têm sido essenciais na descoberta da natureza dinâmica do núcleo. Neste trabalho, estas ferramentas foram aplicadas no estudo da dinâmica e interacções moleculares dentro deste compartimento celular.

As técnicas de *Fluorescence Recovery After Photobleaching* (FRAP) e *Fluorescence Loss In Photobleaching* (FLIP) foram utilizadas na análise do comportamento cinético dos componentes do spliceosoma SmE, $U2AF^{65}$, $U2AF^{35}$, SF1 e SC35 no interior do núcleo de células vivas. O mecanismo de recrutamento dos factores de *splicing* (SFs) para os locais de transcrição é ainda pouco conhecido. Os nossos resultados excluem a hipótese de haver um sinal associado à transcrição que seja responsável por este recrutamento. Sugerem ainda a formação de complexos multi-proteicos distintos do spliceosoma.

A existência destes complexos foi confirmada por técnicas de *Fluorescence Resonance Energy Transfer* (FRET), que mostraram que os SFs podiam interagir uns com os outros mesmo na ausência de *splicing* activo. Foi ainda descoberta uma nova auto-interacção para o factor $U2AF^{65}$, sugerindo os resultados no seu conjunto que a distribuição de SFs no núcleo é compatível com mecanismos de auto-organização.

A mobilidade de mRNPs no núcleo foi estudada utilizando como marcadores moleculares duas proteínas que se ligam ao mRNA marcadas com GFP, PABPN1 e TAP. Foi desenvolvido um método de FLIP para quantificação da mobilidade das fracções ligadas e não ligadas ao mRNA e usado para testar a possibilidade de motores de miosina estarem envolvidos no movimento de mRNPs. Mostramos que tal não acontece e que a inibição de miosina parece antes afectar a transcrição.

Um novo método de FLIP após foto-activação foi desenvolvido para estudar a dinâmica de trocas entre o núcleo e o citoplasma de proteínas nucleares, permitindo a estimação do tempo de permanência de moléculas dentro do núcleo. O método foi utilizado para investigar o papel dos diferentes domínios estruturais da proteína TAP na sua actividade de exportação nuclear.

Abstract

The nucleus is a complex cellular organelle, exhibiting a high degree of organization and also a highly dynamic nature. Live cell imaging using fluorescent proteins (FPs) as molecular tags and photobleaching techniques have been essential in revealing the dynamic nature of the cell nucleus. In this thesis, these tools were used to study molecular dynamics and interactions inside this cellular compartment.

Fluorescence Recovery After Photobleaching (FRAP) and Fluorescence Loss In Photobleaching (FLIP) were used to analyze the kinetic behavior of spliceosome components SmE, U2AF^{65}, U2AF^{35}, SF1 and SC35 in the nucleus of living cells. The recruitment mechanism of splicing factors (SFs) to the sites of transcription is still poorly understood. Our results rule out the hypothesis that a transcription specific signal recruits SFs from the speckles. They also suggest the formation of multi-protein complexes distinct from the spliceosome.

The existence of these complexes was confirmed by Fluorescence Resonance Energy Transfer (FRET) techniques, which revealed that SFs could interact with each other even in the absence of active splicing. A novel U2AF^{65} self-interaction was also detected, suggesting altogether that levels of SFs in speckles are consistent with self-organization mechanisms.

The intranuclear mobility of mRNPs was studied using two GFP-tagged mRNA-binding proteins, PABPN1 and TAP, as mRNA markers. A novel FLIP method was devised to quantify the mobility of the RNA-bound and unbound pools of molecules and used to test whether myosin motors were implicated in mRNP movement. We show that this is not the case and that myosin inhibition appears to affect transcription instead.

A novel FLIP after Photoactivation method was developed to study the nucleocytoplasmic exchange dynamics of nuclear proteins, yielding the permanence times of molecules inside the nucleus. The method was used to study the role of the structural domains of TAP in its shuttling activity.

Resumo

As células são as unidades fundamentais de todos os organismos vivos, as menores porções independentes de matéria viva dotadas da capacidade de auto-replicação. O seu tamanho é tipicamente diminuto, normalmente menor que 100 µm, o que impossibilita a sua observação directa pelo olho humano. Só a invenção do microscópio, um instrumento de importância fundamental para a Biologia Celular, tornou por isso possível a sua descoberta. É através do uso de microscópios que a complexidade do interior das células se torna visível em imagens ampliadas e com uma resolução apenas limitada pelas propriedades da luz utilizada.

Visto ao microscópio, e reforçado por um vasto número de estudos bioquímicos, o interior da célula revela-se um meio altamente organizado e dinâmico onde ocorre de forma coordenada uma complexa rede de interacções entre as moléculas que constituem a célula. Nas células eucariotas, esta organização reflecte-se na existência de vários compartimentos que separam diferentes processos celulares. O núcleo celular, onde é guardada a informação genética da célula em determinadas porções da molécula de ADN denominadas genes, é sem dúvida o mais proeminente destes. É no interior do núcleo que ocorre não só a replicação do ADN mas também a transcrição e processamento (*capping, splicing* e poli-adenilação) da molécula portadora da informação genética, o mRNA, que terá de ser exportada deste compartimento celular para ser traduzida em proteína no citoplasma. A maquinaria envolvida no processamento do mRNA é bastante complexa. A reacção de *splicing* por exemplo, que consiste na remoção de sequências denominadas intrões da molécula de mRNA, é efectuada pelo spliceosoma, um complexo macromolecular formado por um conjunto de *small nuclear ribonucleoproteins* (snRNPs) e um vasto número de proteínas auxiliares denominadas factores de *splicing* (SFs). Apesar do grande número de estudos bioquímicos efectuados, a dinâmica destes mecanismos de processamento em células vivas permanece largamente desconhecida.

A visualização destes processos *in vivo* é aliás um feito recente, apenas tornado possível pela descoberta e clonagem de uma proteína fluorescente denominada GFP (*green fluorescent protein*), com a qual é possível marcar qualquer proteína produzida pela célula. Para além da simples observação da distribuição de

moléculas fluorescentes expressas pela célula viva, a conjugação do uso de GFP com o de microscópios confocais de varrimento *laser* veio permitir a introdução de técnicas de monitorização de dinâmica e interacções moleculares. Nas técnicas de *Fluorescence Recovery After Photobleaching* (FRAP) e *Fluorescence Loss In Photobleaching* (FLIP), a iluminação laser do microscópio é utilizada para destruir de forma controlada e irreversível a fluorescência de proteínas marcadas com GFP (efeito denominado *photobleaching*) numa dada região da célula. Se a população de moléculas em estudo exibir alguma mobilidade, a técnica de FRAP irá detectar um aumento da fluorescência na zona onde foi efectuado *photobleaching*, à medida que as moléculas cuja fluorescência foi destruída são substituídas por novas moléculas fluorescentes. A técnica de FLIP, por seu lado, detectará um decréscimo de fluorescência em zonas distantes da zona de *photobleaching* como resultado de sucessivos pulsos de iluminação *laser* intensa.

Ambas as técnicas são hoje maioritariamente utilizadas de forma qualitativa para averiguar a mobilidade de proteínas dentro da célula, identificando-as como componentes estruturais de determinados compartimentos ou, em alternativa, como entidades dinâmicas que continuamente e de forma cíclica são trocadas entre regiões distintas da célula. Abordagens mais quantitativas têm sido desenvolvidas para a técnica de FRAP, com o objectivo de extrair parâmetros de mobilidade relevantes tais como o coeficiente de difusão e a fracção imóvel das proteínas em estudo. O mesmo não tem acontecido no entanto, com a técnica de FLIP. Um dos objectivos deste trabalho consistiu por isso na exploração do seu potencial em termos de quantificação de dinâmica molecular no interior de células vivas.

As técnicas de FRAP e FLIP foram primeiro utilizadas para estudar a mobilidade e o comportamento cinético de componentes do spliceosoma. Para tal, um conjunto de factores de *splicing* foi marcado com GFP e os seus coeficientes de difusão e fracções imóveis foram quantificados por FRAP. A distribuição nuclear dos factores de *splicing* é bastante característica, concentrando-se estas proteínas em locais de geometria irregular denominados grânulos intercromatínicos, ou *speckles* nucleares. As experiências de FRAP mostraram que os factores de *splicing* são extremamente dinâmicos no interior da célula, continuamente associando-se e dissociando-se dos *speckles* nucleares. Os resultados obtidos mostram no entanto que a mobilidade destas proteínas não só é menor que a esperada como também está relacionada com a capacidade dos SFs interagirem entre si, sugerindo assim a formação de complexos multi-proteicos nos *speckles*. Sabe-se que a reacção de *splicing* não ocorre nestas regiões, mas sim em locais de transcrição activa que se encontram essencialmente distribuídos fora dos *speckles*, não sendo ainda conhecido o mecanismo de recrutamento dos factores de *splicing* para os locais de transcrição. O facto de a inibição de transcrição com drogas específicas levar a um aumento da concentração de SFs nos *speckles* poderia ser explicado pela hipótese de que existiria um sinal activo que recrutaria os factores de *splicing*. Na ausência desse sinal, em virtude da inibição de transcrição, estas proteínas ficariam retidas nos *speckles* nucleares. Experiências de FLIP realizadas em células vivas tratadas com uma droga inibidora de transcrição ou levadas a expressar uma proteína que inibe a reacção de *splicing*, revelaram no entanto um aumento generalizado na mobilidade de factores de *splicing*, em contradição com a hipótese de existência de um sinal activo de recrutamento. Como hipótese alternativa, propôs-se então um modelo estocástico no qual a distribuição de factores de *splicing* é regulada por mecanismos de auto-organização, sendo estes o resultado da difusão destas proteínas pelo núcleo e das interacções que estabelecem entre si.

Com o intuito de detectar estas interacções entre factores de *splicing* e de identificar as zonas onde elas ocorrem foi então utilizada e melhorada a técnica de *Fluorescence Resonance Energy Transfer* (FRET) por *photobleaching* do aceitador, complementada por *Fluorescence Lifetime Imaging Microscopy* (FLIM). Expressámos então em células os mesmos factores de *splicing* desta vez fundidos a variantes cromáticas de GFP denominadas *Cyan Fluorescent Protein* (CFP) e *Yellow Fluorescent Protein* (YFP). As experiências de FRET realizadas mostraram que um grupo de factores de *splicing*, U2AF^{65}, U2AF^{35} e SF1, que se sabe interagirem entre si no spliceosoma e que desempenham um papel importante no reconhecimento de sequências que identificam os intrões no mRNA,, também interagem nos *speckles* nucleares, mesmo na presença da droga inibidora de transcrição. Adicionalmente, descobriu-se ainda uma nova auto-interacção do factor de *splicing* U2AF^{65}. Em função dos resultados obtidos, propôs-se então que os factores de *splicing* entrariam na composição de spliceosomas activos já na forma de pré-complexos proteicos, em vez de se ligarem individualmente ao spliceosoma em formação.

Uma vez correctamente processados e libertados dos sítios de transcrição, as moléculas de mRNA, juntamente com um vasto número de proteínas que a estas se ligam, têm de chegar até aos poros nucleares para serem exportados para o citoplasma. A natureza desta mobilidade intranuclear do mRNA tem sido objecto de discussão ao longo dos últimos anos, desconhecendo-se se o movimento ocorre por difusão passiva ou, pelo contrário, requer mecanismos de transporte activo. Com o propósito de elucidar esta questão, estudámos a mobilidade do mRNA expressando em células vivas duas proteínas marcadas com GFP e que se ligam ao mRNA, marcando-o assim indirectamente: o factor de exportação TAP e a proteína que se liga às caudas de poli-adenina ribonucleicas, PABPN1. Desenvolvemos então um método quantitativo de FLIP que permite caracterizar a cinética de uma mistura de populações fluorescentes difundindo com coeficientes de difusão distintos no interior da célula. Este novo método permitiu então a estimação da fracção de proteína marcada com GFP que se encontrava ligada ao mRNA, bem como a determinação do coeficiente de difusão deste último. Os resultados obtidos mostram que tanto a proteína GFP-PABPN1 como a GFP-TAP difundem pelo núcleo celular essencialmente distribuídas por duas populações com mobilidade distinta. A mais lenta, que se propôs corresponder à fracção ligada às moléculas de mRNA, apresenta um coeficiente de difusão comum nos dois casos de ~ 0.09 $\mu m^2 s^{-1}$, um valor que se revelou consistente com as estimativas mais recentes obtidas por outros métodos para a mobilidade intranuclear de mRNA e que favorecem um mecanismo de difusão passiva.

Testámos de seguida a possibilidade de o movimento de mRNA dentro do núcleo depender de mecanismos activos, nomeadamente da acção de motores de actina e miosina. Para tal, estudámos a mobilidade de mRNA em células expressando GFP-TAP e tratadas com uma droga inibidora de miosina. Os resultados obtidos mostram um aumento na mobilidade de GFP-TAP que se mostrou ser devido não a qualquer efeito na mobilidade de mRNA, mas sim à inibição de transcrição por parte da droga e consequente diminuição de moléculas de moléculas de mRNA, constituindo assim a primeira demonstração *in vivo* do envolvimento de motores de miosina na actividade de transcrição da célula.

O mRNA não é a única molécula a ser exportada do núcleo celular para o citoplasma. Um grande número de proteínas é trocado entre estes dois compartimentos de forma cíclica, num movimento de vai-e-vem (*shuttling*) ao longo do seu ciclo de vida. Com o objectivo de estudar estas trocas e quantificar o tempo de permanência de uma dada molécula num dos compartimentos desenvolveu-se então um método de FLIP após foto-activação que permite determinar a cinética da proteína em casos onde a distribuição desta é bastante desequilibrada, estando praticamente ausente num dos compartimentos. Tal é o caso do factor de exportação TAP, que acompanha o mRNA na sua passagem pelo poro nuclear, mas que é praticamente indetectável no citoplasma. Com esta nova metodologia foi possível determinar o tempo de permanência da proteína TAP no núcleo bem como as diferenças na cinética de exportação provocadas por mutações em diferentes domínios funcionais da proteína.

Em resumo, nesta tese foram desenvolvidas e aplicadas técnicas quantitativas de *photobleaching* no estudo da dinâmica e interacções de proteínas dentro do núcleo celular. A utilidade destes métodos foi demonstrada na obtenção de resultados inovadores em diferentes aspectos chave da biogénese do mRNA, tais como a reacção de *splicing*, o transporte intranuclear de mRNA e a sua exportação para o citoplasma. Juntamente com modelação computacional, as técnicas de *photobleaching* revelam-se assim ferramentas essenciais na compreensão da elaborada organização e arquitectura celular, contribuindo para uma imagem de funcionamento do núcleo cada vez mais alicerçada em fenómenos estocásticos, difusão simples e processos de auto-organização.

1. Introduction

1.1 The eukaryotic cell

Cells are the basic building blocks, the smallest independent units of life (Baluska et al., 2004). They are incredibly complex and diverse structures, capable of self-replication, from which all living organisms are built. Typical cells have diminute sizes, usually less than 100 µm, which makes them too small to be seen by naked eye. Only with the invention of the microscope at the beginning of the seventeenth century was it possible to discover and study them (Mazzarello, 1999). More than two hundred years, though, span between the development of the first compound microscope by Hans and Zacharias Jansen and the formulation of the cell theory in 1838-39, by Matthias Schleiden (Schleiden, 1838) and Theodor Schwann (Schwann, 1839). This was mostly due to chromatic aberrations in the earlier microscopes, which limited the instruments resolving power. When these limitations started to be solved, cellular structures such as the nucleus were finally discovered (Brown, 1833) alongside with the notion that, despite their diversity, all cells share common fundamental properties and organization. The most important of these properties is undoubtedly their ability to self-replicate. All cells originate from pre-existing cells, inheriting the genetic material that encodes their structure and function. This genetic information is the amino acid sequence of all proteins produced by the cell, which is stored in deoxyribonucleic acid (DNA) molecules that must be replicated at each cell division. Cells transcribe this genetic code from DNA into an intermediary molecule of ribonucleic acid (RNA) before translate it into protein, a pathway of genetic flow of information that is known as the central dogma of molecular biology (Alberts, 1994).

Despite the fundamental similarities between different types of cells, there is still a vast diversity in their structure and function. The most important distinction between the two main classes of cells is the presence or absence of the nucleus. All cells are surrounded by plasma membranes, but whereas prokaryotic cells (bacteria and archaebacteria) lack a nuclear envelope, eukaryotic cells (protozoans, algae, fungi and cells of animals and plants) have a membrane-bounded nucleus wherein the genetic material is kept, separating it from the cytoplasm. They are also generally bigger and more complex than prokaryotic cells. Apart from the cytoskeleton, a network of protein filaments that is responsible for cell shape and motility, the cytoplasm of eukaryotic cells is crowded with several membrane-bounded organelles that allow for the compartmentalization of different metabolic activities. These organelles, none of them being present in prokaryotic cells, are the mitochondria, endoplasmic reticulum, Golgi apparatus, lysosomes, peroxisomes and, exclusively in plant cells, chloroplasts and vacuoles. This compartmentalization is a key feature of eukaryotic cells and ultimately essential for its complex metabolism and size (Vellai and Vida, 1999). In prokaryotic cells, the large surface-to-volume ratio resulting from their small size allows for an efficient redistribution of nutrients throughout the interior of the cell. In the bigger eukaryotic cells, however, the limited surface area compared to its volume does not allow for the same behavior. Hence, the requirement for different specialized internal organelles to carry out metabolic functions and even transportation inside the cell, as is the case of the endoplasmic reticulum and the Golgi apparatus, which are specifically dedicated to the sorting and transport of proteins (Alberts, 1994). This confinement of cellular functions can both facilitate biochemical reactions, by gathering substrates and enzymes inside the membrane-bounded compartments, and prevent other reactions altogether by simply keeping potential reagents apart. These mechanisms of regulation are also at work in the case of the nucleus (Macara, 2001). In eukaryotic cells, cellular functions such as the replication and transcription of DNA and the processing of pre-messenger ribonucleic acid (pre-mRNA) to messenger ribonucleic acid (mRNA) all take place inside the nuclear envelope, while mRNA translation, the final process of gene expression, is believed to occur predominantly in the cytoplasm (Iborra et al., 2001). This compartmentalization requires all nuclear proteins to be imported from the cytoplasm (Gorlich and Kutay, 1999), which provides opportunity for regulation. Inside the nucleus, DNA is packaged into a highly organized protein-coated structure called chromatin (Orphanides and Reinberg, 2002). By tightly controlling the access of specific proteins to this genetic material, the presence of a nucleus allows for gene expression to be regulated not only at the level of transcription (Vandromme et al., 1996) but also of mRNA processing (Mangus et al., 2003; Shin and Manley, 2004) and export to the cytoplasm (Izaurralde, 2002).

These mechanisms are exclusive of eukaryotic cells, as prokaryotic mRNA is rapidly translated while its transcription is still in progress (Cooper, 2000). In fact, it has been recently suggested that the appearance of the nucleus, or more importantly, of the chromosome-free cytoplasm as a dedicated translation compartment, was mandatory in allowing slower pre-mRNA processing mechanisms, such as the removal of non-coding sequences (splicing), to occur before translation (Martin and Koonin, 2006). The presence of the nucleus thus plays a central role in the regulation of eukaryotic gene expression (Yoneda, 2000).

1.2 The Nucleus

Seen under the microscope, the nucleus was first described by Robert Brown as a “single circular areola, generally somewhat opaque than the membrane of the cell”. This “areola, or nucleus of the cell as perhaps it might be termed” (Brown, 1833) is now known to be a highly organized and dynamic entity, and not just an amorphous membrane-bounded organelle containing DNA, RNA and proteins.

1.2.1 The Nuclear Envelope

The nuclear envelope (NE) delimits the nuclear compartment (Figure 1.1). It has a complex structure, consisting of membranes, lamina and nuclear pore complexes (NPCs).

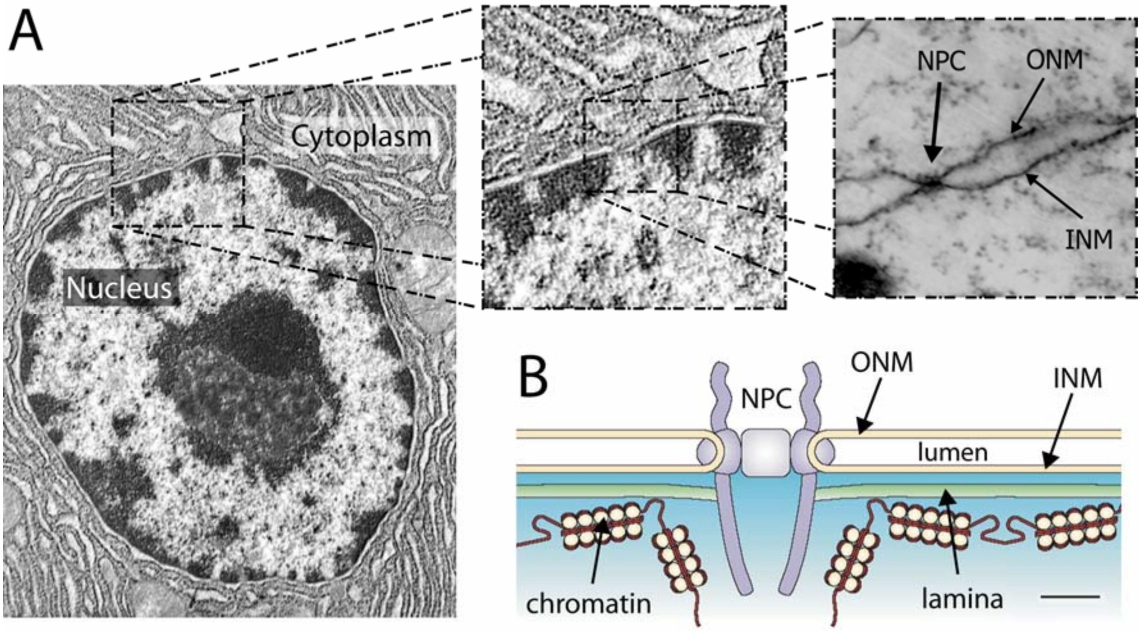

Figure 1.1 – The Nuclear Envelope. **(A)** Electron micrographs of a nucleus show the nuclear envelope with increasing detail, revealing the outer nuclear membrane (ONM), the inner nuclear membrane (INM) and a nuclear pore complex (NPC) where the two membranes are joined. Adapted from the World Wide Web and (Liu et al., 2000) **(B)** Scheme of the nuclear envelope topology, drawn approximately to the known molecular scale of the structures shown. Bar: 50 nm. Adapted from (Burke and Ellenberg, 2002)

The nuclear membranes form two parallel sheets called outer nuclear membrane (ONM) and inner nuclear membrane (INM), which are separated by the lumen and connected around the NPCs. The ONM is continuous with the endoplasmic reticulum, probably sharing evolutionary origins with it (Mans et al., 2004). It has ribosomes bound to its cytoplasmic surface and also provides attachment sites for structural elements of the cytoplasm (D'Angelo and Hetzer, 2006). The INM, on the other hand, contains unique proteins that are specific to the nucleus, as well as binding sites for the lamina and chromatin (Holmer and Worman, 2001). Nuclear membranes are too elastic to mechanically support the NE. It is the nuclear lamina that provides structural support for the nucleus and determines its shape (Gruenbaum et al., 2005). Located underneath the INM, the lamina is a fibrous meshwork of filaments made of proteins called lamins. Like INM proteins, lamins are able to interact with chromatin (Wilson, 2000) and although they are mostly present at the nuclear envelope, they have also been found inside the nucleus (Moir et al., 2000). The INM and ONM constitute the effective barrier that separates the nucleoplasm from the cytoplasm. Only small non-polar molecules are able to diffuse through the phospholipid bilayer that constitutes these membranes. Other molecules, including all nuclear proteins and all cytoplasmic RNAs, must pass through the NPCs to travel between the nucleoplasm and the cytoplasm (Weis, 2003).

NPCs are large multi-protein complexes of more than 100 MDa that perforate the nuclear envelope, forming aqueous channels through which molecular traffic occurs (Rabut et al., 2004b). Their structure is highly symmetrical and overall conserved among all eukaryotes (Stoffler et al., 1999). All NPCs feature a cylindrical central framework of octagonal symmetry flanked on the cytoplasmic side by eight filaments and on the nuclear side by another eight filaments, connected at their tips to form a “basket” (Stoffler et al., 2003). Once assembled, NPCs are maintained throughout interphase in live cells. Because of their interactions with the nuclear lamina, in higher eukaryotes they are even completely immobile within the NE (Rabut et al., 2004b). They are not stationary structures, however (Pante, 2004). NPCs are composed of ~30 different proteins called nucleoporins, with about one third of these having repetitive sequences (FG repeats) that are believed to be important in cargo selectivity (Ribbeck and Gorlich, 2002). These nucleoporins display a wide range of dynamic behavior, with some of them being associated with the NPC over hours while others are extremely dynamic (Rabut et al., 2004a), probably allowing for a modification of transport properties by molecularly remodeling the NPC (Rabut et al., 2004b).

The number of NPCs is limited to only a few thousand in the NE of a mammalian cell (Maul and Deaven, 1977). Given the number of proteins and RNA they have to traffic, this implies that each NPC must be able to maintain at any time a tremendous translocation mass flow. In fact, it has been estimated that this rate can be as high as 100 MDa/s in HeLa cells (Ribbeck and Gorlich, 2001). This means that each NPC is presumably able to translocate the equivalent of its own mass in just one second. There are at least three types of transport allowed through the NPC: passive diffusion, facilitated translocation and unidirectional Ran-dependent transport (Suntharalingam and Wente, 2003). Inert molecules that do not interact with nucleoporins can permeate the NPC at rates consistent with restricted diffusion through a central channel ~10 nm in diameter and ~45 nm in length (Keminer and Peters, 1999). This passive diffusion is fast for small molecules but becomes inefficient as the translocating object approaches a size limit of 30 kDa. Molecules that interact specifically with the nucleoporins repeats, on the contrary, are able to translocate through the NPC with facilitated diffusion rates, in a fully reversible energy-independent manner, even when they are as large as several MDa (Ribbeck and Gorlich, 2001). This facilitated translocation mechanism is still poorly understood. Several models have been proposed, such as the “Brownian affinity gate”, the “selective phase”, the “oily spaghetti” (Fried and Kutay, 2003) and more recently the “reduction-of-dimensionality” (Peters, 2005), all of them suggesting different roles and affinities of the nucleoporins repeats in the interactions with translocating cargo. Finally, substrates that do not interact directly with the nucleoporins but have a nuclear localization signal (NLS) or a nuclear export signal (NES) can still be trafficked across the NPC via soluble transport receptors known as importins or exportins (or karyopherins) (Kubitscheck et al., 2005). In this case, both import and export translocations are mediated by Ran, a small enzyme that can bind and hydrolyze guanosine triphosphate (GTP), therefore providing the energy required for this type of vectorial transport (Gorlich and Kutay, 1999).

Seen through a light microscope in interphase cells, the nucleus reveals itself as a very stable entity delimited by a stiff NE, mechanically constrained inside the cell and exhibiting only small movements over short periods of time. This stability is due not only to the strong interactions between the NE, the cytoskeleton and the endoplasmic reticulum, but also to the internal micro-organization of the nucleus itself, surprisingly much stiffer than the cytoplasm (Tseng et al., 2004).

1.2.2 The Interior of the Nucleus

The NE encloses a highly heterogeneous and dynamic environment (Figure 1.2). The mammalian cell nucleus is arguably the most complex of the cellular organelles, exhibiting both spatial and functional compartmentalization (Misteli, 2005). Its interior can be separated into chromosome territories (CTs), occupied by chromatin, and the remaining interchromatin (IC) space, populated with the macromolecular complexes required for replication, transcription, splicing, repair and degradation (Cremer and Cremer, 2001).

Chromosome territories have complex folded surfaces, with chromatin being globally dispersed throughout the nucleus in a three-dimensional porous structure resembling that of a "sponge" (Visser et al., 2000), permeated by nucleoplasmic channels of various sizes (Misteli, 2005). This likely facilitates the access of certain molecules to genomic sequences buried within CTs and in fact in has been shown that chromatin domains are easily accessible to molecules as large as several hundred kDa (Verschure et al., 2003). Each chromosome occupies its own spatially limited, well-defined nuclear region, however (Figure 1.2B) (Verschure et al., 2002), with little overlap with chromatin from other chromosomes (Gorisch et al., 2005). Chromosome positions appear to be organized according to their size and gene density. Small and gene-rich chromosomes are generally situated towards the interior of the nucleus, whereas large and gene-poor chromosomes tend to be located towards the periphery (Cremer and Cremer, 2001). Their positioning relative to each other is also non-random. The best example of this is the spatial clustering of ribosomal genes located in 2 – 4 distinct chromosomes, which congregate together to form the nucleolus (Figure 1.2D) (Olson et al., 2000), the assembly factory of cellular ribosomes (Carmo-Fonseca, 2002a). Notably, when transcription of ribosomal RNA (rRNA) is inhibited, the nucleolus disassembles (Misteli, 2001a).

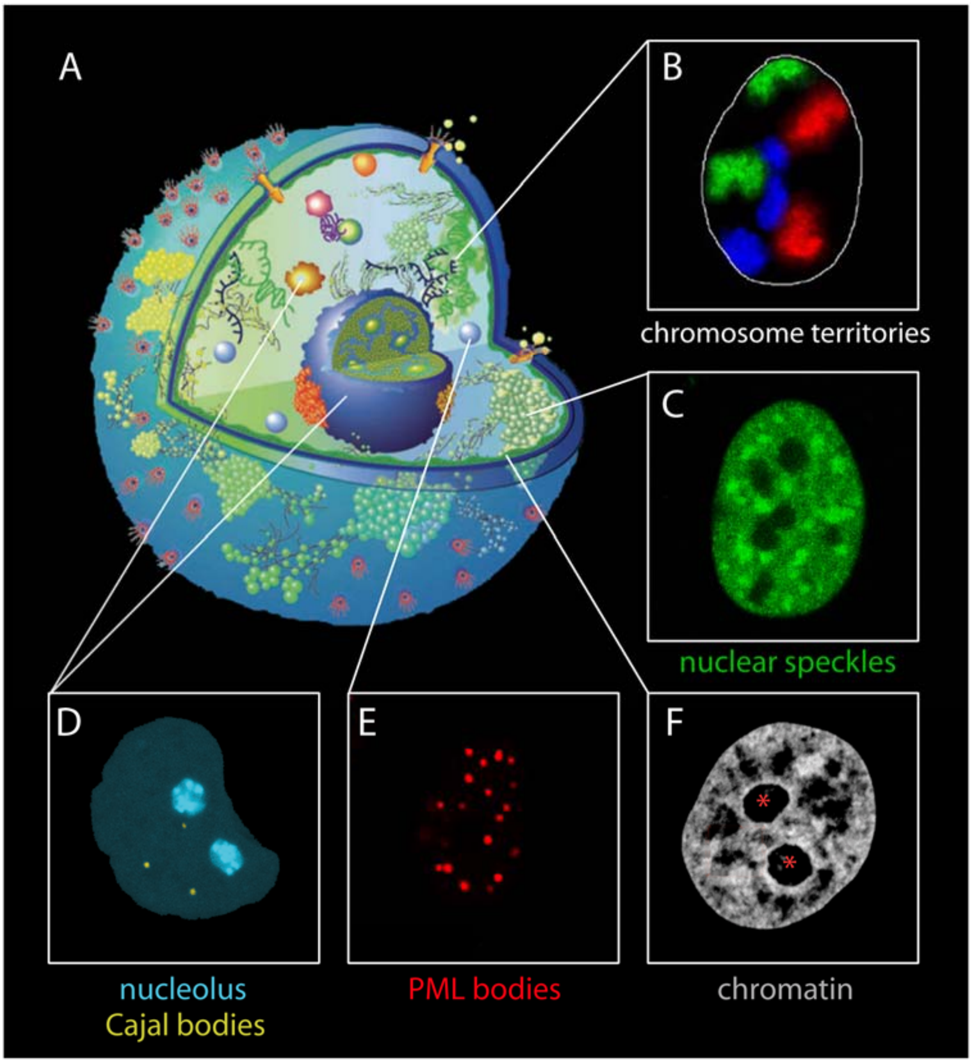

Figure 1.2 – The Interior of the Nucleus. (A) Schematic outline of the cell nucleus showing most of the nuclear domains identified so far (Spector, 2001) **(B)** Human chromosome territories shown in *green*, *red* and *blue* with the nuclear envelope delineated by a white line (Foster and Bridger, 2005) **(C)** Splicing factor compartments or speckles seen by confocal microscopy (Rino et al. *manuscript in preparation*) **(D)** Nucleoli (*blue*) and Cajal bodies (*yellow*) seen by confocal microscopy (Misteli, 2001b) **(E)** Confocal image of PML bodies (Shav-Tal et al., 2005) **(F)** Confocal image showing tagged chromatin (high density, *white*; low density, *grey*), two nucleoli (asterisks) and the interchromatin space (*black*) (adapted from (Cremer and Cremer, 2001)). Note that nuclear compartments lack defining membranes.

Chromatin itself is spatially segregated inside each of these CTs into dense heterochromatin, consisting primarily of silenced genomic loci, and euchromatin, which presumably contains most of the active genome regions (Figure 1.2F) (Carmo-Fonseca, 2002c; Verschure et al., 2002). The vast majority of transcriptionally active sites are located near or at the surface of compact chromatin regions, although some transcription is thought to occur inside CTs as well (Verschure et al., 1999).

The DNA-free interchromatin space starts at nuclear pores (Visser et al., 2000) and spreads between neighboring CTs and chromatin domains inside the CTs (Cremer et al., 2006). Chromatin loops can expand into this IC space, which can be as large as several micrometers in some areas and as narrow as a few nanometers in locations where chromatin surfaces are only kept apart by repulsive electrostatic forces (Cremer and Cremer, 2001). Proteins such as transcription and splicing factors (TFs and SFs respectively) are able to freely wander the entire IC space (Misteli, 2001b). Many of them also concentrate in non-chromatin nuclear bodies, or compartments, that are contained in the more expanded areas of the IC space. The list of all these subnuclear domains is long. Nuclear speckles, Paraspeckles, Cajal bodies, Gems and PML bodies are some of the most commonly observed (Handwerger and Gall, 2006; Spector, 2001). All these nuclear compartments lack defining membranes and have a distinct set of resident proteins that characterizes them (Spector, 2001). Their function remains elusive in most cases. Nuclear bodies can be either sites of functional processing, sites of inaction/storage or merely non-specific aggregates, resultant from excess of protein that is not used in cellular functions (Misteli, 2005).

The promyelocytic leukemia protein (PML) body (Figure 1.2E) and the Cajal body (Figure 1.2D) are the two best-characterized nuclear bodies, even though their function is still not clearly understood. PML bodies have been suggested to function as protein storage sites as well as transcription regulators (Spector, 2001). Cajal bodies are instead thought to play a role in small nuclear ribonucleoproteins (snRNPs, see section 1.3.2) biogenesis and trafficking of both snRNPs and small nucleolar ribonucleoproteins (snoRNPs) (Carmo-Fonseca, 2002a; Ogg and Lamond, 2002; Spector, 2001).

Speckles, also known as splicing factor compartments (SFCs) or SC35 domains, are nuclear bodies enriched in SFs, TFs and small nuclear RNAs (Figure 1.2C) (Lamond and Spector, 2003). Overall, more than 140 proteins have been identified as components of the nuclear speckles (Saitoh et al., 2004), including several kinases and phosphatases as well as structural proteins (Lamond and Spector, 2003). In addition, a population of polyadenylated RNA (poly(A) RNA) has also been localized to these nuclear domains (Politz et al., 2006). Speckles have irregular shape and range in size from one to several micrometers in diameter. Their punctuate appearance as observed by fluorescence microscopy corresponds at the electron microscopy level to both “interchromatin granule clusters” (IGCs) and “perichromatin fibrils” where nascent pre-mRNAs are predominantly localized (Lamond and Spector, 2003). Although sometimes indistinguishable at the fluorescence microscopy level, these two structures are functional and structurally distinct. We will define “nuclear speckles” to be specifically the IGC-component of the splicing factor labeling pattern, distinguishing them from other nuclear structures such as “perichromatin fibrils” and “interchromatin granule-associated zones”, which also contain splicing factors (Fakan, 1994; Spector, 1993; Visa et al., 1993). Nuclear speckles are very dynamic structures, showing transcription-dependent movements at their periphery while remaining in the same neighborhood (Misteli et al., 1997). These peripheral movements are a reflection of the continuous cycling of SFs between the speckles and the nucleoplasm. It is still not known, however, why speckles maintain relatively fixed positions in the nuclei (Pederson, 2002). Unlike nucleoli, speckles do not seem to assemble near specific chromatin loci. They are commonly found in the vicinity of active transcription sites, but do not constitute sites of splicing activity themselves (Misteli, 2000). They are rather considered to be reservoirs or storage sites for SFs, thus regulating their availability throughout the rest of the nucleoplasm (Misteli, 2005). According to this model, SFs are recruited from speckles to nascent pre-mRNAs predominantly localized in perichromatin fibrils (Cmarko et al., 1999). In fact, when transcription is halted by treatment with drugs, SFs accumulate in enlarged, rounded speckles (Melcak et al., 2000). Upon drug removal, speckles rapidly regain their original size and appearance (see Chapter 2). Furthermore, when transcription levels are high due for example to viral infection, SFs concentration in speckles is reduced as they are redistributed to transcription sites (Bridge et al., 1995). In addition to being storage sites, speckles may also play a role in SFs assembly/modification. In support of this idea is the localization at speckles of several kinases and phosphatases that can phosphorylate/dephosphorylate components of the splicing machinery (Lamond and Spector, 2003). Phosphorylation levels are also thought to play a role in speckle dynamics. SFs cycle continuously with fast exchange rates between the speckles and nucleoplasm, where they are able to move rapidly throughout the entire nucleus (Kruhlak et al., 2000; Phair and Misteli, 2000). These exchange rates are thought to be regulated via phosphorylation/dephosphorylation of SFs. The “regulated-exchange” model proposes that phosphorylated SFs are released from speckles and recruited to transcription sites, whereas dephosphorylated SFs tend to self-interact and assemble into speckles (Lamond and Spector, 2003; Misteli and Spector, 1998; Xiao and Manley, 1998).

What determines speckles and other nuclear organelles location and stability? One of the most controversial proposals is that of a nucleoskeleton, or nuclear matrix, a three-dimensional non-chromatin network within the nucleus (Nickerson, 2001) equivalent to the cytoskeleton, that would serve as an anchor site for the different nuclear domains. When chromatin is extracted from cells using high-salt solutions, this matrix is readily observed in electron microscopy (EM) images as a network of 10 nm linear fibers consisting of RNA and proteins crisscrossing the nucleoplasm (Hendzel et al., 1999). Nuclear matrix opponents, however, claim that this meshwork of fibers is nothing but an artifact caused by protein and RNA aggregation during the non-physiological chromatin extraction procedure (Pederson, 2000). The biological reality of the nuclear matrix remains elusive, as well as the molecular identification of its putative components (Misteli, 2005). Candidates such as lamins (Gruenbaum et al., 2005) and actin (Bettinger et al., 2004; Pederson and Aebi, 2002), both of them also detected in the speckles, were suggested to play a role in the nuclear matrix structure but no filaments of these proteins were found inside the nucleus so far. The poly(A) RNA population detected in the speckles is also a dynamic component of these nuclear bodies, remarkably exhibiting the same mobility in the speckles and nucleoplasm (Politz et al., 2006), which argues against its putative role as a structural entity. Adding to the difficulties in clearly defining the composition of a nuclear matrix is the reduced theoretical need to invoke its existence inside the nucleus, claim its opponents (Pederson, 2000).

Nuclear architecture seems to be very dynamic in its nature. Both PML and Cajal bodies, for instance, are able to move inside the nucleus. Chromatin itself displays diffusion-like movement within confined volumes (Marshall et al., 1997). Cajal bodies' mobility is compatible with anomalous diffusion (Carmo-Fonseca et al., 2002; Platani et al., 2002), probably reflecting collisions and transient interactions with chromatin (Saxton, 1994; Saxton, 1996; Wachsmuth et al., 2000). They can also separate into smaller bodies and join to form larger ones (Ogg and Lamond, 2002). PML bodies, on the other hand, surprisingly show different classes of nuclear mobility, ranging from stationary ones to very fast moving bodies, some of them displaying energy-dependent movements (Muratani et al., 2002). Nuclear mobility is not only observed for nuclear bodies, but also for is constituents. Like the SFs that constitute the speckles, it has also been shown that the proteins that constitute the PML and Cajal bodies continuously associate and dissociate from these nuclear compartments, with different exchanging rates (Dundr et al., 2004; Sleeman et al., 2003). Indeed, so far there are few nuclear domains for which an active exchange of the proteins that constitute them has not been observed (Pederson, 2002).

The highly dynamic nature of the nuclear components suggests the nucleus itself might be a self-organized entity (Misteli, 2001a; Misteli, 2005), with diffusion being the essential transport mechanism. In this view, nuclear morphology is a reflection not only of the cell's transcription activity but also of all the molecular interactions between the nuclear components. These stochastic, relatively promiscuous and transient interactions of diffusing molecules would be the mechanisms responsible for the formation of steady-state structures, providing at the same time positive and negative feedback responses essential for system plasticity. Dynamic instability is intrinsic to self-organized structures, which can be rapidly assembled/disassembled in response to cellular needs but remain nonetheless unaffected by fluctuations in many of its components, once in steady-state (Howard and Kruse, 2005). Such may be the case of nuclear bodies such as speckles, which are proposed to be formed by transient molecular interactions (Lamond and Spector, 2003; Misteli, 2001a). According to this model, nuclear diffusion and the different binding kinetics of SFs would be determinant in shaping the speckles morphology and dynamics, with phosphorylation and dephosphorylation acting as feedback mechanisms. SFs are also able to self-interact (Chusainow et al., 2005) (see also Chapter 3), which clearly increases the promiscuity and complexity of their interactions and provides further support to the self-organization model.

We are only beginning to understand how the nucleus components are coordinated in time and space. How nuclear proteins find their targets *in vivo* and organize into complex machineries is still not fully understood. Much clearer are the functions they participate in, particularly in gene expression. Biochemical, genetic and molecular approaches have already characterized in extensive detail the processes involved in mRNA biogenesis, which include transcription, 5'-end capping, splicing, 3´-end processing and export (Alberts, 1994).

1.3 mRNA Biogenesis and Export

The mRNA molecule is the central conduit in the flow of information from DNA to protein. In eukaryotic cells, mRNAs are first synthesized in the nucleus as pre-mRNAs that are further 5'-end capped, spliced, 3'-end cleaved and polyadenylated (Moore, 2005). Once these pre-mRNA processing steps are complete, most mature mRNAs are exported to the cytoplasm, where they serve as blueprints in ribosomal protein synthesis, before being degraded.

1.3.1 Transcription

The first step in the translation of genomic sequence into protein is transcription, the synthesis of RNA under the direction of DNA. DNA molecules store the genetic information that encodes the amino acid sequence of all the proteins produced by the cell, but DNA itself is not involved directly in protein synthesis. Instead, this information is copied, or transcribed, from DNA to mRNA, which then carries the genetic message to the cell's protein-synthesizing machinery. The cell transcribes more types of RNA other than mRNA, however. In fact, much of the transcribed sequences in eukaryotic genomes lie outside areas recognized as genes (Lander et al., 2001). Eukaryotic DNA thus encodes RNA molecules that function without being translated into protein. These non-coding RNAs (ncRNAs) include ribosomal RNAs (rRNAs), transfer RNAs (tRNAs), small nuclear RNAs (snRNAs) and micro-RNA (miRNAs). Transcription of all these RNA molecules is performed by different enzymes called polymerases, of which three types have been identified. RNA polymerase I (RNA Pol I) is responsible for the nucleolar synthesis of the majority of rRNAs, the most abundant of the RNA species. rRNAs form the bulk of the ribosomes, the catalytic and regulatory centers of protein synthesis (Doudna and Rath, 2002). The rRNAs that are not transcribed by nucleolar RNA Pol I are instead synthesized by the nucleoplasmic RNA polymerase III (RNA Pol III), the enzyme that is also responsible for the transcription of tRNAs, the adaptors between the mRNA genetic code and protein sequence, and some snRNAs (Kiss, 2004). Finally, RNA polymerase II (RNA Pol II) catalyzes the synthesis of mRNA precursors for all protein-coding genes, as well as some snRNAs.

The expression of these protein-coding genes is initiated by transcriptional activators that recruit enzymes and remodeling complexes required for chromatin reorganization. In eukaryotic cells, DNA is packaged into chromatin in a highly organized manner, wrapped around core proteins called histones and forming blocks or basic units denominated nucleosomes (Orphanides and Reinberg, 2002). Nucleosome remodeling and histone modifications are thus believed to be required for changing the transcriptional status of chromatin (Janicki et al., 2004). Once chromatin is locally remodeled, proteins denominated general transcription factors (GTFs) are able to bind to specific "promoter" sequences in the DNA and recruit RNA Pol II to the start site of transcription. These mRNA nascent transcription sites are not homogeneously distributed throughout the nucleoplasm, but instead occur in foci known as "transcription factories" which are highly enriched in RNA Pol II (Chakalova et al., 2005; Iborra et al., 1996; Wansink et al., 1993). As there are more active genes than transcription factories in a nucleus at a given time, it is believed that more than one active gene is transcribed in each factory (Jackson et al., 1998; Osborne et al., 2004). The transcription of each of these genes by RNA Pol II is a multi-step process that comprises three different steps: initiation, elongation and termination (Figure 1.3). Transcription begins with the stepwise assembly of the RNA Pol II pre-initiation complex at the promoter (Orphanides and Reinberg, 2002; Woychik and Hampsey, 2002) followed by the separation of the DNA strands and the formation of the first bonds of the RNA chain (Figure 1.3b). The formation of the RNA Pol II elongation complex is then required to disrupt the interactions between RNA Pol II and the promoter, a step which also involves a massive phosphorylation of the carboxy-terminal domain (CTD) of the RNA Pol II large subunit. Inhibition of CTD phosphorylation by the use of drugs such as the kinase inhibitor 5,6-dichloro-1β-D-ribofuranosyl-benzimidazole (DRB) blocks transcription altogether, as well as further pre-mRNA processing (Bird et al., 2004; Chodosh et al., 1989; Yamaguchi et al., 1998). Once the elongation complex is formed, the direct readout of the template encoded in one of the DNA strands then proceeds as RNA Pol II untwists the DNA's double helix and synthesizes pre-mRNA by adding one ribonucleotide at a time to the 3' end of this growing RNA molecule (Figure 1.3c). The double helix is reformed as RNA Pol II advances along the DNA template, allowing the newly synthesized pre-mRNA to detach itself from DNA and be available for co-transcriptional processing events, where it associates with several proteins, thus becoming a messenger ribonucleoprotein particle (mRNP). Transcription proceeds until shortly after RNA Pol II transcribes a DNA “termination” sequence, at which time the export-competent mRNP is cut free from the enzyme (Figure 1.3f).

1.3.2 Co-transcriptional mRNA processing events

Very few RNA molecules are transcribed directly into their final mature form. Instead, most newly transcribed precursor RNAs undergo several modifications in order to yield the mature and fully functional RNA product. Eukaryotic mRNA is no exception to this rule: pre-mRNA molecules are processed by 5’-end capping, splicing, 3’-end cleavage and polyadenylation. These reactions occur mostly during, and not after, transcription (Bentley, 2005; Calvo and Manley, 2003; Kornblihtt et al., 2004; Proudfoot, 2004) and are tightly coupled to each other (Aguilera, 2005; Maniatis and Reed, 2002). Transcription elongation factors, as well as the CTD of RNA Pol II, are thought to play a central role in coupling transcription to pre-mRNA processing events. It is believed that the CTD could actually function as an assembly platform for the different pre-mRNA processing machines, regulating transcription while at the same time controlling the efficiency of capping, splicing and polyadenylation (Fong and Bentley, 2001).

Capping

Capping enzymes are among the first pre-mRNA processing factors to be recruited to the CTD (Figure 1.3b). They bind to the transcript as soon as its 5’-end becomes available, usually after the transcription of the first 20 – 25 nucleotides (Shatkin and Manley, 2000). Transcription is paused at this point, possibly to allow time for the capping reaction (Orphanides and Reinberg, 2002), which consists in the chemical modification of the pre-mRNA 5’-end by the addition of a 7-methylguanosine residue connected to the transcript in an unusual 5’-5’ triphosphate bridge (Lodish et al., 2003). Capping enzymes are able to manipulate early steps in transcription and have thus been suggested to operate a checkpoint that ensures only properly capped mRNA proceeds to the elongation step (Bentley, 2005). Once the pre-mRNA is capped, the nuclear cap binding protein complex (CBC) binds to the cap co-transcriptionally (Aguilera, 2005). CBC thus seems to be the first mRNP protein to assemble on pre-mRNAs. The cap structure not only protects the mRNA from enzymatic degradation, thereby stabilizing it, but it is also important in promoting translation initiation and splicing.

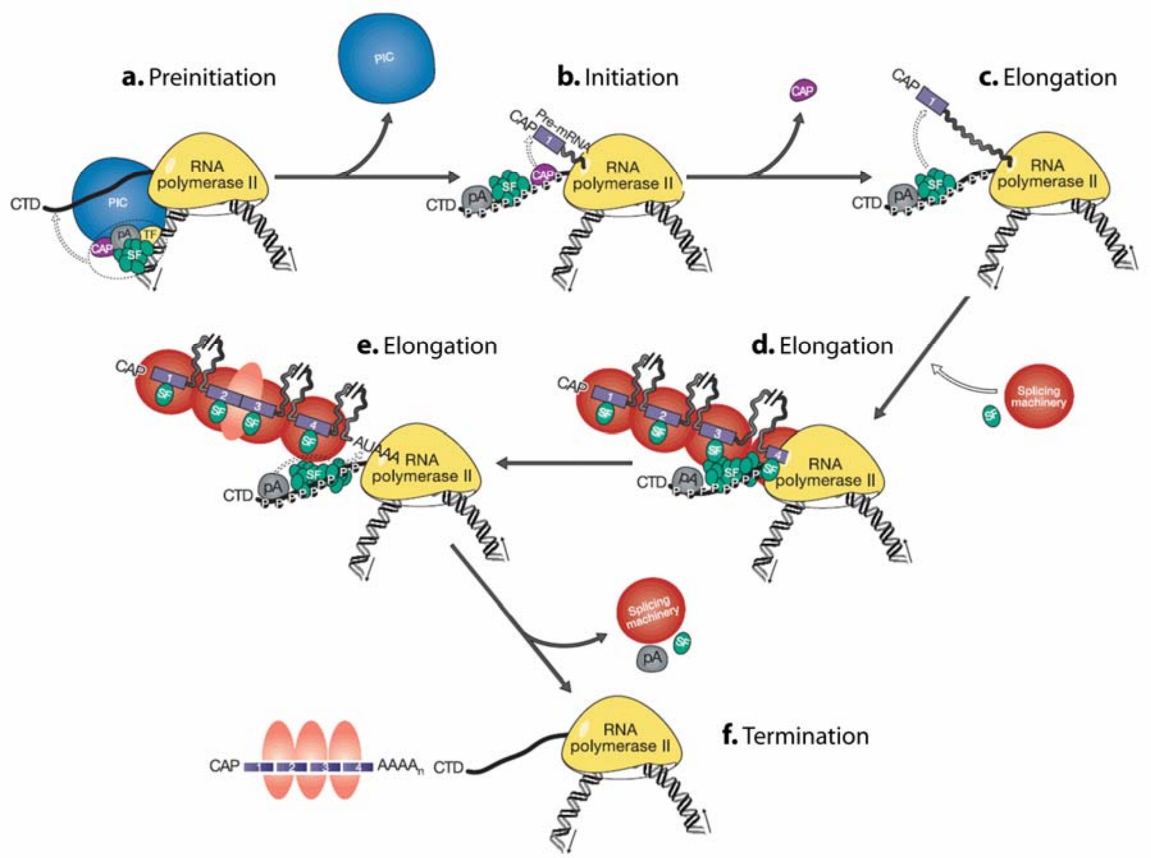

Figure 1.3 – Transcription and co-transcriptional processing events. Model of gene expression factory showing the coupling between the different steps of mRNA biogenesis. DNA is wound through RNA Pol II as the nascent RNA transcript is pushed out from its exit channel. The transcription, capping, splicing and polyadenylation machineries are shown. Exon-exon junction complexes (EJCs) are represented by shaded pink ovals. See text for details of steps **a – f**. PIC, pre-initiation complex; TF, transcription factors; CTD, carboxy-terminal domain; CAP, capping enzymes; SF, splicing factors; pA, polyadenylation factor; P, phosphorylated CTD. Adapted from (Maniatis and Reed, 2002).

Splicing

The mature mRNA molecule always carries nucleotide sequences that mirror its protein product, in accordance with the genetic code specified in the DNA. This code, however, is usually interrupted by long non-coding sequences in eukaryotic DNA, which makes most eukaryotic genes longer than their final mRNA products. Splicing consists precisely in the removal of these non-coding sequences (introns) from the primary transcript, thus joining the coding regions (exons) together. Introns are usually much longer than exons. In human genes, their average size exceeds 10,000 base pairs (bp), roughly 200 times the size of the small exons that flank them (Lander et al., 2001). Their origin and purpose remain a mystery. Introns have been suggested to play an important role in increasing the rate of recombination between parts of the coding regions during meiotic crossing-over, and in improving transcript fidelity by inducing nonsense-mediated decay (NMD) of incorrectly transcribed sequences that have premature termination codons (PTCs) (Roy and Gilbert, 2006). In addition, they also provide the possibility to generate new protein isoforms from the same pre-mRNA molecule, by allowing different choices of splice sites to give rise to different combinations of exons, in a process known as alternative splicing (Black, 2003). Alternative splicing provides the major source of protein diversity from the human genome. It is currently believed that around 60 – 80 % of human genes are alternatively spliced in at least one exon (Soller, 2006), an estimate that has been growing over the years. Changes in splicing patterns can regulate not only the expression of different protein isoforms at the single cell level, but also of protein expression for a population of cells in a tissue specific manner, at the organism level (Black, 2003). Errors in the splicing mechanism or alterations in the regulation of alternatively spliced proteins from genes carrying mutations can lead to several diseases, including cancer (Kalnina et al., 2005; Nissim-Rafinia and Kerem, 2005). Alternative splicing requires not only signal sequences in the nascent transcript degenerate enough to allow for different splice site choices, but also specific protein splicing factors to help in the recognition and selection of the correct splice sites (see below). Splicing must be very accurate: a mistake of only one nucleotide would be enough to cause a change in the reading frame and produce a non-functional protein. It is not surprising then, to find that eukaryotic splicing has to be performed by a remarkably complex ribonucleoprotein machine set about to identify exons and splicing sequences amongst huge stretches of non-coding introns. This macromolecular complex is known as the spliceosome, and of all the mRNA processing machineries, it is the one less is known about concerning recruitment to a nascent transcript (Bentley, 2005).

Active spliceosomes are very dynamic *in vivo* and should be regarded as functional units rather than entities with a well-defined structure. A single, well-characterized spliceosome structure only exists during certain time periods of the splicing reaction, as spliceosome components are replaced during the different steps of intron removal (Wetterberg et al., 2001). In the course of its conformational changes, a spliceosome can contain over 300 different proteins and five RNA molecules (Nilsen, 2003; Valadkhan, 2005). Its major components are the uridine-rich small nuclear ribonucleoprotein particles (UsnRNPs or snRNPs) U1, U2, U4, U5 and U6, each one consisting of a single uridine-rich small nuclear RNA (UsnRNA or snRNA) associated with several particle specific proteins and a core of seven "Sm proteins": B/B', D_1, D_2, D_3, E, F and G (Will and Luhrmann, 2001). snRNP assembly occurs in the cytoplasm shortly after the nuclear export of nascent snRNAs (Kiss, 2004; Yong et al., 2004a). After proper assembly of the Sm protein core and further processing of snRNAs, snRNPs are re-imported to the nucleus via binding to a protein called snurportin1 (SPN1) (Huber et al., 2002; Narayanan et al., 2002). The final maturation steps of snRNPs imported from the cytoplasm are believed to occur in the Cajal bodies (see section 1.2.2), before the snRNPs can participate in pre-mRNA splicing (Carmo-Fonseca, 2002b; Stanek and Neugebauer, 2006; Yong et al., 2004b). In addition to snRNPs, several non-snRNP-associated splicing factors are required for spliceosome assembly and function (Kramer, 1996; Sanford and Caceres, 2004).

A single splicing event occurs through two consecutive transesterification reactions, whereby an exon located upstream of the intron is first cleaved from this intron and then ligated to the downstream exon. The excised intron is subsequently degraded. The exact sites where these reactions must occur are defined by sequences in the intron (Figure 1.4A).

Thus, in higher eukaryotes (metazoans) the 5' splice site is usually signaled by the sequence AG↓GURAGU (where ↓ denotes the splice site, R is a purine (A or G) and invariable nucleotides are underlined), an internal region within the intron called "branch point" contains the elements UACUAAC (where A is the branching nucleotide) and the 3' splice site is marked by YAG↓R (where Y is a pyrimidine (U or C)). In addition, a polypyrimidine tract of variable length is located between the branch point and the 3' splice site. In yeast, consensus sequences equivalent to these ones are sufficient to specify intron excision (except for the poly(Y) tract, which is absent in yeast introns), but in metazoans they are less well conserved and only some nucleotides are invariant. Thus, despite being essential, these sequences are insufficient to determine vertebrate splice sites and additional sequence elements such as "splicing enhancers" and "silencers" are required for splice site selection (Black, 2003; Blencowe, 2000). Moreover, signals from other mRNA processing events such as capping, polyadenylation and the rate of transcription itself have also been shown to influence splice site definition (Maniatis and Reed, 2002).

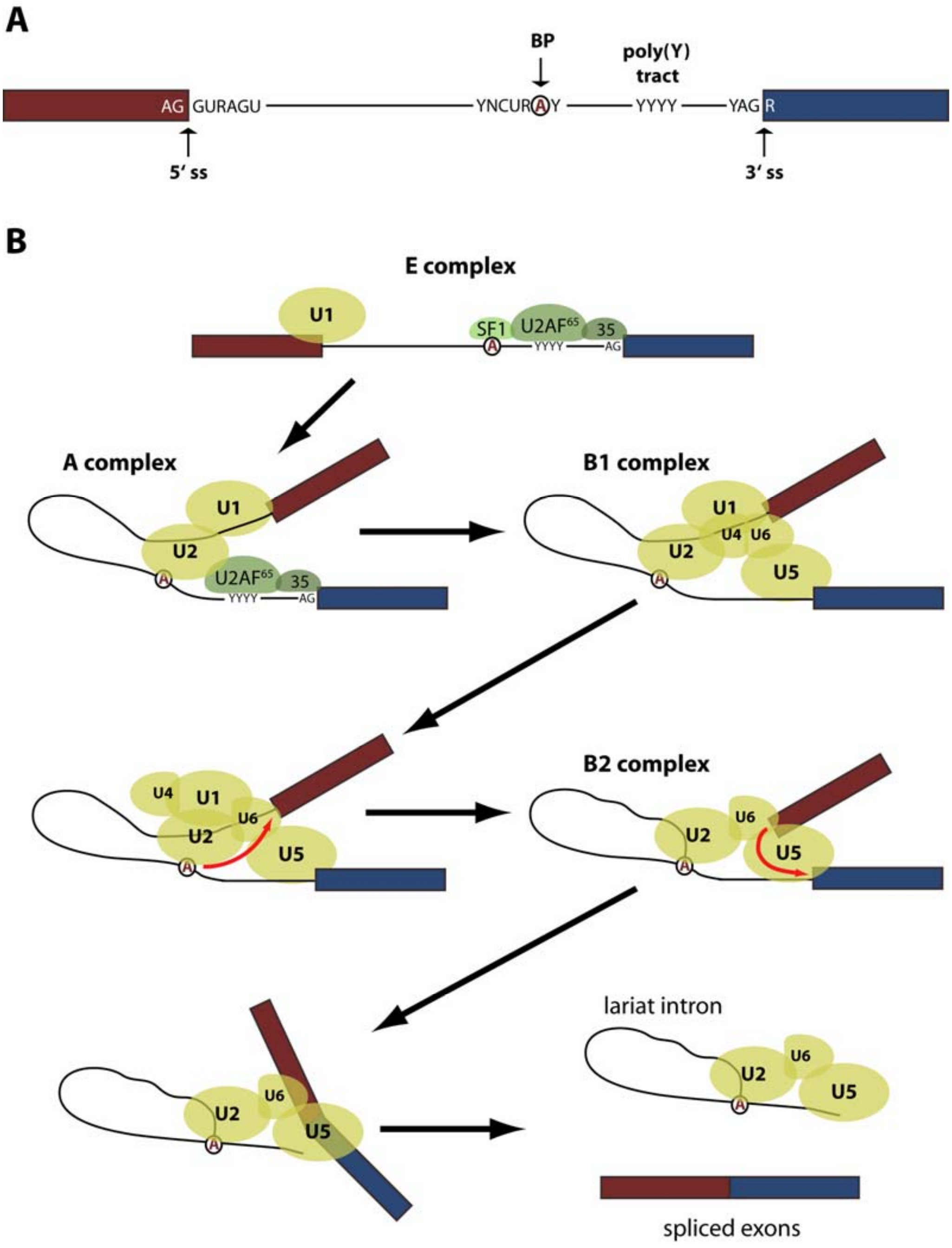

Figure 1.4 – Spliceosome assembly. (A) Schematic representation of an intron with 5', 3', branch point (*BP*) and polypyrimidine (*poly(Y) tract*) consensus sequences. The intron is flanked by two exons (*red* and *blue*) with the 5' and 3' splice sites (*5' ss* and *3' ss*) indicated with arrows. The branching adenosine (*A*) is encircled and highlighted in red. **(B)** Simplified view of the splicing reaction and spliceosome assembly. Only the UsnRNPs (*U1*, *U2*, *U4*, *U5* and *U6*) and the splicing factors SF1, U2AF^{65} and U2AF^{35} (*35*) are shown. Splicing proceeds through two transesterification reactions (*red arrows*) within the active spliceosome complex. Different spliceosome conformations can be found at specific time points and purified as stable complexes (*E*, *A*, *B1* and *B2 complexes*). In the end, the intron sequence is removed and the two flanking exons are joined (see text for details).

The basic mechanism of splicing has been extensively studied using *in vitro* systems in which pre-mRNA is synthesized and spliced in nuclear extracts of cells. Based largely on these *in vitro* experiments, spliceosome assembly is generally thought to occur in a stepwise manner and begins with the recognition of the 5' and 3' splice sites by the U1 snRNP and the heterodimeric U2 snRNP auxiliary factor (U2AF), respectively (Hertel and Graveley, 2005; Sanford and Caceres, 2004). These ATP independent events lead to the formation of an E (early) complex that commits the pre-mRNA to the splicing pathway (Figure 1.4B).

U2AF is composed of a large subunit of 65 kDa (U2AF^{65}) and a smaller one of 35 kDa (U2AF^{35}). U2AF^{65} is an essential splicing factor that binds to the polypyrimidine tract and contacts also the branch point (Guth et al., 2001; Kent et al., 2003), while U2AF^{35} binds to the conserved AG dinucleotide at the 3' splice site and is dispensable for splicing of some introns that contain "strong" polypyrimidine tracts (Pacheco et al., 2006; Pacheco et al., 2004). The branch point is also specifically recognized during the formation of the E complex by the splicing factor 1 / mammalian branch point binding protein (SF1/mBBP), in a cooperative binding with U2AF^{65} (Selenko et al., 2003). These interactions promote the association of the U2 snRNP to the branch point nucleotide in an ATP dependent manner, leading to the formation of the pre-spliceosomal A complex (Sanford and Caceres, 2004). Several proteins of the SR family (all containing conserved sequence motifs of arginine/serine rich (RS) domains) are thought to mediate interactions between adjacent 5' and 3' splice sites, both across the intron and over the exon, stabilizing the A complex and determining correct splice site selection (Hertel and Graveley, 2005; Shen and Green, 2004). Subsequently, the U4/U6·U5 tri-snRNP particle (Liu et al., 2006) associates to the pre-spliceosome to form the B1 complex. At this step, the U1 base pairing interaction with the 5' splice site is replaced by a similar interaction involving the U6 snRNA, while U5 binds to sequences in the 3' exon, thus bringing the two exons closer together. Extensive conformational changes leading to the formation of the B2 complex then dictate the dissociation of U1 and U4 from the complex and promote the first transesterification reaction, whereby the branch point adenosine is connected to the 5' end of the intron, which is cleaved from the upstream exon. The intron is now in a lariat configuration, and more conformational changes are required for the second transesterification reaction to occur, in which the 3' end of the upstream exon is joined with the 5' end of the downstream exon, cleaving the intron from the 3' end splice site. After this final step, the spliced mRNA is released from the complex formed by the lariat intron and the snRNPs, which must disassemble and recycle for another round of splicing. The spliceosome must then form *de novo* on another intron in the nascent transcript.

This stepwise assembly of spliceosomal components has recently been questioned by additional *in vitro* data that revealed the existence of a presumably functional "penta-snRNP" complex in yeast (Stevens et al., 2002). All five spliceosomal snRNPs were thus suggested to be recruited to the nascent transcript together, in a pre-formed complex. In mammalian cells, an even larger complex was found, incorporating not only the five snRNPs but also most of the non-snRNP splicing factors, as well as pre-mRNAs. This complex was called the "supraspliceosome" (Azubel et al., 2006) and it was promptly suggested to be the coordinating entity of all the dynamic processes between mRNA and snRNAs involved in splicing. Whether this *in vitro* data reflects the *in vivo* situation however, remains a matter of debate (Gornemann et al., 2005; Tardiff and Rosbash, 2006). The details of spliceosomal components assembly thus remain poorly understood.

In vivo observations of splicing by electron microscopy (EM) studies indicate that pre-mRNA splicing begins co-transcriptionally, but it often continues after transcription is over, particularly for slower splicing events or exceptionally long introns (Aguilera, 2005; Neugebauer, 2002). Spliceosomes are thought to assemble rapidly as introns appear in the pre-mRNA (Kornblihtt et al., 2004), with splicing factors being quickly recruited to nascent transcripts (Wetterberg et al., 2001) from nuclear speckles (see section 1.2.2). The mechanism of recruitment, though, is unclear. The CTD of RNA Pol II as been suggested to play a role in increasing the association of splicing factors to sites of transcription, but its role as a "landing pad" for snRNPs and SFs, as it occurs for the capping machinery, remains elusive, as no direct binding has been found between spliceosomal components and the CTD (Neugebauer, 2002). Instead, transcription and elongation factors which are known to play a dual role in transcription and splicing have been naturally implicated in linking the two processes together, probably also by recruiting splicing factors themselves (Kornblihtt et al., 2004; Rosonina et al., 2005; Sanchez-Alvarez et al., 2006). The CBC has also been shown to increase the binding efficiency of snRNPs to splice sites (Aguilera, 2005). There is also a kinetic link between transcription and splicing, in addition to a physical one. Timing is of the essence when it comes to splicing.

Splicing factors cannot be recruited to a given intron faster than RNA Pol II transcribes it. Conversely, the time it takes for RNA Pol II to transcribe the whole pre-mRNA would define a maximal time window for co-transcriptional splicing to occur (Neugebauer, 2002). RNAs that are unspliced by the time transcription is terminated would have to be spliced post-transcriptionally, after being released from chromatin (Neugebauer, 2006). The speed at which transcription is performed can then have a profound effect on alternative splicing (Das et al., 2006). Regulation of RNA Pol II processivity by elongation factors, for example, can affect the choice of exon inclusion. Low elongation rates provide enough time for SFs to recognize sub-optimal splice sites that would not be used had a downstream “stronger” splice site already been transcribed by a faster RNA Pol II (Kornblihtt, 2005). Exons that are not identified as such can still be rescued, however, either by slower mechanisms of splice site definition or by slowing the rate of transcription (Kornblihtt, 2006). Interestingly, SFs and snRNPs can also affect transcription, by interacting with elongation factors to stimulate RNA Pol II processivity (Fong and Zhou, 2001). Intron-containing genes are in fact transcribed much more efficiently than its intron-less equivalents (Furger et al., 2002), showing that, as with capping, there is a two-way communication between the splicing and transcription machineries (Zorio and Bentley, 2004).

Splicing also contributes with proteins to the formation of mRNPs, as it catalyzes the binding of the exon-exon junction protein complex (EJC) 20 – 25 nucleotides upstream of the exon-exon junctions (*shaded pink ovals* in Figures 1.3e and 1.3f). This multi-protein complex of ~ 335 kDa is deposited in a temporal fashion and sequence-independent manner on the mRNA as a consequence of the splicing reaction (Custodio et al., 2004; Sanford and Caceres, 2004). The EJC effectively “marks” the RNA as being spliced, serving as a binding platform for proteins involved in mRNA export (see section 1.3.3) and also NMD in case a PTC is found during the first round of translation (Le Hir et al., 2001; Maquat, 2005; Moore, 2005).

Cleavage and Polyadenylation

With the exception of transcripts that code for histones (Gilmartin, 2005; Weiner, 2005), formation of a mature 3’ end in eukaryotic mRNAs involves the co-transcriptional processes of cleavage and polyadenylation, both of them tightly coupled to transcription termination and required for mRNA release from the site of transcription (Buratowski, 2005). Polyadenylation consists in the addition of a protective poly(A) tail of ~ 250 nucleotides at the end of the nascent transcript (Proudfoot and O'Sullivan, 2002; Shatkin and Manley, 2000). A conserved sequence containing the elements AAUAAA together with a downstream GU-rich stretch define the site for polyadenylation (Zorio and Bentley, 2004). These sequences are promptly recognized by the cleavage and polyadenylation specificity factor (CPSF) and the cleavage stimulatory factor (CstF) respectively (Figure 1.5A), as soon as they emerge from the exit channel of RNA Pol II (Proudfoot et al., 2002).

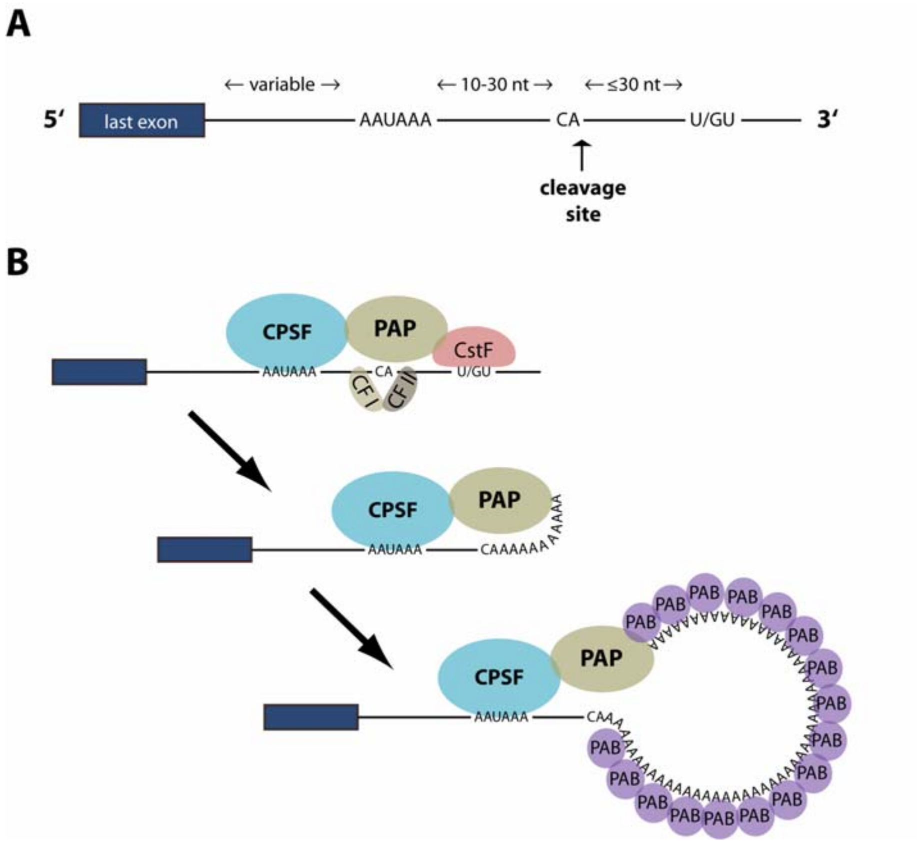

Figure 1.5 – Cleavage and Polyadenylation. (A) Schematic representation of the pre-mRNA poly(A) site with conserved sequence elements and relative distances between them. Adapted from (Gilmartin, 2005). **(B)** Simplified view of the cleavage and polyadenylation reactions. Direct cleavage of the mRNA requires *CPSF*, *CstF* and two additional cleavage factors (*CF I* and *CF II*). Poly(A) polymerase (*PAP*) is also involved in cleavage and, together with CPSF, directs poly(A) addition. PABPN1 (*PAB*) binds the growing poly(A) tail, greatly enhancing the efficiency of polyadenylation and forming 21 nm spherical particles (see text for details). Adapted from (Proudfoot et al., 2002).

Cleavage and polyadenylation factors are recruited to the CTD already during early transcription events (Figure 1.3b), and they have been shown to interact with some early mRNA processing factors (Bentley, 2005; Calvo and Manley, 2003; Proudfoot, 2004), as well as splicing factors (Vagner et al., 2000).

Cleavage itself takes place at a CA dinucleotide located ~ 10 – 30 nucleotides downstream of the AAUAAA sequence and requires the presence of two additional factors, cleavage factor I (CF I) and cleavage factor II (CF II), as well as the poly(A) polymerase protein (PAP) to occur (Figure 1.5B) (Proudfoot et al., 2002).

Following cleavage, PAP together with CPSF starts the process of poly(A) addition (Figure 1.5B). Association of the nuclear poly(A) binding protein (PABPN1, previously designated as PABP2 or PABII) (Kuhn and Wahle, 2004; Mangus et al., 2003) with PAP then greatly increases the efficiency of polyadenylation (Kerwitz et al., 2003) and regulates the length of the poly(A) tail (Bear et al., 2003). PABPN1 is a 33 kDa protein that binds specifically to the poly(A) tail via two RNA binding domains (Kuhn et al., 2003; Tavanez et al., 2005), forming spherical protein-RNA complexes with a diameter of 21 nm (Keller et al., 2000). *In vitro* studies of PABPN1 binding to poly(A) in solution estimated the affinity for an isolated binding site as being in the nanomolar range (Meyer et al., 2002; Wahle et al., 1993) with detectable, albeit weak cooperativity between adjacent PABPN1 molecules (Meyer et al., 2002). The function of the 21 nm spherical particles remains unclear, although there is some speculation that it might be related with measuring the length of the poly(A) tail (Kuhn and Wahle, 2004). PABPN1 is able to shuttle between the nucleus and the cytoplasm, but the presence of a nuclear localization signal (NLS) in its C-terminal domain dictates an active Ran-dependent nuclear import of the protein (Calado et al., 2000). Very little PABPN1 is thus found in the cytoplasm, in a steady-state situation. In the nucleus, PABPN1 localizes to the nuclear speckles (see section 1.2.2) as a consequence of its binding to poly(A) RNA (Calado and Carmo-Fonseca, 2000). mRNPs maintain their PABPN1 coating as they are released from the site of transcription and travel to the nuclear pore (Bear et al., 2003). This only happens, though, if they are correctly spliced and 3’ end processed. Problems with any of these processes result in mRNP retention close or at the site of transcription (Custodio et al., 1999), possibly due to a stalling by the processing machinery that is tethered to the CTD (Custodio and Carmo-Fonseca, 2001). Normal transcripts, on the other hand, are rapidly released to the nucleoplasm once transcription is over, and in there they must find their way to a nuclear pore complex in order to be exported to the cytoplasmic (Carmo-Fonseca et al., 2002).

1.3.3 mRNP movement in the nucleoplasm

How mRNPs move in the nucleoplasm, from the moment they are released from transcription sites until they find a nuclear pore, has been a subject for many studies and a matter of debate over the years (Carmo-Fonseca et al., 2002; Politz and Pederson, 2000; Vargas et al., 2005). The main question as always been related with the nature of the transport method itself: do the transcripts move on their own (i.e., by diffusive processes) or do they require an active transportation mechanism to carry them to a NPC? In the cytoplasm, molecular motors have been implicated in RNA transport along actin microfilaments and microtubules for short-distance and long-range vectorial transport, respectively (Kloc et al., 2002). Early on, the same was thought to happen in the crowded nucleoplasm. The “gene gating” model proposed that all transcripts generated from a particular gene would exit the nucleus exclusively through the closest NPC (Blobel, 1985). Active genes were assumed to be located at the nuclear periphery and the distribution of nuclear pores at the nuclear surface was thought to be non-random, as it reflected the underlying distribution of active genome regions. For a transcript to leave the nucleus, its corresponding gene had thus to be “gated” to a NPC. The same was not proposed for proteins which assembled into the mRNPs, though. “Cytoplasmic synthesized proteins” were thought to reach the mRNP assembly site by “trial and error in and out of the nucleus (by way of nuclear pores)” or by “random entry and diffusion within the nucleus until capture by affinity is accomplished” (Blobel, 1985). One of the predictions of this model would be the non-random distribution of mRNPs in the cytoplasm, as they would be located predominantly in a region adjacent to their “gated” NPC. The finding that some mRNAs in *Drosophila* embryos were exported in a vectorial way and detected within a specific cytoplasmic location encouraged this view (Davis and Ish-Horowicz, 1991), as well as observations of mRNA transcripts in fixed cells that seemed to be localized along nuclear “tracks” (Lawrence et al., 1989). A vectorial transportation mechanism which would require energy consumption and some kind of “solid-state” nuclear structure (Agutter, 1994) was envisioned, with the nuclear matrix being the obvious candidate for such a structure (see section 1.2.2).

This view was far from consensual, however, as some investigators reported that mRNAs from particular genes were observed to be freely scattered throughout the interchromatin space (Zachar et al., 1993), randomly distributed around the transcription site (Femino et al., 1998) in a radial dispersion pattern (Dirks et al., 1995). These results favored instead an mRNP diffusion model, a view further supported by biophysical studies which showed that dextrans and other large exogenous molecules were largely mobile inside the nucleus (Lang et al., 1986; Seksek et al., 1997). This was also consistent with earlier observations that RNAs were able to leave the nucleus through essentially all the nuclear pores (Dworetzky and Feldherr, 1988). EM observations of the distribution of exceptionally big "Balbiani ring" (BR) mRNP particles in the nuclei of *Chironomus tentans* salivary gland cells also suggested random diffusion, with a minimum diffusion coefficient of 0.08 $\mu m^2 s^{-1}$ (Singh et al., 1999). Additional findings that the previously observed distribution of mRNAs in *Drosophila* embryos at a distinctive cytoplasmic location was due to binding to a specific target protein (Lall et al., 1999) helped in clarifying these contradictory observations. The *in situ* observations of "mRNA tracks" on fixed cells remained a matter of discussion though, at least until the emergence of new methodologies that allowed for mRNA distribution and movement to be observed in living cells (Politz and Pederson, 2000). Fluorescence correlation spectroscopy (FCS, see section 1.5.3), performed with oligo(dT) probes that tagged nuclear poly(A) RNA, initially suggested average mRNA diffusion rates to be in the range of 2 to 9 $\mu m^2 s^{-1}$, depending on shape assumptions (Politz et al., 1998). These results strongly supported the idea that mRNPs would be diffusing in the nucleus essentially as they would in an aqueous solution (Politz and Pederson, 2000). The large variation in the measured diffusion coefficients was next improved by the same researchers using "caged" oligo(dT) probes that would only become fluorescent upon photoactivation by UV light. A "rapid imaging system", which was used to track the movement of the "uncaged" signal away from the photoactivated spot, revealed that the poly(A) RNA population was able to access virtually al the interchromatin space. The new estimate for the mRNPs average mobility rate was then found to be in the order of 0.6 $\mu m^2 s^{-1}$ (Politz et al., 1999), a value lower than the diffusion rate in solution, probably due to corralling effects of the chromosome territories (Daneholt, 1999). Importantly, the measured diffusion coefficient was found to be practically the same when measured at 25 or 37ºC, further supporting the absence of a metabolic energy-driven transportation mechanism (Politz et al., 1999). This estimate for the diffusion coefficient of mRNPs was confirmed by our own Fluorescence Recovery After Photobleaching (FRAP, see section 1.5.3) experiments using fluorescent versions of PABPN1 and the export factor TAP (see below) as mRNP tags (Calapez et al., 2002). Our results however, clearly indicated that mRNP movement is significantly reduced when cells are depleted of ATP or incubated at a lower temperature (Calapez et al., 2002). mRNP movement thus seemed to involve a combination of passive diffusion and energy-dependent processes, the later being probably required to counteract obstructions to diffusion or release mRNPs from binding to other intranuclear structures (Carmo-Fonseca et al., 2002).

Whereas the previous methods all looked at a large ensemble of tagged mRNP particles, more recently it has become possible to look at individual RNA molecules using the MS2 labeling system (Shav-Tal et al., 2004b). In this approach, a series of RNA stem-loops are inserted into the transcript, allowing it to be tagged with a fluorescent protein (see section 1.4.2) fused to the bacteriophage coat protein MS2, which forms specific and stable interactions with the stem loops. Using this system, single mRNP movements in the nucleus of living cells once again revealed to be random, consistent with simple diffusion at an average rate of 0.04 $\mu m^2 s^{-1}$ or otherwise corralled motion due to barriers hindering mRNP movement (Shav-Tal et al., 2004a). The much lower value obtained for the diffusion coefficient was proposed to be a result of the highly specific binding of MS2 to the transcript, as in the previous systems one could not exclude that an exchange of the fluorescent protein tags was contributing to the measured mobility rates. Energy-deprivation decreased mRNP mobility as well, and this was shown to be a result of increased constraints imposed by intranuclear structures, following major nuclear reorganization under energy stress that affected both chromatin and interchromatin domains (Shav-Tal et al., 2004a). An alternative technique that was able to track single mRNA molecules using “molecular beacons”, small hairpin-shaped oligonucleotides that only become fluorescent upon binding to their target RNA sequence, once again revealed random diffusion to be the transportation method of choice. The average diffusion rates were estimated at 0.033 $\mu m^2 s^{-1}$ (Vargas et al., 2005), remarkably close to the ones calculated using the MS2 system. mRNP diffusion was also shown to be restricted to the interchromatin space, with transcripts becoming stalled when wandering into dense chromatin domains and requiring energy to resume their motion.

Is 0.04 $\mu m^2 s^{-1}$ fast enough for an mRNP to find a nuclear pore complex within a reasonable amount of time? How efficient is random diffusion at these rates? Theoretical modeling of this question using a walk-and-capture model of a diffusing mRNP yielded a minimum mean capture time by the nuclear envelope of only 1.8 min, assuming a nuclear radius of 8 μm (Kuthan, 2005). In yeast, single mRNPs diffusing at this rate would find a NPC within tens of seconds, instead of minutes.

The increasing amount of data thus supports the growing consensus that mRNPs move inside the nucleus by diffusion, from the moment they are released from the sites of transcription until they associate physically with components of the NPC (Cole and Scarcelli, 2006). Brownian motion (Brown, 1828) is thus increasingly regarded as the method of choice for proteins and RNA to move inside the cellular organelle first described by Robert Brown himself.

1.3.4 mRNP export to the cytoplasm

Of all the transport events between the nucleus and the cytoplasm, mRNA export through the NPC is one of the most elaborate and least understood, due in part to the complex nature of the transport cargo. Functional mRNAs are always associated with several proteins that are deposited onto the nascent transcript during its different processing events (see section 1.3.2) or otherwise bound at later time points. The protein content of these mRNPs is dynamic, as it reflects different phases in the mRNA metabolism (Moore, 2005). It is this protein content that constitutes the target for the export machinery, rather than mRNA itself (Dreyfuss et al., 2002).

The export machinery for cellular mRNAs relies on a group of evolutionary conserved proteins known as nuclear export factors (NXFs), instead of the more vastly used transport receptors known as importins or exportins (or karyopherins, see section 1.2.1) (Izaurralde, 2002). NXFs lack the characteristic Ran-binding domain found in karyopherins (Fried and Kutay, 2003), but are also able to interact with nucleoporins and mediate NPC translocation (Izaurralde, 2001). The human nuclear export factor 1 / Tip-associated protein (NXF1/TAP) is the best characterized of the NXFs (Herold et al., 2000; Kang and Cullen, 1999). The N-terminal cargo-binding region of this 70 kDa shuttling protein contains an NLS recognized by a specific transport receptor (Bear et al., 1999), an RNA binding domain (RBD) (Kang et al.,

1999) and a leucine-rich repeat (LRR) required for viral mRNA export (Braun et al., 1999; Liker et al., 2000). The C-terminal NPC-binding region, on the other hand, comprises a domain related to the nuclear transport factor 2 (NTF2-like) and an ubiquitin-associated domain (UBA), both of them involved in binding to nucleoporins (Figure 1.6A) (Bachi et al., 2000).

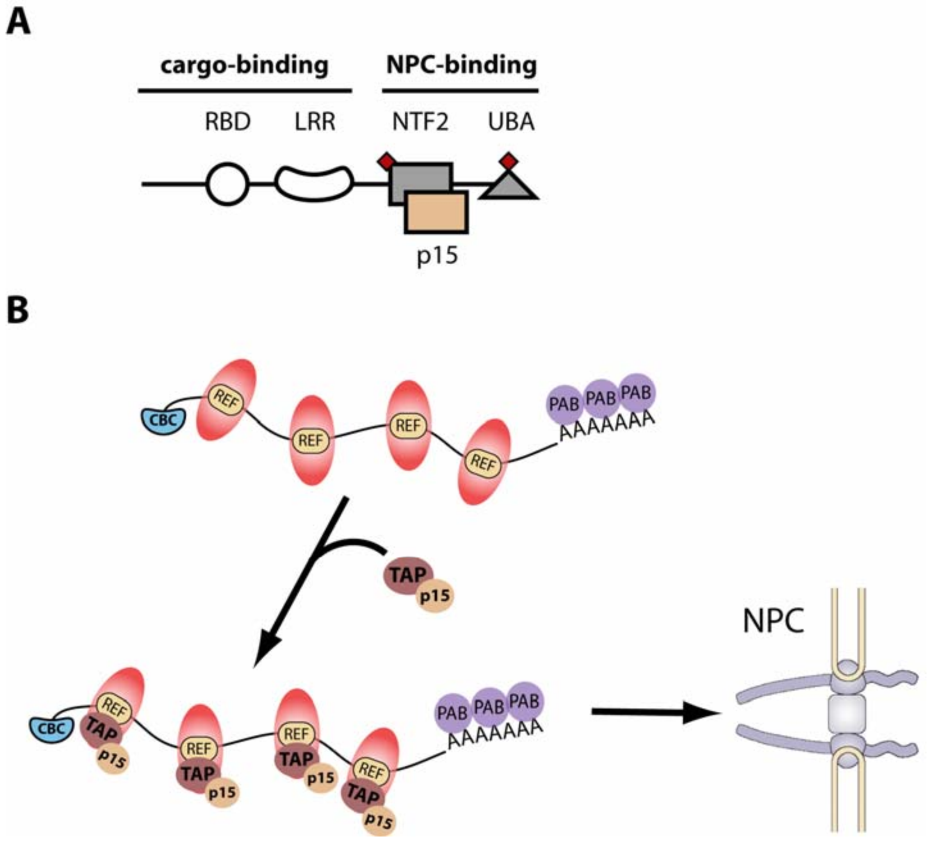

Figure 1.6 – mRNA export by TAP. (A) Structural and functional domains of TAP bound to p15. The cargo-binding domain includes an RNA binding domain (*RBD*) and a leucine-rich repeat (*LRR*), while the NPC-binding region features an NTF2-like domain (*NTF2*) bound to p15 (*light brown rectangle*) and a UBA-like domain (*UBA*). Both the NTF2-like and UBA-like domains feature a nucleoporin-binding site (*red diamond*). Adapted from (Braun et al., 2002). **(B)** TAP is recruited to mRNPs via binding to adaptor proteins, such as the REF1/Aly protein (*REF*), contained in the exon-exon junction complexes (*shaded pink ovals*), and subsequently promotes mRNP export to the cytoplasm via the nuclear pore complexes (*NPC*). CBC, cap binding protein complex; PAB, poly(A) binding protein.

TAP requires heterodimerization with the NTF2-related export protein (NXT1/p15) to ensure proper folding of its NTF2-like nucleoporin-binding site (Wiegand et al., 2002). Binding of the export cofactor p15 to the NTF2-like TAP domain (Suyama et al., 2000) is essential for cellular mRNA export (Herold et al., 2001). The TAP-p15 heterodimer, rather than TAP alone, is thus thought to be the predominant export receptor for cellular mRNAs (Herold et al., 2003).

Although TAP is able to bind directly to mRNA via its RBD domain, this region is not essential for mRNA export *in vivo* (Braun et al., 2001). Instead, adaptor RNA-binding proteins are required to mediate the interaction between the TAP-p15 heterodimer and mRNA (Figure 1.6B) (Dreyfuss et al., 2002; Stutz and Izaurralde, 2003). The RNA export factor binding protein 1 (REF1/Aly), an EJC protein that is recruited during spliceosome assembly and remains tightly associated with the spliced mRNP (Le Hir et al., 2001), is thought to be one of these adaptor proteins, as it is able to interact directly with TAP (Rodrigues et al., 2001). TAP association with mRNPs may involve more adaptor proteins other than REF1, though (Gatfield and Izaurralde, 2002). Additional TAP-binding partners may include several shuttling SR splicing factors (Huang et al., 2003), suggesting that multiple adaptors cooperate in recruiting multiple copies of TAP for efficient mRNP export (Erkmann and Kutay, 2004).

TAP-p15 heterodimers promote the nuclear export of bulk mRNA across nuclear pore complexes by binding to FG-nucleoporin repeats (see section 1.2.1) via the NTF2-like and UBA-like domains, both of them being required for efficient transportation across the central channel of the NPC (Fribourg et al., 2001; Grant et al., 2003; Levesque et al., 2001; Wiegand et al., 2002). At the cytoplasmic filaments of the NPC, a specific nucleoporin (RanBP2/Nup358) has been identified as a major binding site for TAP-p15, restricting its diffusion into the cytoplasm after NPC translocation (Forler et al., 2004). TAP-p15 is thus thought to dissociate from mRNPs and be re-imported to the nucleus via karyopherin adaptors (Bachi et al., 2000), the same presumably happening to REF1/Aly (Kim et al., 2001) and PABPN1 (Bear et al., 2003), but not to other mRNP proteins which will accompany the mRNA all the way to ribosomes, conveying crucial quality control information to the translation machinery and determining mRNA localization and fate (Dreyfuss et al., 2002; Moore, 2005).

1.4 Fluorescent Probes in Cell Biology

The fine details of living cells are not easily accessible to the scientist’s eyes. Living tissue usually scatters light in the visible wavelengths and has often developed mechanisms to prevent photodamage from direct sunlight. Because of this, microscopy specimens had not only to be chemically fixed to improve tissue stability but also dehydrated, refraction index-matched and stained, to increase their optical contrast before they could be seen under a microscope lens. For decades, biologists and microscopists have had to rely on fixed specimens to guess at how the living cells could function (Yuste, 2005). It was only in the last decade that novel imaging techniques, crafted from the physical phenomenon of fluorescence described more than 150 years ago, together with the mid-twentieth century invention of confocal microscopy and the very recent development of genetically encoded fluorophores, have revolutionized the way scientists look at cells.

1.4.1 Fluorescence Principles

The process of fluorescence, first described in 1852 (Stokes, 1852), consists in the emission of light by excited molecules within nanoseconds after the absorption of photons with a shorter wavelength. The difference between the exciting and emitted wavelengths, known as the Stokes shift, depends on the outmost electron orbitals of the fluorescent molecule, or fluorophore. Fluorescent compounds that have not absorbed energy are usually in the lowest vibrational levels of the "ground state" (S_0). Energy absorption results in alterations in the vibrational and rotational states of the molecule, but electronic changes are also possible. These processes are usually represented in a Jablonski diagram (Figure 1.7). When a photon of energy $E = h \times c / \lambda$ (where h is Plank's constant, c is the speed of light and λ is the photon's wavelength in vacuum) is absorbed by a fluorophore, all its energy is transferred to the fluorescent molecule. If the absorbed photon has a high enough energy, a transition to an "excited state" can occur, which moves an electron from a ground state level to an orbital further away from the nucleus (S_1, S_2, S_3, etc.).

This transition occurs within femtoseconds and it requires the minimum energy of the absorbed photon to be equivalent to the energy difference between the lowest energy level of the first excited state (S_1) and the energy level of S_0 occupied by the electron. If the photon's energy is greater than this value then the molecule will also change its vibrational and rotational state and/or move into a higher excited state (e.g. S_2). There is thus a range of wavelengths that can excite a molecule, and these will be reflected in the absorption spectrum of the fluorophore. All the energy absorbed by the molecule is eventually lost, as excited states are very unstable and the fluorophore will tend to return to its low-energy ground state. Rotation and vibrational relaxation will chiefly dissipate some of the absorbed energy to the surrounding medium. “Internal conversion” from the lowest vibrational levels of an excited state (e.g. S_2) to the highest vibrational levels of the next lower energy excited state (e.g. S_1) is also likely to occur.

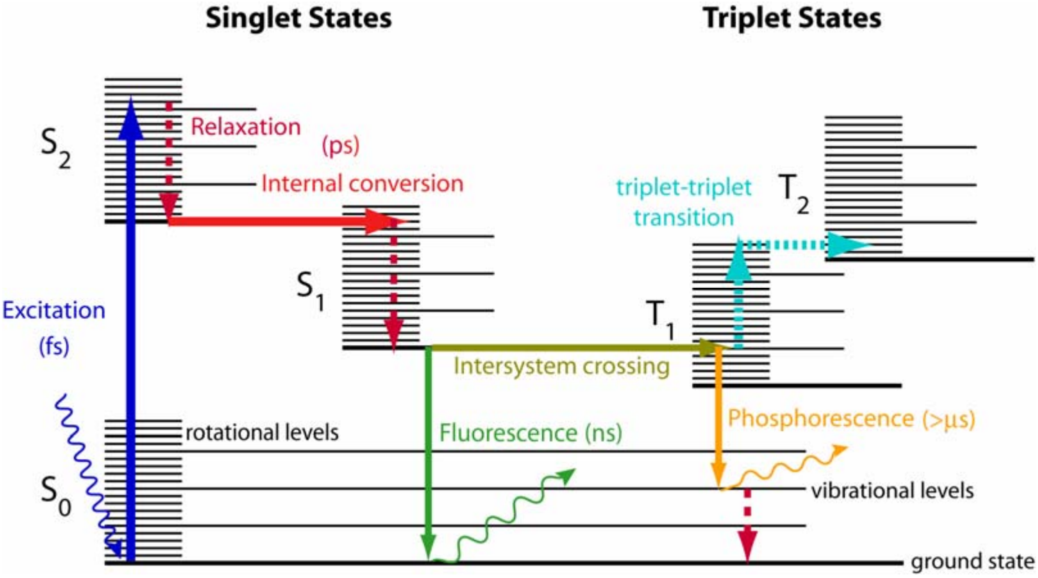

Figure 1.7 – Jablonski diagrams showing the energy states of a molecule and the times that the various steps in fluorescence excitation, emission and phosphorescence take. The electronic levels are indicated by thick black horizontal lines, whereas the vibration and rotational levels are represented by thinner lines. A photon with the appropriate wavelength is absorbed by the molecule and causes a transition to a high vibrational level of the excited electronic state S_2 (*dark blue arrows*). The molecule then undergoes rotational and vibrational relaxations (*dotted dark red arrows*) and internal conversion (*red arrow)* before it reaches the lowest energy level of S_1. Transition to the ground state usually occurs via emission of a photon, by fluorescence (*green arrows*). Alternatively the molecule might undergo intersystem crossing (*brown arrow*) and arrive at a triplet state, where it may cause phosphorescence emission (*orange arrows*) or triplet-triplet transitions *(light blue arrows*) that further delay the emission of light or prevent it altogether. Adapted from (Lichtman and Conchello, 2005).

Together, these phenomena bring the excited molecule to the lowest energy level of S_1 in picoseconds, without emission of radiation. Only then fluorescence occurs, as the molecule returns to any of the vibrational levels of S_0, emitting a photon with energy equivalent to this transition. The wavelength range of an emission spectrum thus reflects the different transitions from the lowest level of S_1 to the different rotation and vibrational levels of the ground state.

It usually takes the molecule a few nanoseconds before this transition from the lowest level of S_1 to the ground state occurs, a duration that is known as the excited state lifetime. The lifetime of a fluorophore can be reduced if another nearby molecule absorbs this energy in a non-radiative manner, preventing the fluorophore from emitting a photon (quenching). These lifetime reductions due to intermolecular interactions can be measured by a technique called Fluorescence Lifetime Imaging Microscopy (FLIM, see section 1.5.4). If the nearby interacting molecule is itself a fluorophore, the absorbed energy can in turn lead to its excitation and subsequent fluorescence, providing certain conditions are met. This phenomenon, known as Fluorescence Resonance Energy Transfer (FRET) can also be probed by a variety of techniques, providing information on intramolecular distances far below the resolution of an optical microscope (see section 1.5.4).

Fluorescence emission is not the only way a fluorophore can lose energy in order to return to the ground state. “Intersystem crossing” into a relatively long-lived triplet excited state (T_0, T_1, etc.) can also occur, whereby the electron inverts its spin state and changes the overall magnetic moment of the molecule. These “forbidden transitions” leave the fluorophore no easy pathway to the low energy ground state, as it has to undergo another “forbidden” spin state change before further relaxation can occur. It may take microseconds before this unlikely event takes place. Triplet states can sometimes reach the ground state by emitting a photon, in a process called phosphorescence, but they can also undergo triplet-triplet transitions into higher triplet states if another photon is absorbed, further delaying any light emission by the molecule. Fluorophores in a triplet-state are also prone to undergo photochemical reactions that irreversibly destroy their fluorescence (a phenomenon known as photobleaching) and/or cause phototoxicity (Lichtman and Conchello, 2005). All fluorophores will eventually photobleach upon extended excitation, as they can only experience a limited number of absorption and emission cycles.

The intrinsic brightness of a fluorophore is determined not only by its photostability, but also by its quantum yield and molar extinction coefficient (Shaner et al., 2005). The quantum yield (Φ) is a measure of the fluorophore’s total light emission over the entire spectral range. It is defined as the ratio between the numbers of emitted and total absorbed photons and has therefore a value between 0 and 1. The molar extinction coefficient (ε), or molar absorption coefficient, corresponds to the absorbance of light per unit path length and per unit of concentration of a given fluorophore. Its value, calculated as $\varepsilon = A / C$ (where A is the absorbance and C the fluorophore's concentration) reflects the probability of a photon to be absorbed by the fluorophore. Higher values for the molar extinction coefficient and the quantum yield will indicate a brighter fluorophore.

Fluorescent dyes, such as fluorescein isothiocyanate (FITC), have been used to tag molecules of interest, be it DNA or protein, ideally by binding to their targets in a very specific manner. Specificity is usually achieved in immunofluorescence techniques through the use of antibodies that recognize the target molecule, and to which the fluorophores are attached. The major disadvantage is that the cells have to be fixed and permeabilized before adding the fluorescently labeled antibodies to them. This rendered live cell imaging impossible, a situation which changed dramatically with the discovery of the green fluorescent protein (GFP).

1.4.2 The GFP Revolution

The Green Fluorescent Protein from the jellyfish *Aequorea victoria* was the first of the fluorescent proteins (FPs) to be discovered (Tsien, 1999). Its intrinsic visible light fluorescence, "slightly greenish in sunlight (…) and exhibiting a very bright, greenish fluorescence in the ultraviolet", as it was first described (Shimomura et al., 1962), is due to its chromophore, a *p*-hydroxybenzylideneimidazolinone (Cody et al., 1993) formed in an autocatalytic reaction from the amino acids 65-67 (Ser-Tyr-Gly) in the native protein (Reid and Flynn, 1997). The wild type 27 kDa monomer of *Aequorea victoria* GFP (avGFP) possesses an 11-stranded β-barrel that gives it a characteristic cylinder shape (β-can), 42 Å long and 24 Å in diameter, with the chromophore almost perfectly buried in a α-helix at the center of this cylinder (Figure 1.8A). This configuration is thought to be responsible for GFP's stability and resistance to denaturation by proteases and quenching by molecular oxygen or pH changes (Ormo et al., 1996).

Cloning of a complementary DNA (cDNA) for avGFP (Prasher et al., 1992) triggered a widespread interest in the protein, as it was realized it could be used as marker for gene expression or, remarkably, as an *in situ* fluorescent tag for virtually any cellular protein (Heim et al., 1995). This is done by fusing the coding sequence of GFP, either by its amino or carboxyl-terminal, in frame with the gene encoding the protein of interest. The resulting chimera can then be stable or transiently transfected into a cell, which will then produce the fusion protein itself (Schmid and Neumeier, 2005; Tsien, 1998).

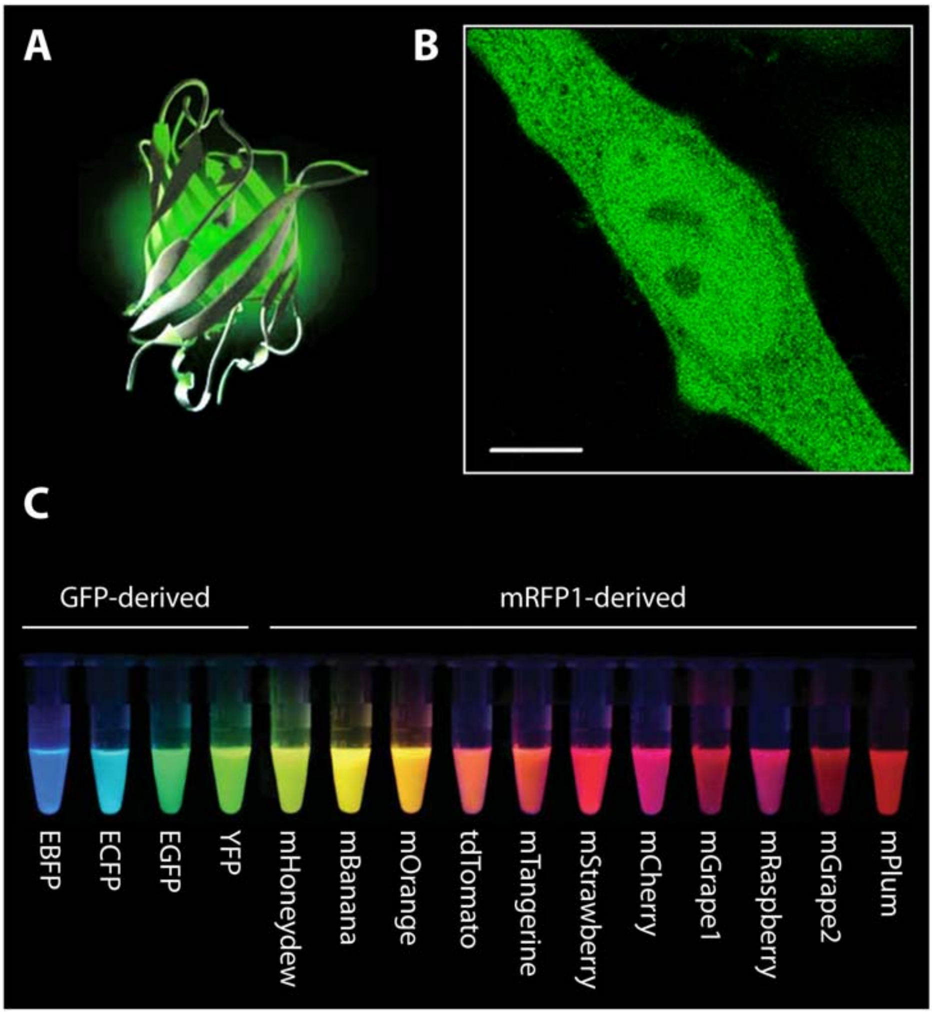

Figure 1.8 – The Green Fluorescent Protein and variants (A) GFP structure revealing a β-can arrangement with the chromophore buried inside the cylinder-shaped molecule. Adapted from the World Wide Web **(B)** Enhanced GFP (EGFP) expressed in a transfected human cell, visualized by confocal microscopy. Bar: 5 µm (Rino et al. *manuscript in preparation*) **(C)** Engineered fluorescent proteins, derived from GFP and the monomeric Red Fluorescent Protein (mRFP1), covering the full visible emission spectrum. Protein samples are shown in purified forms inside *Eppendorf* tubes. Adapted from (Tsien, 2005).

The tagged protein can therefore be visualized in living cells, in a minimally invasive manner, without the need for prior fixation and permeabilization (Figure 1.8B). Imaging of dynamic processes with time-lapse microscopy thus became commonplace with GFP tagging. More advanced applications that ingeniously take advantage of GFP's photobleaching properties, such as the Fluorescence Recovery after Photobleaching (FRAP) and the Fluorescence Loss in Photobleaching (FLIP) techniques (Schmid and Neumeier, 2005), can also be used to study the molecular dynamics of selected proteins (see section 1.5.3). Not all fusions are successful, though, as tagging with GFP can sometimes alter the endogenous protein folding, rendering it non-functional. It is always necessary to check for proper protein function via complementary studies, before any conclusions can be drawn from GFP-tagged protein experiments (Gerdes and Kaether, 1996).

Despite the early enthusiasm and its widespread use, the wild type avGFP still showed some deficiencies, such as an excitation spectrum with two peaks instead of one (at 396 and 475 nm), a relatively reduced maturation speed and a low molar extinction coefficient of 22,000 $M^{-1}cm^{-1}$, when compared to fluorescein's 80,000 $M^{-1}cm^{-1}$. More importantly, the protein also revealed a tendency to dimerize at high concentrations (Cubitt et al., 1995). Serious mutagenesis efforts aiming at optimizing avGFP's properties led to the development of an improved version of the protein, called enhanced GFP (EGFP). This optimized version of the fluorescent protein has two point mutations at amino acids 64 ($Leu^{64}\rightarrow$Phe) and 65 ($Ser^{65}\rightarrow$Thr) that confer it increased brightness ($\Phi = 0.60\,;\varepsilon = 56{,}000\,M^{-1}cm^{-1}$) and stability, with a single excitation peak at 488 nm and an emission maximum at 507 nm (Lippincott-Schwartz and Patterson, 2003; Shaner et al., 2005). Further avGFP mutagenesis trials yielded variants with differing absorption and emission spectra, such as the blue fluorescent protein (BFP), which has a $Tyr^{66}\rightarrow$His substitution that shifts the absorbance peak to 384 nm with emission at 448 nm (Heim and Tsien, 1996) and the cyan fluorescent protein (CFP; $Tyr^{66}\rightarrow$Trp; excitation peak: 433 nm, emission peak: 475 nm). Enhanced versions of BFP and CFP (EBFP and ECFP) were subsequently generated by combining their point mutations with those present in EGFP (Tsien, 1998). Once the crystal structure of avGFP was resolved, trial and error mutagenesis was substituted by rational fluorescent protein design, resulting in the development of the yellow fluorescent protein (YFP, excitation: 514 nm; emission: 527 nm), which has been continuously improving over the years (Patterson, 2004). While the second-generation enhanced YFP (EYFP) is more resistance to pH changes, for example, the more recent third-generation YFP derivatives, the "Citrine" (excitation: 516 nm; emission: 529 nm) and "Venus" (excitation: 515 nm; emission: 528 nm) proteins, have increased photostability and brightness, respectively, but there is not a single YFP version which is superior for all applications (Zhang et al., 2002). A variety of mutations aiming at reducing the limitations of avGFP descendents, including dimerization, chromophore formation and proper protein folding, have culminated in the development of vastly improved fluorescent markers which include monomeric versions of the blue, cyan, green and yellow versions of GFP (mBFP, mCFP, mGFP, mCitrine and mVenus (Zhang et al., 2002)) and also mCerulean (excitation: 433 nm; emission: 475 nm) (Rizzo et al., 2004) and T-Sapphire (excitation: 399 nm; emission: 511 nm) (Zapata-Hommer and Griesbeck, 2003), which are specially suited for FRET applications (see section 1.5.4).

On the other side of the spectrum, a red fluorescent protein from the coral *Discosoma*, called DsRed (Matz et al., 1999), was also mutated to generate a monomeric red fluorescent protein (mRFP1, excitation: 584 nm; emission: 607 nm) (Campbell et al., 2002), which still revealed insufficient brightness and photostability. Recent mRFP1 mutagenesis addressed these problems and culminated in the development of a plethora of new monomeric spectral mutants (Shaner et al., 2004), which range from the greenish mHoneydew (excitation: 487/504 nm; emission: 537/562 nm) to the far red mPlum (excitation peak: 590 nm; emission peak: 649 nm) and include the highly photostable and fast maturing mCherry (excitation peak: 587 nm; emission peak: 610 nm) (Figure 1.8C).

Further innovation came with the recent development of photoactivatable and photoswitchable fluorescent proteins (Lukyanov et al., 2005). These fluorophores are capable of pronounced changes in their spectral properties once irradiated with light of a specific wavelength and intensity. Photoactivatable GFP (PA-GFP) and photoswitchable CFP (PS-CFP) were both developed from avGFP, taking advantage of the wild type protein double excitation peaks. PA-GFP is the result of a single point mutation (Thr^{203}→His) in avGFP (Patterson and Lippincott-Schwartz, 2002). The non-photoactivated form of the protein is characterized by 400 nm excitation and 515 nm emission peaks, with almost no fluorescence emission when excited at 480 – 510 nm. Irreversible photoactivation by intense UV light (~ 400 nm) results in a 100-fold increase of green fluorescence (excitation: 504 nm; emission: 517 nm). Non-photoactivated PS-CFP shows cyan fluorescence instead, with an emission peak at 468 nm (Chudakov et al., 2004). Irreversible photoconversion with intense UV light then provokes a 300-fold increase in green fluorescence (excitation peak: 490nm; emission peak: 511 nm) accompanied with a 5-fold reduction in cyan fluorescence. Photoactivatable red fluorescent proteins have also been developed, such as the monomeric PA-mRFP (Verkhusha and Sorkin, 2005), which requires intense 380 nm activation to exhibit a 70-fold increase in red fluorescence (excitation: 578 nm; emission: 605 nm). Other photoconvertible proteins able to convert irreversibly from green to red upon UV illumination include Kaede (Ando et al., 2002), mEosFP and KikGR (Lukyanov et al., 2005). Reversible conversion, on the other hand, can be achieved with the tetrameric kindling fluorescent protein (KFP1), converted by 488 nm illumination (Chudakov et al., 2003) or Dronpa, which can be activated by 405 nm UV light and deactivated with 488 nm illumination (Ando et al., 2004). The recently developed Dendra (Gurskaya et al., 2006) is the first monomeric protein capable of green (488 nm) photoactivation.

Photoactivation or photoconversion at a specific location inside the cell allows for a selected population of tagged molecules to be rendered visible in a microscope. The dynamics of these molecules can thus be followed directly, without being masked by other similar, but non-photoactivated molecules (Chapman et al., 2005; Deryusheva and Gall, 2004). Photoactivation can thus be regarded as a perturbation to the steady state distribution of fluorescence that is complementary to that of photobleaching, ultimately offering new possibilities for the development of novel fluorescence applications (see section 1.5.3 and also Chapter 5).

1.5 Confocal Fluorescence Microscopy

“An ideal microscope would examine each point in the specimen and measure the amount of light scattered or absorbed by that point”, recalled Marvin Minsky, the inventor of the confocal microscope, in a memoir (Minsky, 1988). Minsky’s invention, which he called a “double focusing stage scanning microscope”, was far sighted and remained largely unnoticed for 30 years, before the use of fluorescence in the 1980s turned it into one of the most exciting instruments available to biologists (Amos and White, 2003). Confocal microscopes do not only improve the resolution of conventional fluorescence microscopes, but are also capable of slicing thin optical sections from living samples, allowing them to be rendered in impressive 3D reconstruction images (Conchello and Lichtman, 2005). The development of the confocal microscope stems from several roots, which include light microscopy, laser-illuminated optics and scanning techniques.

1.5.1 Principles of Light Microscopy

Light is an electromagnetic radiation with a certain wavelength (λ), frequency (υ), intensity and polarization. In vacuum, light waves propagate at speeds of ~ 3×10^8 ms^{-1}. If their wavelengths are comprised roughly between 400 and 700 nm, light waves can be detected by the human eye and interpreted as colors, ranging from red at the longest wavelengths to violet at the shortest wavelengths.

Light is also an elementary particle, called photon, with a certain momentum, energy and spin, but no mass or electric charge. In vacuum, photons travel at speeds of ~ 3×10^8 ms^{-1}. Photons are quanta of light with discrete energy levels that are perceived by the human eye as colors, ranging from the red at the lower energy levels to violet at the highest energy levels. Light intensity is determined by photon density: it can be increased or decreased by changing the number of photons present.

Because light simultaneously exhibits the properties of waves and particles, it is said to possess a dual nature, reflecting the Quantum Mechanic's concept of wave-particle duality which is also valid for matter. The energy (*E*) and frequency (υ) of a light wave/particle are related by Plank's constant *h* ($E = h\upsilon$), a fundamental physical constant. Its wavelength and frequency are also related to each other by the speed of light in vacuum *c* ($c = \lambda\upsilon$). When light is not traveling in vacuum, its speed is reduced by an amount indicated by the refractive index *n* of the material where it is propagating ($n = c/v$). In matter, *n* is always greater than 1. When a beam of light enters a medium with a different refraction index it keeps the same frequency but changes its wavelength. If the incident beam is not perpendicular to the surface of the interface between the two media, the direction of the beam will also change, and refraction is said to occur. The angles of the incident and refracted beams are given by Snell's law: $n_1 \sin\theta_1 = n_2 \sin\theta_2$ (where n_1 and n_2 are the refractive indexes of the first and second medium, θ_1 is the angle of incidence and θ_2 is the angle of refraction) (Figure 1.9A).

When moving to a denser medium, if the angle of incidence is higher than a critical value ($\theta_c = \arcsin(n_2/n_1)$), no refraction occurs and the incident ray is said to undergo total internal reflection. Refraction of light is responsible for a variety of phenomena which include the observation of mirages on the dry sands of a desert and the apparent bending of an object partially submerged in water. More importantly, refraction is also responsible for the light focusing properties of optical devices made of transparent materials (usually glass), which are known as lenses.

Lenses can be either positive or negative depending on whether they converge light into a single focal point (*F*), or diverge it into space. A thin bi-convex positive lens having two light-refracting surfaces and a central optical axis, such as the one represented in Figure 1.9B, will converge all light beams that are parallel to its optical axis and focus them on the focal plane. The distance from the lens to the focus is called the focal length (*f*). If a specimen is placed in the object plane of the lens (represented on the left-hand side of the lens by convention), at a distance *d* greater than the focal length *f*, the lens will form an inverted magnified “real image” of the object at a distance *d’* in the image plane (right-hand side of the lens).

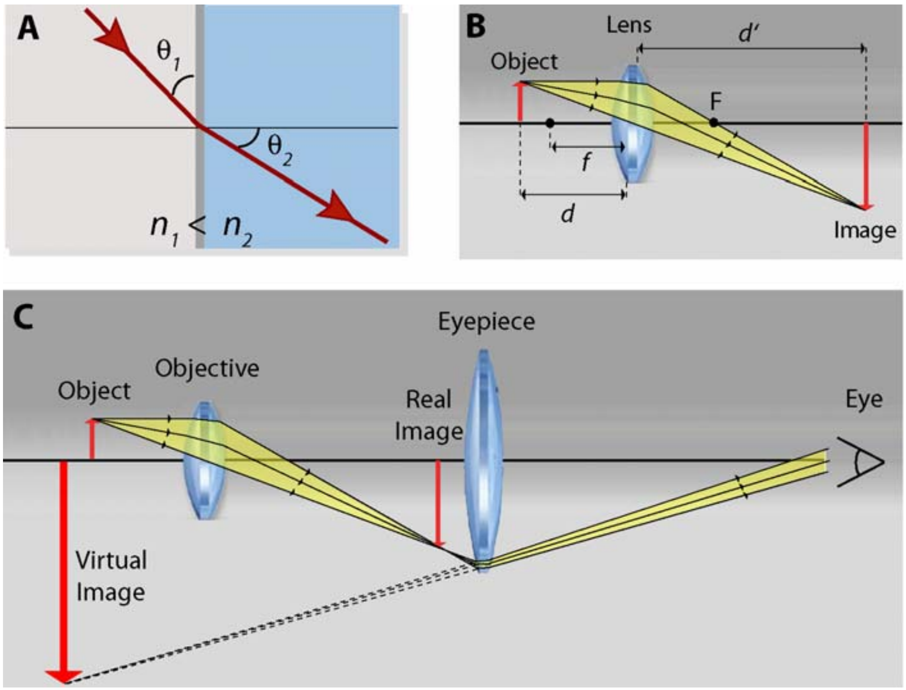

Figure 1.9 – Lenses and the compound microscope (A) Light refraction at the interface between two media with different refractive indexes (n_1 and n_2) **(B)** A positive lens uses refraction to converge light. If the object is at a distance *d* greater than the focal length *f*, the lens will focus the light beams to form an inverted, real image at distance *d’*. *F* represents the focal point. The optical axis is indicated by a horizontal thick black line **(C)** A compound microscope uses two lenses (the *Objective* and the *Eyepiece*) to create a magnified, inverted virtual image of the object.

The relation between these distances is given by $\frac{1}{d}+\frac{1}{d'}=\frac{1}{f}$, whereas the magnification is $M=-\frac{d'}{d}$ (its value is negative because the image is inverted).

However, if the specimen is placed in the object plane at a distance shorter than the focal length, the light rays will diverge from the lens as they can no longer be focused into the focal point. A real image cannot be formed then, but because the light rays will appear to come from a point behind the lens, they still form a non-inverted magnified “virtual image” in the object plane, with magnification given by $M = \frac{d'}{d}$. Used in this way, a single lens can work as a magnifier and thus constitutes the simplest microscope. It was with such an apparatus that van Leeuwenhoek was able to see what he called “animalcules” more than 300 years ago, and described many microorganisms that included protozoa and other unicellular organisms (Mazzarello, 1999). Microscopes can have an increased magnification if multiple lenses are used instead of just one. This is the concept of the compound microscope, developed by Hans and Zaccharias Jansen at the end of the sixteenth century. In its simplest design, the compound microscope consists of two lenses with their optical axis aligned (Figure 1.9C). The first lens, the objective, is placed closer to the object and creates a real, enlarged image of the specimen. This image (which is inverted) is subsequently magnified by the second lens, the eyepiece. This is done by placing the eyepiece close to the image formed by the objective, at a distance which is shorter than this lens focal length. The eyepiece then works as a magnifier, enlarging the real image of the objective into a virtual image which is positioned at a convenient distance for observation (~ 25 cm).

For more than two hundred years after their development, compound microscopes were not able to yield better resolution than simple microscopes because of defects in the manufacturing of lenses which distorted the images by a variety of mechanisms. The most common of these were chromatic, spherical and coma aberrations. Lenses whose refracting index depended on light’s wavelength were prone to cause chromatic aberrations, because the different colors could not be focused together on a single point, leading to image dispersion. Spherical aberrations were caused by lenses having spherical surfaces (almost all of them, because it is the more practical lens design) that were unable to focus light waves passing through its periphery in the same focal point as those passing through its center. This makes focusing impossible, as a point source of light always appears as a spot surrounded by a bright halo or a series of rings. Coma aberrations, on the other hand, are similar to spherical aberrations but are caused by off-axis light that is focused on planes different from the more central ones, provoking a comet-like image elongation (hence the name). These effects were obviously worsened as more lenses were added to a microscope and thus for a long time the simple microscope was also the best one. Only in the nineteenth century was the compound microscope able to surpass the simple microscope in performance. As it slowly evolved into a more reliable instrument, the compound microscope disclosed more and more details of cells and cellular structures such as the nucleus (Brown, 1833), a process which finally culminated in the formulation of cell theory (Schleiden, 1838; Schwann, 1839), more than two hundred years after its development.

Modern-day optical microscopes use one lens to correct the imperfections of another. Such composite lenses effectively correct all the aberrations which existed in the earlier microscopes, but do not improve the instruments resolution. The resolution of a microscope is usually defined as the minimum distance between two point objects that allows them to be distinguished at the image plane (Born and Wolf, 1993; Jonkman et al., 2003). This definition leads to some ambiguity, as there are several criteria for considering two objects as distinguishable (Stelzer, 1998). This difficulty in distinguishing two point objects in the image plane is a direct consequence of diffraction, a phenomenon due to the wave-like behavior of light.

Diffraction is the bending, spreading and interference of waves when they pass through a tight gap or near a barrier. It occurs with any type of wave and consequently, also with light waves that propagate through a lens. Light emanating from a point source object will scatter at the edge of the lens and subsequently recombine in a magnified image through constructive and destructive interference (Figure 1.10A). The image obtained is then composed of a myriad of overlapping light beams originating from the object plane. Because these image-forming light rays are diffracted, a single point source is never imaged as a point, but rather as a diffraction pattern which in the image plane consists of a central disk encircled by a series of fading rings (Airy pattern, Figure 1.10B).

The resolving power of a compound microscope is determined by its objective, with the eyepiece only increasing magnification but not resolution. The Rayleigh criterion defines resolution as the distance at which the maximum of an object’s Airy pattern is above the first minimum of the other object’s Airy pattern (Stelzer, 1998).

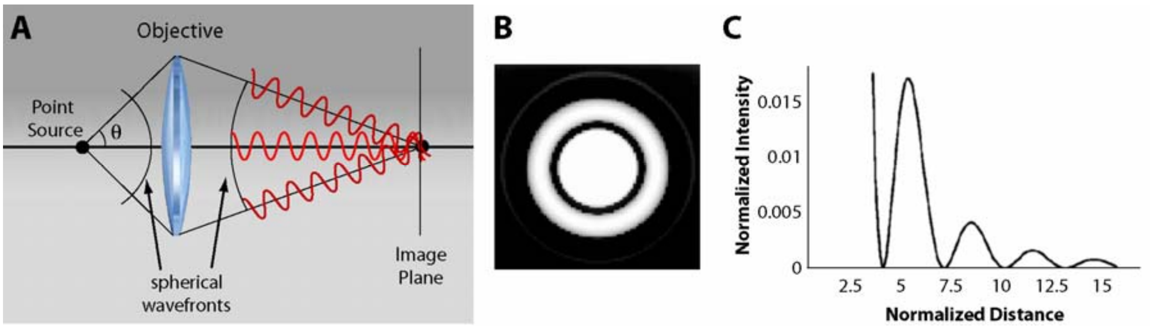

Figure 1.10 – The Airy pattern (A) A point source emits light waves in all directions. A fraction of these is captured by the objective lens, at a cone with a half-angle θ. The light waves are subsequently diffracted and interfere with each other at the image plane **(B)** The Airy pattern is the image of the point source observed in the image plane and consists of a central disk encircled by fading rings. Adapted from (Stelzer, 1998). **(C)** Normalized intensity distribution of a focused point source in the image plane as a function of distance to the optical axis. The scale was chosen so that the higher order maxima could be visualized. Adapted from (Stelzer, 1998).

This is the minimum distance at which these two objects are distinguishable. The lateral resolution of a microscope is then given by $r_{lateral} = \frac{0.61\lambda}{n\sin\theta}$, where λ is wavelength of emitted light, n is the refractive index of the lens and θ the half-angle of the cone of light accepted by the objective lens. The composite $n\sin\theta$ is called the numerical aperture (NA) of the lens, a most relevant parameter which is written conspicuously on every objective, yielding information about its light gathering properties. Objectives with higher NA values will collect more light and have a higher resolving power. However, this resolving power will always be limited by the wavelength of the radiation used, which in light-focusing microscopes implies a diffraction barrier for image resolution at ~ 200 nm. If the size the diffraction spot is the limiting factor in image resolution (rather than lens aberrations, for instance), the image achieved is said to be diffraction limited. The airy pattern also extends in the axial direction, with resolution given by $r_{axial} = \frac{2n\lambda}{NA^2}$.

Light microscopy is considered to have been established in 1873, when Ernst Abbe first demonstrated how the diffraction of light by both the specimen and the objective determined image resolution. Until then, much of microscope design had been trial and error. Abbe's work provided the ground for new lens design, by clearly defining the conditions which must be met in order to achieve a diffraction limited imaging system. The image of a point source object made by an optical device such as a microscope is also called the point spread function (PSF) of the instrument. The amplitude PSF corresponds to the electromagnetic field distribution in the focal region when a plane wave is focused. The intensity PSF, which is the modulus squared of the amplitude PSF, can be visualized by taking images of a point-like object, such as a microscopic bead. The extent of the PSF in different microscopes can thus provide information about their lateral and axial resolutions, and constitutes therefore a useful parameter in comparing the performance of different instruments (Jonkman et al., 2003).

Compound optical microscopes were continuously improved to increase the contrast between the objects of interest in the image and undesired background. The development of fluorescence microscopy provided the best means for this, as only the fluorescently tagged signal would appear visible against an otherwise black background. Fluorescence microscopy required emission and detection filters, as well as dichroic mirrors (beamsplitters) in order to separate the excitation light from the emission light (see section 1.4.1). In modern widefield epifluorescent microscopes, where the whole sample is bathed in light from a mercury or xenon lamp, the same objective is used to illuminate and collect light from a specimen. However, because the entire sample is illuminated, more than 90% of the light collected is out-of-focus fluorescence, which greatly reduces image detail (Conchello and Lichtman, 2005). “The serious problem is scattering. (…) every focal image point will be clouded by aberrant rays of scattered light deflected at points of the specimen that are not the point you're looking at”, diagnosed Minsky. “It occurred to me that the way to avoid all that scattered light was to never allow any unnecessary light to enter in the first place” (Minsky, 1988). His solution to the problem resulted in the invention of a new microscope, the confocal scanning microscope.

1.5.2 The Confocal Scanning Microscope

The “double focusing stage scanning microscope” Minsky invented is similar to a conventional optical microscope where the condenser lens (which is used to evenly illuminate the sample) is substituted by a lens similar to the objective. This lens is used to “image a pinhole aperture on a single point in the specimen” (Minsky, 1988), thus reducing the field of illumination to a point of light with dimensions determined by the pinhole aperture and the objective. The amount of light in the specimen is thus reduced by orders of magnitude, but the focal brightness remains the same. “Still, some of the initially focused light will be scattered by out-of-focus specimen points onto other points in the image plane” (Minsky, 1988). In order to reject those scattered rays, a second pinhole aperture is placed in the image plane that lies beyond the exit of the objective lens. “We end up with an elegant, symmetrical geometry: a pinhole and an objective lens on each side of the specimen” (Minsky, 1988) (Figure 1.11A) that cause the illumination and detection to share the same focus, hence the name confocal.

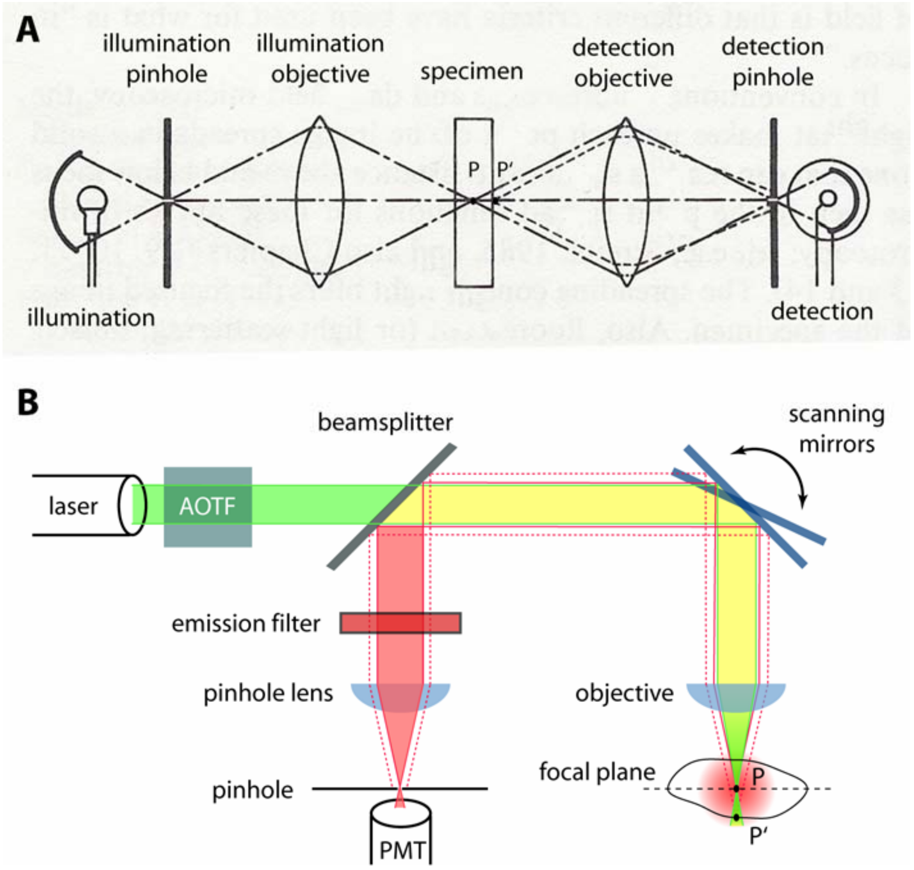

Figure 1.11 – The confocal microscope (A) Layout of the original confocal microscope invented by Marvin Minsky, with a pinhole and an objective on each side of the specimen. The illumination objective forms an image of the illumination pinhole onto a confocal spot *P* in the specimen. The detection objective forms an image of *P* onto the detection pinhole which is confocal with *P* and the illumination pinhole. A point *P’* would not be focused at either pinhole and so it would be less illuminated and light emanating from it would not pass the detection pinhole. Adapted from (Minsky, 1988) **(B)** Layout of a modern laser scanning confocal microscope. The excitation light (*green*) is directed to the sample by the scanning mirrors and focused into the specimen by the objective. The fluorescence emission (*red*) is separated from the excitation by them beamsplitter and the emission filter. Light emitted from a point *P’* which is not in the focal plane is blocked by the pinhole and therefore not detected by the photomultiplier (*PMT*). See text for details. Adapted from (Conchello and Lichtman, 2005).

Because the confocal microscope is only able to illuminate one single point at a time, the sample has to be scanned point by point in order to create an image. The image acquisition in a scanning microscope is thus slower than in widefield techniques, in which the entire image is acquired simultaneously. On the other hand, point by point scanning also allows for the precise control of the intensity of light that is used to excite each point, a key feature that is crucial for photobleaching experiments (see section 1.5.3). In his “double focusing” scanning microscope, Minsky chose to move the specimen and kept the optics fixed. Instead, modern confocal scanning microscopes use moving mirrors to deflect the light beams onto different points in the specimen (Figure 1.11B).

A single objective replaced the illumination and detection objectives in epi-illuminated confocal microscopes. The illumination pinhole is also absent in most modern confocal designs, because the light source is no longer an arc lamp (as the one Minsky used) but a laser beam, which is able to produce collimated coherent plane waves that are focused using the full NA of the objective onto an hourglass-shaped beam with maximum intensity at the focal point (the illumination PSF) (Conchello and Lichtman, 2005).

The intensity of the laser beam delivered to the sample is controlled by an acousto-optical tunable filter (AOTF), a device that relies on a specialized birefringent crystal whose optical properties vary upon interaction with an acoustic wave generated electronically. After being collimated, the laser beam is directed to the objective, which focuses the beam onto the specimen. The location of the beam in the focal plane is controlled by two scanning mirrors which are attached to galvanometers. Together with an additional lens, these mirrors constitute the scanning unit of the microscope which is able to move the laser illuminated spot in the *x* and *y* directions. The plane of focus can also be moved vertically in the sample (*z* direction) by simply adjusting the objective’s distance relative to the specimen. If fluorophores are present in the specimen, the laser beam will excite them throughout the illumination cone, with maximum intensity near the focus, and fluorescent light of a longer wavelength will be emitted in all directions (see section 1.4.1). Some of this light will be collected by the objective (the amount depending on the NA of the objective) and directed back to a beamsplitter, which separates it from the emission light of the laser. An emission filter is used to ensure only fluorescent light emitted by the sample reaches the pinhole lens, which subsequently focus light into the pinhole aperture, before being detected by a photomultiplier tube (PMT). This detection pinhole is in a plane conjugate to the focal plane and serves exactly the same purpose as in Minsky's original design, which is to reject light that originates from planes above and below the focal plane of the specimen. The confocal microscope is thus given depth discrimination capabilities (Stelzer, 1995) and an improved contrast in comparison with widefield microscopes because out-of-focus light does not contribute to image formation.

Confocal laser scanning microscopes (CLSMs) also have an increased resolution in both lateral and axial directions when compared to widefield microscopes. This is due to the differences in the illumination PSF of both instruments. Whereas in a widefield microscope the sample is illuminated with a uniform PSF, in a confocal microscope the illumination PSF is very similar to the detection PSF, and the convolution of both yields narrower peaks for the overall point spread function (Jonkman et al., 2003).

The improved resolution and the ability to obtain thin optical sections from living samples are impressive advantages derived from the point by point scanning technique, but this also gives the confocal microscope some disadvantages when it comes to image acquisition and sample viability. There are several factors which affect image acquisition in confocal microscopy. These include not only the NA of the objective used, but also the laser intensity, the pinhole size, the PMT gain, the scanning speed and the fluorophore concentration (Conchello and Lichtman, 2005). Noise, pixelation and image aberrations (Hell et al., 1993) can be generated by any of these factors, with the adding problem of excessive laser power causing fluorophore photobleaching and/or cell photodamage. A careful consideration of all these parameters is required for proper image acquisition in a confocal microscope.

Speed of image acquisition can be greatly increased by illuminating and detecting more than a confocal point at a time. This is the principle behind the spinning-disk (also called Nipkow disk) confocal microscope, which uses a disk with a series of pinhole apertures to simultaneously image several spots at the same time (Conchello and Lichtman, 2005). Each aperture in the disk illuminates a different point on the specimen and the emitted fluorescence is again focused into another pinhole aperture in the same, or another disk, before being detected by a charge-coupled device (CCD) camera. Rotation of the disks at a high speed results in the generation of an image at video rates (~ 30 frames per second), a feature which is only barely achieved by single pinhole CLSMs if "resonant" oscillating mirrors are used instead of galvanometer-driven ones (Wang et al., 2005). However, because scanning disk microscopes lack the ability to control laser intensity in a defined array of pixels, their use for photobleaching techniques (see below) is reduced.

Optical sectioning can also be performed by alternative microscopy approaches such as multi-photon microscopy. Deep tissue imaging is usually performed with two-photon microscopy (Helmchen and Denk, 2005), a technique that uses longer wavelengths to excite fluorophores in a limited focal region. The excitation of these fluorophores depends on the "simultaneous" absorption of two photons with half the energy of the single photon used in standard fluorescence microscopy. Optical sectioning is thus a result of the required high photon density that is only achieved at the focal spot. Because the illumination wavelength is nearly twice as that of the confocal, the PSF of a two-photon microscope is wider, and therefore the resolution is worse, than in a confocal system (Jonkman and Stelzer, 2002).

Improving the resolution of a confocal system usually requires leaving the light microscopy field and use electron microscopy instead. Since electrons also possess a dual wave/particle behavior, with a characteristic wavelength that is much shorter than that of light, they can also be used to create images of cellular samples. The resolution of a scanning microscope that uses a focused beam of electrons instead of a beam of light can be as high as ~ 0.8 Å, which allows for subcellular structures such as the Golgi apparatus, mitochondria and the nuclear envelope (see Figure 1.1 in section 1.2.1) to be observed in higher detail, albeit in fixed, rather than living samples (Marco et al., 2004).

It is possible to overcome the diffraction barrier in fluorescence microscopy, however, by taking advantage of the nonlinear excitation properties of fluorophores. Fluorescence (spontaneous emission) can be stopped, or quenched, by the phenomenon of stimulated emission, which forces the molecules to relax back to the ground state before emitting a photon (see section 1.4.1). A relatively recent technique known as stimulated emission depletion (STED) microscopy (Bain et al., 2003; Dyba et al., 2003; Hell and Wichmann, 1994; Willig et al., 2006) achieves this by using two lasers instead of one to illuminate the sample. The concept of STED is to reduce the size of the fluorescent spot in a scanning microscope by depleting the excited state of the fluorophores located at the outer regions of this spot. The excitation is first performed by an ultra short (0.2 ps duration) laser pulse that is focused onto a diffraction limited spot in the sample, as in a confocal system. Depletion follows almost immediately, caused by a second laser pulse of 40 ps, tuned to the red edge of the spectrum and with a particular focal distribution that resembles that of a doughnut (Klar et al., 2000). This focal distribution is achieved by using the interference properties of a special phase plate through which the depletion laser pulse has to pass. The diffraction barrier is broken by saturating the depletion everywhere in the focal region except at the central minimum of the doughnut-shaped distribution. Only fluorophores that happen to be close to the focal point contribute to the detected signal and the resolution is thus improved beyond the diffraction barrier, recently reaching values of 15-20 nm in biological samples (Donnert et al., 2006).

1.5.3 Photobleaching techniques: looking into molecular dynamics

All biological phenomena are dynamic. The advent of live cell imaging using GFP (or other fluorescent proteins) as a molecular tag triggered a large number of studies on the localization and dynamics of cellular proteins. Virtually any cellular structure can be visualized by fluorescently tagging its constituent molecules. Time-lapse microscopy studies with such tagged proteins soon revealed a highly dynamic cellular environment (Eils et al., 2000; Marshall et al., 1997; Misteli et al., 1997; Muratani et al., 2002; Platani et al., 2002). However, even though the movement of cellular structures could be tracked over time and even quantified, the dynamics of its individual component molecules inside the cell remained elusive for most cases, as they could only be detected at the scale of the cellular structures they belong to (Lippincott-Schwartz et al., 2003). Rather than simple time-lapse microscopy, the analysis of the kinetic behavior of GFP-tagged proteins requires more advanced fluorescence imaging methods such as the techniques of fluorescence recovery after photobleaching (FRAP) and fluorescence loss in photobleaching (FLIP), that ingeniously take advantage of GFP’s photobleaching properties.

Fluorescence Recovery after Photobleaching (FRAP)

Photobleaching (see section 1.4.1) is usually avoided in fluorescence microscopy. The irreversible loss of fluorescence by dye molecules is considered the most serious reason why fluorescent signals are not as bright as they should be, and special care is usually taken at using no more light than absolutely necessary to image a specimen (Conchello and Lichtman, 2005).

However, instead of being avoided altogether, photobleaching can also be used in a controlled way as a means of perturbing the distribution of fluorescent molecules in a sample. Subsequent relaxation back to the steady state distribution can then yield information on molecular dynamics. The first precise measurements on the lateral mobility of surface proteins in the living cell were carried out using this deliberate photobleaching process more than thirty years ago (Cone, 1972; Poo and Cone, 1973). The technique, which was subsequently performed in a variety of cell surface membranes, has been given various names, such as fluorescence microphotolysis (FM) (Edidin et al., 1976; Peters et al., 1974), fluorescence photobleaching recovery (FPR) (Axelrod et al., 1976b; Eldridge et al., 1980), fluorescence recovery after photobleaching (FRAP) (Braga et al., 2004a; Jacobson et al., 1976) or even fluorescence redistribution after photobleaching (also FRAP) (Houtsmuller and Vermeulen, 2001; Koppel, 1979).

In FRAP, a selected region of interest (ROI) in a cell is illuminated with a high intensity focused laser beam (Figure 1.12A). As a consequence, fluorescently tagged molecules present within that ROI during the bleach pulse are irreversibly photobleached. Subsequent movement of bleached molecules out of the bleached region and movement of surrounding unbleached molecules into the bleached area then lead to a recovery of fluorescence, which is monitored over time at low laser power to prevent further bleaching. The rate of fluorescence recovery is related with the overall mobility of the molecule which, depending on the protein being studied, can be the result of diffusion, binding/association, transport processes or a combination of all these (Lippincott-Schwartz et al., 2003). Fluorescence recovery curves (Figure 1.12B) are typically obtained after the recovery data is normalized to correct for fluorescence loss due to imaging (Phair and Misteli, 2000).

The recovery event is usually followed until a fluorescence intensity plateau is achieved. If the protein under study is completely mobile, this plateau will correspond to the initial pre-bleach fluorescence value, provided the bleach area is much smaller than the total area the protein is allowed to roam (typical FRAP experiments in the nucleus of living cells, for instance, are performed in circular regions with a diameter of ~ 1 μm (Braga et al., 2004a; Phair and Misteli, 2000)).

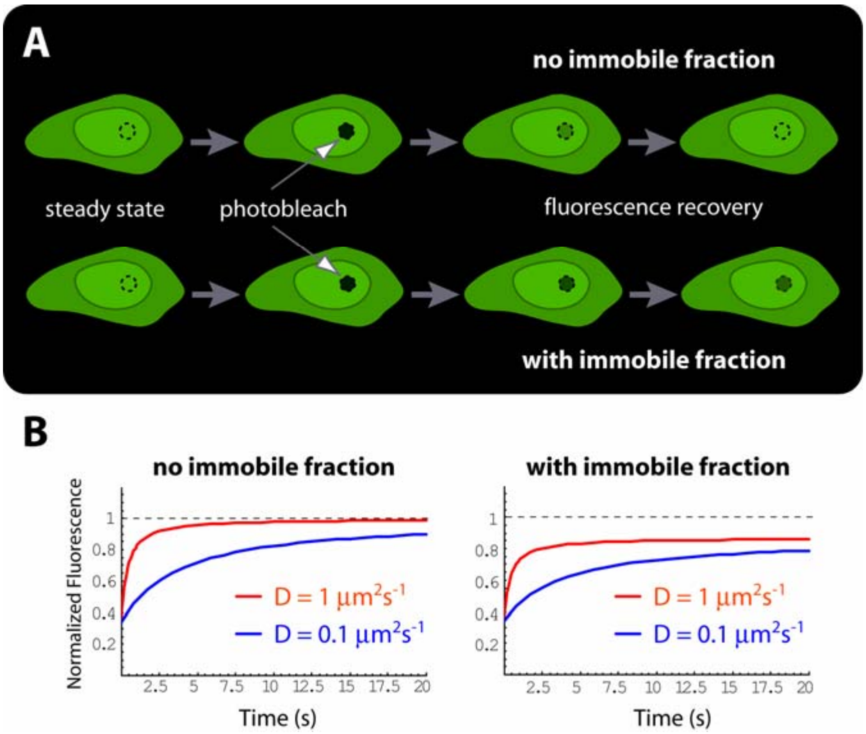

Figure 1.12– Fluorescence Recovery after Photobleaching (A) A cell expressing fluorescently tagged molecules is imaged at low laser intensity before and after photobleaching of a circular region of interest (*dashed black contour*). Complete fluorescence recovery of the bleached area only occurs if there is no immobilization of fluorescent molecules at the bleached region. **(B)** Fluorescence recovery in the bleached area is monitored over time and plotted in a FRAP curve. The graphs depict simulations of FRAP experiments for molecules diffusing at 1 $\mu m^2 s^{-1}$ (*red lines*) and 0.1 $\mu m^2 s^{-1}$ (*blue lines*) in a situation where there is no immobile fraction (*left graph*) and where 20% of the molecules are immobile at the bleach region (*right graph*).

If the bleach area is too big, a large percentage of the total number of fluorescent molecules will be bleached, and the total fluorescence of the cell will decrease. If this is not the case though, and still the plateau does not correspond to the initial pre-bleach value, then a percentage of molecules could be permanently immobilized in the bleach area, due to binding or other tethering mechanisms. Longer acquisition times should be performed to ensure this is the case, as “immobile fractions” can often correspond to transiently bound molecules whose binding kinetics are longer than the time scale of the FRAP experiment.

It should be emphasized that FRAP recovery curves always reflect the dynamic behavior of a system in a steady-state situation. Only the fluorescent tag

(GFP or other fluorescent protein) that is attached to the molecule of interest is affected by photobleaching. The tagged protein is thus rendered invisible to the microscope, but it is not destroyed or altered in any other form. Despite the decrease in the number of fluorescent molecules, the total number of molecules (bleached and unbleached) are generally kept constant throughout the experiment and their functional properties remain unchanged (Lippincott-Schwartz et al., 2003; Phair et al., 2004b).

FRAP can be performed with most standard confocal laser scanning microscopes, which adds to the increased availability and popularity of the technique (Braga et al., 2004b). The intensity of the laser beam can be controlled by the AOTF in each pixel of the image, thus allowing for the bleach region to be defined in virtually any shape or pattern (Lippincott-Schwartz et al., 2003). Switching between a low intensity laser beam (used in scanning) and a high intensity illumination (used for bleaching) occurs in microseconds (Klonis et al., 2002), which implies that bleaching of a circular region with a diameter of 1 μm can be performed in milliseconds. Depending on the kinetic behavior of the molecule under study, a millisecond long bleach-pulse can be considered almost instantaneous (for molecules with low mobility rates) or otherwise too slow to prevent significant diffusion to occur during the bleach procedure (for molecules with a high mobility rate) (Braga et al., 2004a).

The most straightforward FRAP application is to selectively bleach an organelle or cellular compartment to reveal information on the mobility of its component molecules (Lippincott-Schwartz et al., 2001). Whether a cellular structure is formed by stably bound proteins or otherwise cycling molecules can be simply essayed by performing this type of FRAP experiment (Festenstein et al., 2003; Lippincott-Schwartz and Zaal, 2000). Likewise, proteins can be probed for shuttling activity between the nucleus and the cytoplasm (or other cellular compartments) by performing FRAP in one of these compartments (Howell and Truant, 2002; Koster et al., 2005). By qualitatively comparing the recovery curves for the same molecule in different conditions (e.g. under drug treatment or after the introduction of mutations in the protein sequence), one can also probe for mobility changes that are of biological significance (Desterro et al., 2003; Gialitakis et al., 2006; Tavanez et al., 2005).

More quantitative approaches in the analysis of FRAP experiments aim at extracting relevant parameters that can be used to compare two different recovery curves. One such parameter is the half-time of recovery, or any other time point at which the fluorescence in the bleached region reaches a defined percentage of recovery (Cheutin et al., 2003; Harrer et al., 2004; Sunn et al., 2005). Alternatively, one can also measure the percentage of recovery at a fixed time point for different FRAP curves (McDonald et al., 2006).

Fitting the recovery data to a given mathematical function is also a possibility. Curve fitting of FRAP data is used in mathematical modeling to determine parameters that are more closely related to the kinetic behavior of the protein, such as its diffusion coefficient (see section 1.6.1), immobile fraction or binding/dissociation rate constants (see section 1.6.2) (Carrero et al., 2003; Klonis et al., 2002; Phair et al., 2004a; Phair and Misteli, 2001; White and Stelzer, 1999). An empirical fitting formula, for instance, was devised for strip-bleaching FRAP, assuming one-dimensional recovery in the calculation of protein diffusion coefficients in membranes (Ellenberg et al., 1997). Another approach is to fit the recovery data with a single exponential function (Belgareh et al., 2001; Lang et al., 1986) or a sum of exponentials (Handwerger et al., 2003; Kimura and Cook, 2001). Nevertheless, special care should be taken when FRAP data is fitted with poly-exponential functions, particularly when diffusive processes have to be taken into account in binding-related models (Sprague et al., 2004). Even though diffusion-like recovery curves can sometimes be fitted with two or more exponentials (as in (Kimura et al., 2002)), the extensive work of Sprague and coworkers has recently shown that this type of fitting often yields incorrect information, with estimated binding parameters that can be off by two orders of magnitude (Sprague et al., 2006).

Quantifying the mobility rates and binding kinetics of molecules inside the cell is not an easy assignment. Over the years, many quantitative methods were devised to extract reliable diffusion and binding parameters from different FRAP data. The first of these was developed thirty years ago, by Axelrod and coworkers, for proteins that were diffusing in a membrane (Axelrod et al., 1976a). In Axelrod's setup, photobleaching was performed by a stationary high-intensity laser beam focused in a small spot of the membrane. Fluorescence recovery was monitored by a non-scanning microscope using the same, although greatly attenuated, laser beam. The theoretical recovery curves for the idealized FRAP cases of pure two-dimensional diffusion, uniform flow and simultaneous diffusion and flow were devised under the assumption that the membrane was an infinite two-dimensional medium (recovery would only occur from diffusion of molecules in the same plane) and that bleaching took a negligible amount of time compared to diffusion. Under these conditions, the normalized fluorescence recovery in a circular bleach area (with a Gaussian fluorescence intensity profile) due to pure diffusive processes could be described by the curve: $f(t) = \sum_{n=0}^{\infty}\left[(-\kappa)^n / n!\right]\left[1 + n\left(1 + 8Dt/\omega^2\right)\right]^{-1}$, where κ is the bleach constant (a measure of the amount of molecules bleached), ω is the bleach area radius (half-width at e^{-2} height of the Gaussian intensity profile) and D is the diffusion coefficient. The immobile fraction, on the other hand, could be calculated with the formula: $IF = \left[\hat{F}(-) - \hat{F}(\infty)\right] / \left[\hat{F}(-) - \hat{F}(0)\right]$, where $\hat{F}(-)$ represents the fluorescence before bleaching, $\hat{F}(\infty)$ the final fluorescence plateau and $\hat{F}(0)$ the fluorescence immediately after bleaching. A simplified procedure for FRAP routine analysis was also presented, consisting of a three point fit of the data which used the half-time of recovery ($\tau_{1/2}$) and the bleach area radius (ω) to calculate the diffusion coefficient D according to the formula: $D = (\omega^2 / 4\tau_{1/2})\gamma_D$, where γ_D is a parameter that depends upon beam shape, type of transport and the amount of bleaching (κ) (Axelrod et al., 1976a).

The pioneer work of Axelrod and others established the basis of photobleaching theory, which at the time was only used to probe the mobility of fluorescently tagged constituents of the cellular membrane (Houtsmuller and Vermeulen, 2001). The development of the confocal laser scanning microscope in the 1980s facilitated the implementation of the technique, but it was the revolution caused by GFP tagging of intracellular proteins that ultimately turned FRAP into a very popular tool for studying the behavior of proteins in living cells (Houtsmuller, 2005). Based on Axelrod's theory, several other mathematical approaches to the analysis of FRAP data were developed according to the shape and intensity profile of the bleached area. Rectangular intensity distributions (Soumpasis, 1983), strip bleaching (Houtsmuller et al., 1999; Presley et al., 1997) or periodic bleaching patterns (Koppel and Sheetz, 1983; Smith and McConnell, 1978) were used by several investigators. The later relied on spatial Fourier analysis to solve the diffusion equation (see section 1.6.1), an approach that was also used for circular ROI bleaching (Berk et al., 1993;

Tsay and Jacobson, 1991) but revealed itself inappropriate for CLSMs, because of the relatively low signal-to-noise ratios and potential bleaching during image acquisition.

Three-dimensional models were developed specifically for CLSMs equipped with low NA lenses, using either a stationary beam for bleaching (Blonk et al., 1993) or a disc-shaped geometry that is bleached by the scanning laser of the CLSM (Braeckmans et al., 2003). Both methods could still be applied with high NA lenses, provided that the sample thickness was smaller than the axial size of the bleaching PSF, but in any case required short bleaching pulses in order to minimize diffusion during the bleach phase. Two-dimensional (2D) and three-dimensional (3D) models have also been developed based on numerical approaches (Kubitscheck et al., 1994; Kubitscheck et al., 1998; Peters and Kubitscheck, 1999) which require, however, intense computations that are too complex for practical cell biology usage.

A new approximate FRAP model that can be used in any standard CLSM was developed recently in order to solve these limitations (Braga et al., 2004a). This method takes into account diffusion during bleaching and is valid for objective lenses with high NA, in both 2D and 3D approximations. The bleaching profiles generated by the scanning beam of a CLSM are approximated by an exponential of a Gaussian (both in the radial and axial directions). When compared to immobile molecules, diffusion of highly mobile proteins during the bleach phase leads to a less pronounced, larger-radius postbleach profile. Fitting these postbleach profiles to an exponential of a Gaussian shape yields values for the bleaching efficiency (K_M) and profile width (ω_M) of mobile molecules which are different than those expected for immobile proteins. An analytical solution for FRAP recovery curves is obtained by solving the diffusion equation with such exponential of a Gaussian bleach shapes, thereby implicitly taking diffusion during bleaching into account. The method is shown to be accurate for a wide range of diffusion coefficients and suitable for use in any standard CLSM with any type of objective. In particular, it yields better estimates for the diffusion coefficient for highly mobile molecules than Axelrod's formula, which systematically underestimates them (Braga et al., 2004a).

The diffusion coefficient is the most prominent parameter obtained from a FRAP experiment. However, most functional proteins interact with cellular structures and therefore do not display a pure diffusive behavior (Carrero et al., 2004b). Protein interactions affect FRAP recoveries either by reducing the measured diffusion coefficient (which is then termed an effective diffusive coefficient, see section 1.6.2) or by altering the shape of the recovery curve altogether. The size of the bleach area can be varied to confirm whether we are in the presence of a pure diffusive recovery or not. For circular bleach regions, the recovery will change with an ω^2 dependence (where ω represents the bleach radius) for diffusive movements only (Wu et al., 1978). Quantitative approaches to extract binding data from FRAP experiments have also been devised over the years. Reaction-diffusion models (see section 1.6.2) were developed assuming that one of the substrates was immobilized and that the recovery was limited either by diffusion (Kaufman and Jain, 1990) or by the chemical reaction itself, assuming that diffusion could be safely ignored (Bulinski et al., 2001; Dundr et al., 2002; Kaufman and Jain, 1991; Phair et al., 2004a). Compartmental modeling (see section 1.6.1) was also used in FRAP experiments with rectangular bleach regions in an attempt to simplify the full reaction-diffusion model (Carrero et al., 2003). Again, assuming a reaction-limited case, the rate constants for binding could be extracted from exponential fits of the recovery curve (Carrero et al., 2004a). Nevertheless, the diffusion coefficient could not be estimated in a straightforward manner and both the appropriateness of the assumptions made and the quality of the estimates have been questioned by others (Sprague et al., 2004).

A thorough, systematic, analysis of spot photobleaching FRAP applied to reaction-diffusion systems was presented by Sprague and coworkers (Sprague et al., 2004). A complete solution for either single or multiple independent binding interactions was found by performing Laplace transforms of the reaction-diffusion equations. The inverse transform of this analytical solution yields a predicted FRAP recovery as a function of time, which can be fitted to experimental data. All possible FRAP behaviors for a single reaction in the presence of diffusion were studied and three simplified cases were described as being “pure-diffusion dominant” (free diffusion), “effective diffusion” (when the reaction process is much faster than diffusion) and “reaction dominant” (when diffusion is very fast compared to binding and to the FRAP time-scale). Depending on the diffusion coefficient and the binding rates of the chemical reaction (k_{on} and k_{off}, see section 1.6.2), FRAP recovery curves can be successfully studied with one of these simplified approaches or with a “hybrid model” analysis only, which can predict the ratio between diffusive and binding parameters rather than their unique values (Sprague et al., 2004). In particular, this study showed that slow FRAP recovery curves do not necessarily imply a reaction-limited case (where diffusion can be safely ignored) and that fitting a poly-exponential function to a FRAP recovery curve may yield parameters which are unrelated with the nature of the processes that are occurring (Sprague and McNally, 2005). Ignoring a role for diffusion when modeling binding to a single spatially localized cluster of binding sites can also lead to serious errors in parameter estimation, as shown in a follow-up study by the same authors (Sprague et al., 2006).

In a more recent study, the reaction-diffusion equations were solved numerically using a finite difference approach (see section 1.6.1), which allowed for the real cell geometry and inhomogeneous distributions of binding sites to be taken into account (Beaudouin et al., 2006). Non steady-state conditions, such as those present in slowly assembled cellular structures, are addressed in another recent work, which devised an approximate method for determining the binding rate constants, together with the rates of assembly and disassembly of the structure (Lele and Ingber, 2006).

Fluorescence Loss in Photobleaching (FLIP)

Variants of the FRAP technique started to be devised shortly after the development of this photobleaching method. The first of these was called continuous fluorescence microphotolysis (CFM), and consisted in replacing the single bleach pulse used in FRAP with continuous bleaching (Brunger et al., 1985; Peters et al., 1981). Fluorescence intensity in the bleached area was recorded over time, as in FRAP. This fluorescence would decrease exponentially, provided that the bleaching time was similar to the characteristic diffusion time. Estimates of diffusion coefficients, together with binding parameters could then be obtained by fitting exponentials to the fluorescence loss (Wachsmuth et al., 2003).

Fluorescence Loss in Photobleaching (FLIP), also called fluorescence loss induced by photobleaching, is similar to CFM but uses repetitive bleach pulses rather than continuous bleaching. In addition, the fluorescence loss is not measured in the bleached area but in a distant region instead (Figure 1.13A) (Cole et al., 1996). FLIP is mainly used to probe for protein mobility and continuity between cellular compartments (Lippincott-Schwartz et al., 2001). In this approach, a cell expressing fluorescently labeled proteins is repeatedly imaged between each bleach pulse. Any regions in the cell that are connected with the bleached area will also lose fluorescence due to movement of proteins into the bleached region. By contrast, the fluorescence in unconnected distant areas will not be affected by bleaching (Goodwin and Kenworthy, 2005; Lippincott-Schwartz et al., 2003).

Even though the rate of fluorescence loss is directly related with the kinetics of the bleached molecules, few attempts have been made at using FLIP as a quantitative tool to estimate mobility parameters, such as diffusion coefficients. Kinetic modeling approaches have been applied to FLIP experiments in order to derive association and dissociation rate constants for proteins in nuclear compartments (Phair and Misteli, 2000; Phair and Misteli, 2001). These approaches, however, assumed that the proteins were essentially in a reaction-dominant regime, were diffusion could be safely ignored (the “free” pool of diffusing protein was always assumed to be “well-mixed” in the nucleus) (Phair et al., 2004a).

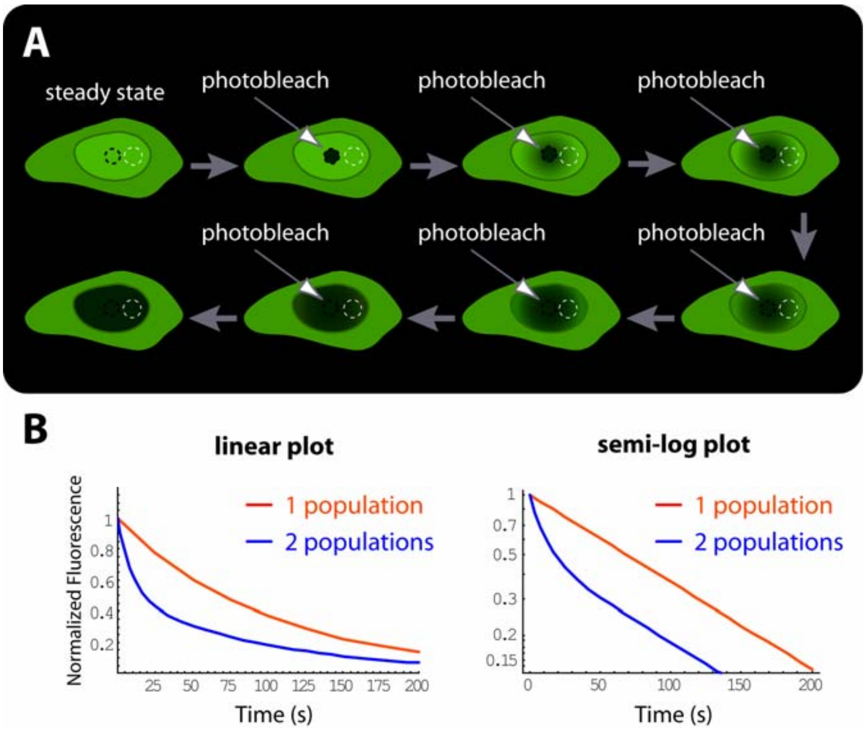

Figure 1.13 – Fluorescence Loss in Photobleaching (A) A cell expressing fluorescently tagged molecules is repeatedly bleached on a circular region of interest (*dashed black contour*) and imaged between bleach pulses. Fluorescence loss is monitored over time in a different region (*dashed white contour*) **(B)** Fluorescence loss in the region of interest is normalized and plotted in a FLIP curve. The graphs depict the same simulations of FLIP experiments for a single population of diffusing molecules (*red lines*) and a mixture of two independent populations present in equal amounts (*blue lines*). A single diffusing population will appear as a single exponential on a linear plot (*left graph*) and a straight line in a semi-log plot (*right graph*). See text for details.

FLIP can also be used to identify two independent populations of diffusing molecules in a living cell nucleus, allowing, in addition, to estimate the proportion of each one of them, based on the observed exponential decay of fluorescence (Calapez et al., 2002). Such information cannot be obtained from a FRAP experiment, as a mixture of two mobile populations yields a single diffusion coefficient estimate, which will be lower than the weighted mean of the individual diffusion coefficients of each population (Braga et al., 2004b). In this FLIP setup, the fluorescence decline is mainly due to diffusion of tagged molecules into the bleach area during each bleach pulse. If there is a single population of diffusing molecules, the normalized loss of fluorescence will follow an exponential curve (a straight line when plotted on semi-log graphs). However, if there are two populations (one diffusing faster than the other), fluorescence decay will correspond to the sum of two exponentials (Figure 1.13B). A novel method to characterize and estimate the mobility rates of these different populations of diffusive molecules by FLIP is presented in Chapter 4. The new method allows for the determination of both the proportion and the effective diffusion coefficient of each population of molecules, thus constituting the first quantitative approach in FLIP to measure mobility parameters of molecules.

Nucleocytoplasmic shuttling activity of tagged molecules can also be assessed qualitatively with FLIP, by repeatedly bleaching a small region either in the nucleus or in the cytoplasm (Koster et al., 2005). However, this approach is not appropriate when the steady-state levels of fluorescence are such that the vast majority of protein is present in one of the compartments and virtually absent in the other. A novel and more suitable method to quantitatively determine the kinetics of a shuttling protein in such cases is presented in Chapter 5. This new approach integrates FLIP with photoactivation (see section 1.4.2) and uses a two-compartment model to study the kinetics of a shuttling protein. The novel method was successfully applied in the estimation of the time of permanence inside the nucleus of the export factor TAP/p15 (see section 1.3.4).

Additional fluorescence methods for measuring molecular mobility

Bleaching an entire cell or cellular compartment with the exception of a region of interest is the concept behind the inverse FRAP (iFRAP) technique (Figure 1.14A).

Fluorescence loss, instead of recovery, is subsequently monitored over time in this region (Figure 1.14B) thus yielding information on the mobility rate and/or residence time of the tagged protein in that area (Dundr et al., 2002; Lippincott-Schwartz et al., 2003).

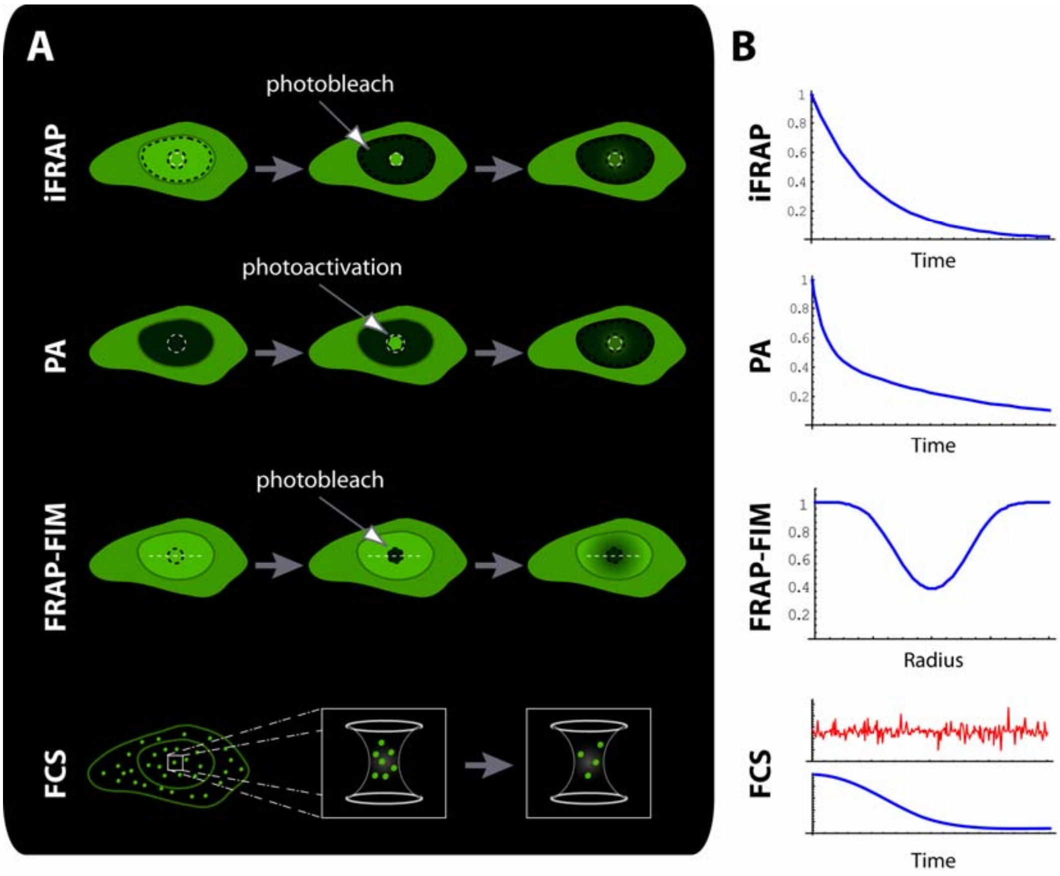

Figure 1.14 – Additional fluorescence methods for measuring molecular mobility parameters (A) Schematics of the inverse FRAP (*iFRAP*), photoactivation (*PA*), FRAP for immobilization measurement (*FRAP-FIM*) and fluorescence correlation spectroscopy (*FCS*) techniques. Bleached/photoactivated regions are outlined by dashed black contours. Monitored regions are outlined by dashed white circles (*iFRAP* and *PA*) or by a dashed white line (*FRAP-FIM*). In *FCS* the monitored region is limited to a focal volume of less than one femtoliter (*hourglass-shaped volumes*) **(B)** Normalized fluorescence curves obtained from the different techniques are plotted over time (*iFRAP* and *PA*) or over the bleach radius (*FRAP-FIM*). In FCS, the fluorescence fluctuation curves (*red graph*) are used to calculate the autocorrelation function (*blue graph*). See text for details.

Because iFRAP requires photobleaching to be performed in such large areas, a considerable amount of time is spent in the bleach process, rendering the technique appropriable only for molecules with slow kinetics such as GFP-tagged nucleoporins that have high residence times at the NPCs (Rabut et al., 2004a). Photoactivation (PA) or photoconversion techniques (see section 1.4.2) circumvent this limitation by introducing the same steady-state perturbation (highlighting molecules in the region of interest only) albeit in a much reduced time interval. In addition, newly synthesized molecules remain unobserved, as only the photoactivated pool is visible (Lippincott-Schwartz et al., 2003).

FRAP for immobilization measurement (FRAP-FIM) specifically aims at quantifying the percentage of immobile molecules in a given region of the cell (Houtsmuller et al., 1999; Rademakers et al., 2003). In this method, spot bleaching is performed by a relatively long bleach pulse (~ 5s) at low laser intensity, allowing for diffusion of molecules to occur during the bleach phase. Confocal images of the cell are acquired just before and a number of seconds (~ 5s) after bleaching. These images are then used to calculate the fluorescence ratio before and after bleaching as a function of distance (*d*) to the bleached spot (Figure 1.14B).

The average immobilized protein fraction p ($0<p<1$) is obtained by fitting this experimental fluorescence ratio profile ($FRP_{\exp}$) to the weighted sum of the fluorescence ratio profiles obtained for nuclei containing immobile molecules only ($FRP_{100\% immobile}$) and nuclei containing mobile molecules only ($FRP_{100\% mobile}$), according to the formula $FRP_{\exp}(d) = p \times FRP_{100\% immobile}(d) + (1-p) \times FRP_{100\% mobile}(d)$. Transiently immobilized molecules at the bleached region can be followed by recording postbleach images at increasing time intervals. By plotting the average immobile fraction as a function of time, one can estimate the average binding time of the molecules at the region of interest, provided the system is in a reaction dominant regime (Houtsmuller and Vermeulen, 2001).

Fluorescence correlation spectroscopy (FCS) contrasts with the fluorescence techniques that require photobleaching or photoactivation of tagged molecules (Elson and Magde, 1974; Elson, 2004; Gosch and Rigler, 2005; Schwille, 2001). In FCS the primary parameter of interest is not fluorescence emission intensity itself, but rather spontaneous fluctuations in the intensity of a small system that are caused by minute deviations from thermal equilibrium. FCS aims at detecting fluctuations caused by very few molecules (which usually represent noise patterns in the previous techniques) and therefore can only function properly if both the molecule concentration and the observation volume are greatly reduced when compared with other fluorescence methods. FCS thus uses femtoliter detection volumes and nanomolar concentrations of tagged molecules, instead of the micromolar to milimolar concentrations required for FRAP (Schwille et al., 1999; Schwille and Haustein, 2000). The intensity fluctuations caused by molecules moving in and out of the monitored volume can be recorded (Figure 1.14B, *red graph* in *FCS*) and quantified in their strength and duration by temporally autocorrelating the intensity signal. Autocorrelation analysis aims at measuring the self-similarity of a time series signal, thus describing the persistence of information carried by it (Schwille and Haustein, 2000). The autocorrelation curve that is obtained (Figure 1.15B, *blue graph* in *FCS*) is interpreted by fitting to equations that are derived for different diffusion models. Calibration with dye solutions then yields the concentration and diffusion coefficient of the labeled particles in the observation volume (Bacia and Schwille, 2003).

1.5.4 FRET and FLIM: looking into molecular interactions

Determining the dynamic behavior of a protein inside the living cell is of paramount importance to understand the biological processes it is involved in. Likewise, determining when and where specific protein partners associate with one another is crucial for the characterization of such processes and ultimately vital for systems biology approaches (Aloy and Russell, 2006).

Protein-protein interactions are not directly discernible by light microscopy. The relative proximity of two proteins tagged with different fluorophores can only be determined by conventional fluorescence microscopy to the scale of roughly ~ 200 nm, the limit of optical resolution imposed by the diffraction barrier (see section 1.4.1). However, protein-protein interactions require proximity distances similar to the size of proteins, which are typically in the range of 1 – 10 nm (Kenworthy, 2001). This degree of resolution can only be achieved in light microscopy through the use of fluorescence resonance energy transfer (FRET) methods, such as acceptor photobleaching FRET or fluorescence lifetime imaging microscopy (FLIM), extremely sensitive techniques that allow for the determination of the relative proximity between labeled protein partners (Wallrabe and Periasamy, 2005; Wouters et al., 2001).

FRET Principles

Fluorescence resonance energy transfer, also called Förster resonance energy transfer, is a phenomenon that occurs when two different fluorophores (called donor and acceptor) with overlapping emission/absorption spectra are in close proximity to each other and in a suitable orientation (Selvin, 2000; Truong and Ikura, 2001; Voss et al., 2005). FRET involves the non-radiative transfer of energy (no photons are emitted) from an excited state in the donor fluorophore to the nearby acceptor (Figure 1.15).

The energy transfer efficiency E is related to the distance r between the donor and acceptor fluorophores by $E = 1/\left[1 + (r/R_0)^6\right]$, where R_0 is the Förster radius, the distance at which the efficiency of energy transfer is 50% of maximum. The Förster radius depends on the extent of overlap between the donor emission and the acceptor excitation spectra, the absorption coefficient of the acceptor, the quantum yield of the donor and the relative orientation of the donor and acceptor (the donor and acceptor transition dipoles must be aligned relative to each other).

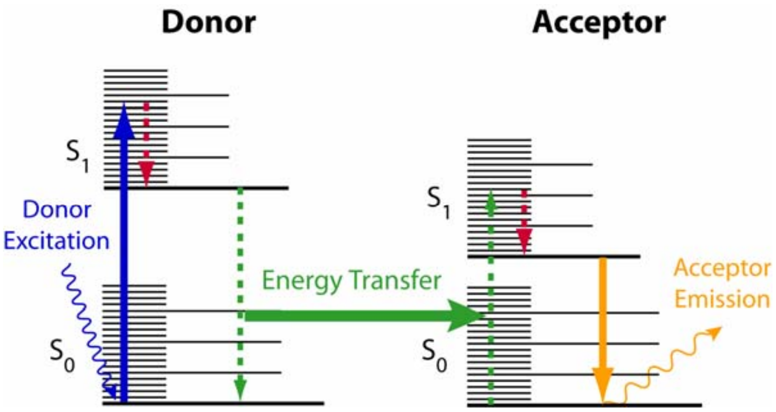

Figure 1.15 – Fluorescence Resonance Energy Transfer. Jablonski diagrams showing the energy states of a donor and acceptor molecules in FRET. A photon of appropriate wavelength is absorbed by the donor molecule and causes a transition to an excited electronic state (*dark blue arrows*). This donor molecule then undergoes rotational and vibrational relaxations (*dotted red arrows*) before it reaches the lowest energy level of the excited state. Transition to the ground state usually occurs via emission of a photon, by fluorescence. In close proximity to the acceptor, however, donor fluorescence is quenched and energy is transferred to the acceptor (*green arrows*), which then undergoes rotational and vibrational relaxations (*dotted dark red arrows*) before emitting a photon at a longer wavelength (*orange arrows*).

The value of R_0 effectively defines the resolution of FRET, which is typically < 10 – 100 Å. Because FRET falls off as the sixth power of the distance between the donor and acceptor, when these molecules are separated by distances greater than $2R_0$ no FRET occurs. The phenomenon of FRET can thus be applied in fluorescence microscopy to distinguish proteins that are merely co-localized in the same compartment from those that are undergoing protein-protein interactions (Kenworthy, 2001). The earliest use of GFP in a FRET pair involved a BFP donor and an EGFP acceptor (Heim and Tsien, 1996), a combination that was later replaced by the a ECFP/YFP pair due to the improved brightness and photostability of ECFP when compared to BFP (Pollok and Heim, 1999). ECFP/YFP quickly became the most commonly used FRET pair, with ECFP being currently replaced by its improved version Cerulean (see section 1.4.2), which has a higher quantum yield, extinction coefficient and, most importantly, a single fluorescence lifetime (Rizzo et al., 2004). Other known FRET pairs include the recently developed mOrange and T-Sapphire (Shaner et al., 2004) and Cerulean and Dronpa (Lukyanov et al., 2005). FRET microscopy approaches can be divided into intensity based methods and fluorescence decay kinetics based methods (Wouters et al., 2001). Intensity based FRET techniques take advantage of the fact that excitation of a donor fluorophore in FRET results in quenching of donor emission and in an increased, sensitized acceptor emission. Detection of FRET through sensitized emission of the acceptor is a complex task that requires correction of both leak-through of the donor emission and direct excitation of the acceptor (Day, 1998; Gordon et al., 1998; Nagy et al., 1998; Xia and Liu, 2001). These corrections often involve the acquisition of images from samples with the donor alone and the acceptor alone, a pitfall that can lead to errors in the estimation of the correction parameters because the quantum yields of the donor and the acceptor might vary in the different samples (Wouters et al., 2001).

Acceptor Photobleaching FRET

Another approach consists in measuring the donor fluorescence specifically, by using appropriate emission filters that eliminate the leak-through of acceptor emission (Bastiaens and Pepperkok, 2000). FRET can then be detected by comparing the quenched with the unquenched donor emission after specific photobleaching of the acceptor fluorophore (Figure 1.16) (Bastiaens et al., 1996; Wouters et al., 1998).

The principle behind acceptor photobleaching FRET is that energy transfer is reduced or eliminated when the acceptor is irreversibly bleached, thereby causing an increase in donor fluorescence. An apparent energy transfer efficiency $E_D(i)$ can be defined for each position *i* in the image as $E_D(i) = 1 - F^D(i)/F^{DA}(i)$, where $F^{DA}(i)$ and $F^D(i)$ are the donor fluorescence intensities at position *i* before and after bleaching of the acceptor, respectively. This apparent energy transfer efficiency corresponds to the true FRET efficiency *E* multiplied by the fraction of donor tagged molecules $\alpha_D(i)$ that are in a complex at position *i*: $E_D(i) = E \cdot \alpha_D(i)$.

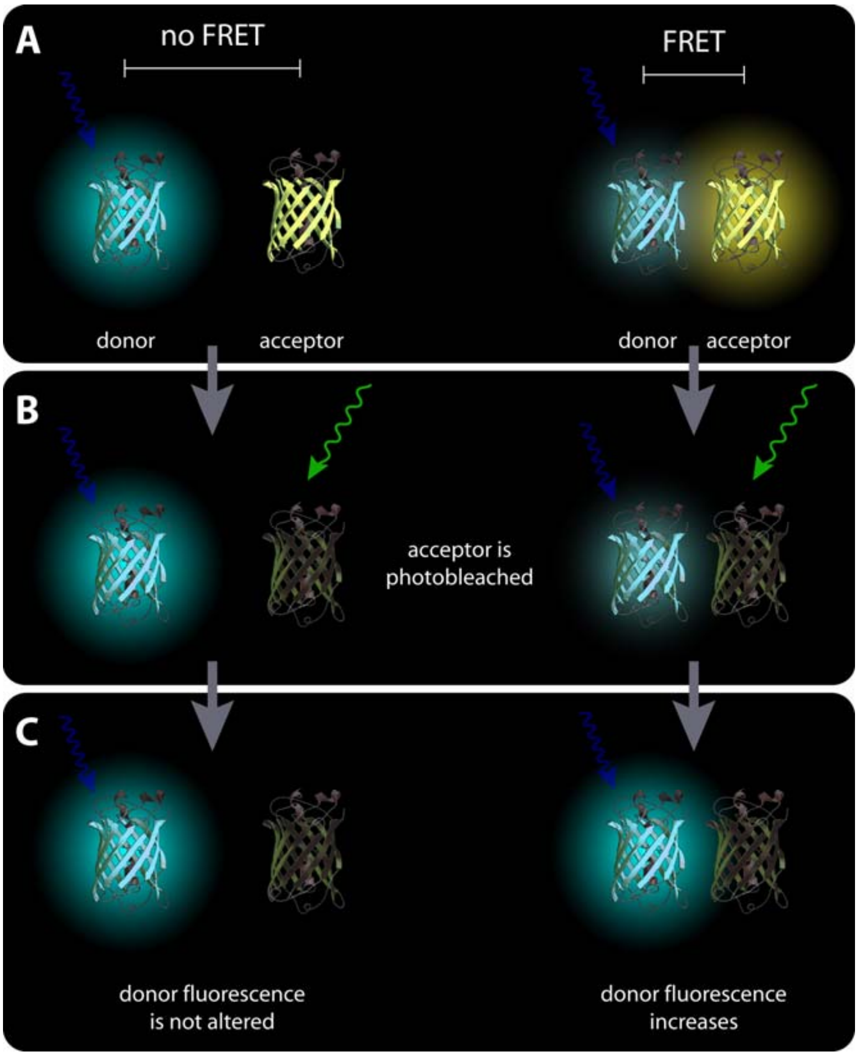

Figure 1.16 – Acceptor Photobleaching FRET (A) FRET between a donor and an acceptor molecule only occurs if the distance between them is in the order of a few nanometers. FRET causes the donor fluorescence to be quenched while the acceptor undergoes sensitized emission. **(B)** Acceptor photobleaching FRET assesses protein-protein interactions by bleaching the acceptor molecules with a high intensity laser *(green arrow)*. **(C)** If the donor fluorescence was being quenched by FRET, it will increase after the acceptor has been bleached.

Acceptor photobleaching FRET has been mostly performed using widefield microscopes, with implementations in confocal systems being recently described for the CFP/YFP pair (Karpova et al., 2003). Average FRET efficiencies are typically calculated for a region of interest in the cell by taking a series of images before and after bleaching. This average FRET is then plotted in a graph and compared to non-bleached squares (Chusainow et al., 2005; Karpova et al., 2003). An improved method for acceptor photobleaching FRET is presented in Chapter 3. This method uses image registration techniques and fluorescence normalization to correct for cell movement and bleaching due to imaging, respectively. FRET efficiencies are calculated in each point of the image, yielding FRET efficiency maps that can be overlaid to the original confocal image of donor intensity in the cell, thus providing spatial information on protein-protein interactions for large regions of interest.

Fluorescence Lifetime Imaging Microscopy (FLIM)

Kinetic-based approaches for FRET determination measure the excited state decay kinetics of the donor or the acceptor, instead of their fluorescence intensity. The most widely used of these approaches is fluorescence lifetime imaging microscopy (FLIM) (Gadella and Jovin, 1995; Wallrabe and Periasamy, 2005; Wouters and Bastiaens, 1999), which detects the decrease in fluorescence lifetime of the donor due to the depopulation of its excited state by FRET (see section 1.4.2). FLIM determines a single lifetime value for each position in an image. This measured lifetime is a nonlinear function of the true lifetimes and the populations of bound and unbound donor molecules in that position (Wouters et al., 2001). As in acceptor photobleaching FRET, an apparent energy transfer efficiency $E_L(i)$ can be defined at each position i as $E_L(i) = 1 - \tau(i)/\tau_D$, where $\tau(i)$ is the average lifetime detected at position i and τ_D is the true lifetime of the free donor. The fluorescence lifetime is independent of probe concentration and light path in a microscope, but can vary in an image due to environmental influences.

Two different FLIM implementations can be distinguished. In time-domain FLIM, a short laser pulse excites the fluorophore and the subsequent emission is measured time-resolved, thus originating a decay curve which can be fitted to a lifetime value. In frequency-domain FLIM, a modulated excitation light is used to excite the fluorophore and the lifetime is determined by measuring either the phase shift or the decrease in modulation depth in the emission. Time-domain and frequency domain FLIM have been applied to both widefield (Oida et al., 1993; Squire and Bastiaens, 1999; van Munster and Gadella, 2005) and scanning microscopy (Carlsson and Liljeborg, 1997; Sanders et al., 1995).

In widefield frequency-domain FLIM, the phase and modulation depth of the emitted light are measured for each pixel in the image by recording a series of images and using Fourier analysis. If the phase and modulation depth of the excitation are known, the lifetime of the sample can be determined by the excitation and emission phases (φ_{ex} and φ_{em}) using $\tau_{\varphi} = \tan(\varphi_{em} - \varphi_{ex}) \cdot \omega^{-1}$ or by the excitation and emission modulation depths (M_{ex} and M_{em}) using $\tau_M = \sqrt{(M_{ex} / M_{em})^2 - 1} \cdot \omega^{-1}$, where ω is the angular frequency used for modulation. The lifetime can thus be calculated in two different ways. If the fluorophore has a mono-exponential decay, τ_{φ} and τ_M will be equal. However, if the fluorescence decay is multi-exponential because the fluorophore has different lifetime components, then $\tau_{\varphi} < \tau_M$ (van Munster and Gadella, 2004b). When FRET occurs though, both the phase-determined and modulation-determined lifetimes are reduced (Vermeer et al., 2004).

1.6 Kinetic modeling of molecular dynamics

Brownian motion is likely to be the predominant mode of molecular movement in the nucleus of living cells (Carmo-Fonseca et al., 2002; Phair and Misteli, 2000; Politz et al., 2006). This “motion consisting of alterations in the relative positions” of particles which did not “arose from currents in the fluid (…) but belonged to the particle itself”, as it was first described by Robert Brown (Brown, 1828), is perceived at a macroscopic scale as diffusion, the process by which matter spontaneously spreads from regions of higher concentration towards regions of lower concentration.

1.6.1 Modeling Diffusion

Diffusional behavior is based on the assumption that the particles, or molecules, undergo a random walk in the space available to them. This random walk or “Brownian molecular motion” is the result of a multitude of chance collisions with other particles in the fluid they are immersed in. Each particle moves independently of the others, in successive minute steps that have no preferential direction in space and are independent of each other. These steps, or jumps, of length Δr at time intervals Δt are mathematically described by Gaussian deviates with zero mean ($\langle \Delta r \rangle = 0$) and standard deviation $\sqrt{2D\Delta t}$ in each spatial direction. The parameter D is called the diffusion coefficient, a quantity with dimensions length^{2}time^{-1}. Even though the jumps have zero mean displacement, their mean square displacement relative to the origin position is proportional to time: $\langle \Delta r^2 \rangle = 2nDt$, with n representing the dimension of the space the movement occurs in. Thus, in three dimensions the mean squared displacement of a particle is proportional to 8Dt.

The diffusion coefficient can be predicted for spherical particles using the Stokes-Einstein relation: $D = kT / 6\pi\eta a$, where k represents the Boltzmann constant, T the absolute temperature, η the viscosity of the medium and a the hydrodynamic radius of the particle (Einstein, 1956).

Macroscopically, these random molecular motions are responsible for the diffusional process by which matter is transported from regions of high concentration in a medium to regions of lower concentration, without the influence of any convection currents. Macroscopic diffusion shares an obvious analogy with the transfer of heat by conduction, a process which is also due to random molecular motions. The mathematical theory of diffusion in isotropic media is therefore also based on the hypothesis that the flux of a diffusing substance through a section of the medium is proportional and of opposite direction to the concentration gradient measured at a normal to the section (Crank, 1975). This relationship is called Fick’s first law of diffusion: $\vec{J} = -D\vec{\nabla}C$, with $\vec{J}$ being the flux of substance at a normal to the section, C the concentration and D the macroscopic diffusion coefficient. The minus sign accounts for the fact that diffusion occurs in opposite direction to the concentration gradient, therefore homogenizing the concentration of substance in the medium.

Fick's second law of diffusion is obtained by combining the first law of diffusion with the conservation of mass law $\partial C / \partial t = -\vec{\nabla} \cdot \vec{J}$, yielding $\partial C / \partial t = \vec{\nabla} \cdot \left(D \cdot \vec{\nabla} C\right)$. In an isotropic medium where D does not depend on the concentration, we obtain the macroscopic diffusion equation $\partial C / \partial t = D \nabla^2 C$, which can be used with appropriate initial and boundary conditions to describe the evolution in time and space of the concentration of a large number of diffusing molecules (Kuthan, 2005).

Analytical solutions to the diffusion equation cannot be obtained in complex geometries like the cell nucleus. Numerical solutions must be found instead, for instance by implementing finite differences approximations to the diffusion equation. In compartmental modeling approaches, the nucleus is modeled as a grid of square elements with a finite grid step. Diffusion is only allowed between nearest neighbors. The geometry of the cell is thus taken into account, so that at the border, for instance, diffusion can only occur between neighbor grid elements that are inside the nucleus. Approximating the diffusion equation by finite differences results in a system of coupled ordinary differential equations (ODE), one of each element in the grid. In Chapter 4 such compartmental modeling approaches are used to develop a novel method to characterize and estimate the mobility rates of different populations of diffusive molecules by FLIP.

1.6.2 Modeling diffusion and chemical interactions

All functional proteins must interact with other molecules or structures in the cell and therefore do not display a pure diffusive behavior (Carrero et al., 2004b). Systems where binding and diffusion are simultaneously occurring can be described by the reaction-diffusion equations:

$$\begin{cases} \partial F / \partial t = D_F \nabla^2 F - k_{on} S \cdot F + k_{off} C \\ \partial S / \partial t = D_S \nabla^2 S - k_{on} S \cdot F + k_{off} C \\ \partial C / \partial t = D_C \nabla^2 C + k_{on} S \cdot F - k_{off} C \end{cases}$$

where F and S represent the concentrations of two different species that interact to form the complex C ($F + S \rightarrow C$), D_F, D_S and D_C are the diffusion coefficients of the different species and k_{on} and k_{off} are the association and dissociation rate constants respectively (Sprague et al., 2004). Analytical solutions to these nonlinear reaction-diffusion equations can only be found for very simple cases, such as instantaneous reactions that occur between a diffusing species and an immobilized substrate ($D_S = 0$). In this case, the chemical reaction can be considered infinitely fast compared to diffusion, so that a chemical equilibrium is achieved at any time point (Crank, 1975). The reaction diffusion equation is then reduced to a simple diffusion equation, with a slowed down "effective diffusion coefficient" given by $D_{eff} = D/(1 + k_{on} \cdot S / k_{off})$.

The presence of binding sites can also have more profound effects on diffusing species rather than just lowering their mobility rates. Binding, as well as obstructions and traps, may lead to anomalous subdiffusion (Saxton, 1994; Saxton, 1996; Saxton, 2001), in which molecular movement is delayed and the mean square displacement is not proportional to time, but to a fractional power of time less than one: $\left\langle \Delta r^2 \right\rangle \propto t^{\alpha}$, where α is the anomalous diffusion exponent (Weiss and Nilsson, 2004). Obstacles and traps are likely to be present in the crowded nuclear environment (see section 1.2.2), forcing molecules to undergo anomalous subdiffusion at short timescales. At long timescales, however, diffusion is normal (Saxton, 1994). Binding can give much lower coefficients than pure obstruction can, but binding itself only contributes to anomalous subdiffusion if the system is not at an initial thermal equilibrium (Saxton, 1996).

2. *In vivo* dynamics of mRNA splicing factors revealed by photobleaching techniques

2.1 Abstract

Splicing of intronic sequences from pre-mRNA, a crucial step in the pathway of mRNA biogenesis of higher eukaryotes, is performed by a very dynamic multi-component macromolecular machine called the spliceosome. Although the spliceosome assembly and cycle have been extensively studied at the molecular level, very little is known about the dynamics of spliceosome components *in vivo*.

We used photobleaching techniques such as FRAP (Fluorescence Recovery After Photobleaching), FLIP (Fluorescence Loss In Photobleaching) and FRAP-FIM (FRAP For Immobilization Measurement) to analyze the mobility and kinetic behavior of spliceosome components in the nucleus of living cells. The snRNP component SmE and the splicing factors U2AF^{65}, U2AF^{35}, SF1 and SC35 were tagged with GFP and their effective diffusion coefficients together with immobile fractions were obtained with FRAP performed in the nucleoplasm and in the speckles. The results show that splicing factors are highly dynamic in the cell nucleus, rapidly and continuously associating and dissociating from nuclear speckles. However, their mobility inside the nucleus is much lower than expected and is correlated with the ability of these proteins to interact with each other. Their reduced mobility in the speckles further suggests the formation of multi-protein complexes in these nuclear domains.

The recruitment of splicing factors from the speckles to the sites of transcription was also addressed with photobleaching techniques. Inhibition of transcription leads to an increase of splicing factors concentration in the speckles. However, photobleaching experiments show that the mobility of splicing factors is increased after inhibition of transcription, both in the speckles and in the nucleoplasm. This excludes the hypothesis that a transcription specific signal recruits splicing factors from the speckles.

Taken together, our results suggest that the levels of splicing factors in the different nuclear domains are consistent with self-organization mechanisms, with recruitment to the speckles being independent of the transcriptional state of the cell and assembly at the spliceosome probably occurring with pre-assembled particles, rather than stepwise addition of discrete components.

2.2 Introduction

The spliceosome is a very dynamic RNA-protein macromolecular machine that is responsible for the splicing of intronic sequences from pre-mRNA, a crucial step in the pathway of mRNA biogenesis of higher eukaryotes (see section 1.3.2 in Chapter 1). The spliceosome undergoes major structural changes during the splicing reaction and its components must be recycled for a new round of splicing after exon ligation and release of mRNA. Even though the spliceosome cycle has been extensively studied at the molecular level, very little is known about the dynamics of its components *in vivo*. The aim of this chapter is to better understand the kinetic behavior of spliceosome components, their dynamics and recruitment mechanism to transcription sites, where splicing occurs. We used photobleaching techniques such as FRAP (Fluorescence Recovery After Photobleaching), FLIP (Fluorescence Loss In Photobleaching) and FRAP-FIM (FRAP For Immobilization Measurement) (see section 1.5.3 in Chapter 1) to analyze the mobility of spliceosome components, and its dependence on the transcriptional state of the cell.

In the nucleus of mammalian cells, components of the spliceosome are found distributed throughout the nucleoplasm, concentrated in nuclear speckles and excluded from nucleoli (see section 1.2.2 in Chapter 1). Like other non-chromatin membraneless domains of the nucleus, nuclear speckles have been proposed to be formed and maintained by self-organization mechanisms. Nuclear speckles are thought to constitute reservoirs or storage sites for splicing factors, which would then be recruited to sites of active transcription by a yet unknown mechanism. Observations that transcription inhibition leads to larger and rounder speckles suggested that recruitment of SFs to nascent transcription sites could rely on a transcription coupled signal. In the absence of such a signal, SFs would accumulate at the nuclear speckles, presumably ceasing or reducing their shuttling activity. We tested this hypothesis by performing FLIP experiments in cells expressing GFP-tagged versions of the splicing factors U2AF^{65}, U2AF^{35} and SF1, both in untreated cells and in cells treated with the transcription inhibitor DRB. Our results show that inhibition of transcription leads instead to an overall increase in SFs dynamics, contradicting the hypothesis that a transcription-dependent signal would be necessary to release SFs from nuclear speckles.

In order to study the mobility of spliceosome components inside the nucleus, we performed FRAP and FRAP-FIM experiments on cells expressing GFP-tagged versions of the snRNP component SmE and the splicing factors U2AF^{65}, U2AF^{35}, SF1 and SC35. The effective diffusion coefficients of these proteins, together with immobile fractions, were obtained with FRAP performed in the nucleoplasm and in the speckles. The results show that splicing factors are highly dynamic in the cell nucleus and that they constantly associate and dissociate from nuclear speckles with a high turnover rate. However, splicing factors diffuse inside the nucleus with a much lower rate than exogenous dextrans of similar size which are not expected to interact with any endogenous proteins. In contrast, mutant versions of U2AF^{65} and SF1 that lack specific protein binding domains show diffusion rates similar to those of exogenous dextrans of similar molecular weight, suggesting that splicing factors mobility in the nucleoplasm is correlated with the ability of these proteins to interact with each other. Their reduced mobility in the speckles further suggests the formation of multi-protein complexes in these nuclear domains.

The kinetics of splicing factors in active spliceosomes was more specifically studied using adenoviral infected cells. In contrast to non-infected cells, where splicing sites are distributed throughout the nucleoplasm, cells infected with adenovirus have all their splicing machinery recruited to viral transcription rings. FRAP experiments performed in adenoviral infected cells show that the residence times of splicing factors in the spliceosome are very small, with binding occurring at faster or comparable rates than diffusion itself.

2.3 Materials and Methods

Cell culture, transfections and drug treatment

HeLa cells were cultured as monolayers in Modified Eagle's Medium (MEM) supplemented with 10% fetal calf serum (Invitrogen, Paisley, Scotland). Cells were plated and observed in glass bottom chambers (MatTek, Ashland, MA). For imaging, the medium was changed to D-MEM/F-12 without phenol red supplemented with 15 mM HEPES buffer (Invitrogen). HeLa subconfluent cells were transiently transfected with FuGENE6 reagent (Roche Biochemicals, Indianapolis, IN) using 1 μg of DNA, and analyzed at 16-24h after transfection. DRB (Sigma-Aldrich, St. Louis, MO) was used at 75 µM from a stock solution of 11 mM in ethanol.

Confocal Microscopy

Live cells were imaged at 37ºC maintained by a heating/cooling frame (LaCon, Staig, Germany) in conjunction with an objective heater (PeCon, Erbach, Germany). Images were acquired on a Zeiss LSM 510 confocal microscope (Carl Zeiss, Jena, Germany) using a PlanApochromat 63x/1.4 objective. FITC and EGFP fluorescence were detected using the 488 nm laser line of an Ar laser (25 mW nominal output) and a LP 505 filter. Cy3 fluorescence was detected using a 543 nm HeNe laser (1 mW) and a LP 560 filter. The pinhole aperture was set to 1 Airy unit. Time-lapse 3D imaging of selected cells was performed on the confocal microscope immediately after DRB treatment and/or DRB removal. For this, a total of up to 200 z-stack series were acquired over time for each cell, each z-stack having between 15 and 20 images and with 0.60 µm of distance between each image in the stack. Image size was 512 × 512 pixels and the pixel width was 72 nm. The time between each z-stack acquisition depended on its number of images, and varied between 20 and 60 s. Maximum projection images were generated from each z-stack and processed with ImageJ (http://rsb.info.nih.gov/ij/) using a rigid body registration algorithm to correct for cell displacement during image acquisition. Movies of cells after treatment or removal of DRB were then generated and time-annotated. Fluorescence intensity values in speckle and nucleoplasmic regions were measured over time in registered projection images also using ImageJ.

FLIP analysis

In each FLIP experiment, cells were repeatedly bleached in a region of interest (ROI) that corresponded to half of the total nuclear area, and imaged between bleach pulses. Bleaching was performed by scanning the defined ROI with 3 iterations of the 488 nm laser line, at maximum intensity. Bleach pulse duration ranged from 2.2 to 3.1 s, depending on the size of the bleached region. Repetitive bleach pulses were achieved using the FLIP Macro for LSM software developed by Gwénaël Rabut (http://www.embl-heidelberg.de/ExternalInfo/ellenberg/homepage/macros.html).

Image size was 512 × 512 pixels and the pixel width was 48 nm. For imaging, the laser power was attenuated to 0.1-0.2% of the bleach intensity. Images were background subtracted and registered to correct for cell displacement during image acquisition using ImageJ. Fluorescence intensity values in speckle and nucleoplasmic regions were measured over time in registered projection images using ImageJ. The data was then normalized to correct for loss of fluorescence due to image acquisition, using non-bleached cells to estimate imaging bleach kinetics. Loss of fluorescence due to imaging could reach 10-20% over the time course of the experiment.

Quantitative FRAP analysis

FRAP experiments were performed essentially as described (Braga et al., 2004a). Each FRAP experiment of FITC-labeled dextrans started with three image scans followed by a bleach pulse of 242 ms on a spot with a diameter of 21 pixel (1.19-µm radius). A series of 97 single section images (of size 256x30 and pixel width 114 nm) was then collected at intervals of 29.82-ms, with the first image acquired 2 ms after the end of bleaching. For EGFP-tagged splicing factors, bleaching was performed on a spot with a diameter of 25 pixel (0.59-µm radius) for 110 ms. A series of 97 single section images (of size 512x50 and pixel width 48 nm) was then collected at intervals of 78.40 ms, again with the first image acquired 2 ms after the end of bleaching. For imaging, the laser power was attenuated to 1% of the bleach intensity.

For each FRAP time series, the background and nuclear regions were identified using an implementation of the ICM segmentation algorithm (Calapez et al., 2002) in Matlab software (Mathworks, Natick, MA). The average fluorescence in the nucleus *T(t)* and the average fluorescence in the bleached region *I(t)* were calculated for each background subtracted image at time *t* after bleaching. FRAP recovery curves were normalized as described previously (Phair and Misteli, 2000),

$$Irel(t) = \frac{I(t)}{I_0}\frac{T_0}{T(t)}$$

where T_0 is the fluorescence in the nucleus before bleaching and I_0 is the fluorescence in the bleached region before bleaching. This normalization corrects for the loss of fluorescence caused by imaging which was typically < 5%.

FRAP recovery curves were fitted to a recovery function that takes into account diffusion of highly mobile molecules during the bleach phase, essentially as described (Braga et al., 2004a),

$$Irel(t) = (1-\gamma)\hat{F}_M(t) + \gamma\hat{F}_{im}$$

where γ is the fraction of immobile molecules, and $\hat{F}_M$ and $\hat{F}_{im}$ are the normalized fluorescence intensities of the mobile fraction and of the immobile molecules, respectively. The fitting procedure yielded diffusion coefficient and immobile fraction values. Image processing routines also outputted the normalized fluorescence profile of the first postbleach image, from which the values of the parameters w_M and K_M (used in the determination of $\hat{F}_M$) were obtained (see (Braga et al., 2004a) for more details). All fitting procedures were performed using the NonLinearRegress function of Mathematica 5.0 (Wolfram Research, Champaign, IL).

FRAP-FIM

FRAP for Immobilization Measurement experiments were performed essentially as described (Houtsmuller et al., 1999). A small circular area in the nucleus (~ 1.2 µm radius) which coincided with a nuclear speckle was bleached for a relatively long period (~ 7.4 s) with the aim of irreversibly bleaching a significant proportion of the GFP-tagged molecules in the nucleus. Subsequent postbleach images were acquired every 250 ms, with the laser power attenuated to 1% of the bleach intensity. The background and nuclear regions were identified using an implementation of the ICM segmentation algorithm (Calapez et al., 2002) in Matlab software. The fluorescence intensity ratio ($I_{postbleach}/I_{bleach}$) was then plotted as a function of distance to the center of the bleach area, generating a fluorescence ratio profile (FRP). The bleaching parameters K and ω were estimated by fitting the FRP to the formula

$$FRP(r) = \exp\left(-K\exp\left(\frac{-2r^2}{\omega^2}\right)\right).$$

where r is the distance to the bleach area origin. A chimera formed by fusing GFP-PABPN1 to the Cajal body protein p80-coilin (GFP-PABPN1-coilin), which is predominantly immobile in the nucleus was used as 100% immobilization control, whereas GFP alone was used as 0% immobilization control.

2.4 Results

2.4.1 GFP-tagged splicing factors localize as the endogenous proteins and engage in active endogenous complexes

Within the mammalian cell nucleus most splicing factors are distributed throughout the nucleoplasm and concentrate in nuclear speckles. To compare the subcellular localization of the GFP-tagged splicing factors with the localization patterns of the corresponding endogenous proteins, we transiently transfected HeLa cells with the GFP-fusion constructs GFP-U2AF^{65}, GFP-U2AF^{35} and GFP-SF1. Western blot analysis confirmed the expression of fusion proteins with the expected molecular weight. After overnight expression, transfected cells were fixed, immunostained with an antibody specific for the Sm family of snRNP proteins – anti-Y12, and analyzed by confocal microscopy (Figure 2.1).

All GFP-tagged proteins concentrated in speckles and in a diffuse nucleoplasmic pool, as expected. Identical localization patterns were observed for snRNP proteins as it can be assessed by the perfect co-localization in the merged images (Figure 2.1). Although properly localized, co-immunofluorescence experiments are not sufficient to demonstrate the engagement of exogenously expressed proteins in functional endogenous complexes. To confirm biochemically that the GFP-tagged proteins U2AF^{65}, U2AF^{35} and SF1 interact with endogenous splicing partners we performed co-immunoprecipitation assays of these proteins using an anti-GFP antibody and a monoclonal antibody directed against U2AF^{65} (Gama-Carvalho et al., 1997). Both GFP-U2AF^{65} and GFP-SF1 were co-immunoprecipitated with anti-U2AF^{65} specific antibody (*data not shown*) consistent with well described interactions between endogenous proteins (Selenko et al., 2003; Zhang et al., 1992).

To further examine the *in vivo* function of the expressed GFP-tagged proteins we took advantage of an IgM splicing reporter (Pacheco et al., 2004). This splicing reporter has two alternative 3' splice sites which are used according to the cellular ratio of functional U2AF^{65}/U2AF^{35}. Co-transfection with either GFP-U2AF^{65} or GFP-U2AF^{65} and GFP-U2AF^{35} caused a switch in the splice site usage (*data not shown*), demonstrating that these GFP-tagged splicing factors function properly in selection of alternative splice sites *in vivo*.

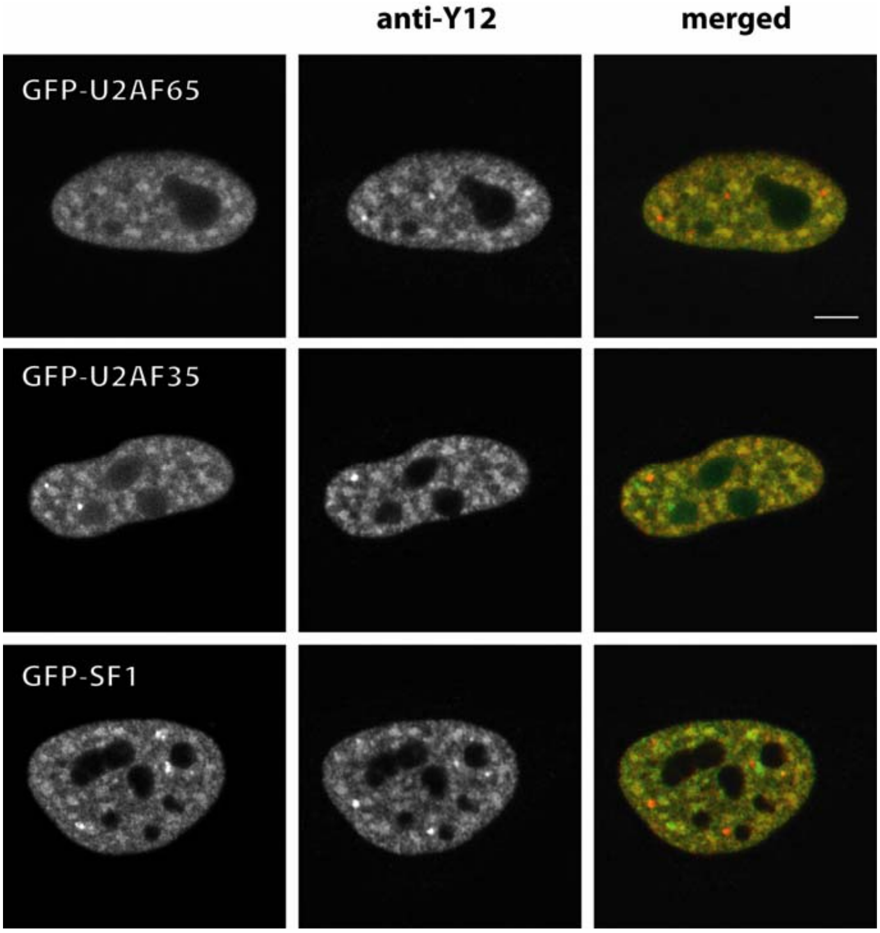

Figure 2.1 – GFP-tagged U2AF^{65}, U2AF^{35} and SF1 co-localize with endogenous Sm proteins. Immunofluorescence images of Cy3-labelled anti-Y12 in cells transfected with GFP construct of the splicing factors U2AF^{65}, U2AF^{35} and SF1. All the GFP fusions show the same speckled nucleoplasmic distribution as endogenous Sm proteins detected by Y12 (note, however, the absence of Cajal bodies in the GFP constructs images). Bar: 5 µm.

Based upon the above combination of fluorescence microscopy and biochemical data we can conclude that GFP-tagged U2AF^{65}, U2AF^{35} and SF1 are active *in vivo* and indistinguishable from endogenous splicing factors.

2.4.2 Transcription inhibition by DRB causes a redistribution of splicing factors in the cell nucleus

Having established that GFP-tagged U2AF^{65}, U2AF^{35} and SF1 are functional *in vivo*, we next studied their subcellular localization in the absence of splicing activity. HeLa cells were treated with 5,6-dichloro-1β-D-ribofuranosyl-benzimidazole (DRB), a drug that inhibits elongation causing premature transcription termination (see section 1.3.1 in Chapter 1). Time-lapse analysis of cells expressing GFP-U2AF^{65}

revealed a rapid redistribution of molecules induced by DRB (Figure 2.2 and movie 1 in Supplementary Material).

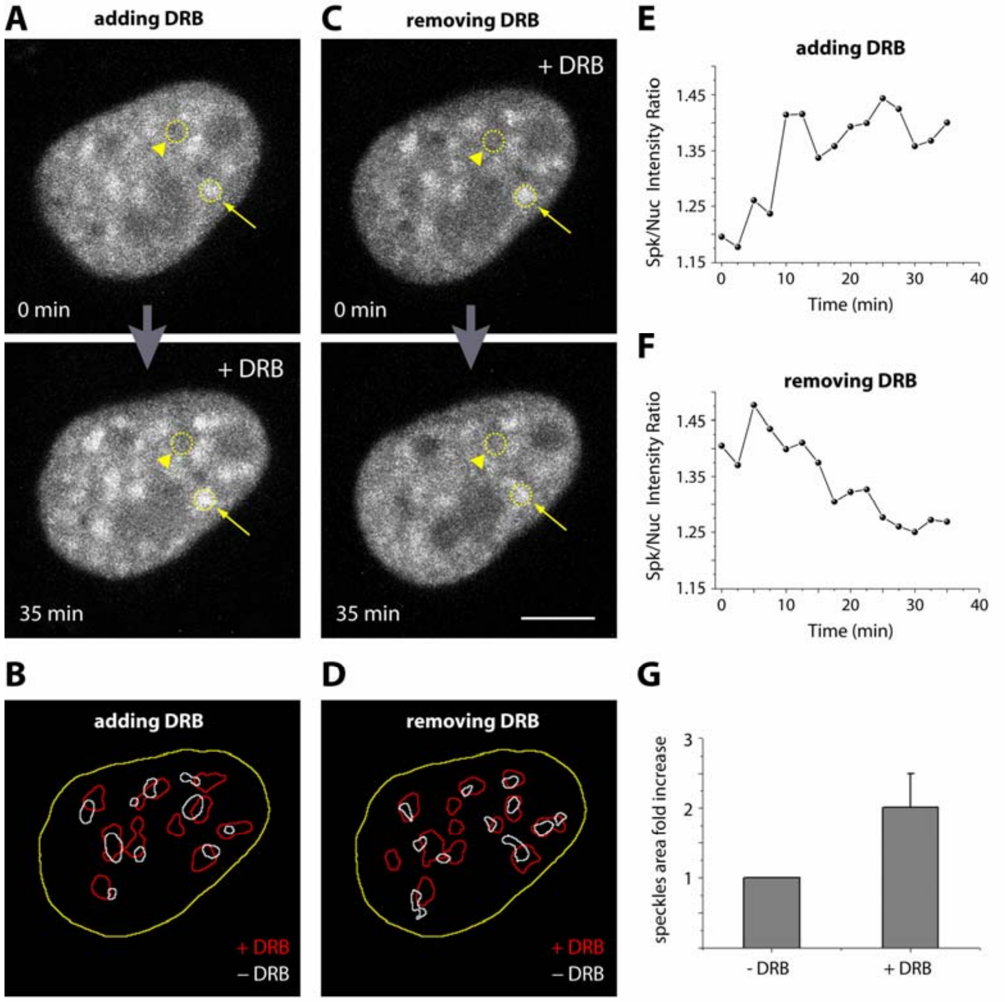

Figure 2.2 – The transcription inhibitor DRB induces a reversible accumulation of GFP-U2AF^{65} in enlarged nuclear speckles. (A) Steady-state distribution of GFP-U2AF^{65} in the nucleus of a HeLa cell after addition of DRB. Top panel depicts the cell imaged immediately upon addition of DRB. Bottom panel shows the steady-state distribution 35 min after DRB addition. **(C)** The same cell was imaged immediately after DRB removal (*top panel*) and 35 min later. Note that the final steady-state situation is very similar to the initial one (*top panel in* **A**). The arrowheads point to the nucleoplasm, the arrows to the nuclear speckles. Bar: 5 µm. **(B and D)** Threshold segmentation of images in **A** and **C** reveals the outline of nuclear speckles in the presence (*red outlines*) and absence (*white outlines*) of DRB. The nuclear boundary is outlined in yellow. **(E and F**) Plot of the ration between fluorescence intensities in the nuclear speckles and in the nucleoplasm over time, after addition (**E**) or removal (**F**) of DRB. **(G)** Quantification of the nuclear speckles areas in **B** and **D** reveal an approximate two-fold increase of speckles size, when transcription is inhibited by DRB.

In less than 10 minutes after addition of the drug to the medium, the GFP-U2AF^{65} fluorescence decreased in the nucleoplasm and accumulated in bigger and rounder speckles (Figure 2.2A). The fluorescence intensities in the nuclear speckles and in the nucleoplasm were estimated and the corresponding ratio was calculated over time (Figure 2.2E). While in non-treated cells the ratio was 1.27 ± 0.07, after DRB treatment the ratio increased to 1.42 ± 0.08 (Figure 2.2E). In parallel, the average area fold increase of each nuclear speckle was measured to be 2.05 ± 0.81 (Figure 2.2G). This effect was completely reverted after removal of the drug (Figure 2.2C and F and movie 2 in Supplementary Material).

Despite a decrease in the relative fluorescence intensity, splicing proteins were still significantly detected in the nucleoplasm of DRB-treated cells, indicating that spliceosomal components can localize to this compartment even in the absence of nascent pre-mRNAs. Our quantitative estimates further suggest that a larger pool of splicing proteins localizes to nuclear speckles in DRB-treated cells, consistent with the hypothesis that spliceosomal components are recruited to the speckles when not actively engaged in splicing. As more splicing proteins localize to nuclear speckles, these structures become approximately two-fold larger, while the relative concentration of the molecules within the compartment increases only by a factor of 1.12. Thus, the density of binding sites for splicing proteins at the nuclear speckles increases only marginally in response to DRB treatment.

2.4.3 Kinetics of splicing proteins in the living cell nucleus

What controls the trafficking of spliceosomal components in and out of the nuclear speckles remains unknown. One possibility is that splicing factors move by simple diffusion. Alternatively, or additionally, splicing factors may receive an active recruitment signal to enter or leave the nuclear speckles, originating from the sites of transcription for instance. In this hypothesis, inhibition of transcription would result in the absence of a recruitment signal, leading to retention of splicing factors at the nuclear speckles. If this was the case, splicing factors turnover at this “storage compartment” should be very low, as they would remain there until required for new splicing activities. Only when the transcription activity is restored could the splicing factors leave the speckles. In order to test this hypothesis, we performed FLIP experiments to study the dynamics of SFs in cells where transcription was inhibited.

A high intensity laser was used to irreversibly destroy the GFP fluorescence in an area that corresponded to half of the cell nucleus. The same area was repeatedly bleached while the loss of fluorescence in a non-bleached area was monitored (Figure 2.3A). A slower turnover of SFs at the speckles would imply slower fluorescence decay in unbleached speckles of DRB treated cells. Contrary to the predictions, experiments performed on HeLa cells treated with DRB and expressing GFP-U2AF^{65}, GFP-U2AF^{35} and GFP-SF1 yielded a faster fluorescence loss in the speckles, when compared to untreated cells ($p<0.0001$ for GFP-U2AF^{65} and GFP-U2AF^{35} and $p<0.005$ for GFP-SF1). Quantification of fluorescence intensities in nuclear speckles over time consistently revealed significantly faster kinetics (Figure 2.3B).

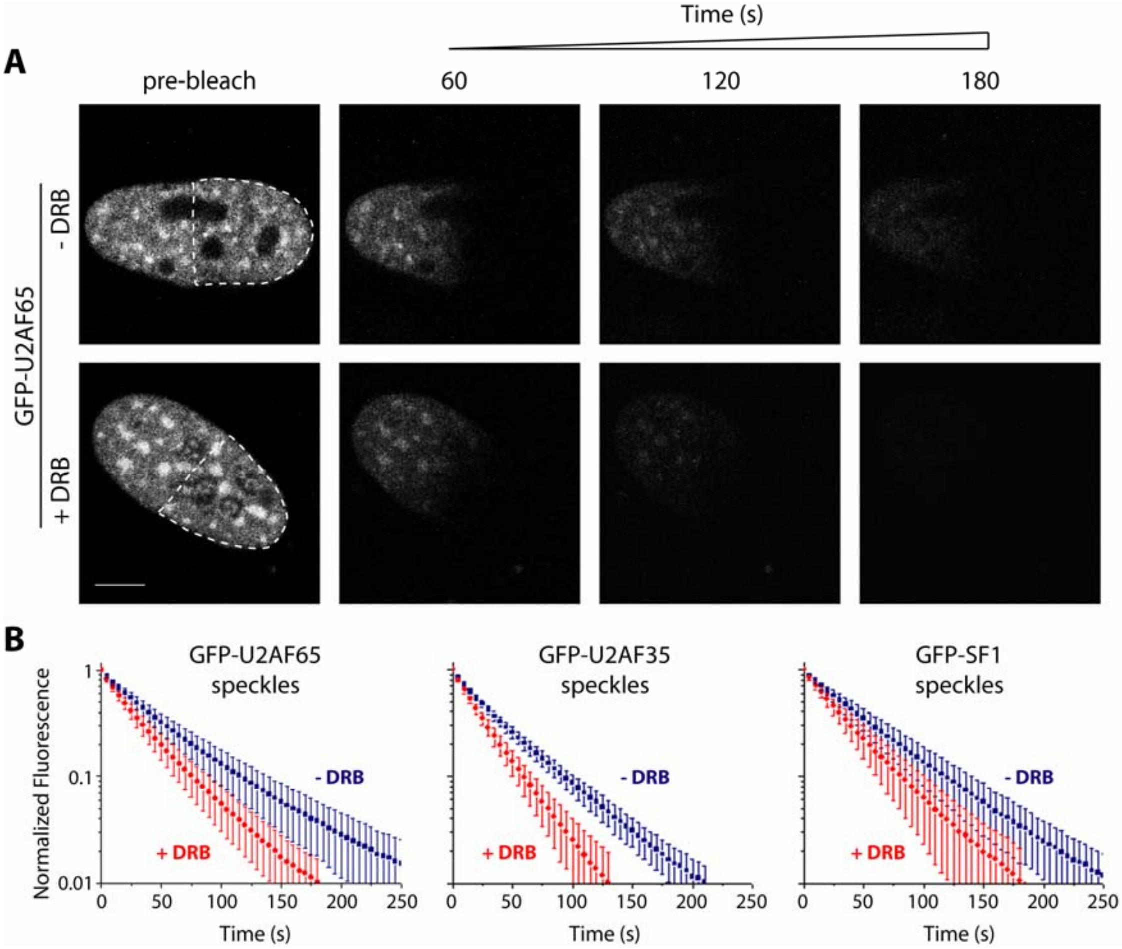

Figure 2.3 – Splicing factors remain mobile in cells treated with DRB (A) FLIP experiments were performed on cells mock treated (- *DRB*) or treated with DRB for 30 min (+ *DRB*). **(B)** The fluorescence decay was analyzed over nuclear speckles. Each decay curve corresponds to a pool of three independent experiments, with ten different cells analyzed per experiment. Error bars represent standard deviations. The differences observed in the FLIP curves between DRB treated and untreated cells was found to be statistically significant ($p<0.0001$ for GFP-U2AF^{65} and GFP-U2AF^{35} and $p<0.005$ for GFP-SF1).

Because drugs such as DRB can cause multiple effects on cells, we decided to use an alternative approach to inhibit splicing activity. We took advantage of snurportin1 (SPN1, see section 1.3.2 in Chapter 1), a nuclear import adaptor for spliceosomal snRNAs. A deletion mutant of SPN1 lacking the residues 1-65 retains the binding activity to snRNAs but strongly inhibits their nuclear import (Huber et al., 1998), efficiently competing with endogenous SPN1 for binding to spliceosomal snRNPs. The SPN1Δ1-65 mutant induces a redistribution of spliceosomal components similar to that observed when cells are treated with transcription inhibitors (*data not shown*). When expressed in living cells, this dominant negative mutant of SPN1 has been shown to impair splicing specifically, while transcription remains largely unaffected (Carvalho, T. *personal communication*). Since the expression of SPN1Δ1-65 inhibits splicing *in vivo*, we asked whether splicing factors are still moving out of the nuclear speckles in cells that express this dominant-negative protein. HeLa cells were co-transfected with CFP fused to either SPN1wt or SPN1Δ1-65 and GFP-tagged splicing factors. A high intensity laser was again used to repeatedly photobleach GFP-U2AF^{65} and GFP-SmE in approximately half of the cell nucleus and the loss of fluorescence in nuclear speckles outside the bleached region of the nucleus was monitored (Figure 2.4).

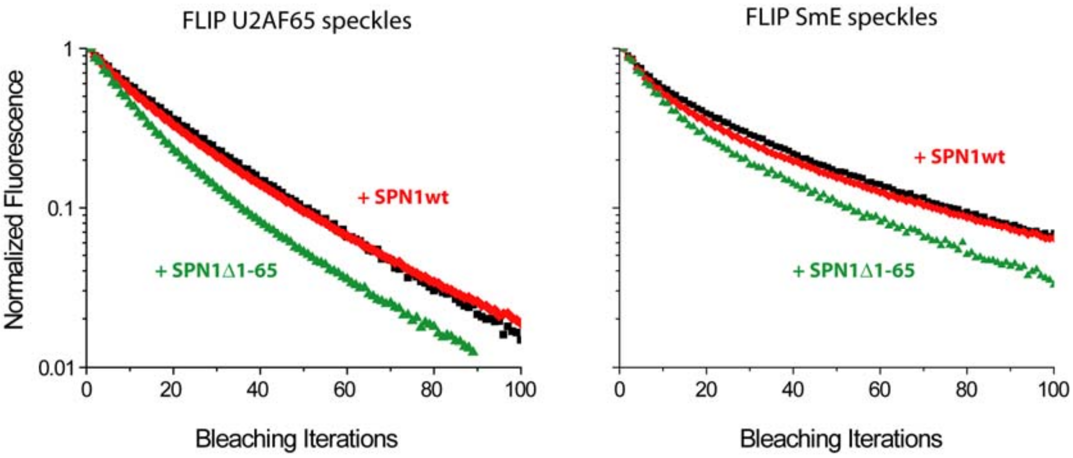

Figure 2.4 – A deletion mutant of snurportin1 affects splicing factors mobility in living cells. FLIP experiments were performed on cells expressing U2AF^{65} and SmE together with either the wild type (+ *SPN1wt*, *red curves*) or a dominant negative mutant (+ *SPN1Δ1-65*, *green curves*) of the spliceosomal snRNAs nuclear import factor snurportin1. The fluorescence decay was analyzed over nuclear speckles. The results obtained for U2AF^{65} and SmE alone are also shown (*black curves*). Each decay curve corresponds to a pool of three independent experiments, with ten different cells analyzed per experiment.

The results show that the fluorescence decay curves were significantly faster ($p<0.0001$) in cells expressing SPN1Δ1-65. We therefore conclude that spliceosome components shuttle in and out of the nuclear speckles independently of ongoing spliceosomal activity and that the turnover rate increases when splicing is inhibited.

We next used FRAP to analyze the relative mobility of the splicing proteins in the nucleoplasm and nuclear speckles. The fluorescence of a small area located in each of these regions was irreversibly photobleached using a high intensity laser and subsequent recovery due to movement of non-bleached molecules into the bleached area was recorded by time lapse imaging. By fitting an appropriate theoretical function to the recovery curve, we can determine both the effective diffusion coefficient *D* of the GFP-tagged protein and its immobile fraction (Figure 2.6).

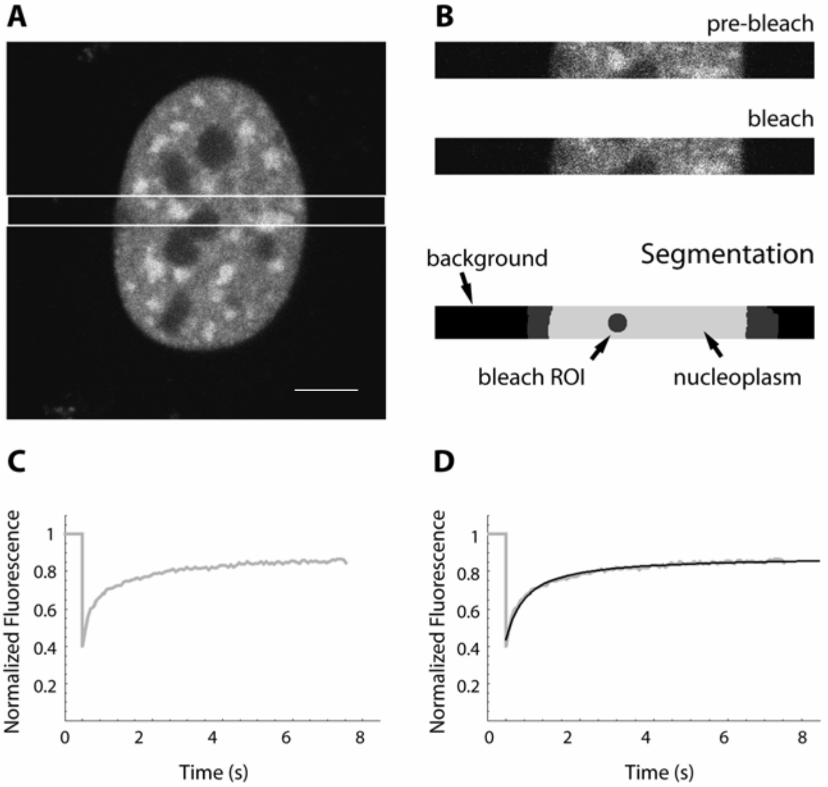

Figure 2.6 – FRAP Experiment. (A) Hela cell expressing GFP-tagged U2AF^{65}, which localizes to the nucleoplasm and concentrates in nuclear speckles. The white box indicates the region scanned in the FRAP experiment. Bar: 5 μm. **(B)** Pre- and post-bleach images of the scanned region depicted in **A**. These images were segmented for quantification of fluorescence intensity. Note that the bleach region includes a nuclear speckle. **(C)** Recovery of fluorescence intensity (*I*) is monitored over time. *I* is corrected for background intensity and the amount of total fluorescence loss during the bleach and imaging. The recovery curve (*grey line*) corresponds to a pool of three independent experiments, with ten different cells analyzed per experiment. **(D)** The experimental FRAP recovery curve is fitted to an appropriate theoretical recovery function yielding values for the apparent diffusion coefficient *D* and the immobile fraction.

We performed FRAP experiments on the nucleoplasm and on the nuclear speckles of cells expressing GFP-SmE (~ 37 kDa), GFP-U2AF^{65} (~ 92 kDa), GFP-U2AF^{35} (~ 63 kDa), GFP-SF1 (~ 92 kDa) and GFP-SF3a120 (~ 147 kDa) and GFP-PABPN1-coilin, for comparison with an immobile protein (Figure 2.7). Quantification of FRAP recovery curves yielded effective diffusion coefficient values ranging from 0.70 to 1.84 $\mu m^2 s^{-1}$ in the nucleoplasm and 0.30 to 1.22 $\mu m^2 s^{-1}$ in the nuclear speckles (see Table 2.1).

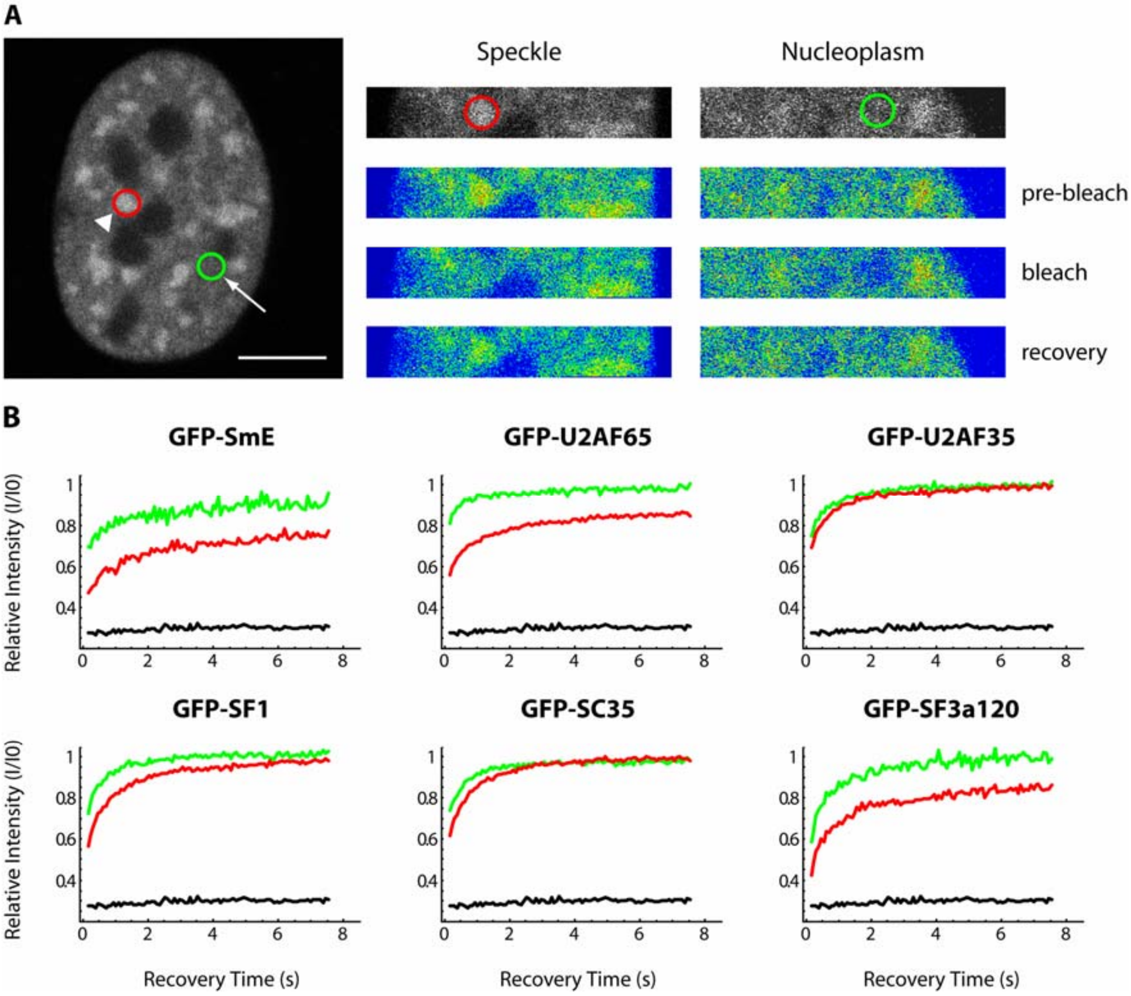

Figure 2.7 – FRAP analysis of splicing proteins in the different sub-nuclear compartments (A) FRAP experiments were performed in the speckles (*arrowhead, red circle*) and in the nucleoplasm (*arrow, green circle*) of HeLa cells expressing GFP-tagged splicing proteins. FRAP sequences of pre-bleach, post-bleach and 8 s recovery images are shown in pseudo-color for bleaching performed in the speckles and in the nucleoplasm. Bar: 5 µm. **(B)** FRAP recovery curves of indicated GFP-tagged splicing proteins in the speckles (*red curves*) and nucleoplasm (*green curves*). Each recovery curve corresponds to a pool of three independent experiments, with then different cells analyzed per experiment. The recovery for the immobile protein GFP-coilin-PABPN1 is shown for comparison (*black curve*).

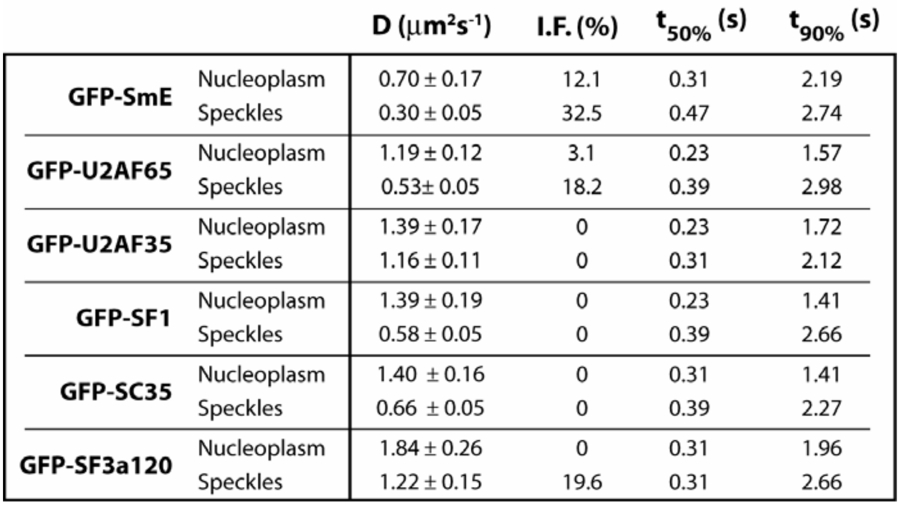

		D ($\mu m^2 s^{-1}$)	I.F. (%)	$t_{50\%}$ (s)	$t_{90\%}$ (s)
GFP-SmE	Nucleoplasm	0.70 ± 0.17	12.1	0.31	2.19
	Speckles	0.30 ± 0.05	32.5	0.47	2.74
GFP-U2AF65	Nucleoplasm	1.19 ± 0.12	3.1	0.23	1.57
	Speckles	0.53± 0.05	18.2	0.39	2.98
GFP-U2AF35	Nucleoplasm	1.39 ± 0.17	0	0.23	1.72
	Speckles	1.16 ± 0.11	0	0.31	2.12
GFP-SF1	Nucleoplasm	1.39 ± 0.19	0	0.23	1.41
	Speckles	0.58 ± 0.05	0	0.39	2.66
GFP-SC35	Nucleoplasm	1.40 ± 0.16	0	0.31	1.41
	Speckles	0.66 ± 0.05	0	0.39	2.27
GFP-SF3a120	Nucleoplasm	1.84 ± 0.26	0	0.31	1.96
	Speckles	1.22 ± 0.15	19.6	0.31	2.66

Table 2.1 – Quantitative FRAP analysis of splicing proteins dynamics in the different sub-nuclear compartments. Experimental values obtained for the diffusion coefficient (**D**), apparent immobile fraction (**I.F.**), recovery time at 50% of initial fluorescence (**$t_{50\%}$**) and recovery time at 90% of initial fluorescence (**$t_{90\%}$**) in the speckles and nucleoplasm of HeLa cells transfected with the indicated GFP-tagged splicing proteins. See figure 2.7 for FRAP recovery curves.

These values are significantly lower than the expected diffusion coefficient for a protein with a molecular weight of approximately 100 kDa (~ 20 $\mu m^2 s^{-1}$, considering the fusion of 27 kDa GFP with an average splicing protein). This suggests that splicing proteins do not diffuse in the nucleus as individual particles but rather interact with other nuclear molecules, possibly other splicing proteins, forming pre-spliceosome complexes.

FRAP experiments performed on cells treated with DRB showed that none of the proteins tested was significantly immobilized in response to the drug, as expected if their movement was dependent on the presence of nascent pre-mRNAs. On the contrary, the recovery rate tended to be even faster in the speckles DRB-treated cells (Figure 2.8), in accordance with the results obtained in FLIP experiments.

This implies that, irrespective of the drug treatment, unbleached splicing proteins are constantly moving into the bleached speckles replacing bleached molecules that presumably exited in the meantime.

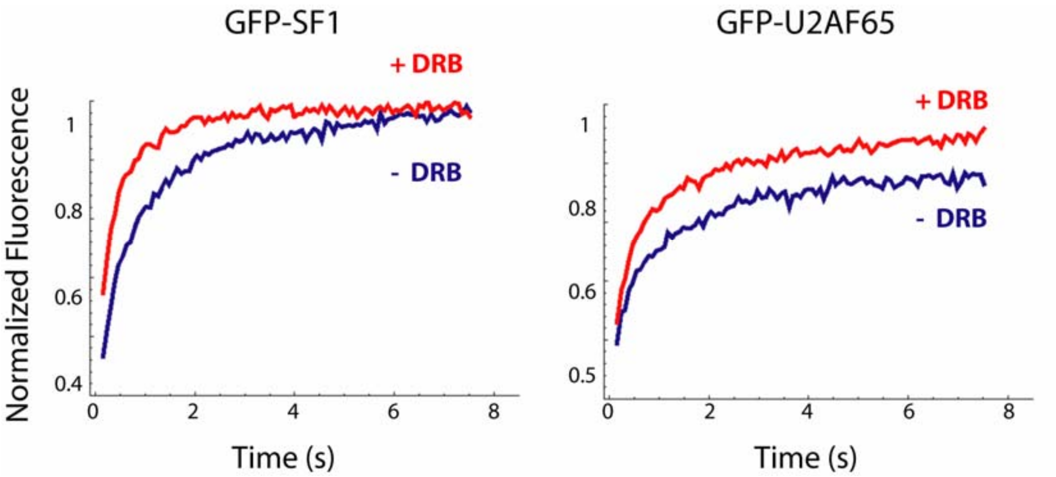

Figure 2.8 – Splicing factors mobility is increased in the speckles of cells treated with DRB. FRAP experiments were performed for GFP-SF1 and GFP-U2AF^{65} on cells mock treated (- DRB) or treated with DRB for 30 min (+ DRB). Each recovery curve corresponds to a pool of three independent experiments, with then different cells analyzed per experiment. Shown are the recoveries observed in a circular area with radius 1.19 μm that corresponded to a nuclear speckle.

The existence of an apparent immobile fraction for GFP-U2AF^{65} in the speckles (~ 18%) prompted us to perform FRAP-FIM experiments in these nuclear regions, as a long residence time for a subpopulation of U2AF^{65} could reflect a putative docking to these subnuclear domains. In apparent contradiction with the FRAP results, no transient immobilization of GFP-U2AF^{65} was found at the nuclear speckles (Figure 2.9).

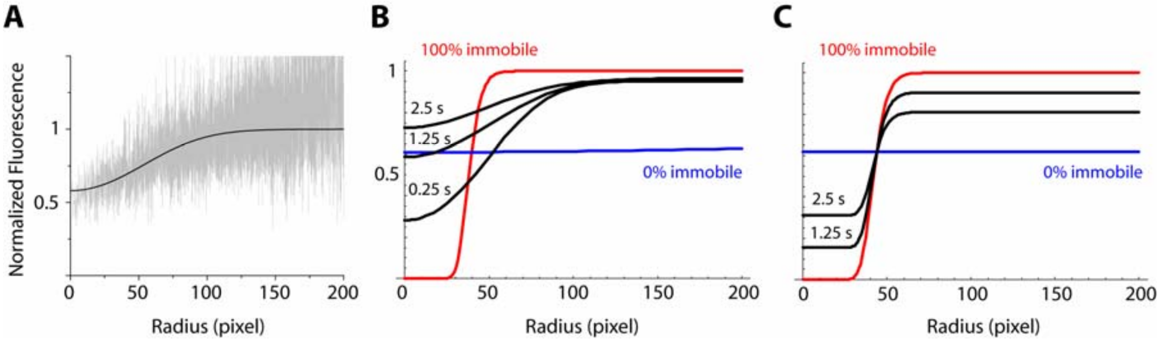

Figure 2.9 – FRAP-FIM analysis of GFP-U2AF^{65} immobilization at the nuclear speckles. **(A)** Fluorescence Ratio Profile (FRP) measured 1.25 s after bleaching a circular region of ~ 1.2 μm radius (30 pixels) that coincided with a nuclear speckle, in a HeLa cell expressing GFP-tagged U2AF^{65}. The experimental values (*gray*) were fitted to an appropriate function (*black line*) which yielded the bleach parameters. **(B)** FRPs fits obtained for HeLa cells expressing GFP-coilin-PABPN1 (*100% immobile, red line*), GFP (*0% immobile, blue line*) and GFP-U2AF^{65} at the indicated time points (*black lines*). Note that the GFP-U2AF^{65} FRPs widen over time, contrary to what would be expected for transient immobilization at the speckles (simulated FPR curves in **C**, assuming an average immobilization time of 5 s).

The Fluorescence Ratio Profiles (FRPs) obtained with FRAP-FIM for cells expressing GFP-U2AF^{65} are not consistent with the existence of a long residence time subpopulation of this splicing factor at the speckles (compare Figures 2.9B and 2.9C). Instead, transient interactions occurring at the same or faster timescale than diffusion itself are presumably responsible for the diffusive-like evolution of FRPs over time. FRAP experiments performed over a longer time period indeed show that there is no "immobile fraction" of GFP-U2AF^{65} at the nuclear speckles (Figure 2.10D).

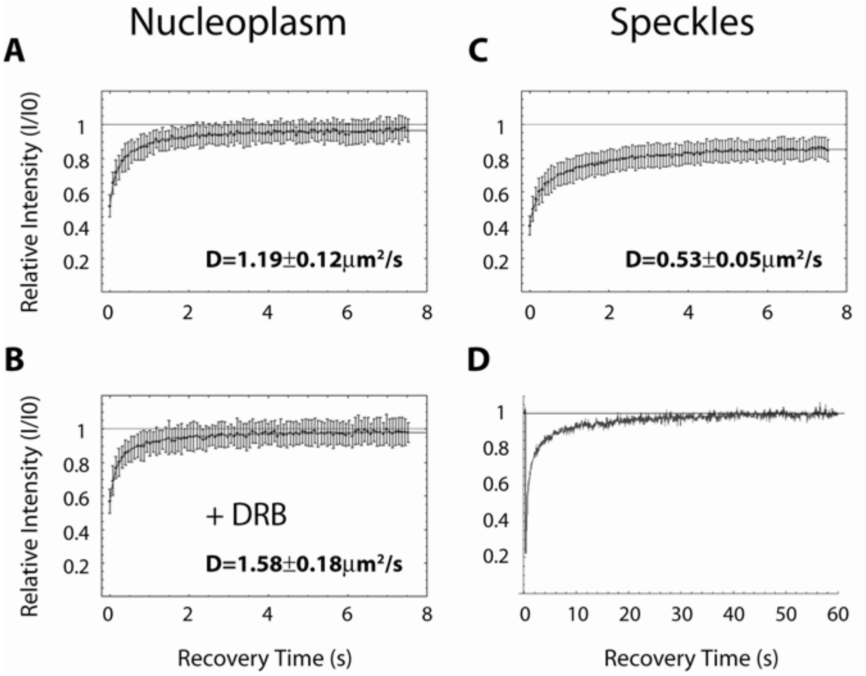

Figure 2.10 – FRAP analysis of U2AF^{65} dynamics. HeLa cells expressing GFP-U2AF^{65} were imaged before and during recovery after bleaching a circular region with radius 1.19 μm, corresponding either to a speckle or a nucleoplasmic area. Recovery curves are shown for the nucleoplasm in cells without DRB treatment (**A**) and after 30 minutes of DRB addition to the medium (**B**). Each recovery curve corresponds to a pool of three independent experiments, with then different cells analyzed per experiment. DRB treatment increases the mobility of GFP-U2AF^{65} in the nucleoplasm. A much slower fluorescence recovery is obtained for GFP-U2AF^{65} in the speckles of untreated cells (**C**), presumably due to binding reactions occurring in this region. This is also reflected in the reduction of the effective diffusion coefficient estimated by FRAP (from 1.19 $\mu m^2 s^{-1}$ in the nucleoplasm to 0.53 $\mu m^2 s^{-1}$). Complete fluorescence recovery is only obtained after ~ 30 s, as shown in a single cell recovery (**D**). Error bars represent mean ± standard deviation.

To investigate whether the reduced mobility of splicing factors in living cell nuclei was in fact due to interactions among them or other splicing factors proteins we performed FRAP experiments on HeLa cells expressing GFP-U2AF$^{65}\Delta35$ (~ 83 KDa), a deletion mutant of U2AF^{65} that lacks the U2AF^{35} interaction domain, and

GFP-SF1R$_{21}$D (~ 96 KDa), a single point mutant that is unable to bind to U2AF^{65} and fails to concentrate at the nuclear speckles (Selenko et al., 2003).

Both mutants showed the same rapid recovery (Fig. 2.12), with a *D* value of 7.48 μm^{2}s^{-1} that is even higher than the diffusion coefficient found for 70 KDa dextrans (5.9 μm^{2}s^{-1}, *experimental data not shown*).

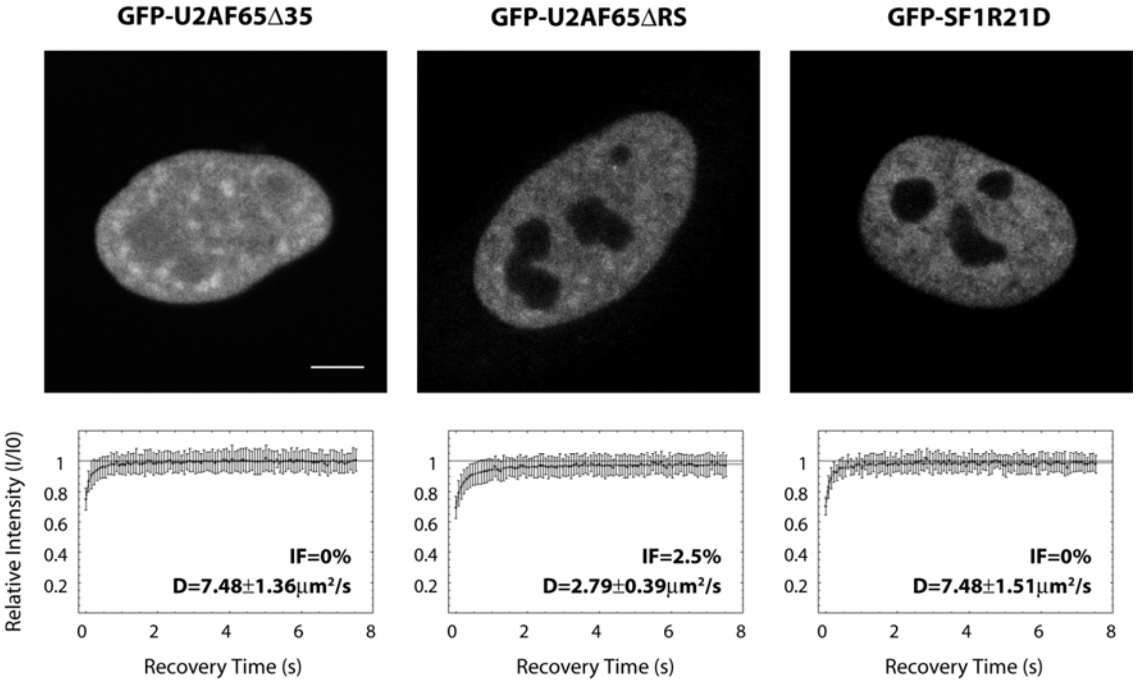

Figure 2.12 – FRAP analysis of splicing proteins mutants FRAP experiments were performed in HeLa cells expressing GFP-tagged mutants of the splicing proteins U2AF^{65} and SF1. U2AF^{65}Δ35 and U2AF65ΔRS are deletion mutants of U2AF^{65} that lack the U2AF^{35} interaction domain and the RS domain, respectively. SF1R$_{21}$D is a single point mutant that is unable to bind to U2AF^{65} and fails to concentrate at nuclear speckles. Each recovery curve corresponds to a pool of three independent experiments, with then different cells analyzed per experiment. Error bars represent standard deviations. D values represent mean ± standard error. IF, immobile fraction. Bar: 5 μm.

GFP-U2AF^{65}Δ35 accumulates at nuclear speckles, but its mobility is the same as measured in the nucleoplasm (*data not shown*). Because U2AF^{65}Δ35 is a deletion mutant of U2AF^{65} and therefore has a lower molecular weight than that of the wild type protein (83 KDa versus 92 KDa), we next asked if the difference in molecular size alone could account for the measured change in mobility. FRAP experiments performed on GFP-tagged U2AF^{65}ΔRS, a mutant of U2AF^{65} that lacks the RS domain and has the same molecular weight as U2AF^{65}Δ35 (~ 83 KDa) yielded a *D* value of 2.69 μm^{2}s^{-1} (Fig. 2.12), implying that interactions mediated by different binding domains, but not molecular weights, are responsible for these changes in U2AF^{65}

mobility. Furthermore, since the ratio of the diffusion coefficients of two proteins is inversely proportional to the cubic root of the ratio of their molecular weight, a difference of 9 KDa between GFP-U2AF$^{65}\Delta$35 and GFP-U2AF^{65} would only account for a 1.04 fold difference in the diffusion coefficients, instead of the 6.3 fold increase measured. Taken together, our data suggests that the mobility of GFP-U2AF^{65}, GFP-U2AF^{35} and GFP-SF1 is correlated with the ability of these proteins to interact with each other, and that the reduced mobility of these splicing factors in the speckles might be due to the formation of a multi-protein complex distinct from the spliceosome.

In order to monitor more directly the kinetic behavior of splicing proteins in the sites where the spliceosome is assembled, we used the FRAP technique in conjunction with an adenovirus model. Our rationale was that by using adenovirus infected cells, in which all splicing machinery is recruited to viral transcription rings, we would overcome the problem of having splicing sites distributed throughout the nucleoplasm and FRAP data that reflected not only the behavior of protein bound to the spliceosome, but also of free protein. FRAP experiments performed in the transcription rings of adenoviral infected cells expressing GFP-tagged splicing factors yielded very fast recovery rates for the vast majority of them (Figure 2.13).

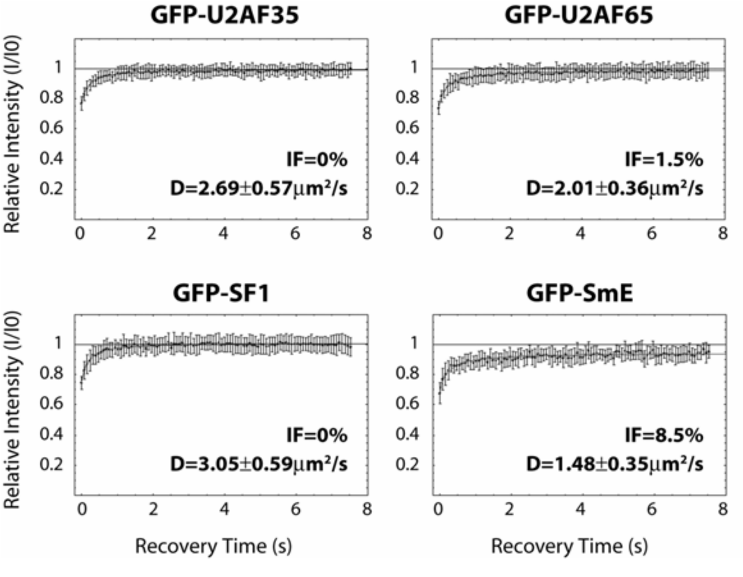

Figure 2.13 – FRAP analysis of splicing proteins in adenoviral infected cells. FRAP experiments were performed in the transcription rings of HeLa cells infected with adenovirus and expressing GFP-tagged splicing proteins. Each recovery curve of indicated GFP-tagged splicing proteins corresponds to a pool of three independent experiments, with then different cells analyzed per experiment. Error bars represent standard deviations. D values represent mean ± standard error. IF, immobile fraction.

The measured values for the effective diffusion coefficients in the viral transcription rings are even higher that those measured in the nucleoplasm of non-infected cells (for GFP-U2AF^{65} the *D* value increased from 1.19 to 2.01 $\mu m^2 s^{-1}$), implying that the residence times of splicing factors in the spliceosome are very small, with binding occurring at faster or comparable rates than diffusion itself.

We then asked whether simple diffusive processes, together with changes in the number of binding sites available in the nucleoplasm would be enough to explain the differences in steady state distributions of splicing factors following transcription inhibition.

We used a simple Monte Carlo model which simulates molecular movement as Brownian motion and interactions of splicing factors as stochastic events. Our goal was to determine to what extent this purely stochastic model could explain the experimental results observed. In the model, splicing factors interact with immobile targets. Different reaction parameters (pseudo-on and off rates) were assigned to nucleoplasm and speckles (circular regions with chosen radii of 8 μm and 0.7 μm, respectively), based on steady-state fluorescent images and FRAP data. Free molecules (i.e. neither bound to the splicing sites nor to the speckles) were assumed to diffuse with an effective diffusion coefficient of $D_{free} = 1.58\,\mu m^2 s^{-1}$, determined experimentally by FRAP using DRB treated cells expressing GFP-U2AF65 (Figure 2.10B). Transcription inhibition by DRB reduces the total number of splicing sites, a change which was modeled as a decrease in the pseudo-on rate in the nucleoplasm.

The Monte Carlo model successfully reproduced the experimental observations of increased splicing factors concentration at the speckles, upon DRB addition (*data not shown*). To test whether the observed behavior of splicing factors was due to a change in the number of splicing sites, or to an increased affinity at the speckles instead, FLIP simulations were performed for each of these conditions (Figure 2.11). As expected, the rate of fluorescent decay under normal conditions was very similar to the experimental data, taking into account that the simulation parameters were chosen to best fit the microscopic observations. Introducing a decrease in the pseudo-on rate ($k^*_{on,nuc}$) for the splicing sites resulted in increased rates of fluorescence loss from unbleached speckles (Figure 2.5B), whereas increasing the affinity of splicing factors to the speckles ($k^*_{on,spk}$) had the opposite effect (Figure 2.5C).

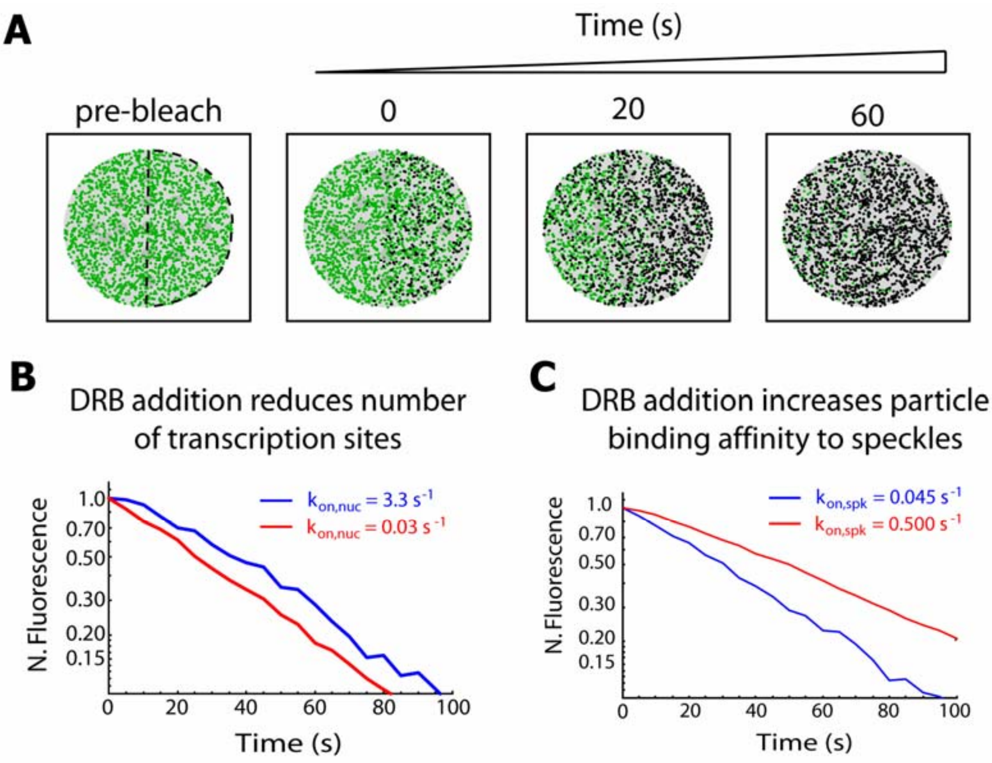

Figure 2.11 – Modeling FLIP experiments in the cell nucleus according to a stochastic model (A) Schematic illustration of a simulated FLIP sequence. The green dots represent the positions of unbleached molecules, while the black dots represent the bleached ones. The area that was repeatedly bleached corresponds to the right-half of the circle that defines the nucleus. The system was in a steady-state situation before repetitive bleaching started. Fluorescence was monitored in the unbleached portion of the circle, both in a nuclear speckle and in a nucleoplasmic region of the same size and at the same distance from the bleached region. **(B and C)** FLIP decay curves were generated by counting the number of fluorescent molecules inside the monitored regions at defined time intervals. For normalization, these values are divided by the number of fluorescent molecules in those regions immediately before bleaching. The values of $k^*_{on,nuc}$ and $k^*_{on,spk}$ in the presence (*red*) and absence *(blue*) of DRB are shown for simulations where DRB addition was modeled as a reduction in the number of transcription sites (**B**) or as an increase in the SFs affinity to speckles (**C**). Note that the fluorescence decay is faster for cells treated with DRB in (**B**), but not in (**C**).

Thus, decreasing the number of nucleoplasmic binding sites in the model is sufficient to reproduce the faster kinetics of splicing factors observed in cells when splicing is inhibited. Furthermore, our analysis argues against the view that splicing inhibition leads to an increased affinity of splicing factors to the nuclear speckles.

2.5 Discussion

The *in vivo* dynamics of several splicing factors in the nuclei of HeLa cells was analyzed using time-lapse microscopy, photobleaching techniques such as FRAP, FLIP and FRAP-FIM and Monte-Carlo simulations. We have shown that splicing factors are highly dynamic inside the nucleus. They cycle continuously with fast exchange rates between the speckles and nucleoplasm, where they are able to move rapidly throughout the entire nuclear volume. Similar results have been reported for photobleaching experiments performed with other splicing factors (Kruhlak et al., 2000; Phair and Misteli, 2000). Even though splicing factors show a high mobility inside the nucleus, their effective diffusion coefficients as measured by FRAP are considerably lower than what would be expected for free diffusing molecules of the same molecular weight. The effective diffusion coefficients measured for SFs ranged from 0.70 to 1.84 $\mu m^2 s^{-1}$ in the nucleoplasm and 0.30 to 1.22 $\mu m^2 s^{-1}$ in the nuclear speckles. For comparison, GFP alone is able to move relatively freely throughout the nucleus at 33.3 ± 3.6 $\mu m^2 s^{-1}$ (Braga et al., 2004a). Since the ratio of the diffusion coefficients of two proteins is inversely proportional to the cubic root of the ratio of their molecular weight, an inert protein with the same molecular weight as GFP-U2AF^{65} for instance, would have an expected diffusion coefficient of ~ 22 $\mu m^2 s^{-1}$. Yet, we measured an effective diffusion coefficient of 1.19 $\mu m^2 s^{-1}$ for GFP-U2AF^{65} in the nucleoplasm. FRAP experiments performed with FITC-labeled dextrans of different molecular weights that were microinjected into the nuclei of HeLa cells provide further data for mobility comparisons (Braga et al., 2004a). Again, the effective diffusion coefficients of all the splicing factors we studied were consistently lower than that of dextrans of similar size (5.9 $\mu m^2 s^{-1}$ for a 70 kDa dextran). In fact, the D values measured in the nucleoplasm for all splicing factors were even lower than that of a 500 kDa dextran (1.7 $\mu m^2 s^{-1}$) and in the nuclear speckles these mobility rates were even more reduced.

The engagement of splicing factors to active spliceosomes, which are distributed throughout the nucleoplasm, is most likely to be the cause for the reduced mobility of SFs at this nuclear compartment. We studied the kinetics of these binding reactions more directly by performing FRAP on adenoviral infected cells, which have all transcription and splicing machinery recruited to viral transcription rings. We found the residence times of splicing factors in these domains to be very small, with binding occurring at rates which are comparable or even faster than diffusion itself. This was reflected in the FRAP recovery curves as an "effective diffusion" behavior, characteristic of very fast reaction-diffusion systems (see section 1.5.3 in Chapter 1), with effective diffusion coefficients ranging from 1.48 to 3.05 $\mu m^2 s^{-1}$.

The reduced mobility rates of splicing factors at the speckles, which are devoid of active spliceosomes (Cmarko et al., 1999; Misteli and Spector, 1999), suggested the formation of large multi-protein complexes distinct of the spliceosome. We tested this hypothesis by performing FRAP experiments on cells expressing mutants of splicing factors that lacked specific domains responsible for interactions between them. The results in fact showed that the mobility of splicing factors both in the speckles and in the nucleoplasm is correlated with the ability of these proteins to interact with each other. Abolition of a specific $U2AF^{35}$-binding domain in $U2AF^{65}$ and the introduction of a point mutation on SF1 that abolished its binding to $U2AF^{65}$ greatly increased the mobility of these mutant splicing factors to rates similar to those of inert molecules of the same size. Interestingly, the point mutation in SF1 that abolished the binding of this protein to $U2AF^{65}$ also disrupted its association to the nuclear speckles. Binding of SFs to the speckles thus seems to depend on interactions among them, even though no "resident population" of a given splicing factor was found at these nuclear domains. FRAP data for GFP-$U2AF^{65}$ at first indicated the presence of an apparent "immobile fraction" at the speckles, which however was shown by FRAP-FIM to correspond to transient, rapid interactions again occurring at a timescale comparable or faster than diffusion itself. FRAP experiments performed over a longer time period consistently revealed a complete recovery of GFP-$U2AF^{65}$, arguing against the existence of a putative "docking" population of GFP-$U2AF^{65}$ at the speckles.

Nevertheless, in the absence of transcription, the concentration of splicing factors is increased at the speckles, which approximately double in size and acquire a rounder appearance, in accordance with the proposed role of storage/reservoir sites for these subnuclear structures (Misteli, 2005). This phenomenon could be due to the existence of a transcription-coupled "recruiting" signal that would target the SFs from the speckles to the sites of active splicing. The lack of such a signal in transcription inhibited cells would then be responsible for longer retention times of SFs at the speckles and therefore increased concentration at these domains.

To investigate the existence of such a transcription-dependent recruiting signal we performed FLIP experiments in mock-treated cells and in cells treated with the transcription inhibitor DRB. By photobleaching half of the cell nucleus repeatedly and measuring the fluorescence loss in unbleached speckles, we could directly compare the kinetics of SFs in untreated and treated cells. Surprisingly, the fluorescence loss was faster in the speckles of DRB-treated cells. This result was also obtained when splicing, rather than transcription, was directly inhibited by using a dominant negative mutant of the snRNPs import factor snurportin1. Interestingly, the same behavior has been reported previously for another splicing factor, ASF/SF2, that showed a slight increase in mobility following transcription inhibition (Kruhlak et al., 2000).

As these results exclude the hypothesis of a specific signal for targeting splicing factors to transcription sites, we hypothesized that SFs are constantly shuttling in and out of the nuclear speckles but they are transiently retained in transcription sites. The speckles and the transcription sites would thus act as two distinct binding regions for SFs that are effectively competing with each other, being the steady-state situation a reflection of the different binding affinities of SFs to each region. In the absence of splicing, the transient retention at the transcription sites would disappear and SFs would be rapidly re-targeted to the speckles. Thus, the increase of SFs concentration at the speckles would be a direct consequence of their increased mobility in the nucleoplasm. With the decrease in the competition between speckles and transcription sites, SFs would have a higher chance of reaching a speckle and getting bound to it. The increased rates of fluorescence loss in FLIP experiments performed on transcription-inhibited cells were also a result of the increased mobility in the nucleoplasm, as faster diffusing SFs would now have a higher probability of moving into the bleached area. Our hypothesis was tested with Monte-Carlo simulations that relied exclusively on stochastic processes to model the dynamics of SFs, with movement being modeled as Brownian motion and binding to the speckles and transcription sites as random events whose probability depended on the on- and off-rate binding constants. Since transcription inhibition reduces the number of nascent transcripts available for splicing, it was modeled as a reduction in the number of binding sites at the nucleoplasm (a decrease in the on-rate constant in the nucleoplasm). Simulations of both time-lapse microscopy and FLIP experiments in mock-treated cells and in cells treated with DRB yielded results which are consistent with our experimental observations.

We thus show that the recruitment of splicing factors to the nuclear speckles is independent of the transcriptional state of the cell, as previously proposed by others (Carrero et al., 2006; Misteli, 2001a) and that the levels of SFs in the different nuclear domains are compatible with stochastic models of self-organization (see section 1.2.2 in Chapter 1). In addition, the existence of large multi-protein complexes distinct of the spliceosome, as suggested by FRAP data, indicates that the assembly of the splicing machinery probably occurs with pre-assembled particles, rather than stepwise addition of discrete components.

3. mRNA splicing factors interactions studied with FRET techniques

3.1 Abstract

The membraneless structures of the nucleus have been proposed to be formed and maintained by self-organization mechanisms. In this view, subnuclear structures such as nuclear speckles would be formed as a consequence of stochastic, transient interactions occurring between its component proteins, which include a broad range of splicing factors. To visualize and spatially map the interactions between different splicing factors, we performed Acceptor Photobleaching FRET and Fluorescence Lifetime Imaging Microscopy (FLIM) using YFP and CFP tagged versions of U2AF^{65}, U2AF^{35} and SF1, which are known to interact at the active spliceosome. The results show that U2AF^{65} is able to interact with both U2AF^{35} and SF1 in the speckles and nucleoplasm even in the presence of DRB, which indirectly prevents spliceosome assembly. We were also able to detect a novel self-interaction of U2AF^{65}. Taken together, our results suggest that splicing factors accumulate in the nuclear speckles already assembled in a complex, even in the absence of splicing, thus favoring a view where spliceosomes are brought together onto pre-mRNA as large pre-assembled particles rather than by stepwise addition of discrete components.

3.2 Introduction

The nucleus is a highly heterogeneous and dynamic organelle. The dynamic nature of nuclear components suggests the nucleus might be a self-organizing entity (Misteli, 2001a; Misteli, 2005), with nuclear morphology being a reflection of all the molecular interactions between the nuclear components. In this view, steady-state structures such as the nuclear speckles would be formed as a consequence of the stochastic, relatively promiscuous and transient interactions occurring between splicing factors that are diffusing in the nucleus (Lamond and Spector, 2003; Misteli, 2001a). Nuclear diffusion and the different binding kinetics of SFs would then be determinant in shaping the speckles morphology and dynamics.

Photobleaching experiments performed on HeLa cells expressing GFP-tagged splicing factors revealed that their mobility rates were correlated with the ability of these proteins to interact with each other (see Chapter 2). In the speckles, which are devoid of active spliceosomes, this reduced interaction-dependent mobility of splicing factors further suggested the existence of pre-assembled complexes distinct of the spliceosome.

The aim of this chapter is to detect and spatially map these interactions between the splicing factors U2AF^{65}, U2AF^{35} and SF1, which are known to interact at the active spliceosome, using YFP and CFP tagged versions of these proteins. We have developed an improved Acceptor Photobleaching FRET method and used Fluorescence Lifetime Imaging Microscopy (FLIM, see section 1.5.4 in Chapter 1) to study molecular interactions in the nucleoplasm and in the nuclear speckles of HeLa cells.

The results show that U2AF^{65} is able to interact with both U2AF^{35} and SF1 in the speckles and nucleoplasm even in the presence of DRB, which indirectly prevents spliceosome assembly. Splicing factors mutants that lack specific interaction domains, as expected, do not show a significant FRET signal.

Self-organization models for speckles formation suggest that splicing factors self-interactions are prone to occur, thus increasing the promiscuity and complexity of their interactions. Recently, an interaction of this type has been reported for U2AF^{35} (Chusainow et al., 2005). Our results demonstrate for the first time that U2AF^{65} is also able to self-interact, thus adding to the increasing data supporting self-organization models for speckles assembly and maintenance.

3.3 Materials and Methods

Cell culture, transfections and drug treatment

HeLa cells were cultured as monolayers in Modified Eagle’s Medium (MEM) supplemented with 10% fetal calf serum (Invitrogen, Paisley, Scotland). Cells were plated and observed in glass bottom chambers (MatTek, Ashland, MA). For imaging, the medium was changed to D-MEM/F-12 without phenol red supplemented with 15 mM HEPES buffer (Invitrogen). HeLa subconfluent cells were transiently transfected with FuGENE6 reagent (Roche Biochemicals, Indianapolis, IN) using 1 μg of DNA, and analyzed at 16-24h after transfection. DRB (Sigma-Aldrich, St. Louis, MO) was used at 75 μM from a stock solution of 11 mM in ethanol.

Acceptor Photobleaching FRET

FRET between splicing factors tagged with the donor CFP and the acceptor YFP was measured using the acceptor photobleaching method (Kenworthy, 2001) on a Zeiss LSM 510 confocal microscope (Carl Zeiss) operating a 25 mW argon laser. Cells were imaged using the PlanApochromat 63x/1.4 oil immersion objective at zoom 5 (pixel width 57 nm). CFP fluorescence was detected using the 458 nm laser line and a BP 470-500 nm filter, while YFP was excited with the 514 nm laser line and its fluorescence detected using a LP 530 nm filter. Detector gains were adjusted in order to eliminate cross-talk and achieve a good dynamic range. In the acceptor photobleaching method, if FRET is occurring between the donor and the acceptor, then photobleaching of the acceptor (YFP) should yield a significant fluorescence increase of the donor (CFP). Bleaching of the YFP was performed in a rectangular region of interest (ROI) in the cell, using the 514 nm argon laser line at 100% intensity and 40 bleach iterations (the time of bleach ranged from 8 to 12 s, depending on ROI size). A series of 4 images from the donor channel were taken before and after bleaching, with laser intensity set to 30%. The pre and postbleach image series were then background subtracted and processed with ImageJ (http://rsb.info.nih.gov/ij/) using a rigid body registration algorithm to correct for cell displacement during image acquisition. FRET energy transfer efficiency is given by $E_{FRET} = 1 - (F_{DA} / F_D)$, where F_{DA} is the donor fluorescence in the presence of the acceptor (before YFP bleaching) and F_D is the donor fluorescence alone (after YFP bleaching). FRET efficiency maps were generated using Mathematica 5.0 (Wolfram Research). The pre- and postbleach image series were corrected for fluorescence loss due to scanning by multiplying each pixel intensity value by the ratio of total average image intensities (excluding the bleached ROI) between each image and the first image of the series. The pre- and post-bleach image series were then averaged to create single pre and post-bleach images, which were further convoluted with an 11x11 pixel filter to reduce image noise. FRET efficiency values were then calculated for each pixel in the image that had an intensity value above a certain threshold, thereby avoiding calculation of E_{FRET} in the background and in areas of reduced intensity where the signal-to-noise ratio is lower. In addition, mask images were also generated for border regions of the cell (nuclear membrane and nucleoli periphery) where the fluorescence gradient was steeper, thus preventing the calculation of FRET efficiencies in these regions as minor cell displacements uncorrected by the registration procedure were prone to produce false positive FRET signals. The calculated FRET efficiencies were then color coded for each pixel, ranging from 0 (blue) to 0.3 (red), and superimposed to the pre-bleach donor image, yielding the FRET efficiency maps.

Fluorescence Lifetime Imaging Microscopy

FLIM images were recorded on a instrument described extensively elsewhere (van Munster and Gadella, 2004a) based on frequency-domain lifetime detection (van Munster and Gadella, 2005). Basically, excitation light is modulated at 75 MHz and fluorescence images are recorded by a CCD camera through a gated image intensifier also modulated at 75 MHz. By recording fluorescent images at different phases between excitation light and intensifier, changes in phase and modulation depth of the emitted light relative to the excitation can be detected. From this the two lifetimes are derived: τ_φ and τ_M, based on the phase shift and modulation, respectively. The instrument is based on an inverted wide-field microscope (Axiovert 200M, Carl Zeiss). CFP lifetime images were recorded using 442 nm excitation, a 63 x NA 1.3 oil objective (Carl Zeiss), a 455LP dichroic and a 480 / 40 nm band-pass filter (all filters from Chroma, Rockingham, USA). Per lifetime recording, 8 phase images were recorded with an exposure time of 800 ms each. The order in which the images were recorded was chosen in such a way to limit the effects of Photobleaching (van Munster and Gadella, 2004b). Recorded images were analyzed for the occurrence of Photobleaching and corrected for this if necessary. After calculation of the lifetimes the average phase and modulation lifetime of each cell was determined by averaging the pixels constituting the cell.

3.4 Results

3.4.1 U2AF^{65} interacts with U2AF^{35} and SF1 at the nucleoplasm and speckles even in the absence of splicing

Having previously shown that splicing factors mobility and accumulation at the nuclear speckles is dependent on interactions between these proteins (see Chapter 2) we decided to use FRET techniques to detect and spatially map these interactions.

For this, we prepared different CFP and YFP constructs U2AF^{65}, U2AF^{35} and SF1 to use as donor-acceptor pairs in confocal Acceptor Photobleaching FRET experiments (Karpova et al., 2003; Wouters et al., 2001). In this technique, cells co-expressing the CFP and YFP tagged proteins of interest are fixed in coverslips and imaged on a confocal microscope. FRET between the donor (CFP-tagged splicing factor) and the acceptor (YFP-tagged splicing factor) is detected by irreversibly photobleaching the acceptor in a region of interest and comparing donor emission before and after bleaching. If FRET was occurring, then donor fluorescence emission will increase in the bleached region (see section 1.5.4 in Chapter 1). FRET Efficiency Maps were then generated using our improved Acceptor Photobleaching method, which allowed for a spatial mapping of detected interactions (Figure 3.1; see also Materials and Methods and Appendix 3.A).

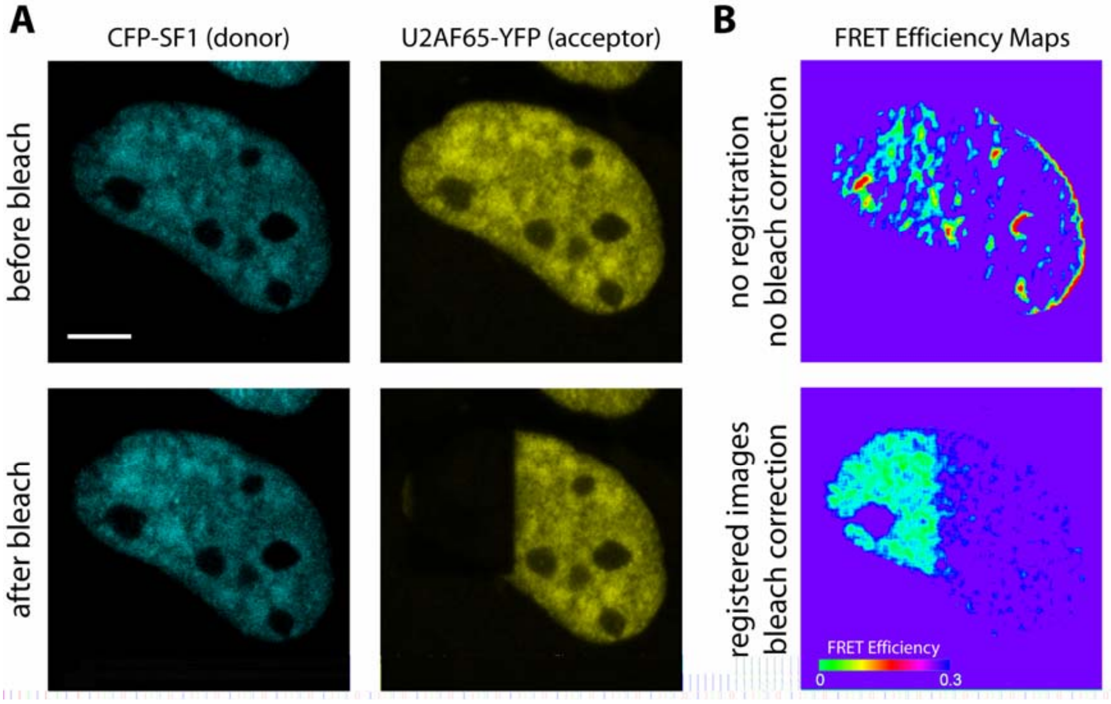

Figure 3.1 – Improved Acceptor Photobleaching FRET method (A) Pre- and post-bleach example images of donor (CFP-tagged SF1) and acceptor (YFP-tagged U2AF^{65}) obtained in an Acceptor Photobleaching FRET experiment. Bleaching is performed in a rectangular region of interest corresponding to approximately one third of the nucleus. Notice the increase in the donor fluorescence in the bleached region (*lower left panel*), indicative of the occurrence of FRET between the donor and the acceptor. Bar: 5 µm. **(B)** FRET Efficiency Maps obtained from the experiment shown in **A**, with no image registration and correction of photobleach due to imaging (*top panel*) and with image registration, fluorescence normalization and cell border mask applied (*bottom panel*). Notice the artifact FRET signals in the uncorrected, unregistered FRAP Efficiency Map caused by cell displacement.

Acceptor Photobleaching FRET performed on cells co-expressing CFP-U2AF^{35} and YFP-U2AF^{65} showed a clear FRET signal at the speckles and nucleoplasm, indicating that these splicing factors are interacting directly in both regions (Figure 3.2, *middle left panel*).

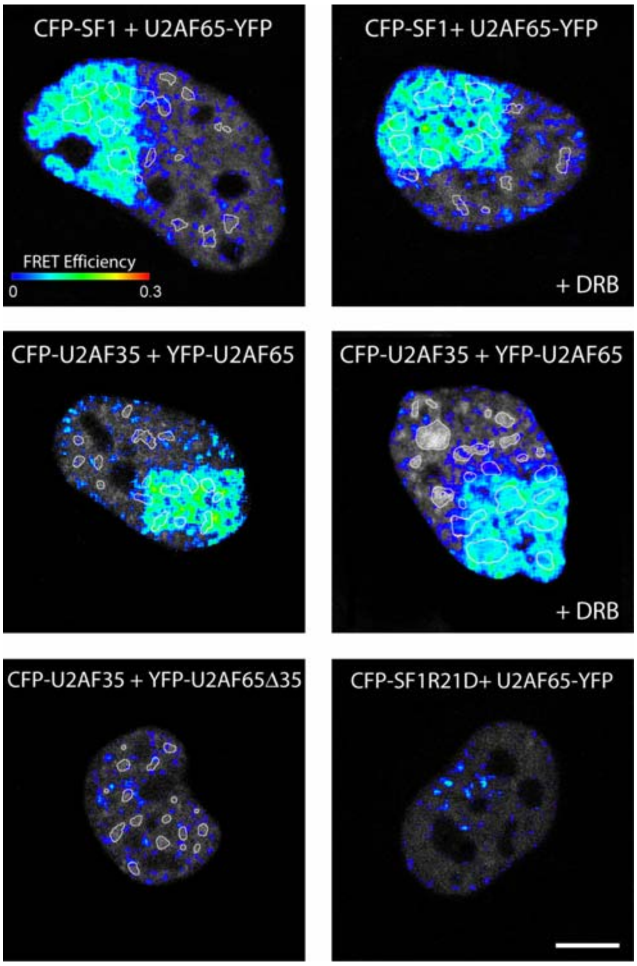

Figure 3.2 – Acceptor Photobleaching FRET between the splicing factors U2AF^{65} and U2AF^{35} and SF1. FRET Efficiency Maps were generated from Acceptor Photobleaching FRET experiments and superimposed to the corresponding pre-bleach donor images. Donor and acceptor pairs are indicated for each case. The nuclear speckles are outlined (*white contours*). U2AF^{65} is shown here to interact with U2AF^{35} and SF1 in the speckles and in the nucleoplasm of HeLa cells even in the presence of DRB, which indirectly prevents spliceosome assembly. Mutants of these splicing factors, as expected, do not show a significant FRET signal: no interactions are seen between U2AF^{35} and U2AF^{65}Δ35 and between U2AF^{65} and SF1R$_{21}$D. Bar: 5 µm.

The same result was obtained when we co-expressed CFP-SF1 together with U2AF^{65}-YFP (Figure 3.2, *top left panel*), but not with YFP-U2AF^{65} (*data not shown*). This is probably due to an increase in the distance between donor and acceptor in the later case, which is in agreement with the findings that an interaction between U2AF^{65}

and SF1 is mediated by the C-terminal RRM (RRM3) of U2AF^{65} and a N-terminal peptide of SF1 (Selenko et al., 2003). As expected, no FRET signal was detected between CFP-U2AF^{35} and the U2AF^{35}-binding impaired deletion mutant YFP-U2AF$^{65}\Delta35$ and, likewise, between the U2AF^{65}-binding impaired point mutant CFP-SF1R$_{21}$D and U2AF^{65}-YFP (Figure 3.2, *lower panels*).

We next asked whether these interactions between U2AF^{65} and both U2AF^{35} and SF1 still occurred in the absence of splicing. To investigate this, we performed Acceptor Photobleaching FRET experiments on cells that were treated with 5,6-dichloro-1-*b*-d-ribofuranosylbenzimidazole (DRB), a Pol II transcription inhibitor that indirectly disrupts also the formation of new active spliceosomes. As expected, upon treatment with DRB, the typical speckled pattern of splicing factors in the cell nucleus changed dramatically to enlarged, round speckles in transcriptionally inactive cells (Melcak et al., 2000; O'Keefe et al., 1994). FRET Efficiency maps again showed that the interactions between CFP-SF1 and U2AF^{65}-YFP, and between CFP-U2AF^{35} and YFP-U2AF^{65} occurred both at the speckles and nucleoplasm (Figure 3.2, *top and middle right panels*), and were thus independent of ongoing splicing reactions.

In order to validate the Acceptor Photobleaching FRET results and cross-compare with a different method, we also performed wide-field frequency domain FLIM microscopy on live cells co-expressing our CFP and YFP-tagged splicing factors. In frequency domain FLIM, the mean donor fluorescence lifetime is measured using two different approaches: the phase shift information yields the phase determined lifetime (τ_φ) whereas the modulation depth decrease yields the modulation lifetime (τ_M), both of them being typically in the order of a few nanoseconds. If FRET is occurring, then both the phase and modulation lifetimes of the donor will decrease in presence of the acceptor, compared to the values of phase and modulation lifetimes of the donor alone (van Munster and Gadella, 2005). FLIM experiments performed on live cells expressing donor CFP constructs alone yielded an average fluorescence phase lifetime of 2.36 ± 0.09 ns and a modulation lifetime of 3.02 ± 0.15 ns ($n = 101$). When cells were co-expressing CFP-U2AF^{35} and YFP-U2AF^{65}, however, FLIM showed a clear reduction of both phase and modulation donor lifetimes (2.11 ± 0.13 ns and 2.73 ± .019 ns, respectively; $n = 32$) and this effect was also observed when the cells were treated with the transcriptional inhibitor DRB ($\tau_\varphi = 2.08 \pm 0.09$ ns and $\tau_M = 2.61 \pm 0.09$ ns; $n = 27$), indicating the occurrence of FRET interactions between CFP-

U2AF^{35} and YFP-U2AF^{65} even when splicing was indirectly inhibited (Figure 3.3, *left graph*).

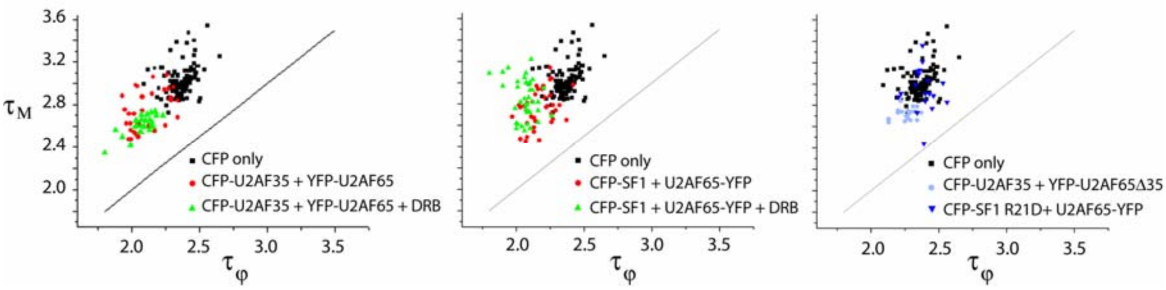

Figure 3.3 – FLIM. Fluorescence Lifetime Imaging Microscopy was performed on HeLa cells expressing the same constructs used in the Acceptor Photobleaching FRET. The average phase (τ_φ) and modulation (τ_M) lifetimes of the donor were calculated for each cell. FRET is shown to occur if both of these values are reduced when compared to the values of the donor CFP alone (*black dots*). Again, U2AF^{65} shows an interaction with both U2AF^{35} and SF1 even if splicing is indirectly inhibited by the presence of DRB, but no interaction is seen between U2AF^{65}Δ35 and U2AF^{35} and between SF1R$_{21}$D and U2AF^{65}.

Again, the same reduction in the donor lifetimes was detected by FLIM on live cells co-expressing CFP-SF1 and U2AF^{65}-YFP in the presence ($\tau_\varphi = 2.06 \pm 0.08$ ns and $\tau_M = 2.84 \pm 0.18$ ns; $n = 38$) and absence ($\tau_\varphi = 2.17 \pm 0.10$ ns and $\tau_M = 2.76 \pm 0.17$ ns; $n = 38$) of DRB (Figure 3.3, *middle graph*), but not CFP-SF1 and YFP-U2AF^{65} (*data not shown*). As expected, no significant reduction in both donor phase and modulation lifetimes was observed when cells were co-expressing CFP-U2AF^{35} together with YFP-U2AF^{65}Δ35 ($\tau_\varphi = 2.26 \pm 0.07$ ns and $\tau_M = 2.73 \pm 0.06$ ns; $n = 21$), and CFP-SF1R$_{21}$D together with U2AF^{65}-YFP ($\tau_\varphi = 2.39 \pm 0.09$ ns and $\tau_M = 2.95 \pm 0.20$ ns; $n = 10$) (Figure 3.3, *right graph*), indicating that no direct protein-protein interactions were detected between these proteins.

3.4.2 Self-interaction of U2AF^{65} *in vivo*

Together with FRET studies that allowed us to visualize direct interactions between U2AF^{65} and U2AF^{35} and between U2AF^{65} and SF1, we were also able to detect a novel U2AF^{65} self-interaction. Taking advantage of the fact that we had two different CFP- and YFP-tagged U2AF^{65} constructs available, with the fluorophores being fused at either the amino or carboxyl terminus, we performed Acceptor Photobleaching FRET and FLIM on cells expressing the four different donor-acceptor possible combinations, namely: U2AF^{65}-CFP + U2AF^{65}-YFP, U2AF^{65}-CFP + YFP-U2AF^{65}, CFP-U2AF^{65} + U2AF^{65}-YFP and CFP-U2AF^{65} + YFP-U2AF^{65} (Figure 3.4).

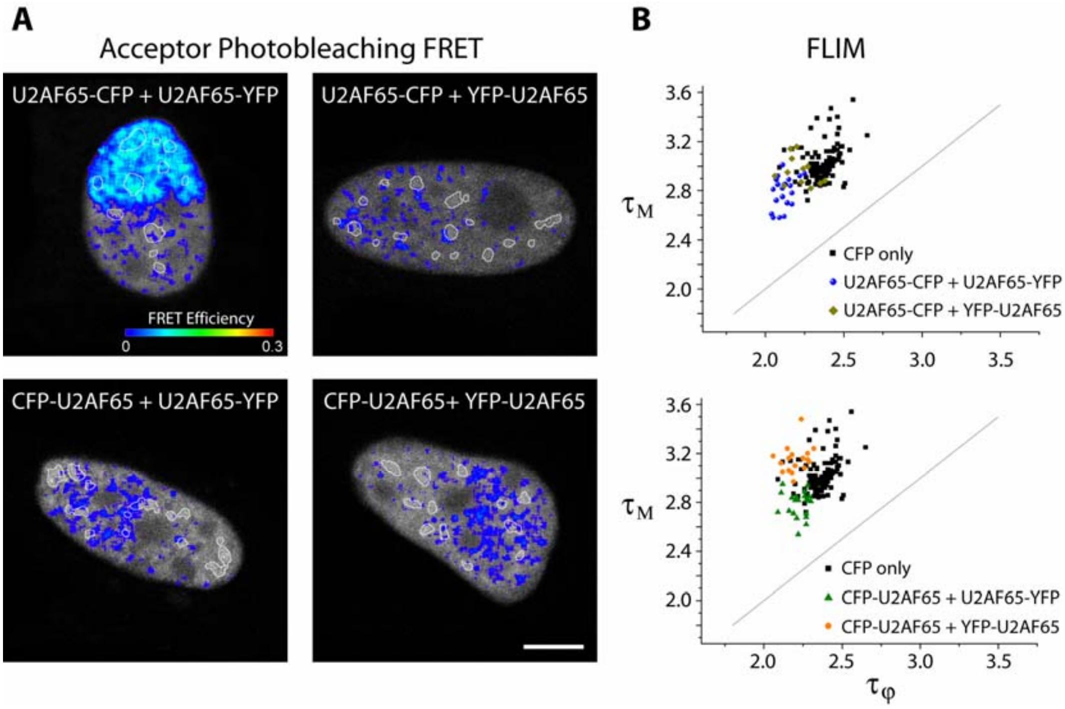

Figure 3.4 – Self-interaction of GFP-U2AF^{65} (A) Efficiency Maps of Acceptor Photobleaching FRET performed on HeLa cells expressing different combinations of CFP and YFP-tagged U2AF^{65}. Donor and acceptor pairs are indicated for each case. FRET is only detected when both the donor CFP and the acceptor YFP are placed in U2AF^{65} C-terminus. The nuclear speckles are outlined (*white contours*). Bar: 5 µm. **(B)** FLIM measurements performed on HeLa cells expressing the same constructs as in **A**. The average phase (τ_φ) and modulation (τ_M) lifetimes of the donor were calculated for each cell and again, FRET is only shown to occur if both the donor CFP and the acceptor YFP are placed in U2AF^{65} C-terminus.

Since no known domain of U2AF^{65} self-interaction has been reported to date, our aim was to probe for positive FRET results by placing the fluorophores at different regions, as the distance between donor and acceptor fluorophores is a crucial factor for FRET to occur (e.g. FRET is detected between CFP-SF1 and U2AF^{65}-YFP, but not YFP-U2AF^{65}). It has been reported previously that no direct protein-protein interaction was detected by FRET in cells co-expressing CFP-U2AF^{65} and YFP-U2AF^{65} (Chusainow et al., 2005). We confirmed this result with Acceptor Photobleaching FRET (Figure 3.4A, *lower right panel*) and FLIM (Figure 3.4B, *lower graph*) and found that the same was true for two other combinations of donor-acceptor pairs: U2AF^{65}-CFP + YFP-U2AF^{65} and CFP-U2AF^{65} + U2AF^{65}-YFP (Figure 3.4). However, when Acceptor Photobleaching FRET was performed on cells co-expressing U2AF^{65}-CFP and U2AF^{65}-YFP, a clear FRET signal was measured at the nucleoplasm and speckles (Figure 3.4A, *upper left panel*). This direct protein-protein interaction was confirmed by FLIM: both phase and modulation donor fluorescence lifetimes decreased, compared to the values of CFP donor constructs alone ($\tau_{\varphi} = 2.12 \pm 0.06$ ns and $\tau_M = 2.79 \pm 0.12$ ns ($n = 23$) versus 2.36 ± 0.09 ns and 3.02 ± 0.15 ns, respectively).

The self-interaction of U2AF^{65} was confirmed biochemically by co-transfecting HeLa cells with hemagglutinin (HA) and GFP-tagged versions of U2AF^{65}. Cell extracts were prepared after 24 hours of expression and the U2AF^{65} homodimerization analysed by immunoprecipitation using the monoclonal antibody directed against GFP coupled to Protein A/G PLUS-agarose. The immunoprecipitated proteins were then separated by SDS-PAGE and probed on western blot with anti-HA antibody. HA-U2AF^{65} was immunoprecipitated with an anti-GFP antibody from cell extracts of cells co-expressing GFP-U2AF^{65} and HA-U2AF^{65} (*data not shown*). No HA-U2AF^{65} was immunoprecipitated from HeLa cells co-transfected with GFP and HA-U2AF^{65}. Thus, the biochemical assay confirm the existence of a novel U2AF^{65} self interaction as shown by both FRET and FLIM methods.

3.5 Discussion

The protein-protein interactions between the splicing factors U2AF^{65}, U2AF^{35} and SF1 have been analyzed in the nucleus of living cells using FLIM. In addition, an improved Acceptor Photobleaching FRET methodology was developed in order to spatially map these interactions in fixated cells. This method uses image registration techniques and fluorescence normalization to correct for cell movement and bleaching due to imaging, respectively. FRET efficiencies are calculated in each point of the image, yielding FRET efficiency maps that can be overlaid to the original confocal image of donor intensity in the cell, thus providing spatial information on protein-protein interactions for large regions of interest.

This optimized Acceptor Photobleaching FRET methodology effectively corrects for “false FRET” results between CFP and YFP-tagged proteins reported by others (Karpova et al., 2003) by normalizing the fluorescence to the initial pre-bleach values using the average fluorescence intensity of the unbleached ROI (see Materials and Methods and Appendix 3.A). In addition, FRET efficiencies are calculated using average pre- and postbleach images calculated from a series of 4 different images each, instead of using a single pre- and postbleach image, thus considerably reducing "pseudo-FRET" signals that sometimes occur upon illumination of CFP with an intense 514 nm laser (Karpova et al., 2003).

The FRET Efficiency Maps obtained with this method show that U2AF^{65} interacts with both U2AF^{35} and SF1 both in the speckles and in nucleoplasm of mock-treated cells and cells treated with the transcription inhibitor DRB. This implies that these splicing factors accumulate in the speckles already assembled in a complex, even in the absence of splicing. FRET signals detected in the nucleoplasm are likely to reflect interactions occurring at transcription sites distributed throughout the nucleus interior. The fact that these FRET signals do not disappear from the nucleoplasm when cells are treated with DRB indicates that these splicing factors are able to interact and probably form complexes also in the nucleoplasm, even if no transcription sites exist. In alternative, or in addition, these nucleoplasmic FRET signals may also be a consequence of ongoing splicing activity occurring in transcripts that were already being transcribed by RNA Pol II when DRB was added to the cells medium, but have not been completely transcribed yet. DRB has been shown to have little or no effect on the elongation of growing RNA chains and allows finished mRNA molecules to be detached from the transcription site (Egyhazi, 1975).

The existence of a pre-assembled complex which includes U2AF^{65}, U2AF^{35}, SF1 and eventually other splicing factors is further supported by *in vivo* data on the dynamics of these proteins obtained with the FRAP technique (see Chapter 2). The diffusion coefficient values obtained for each of the GFP-tagged SFs was consistently lower than that of exogenous dextrans of similar size and furthermore it was correlated with the ability of these proteins to interact with each other. This reduced mobility can then be caused by transient interactions between the splicing factors and/or by the formation of large pre-assembled complexes that would necessary diffuse with lower rates at the nucleoplasm.

Our FRET results indeed show that U2AF^{65} can interact with its spliceosome partners U2AF^{35} and SF1 in the speckles and in the nucleoplasm, suggesting that pre-assemble particles might be formed prior to spliceosome assembly. However, this does not necessarily imply that these SFs are stably bound to a large diffusing complex. Such a pre-assembled complex might instead be formed transiently or have its components continuously recycled as a result of transient interactions and binding competition between them.

The highly dynamic nature of the studied splicing factors is consistent with self-organization models that rely on stochastic and relatively promiscuous interactions between proteins as the mechanisms responsible not only for the appearance of steady-state structures such as the nuclear speckles but also for the formation of these pre-assembled SFs complexes. In support of this model is the recent finding of a U2AF^{35} self-interaction (Chusainow et al., 2005) and our own discovery of a U2AF^{65} self-interaction, which clearly increase the chances of spontaneous and stochastic complex formation and adds to the promiscuity of interactions observed between splicing factors.

Taken together, our results indicate that the assembly of the splicing machinery probably occurs with pre-assembled particles rather than stepwise addition of discrete components. Furthermore, the formation of these pre-assembled complexes, as well as that of the nuclear speckles, is compatible with models that rely on self-organization mechanisms.

Appendix 3.A - Mathematica Notebook for FRET Efficiency Maps calculation

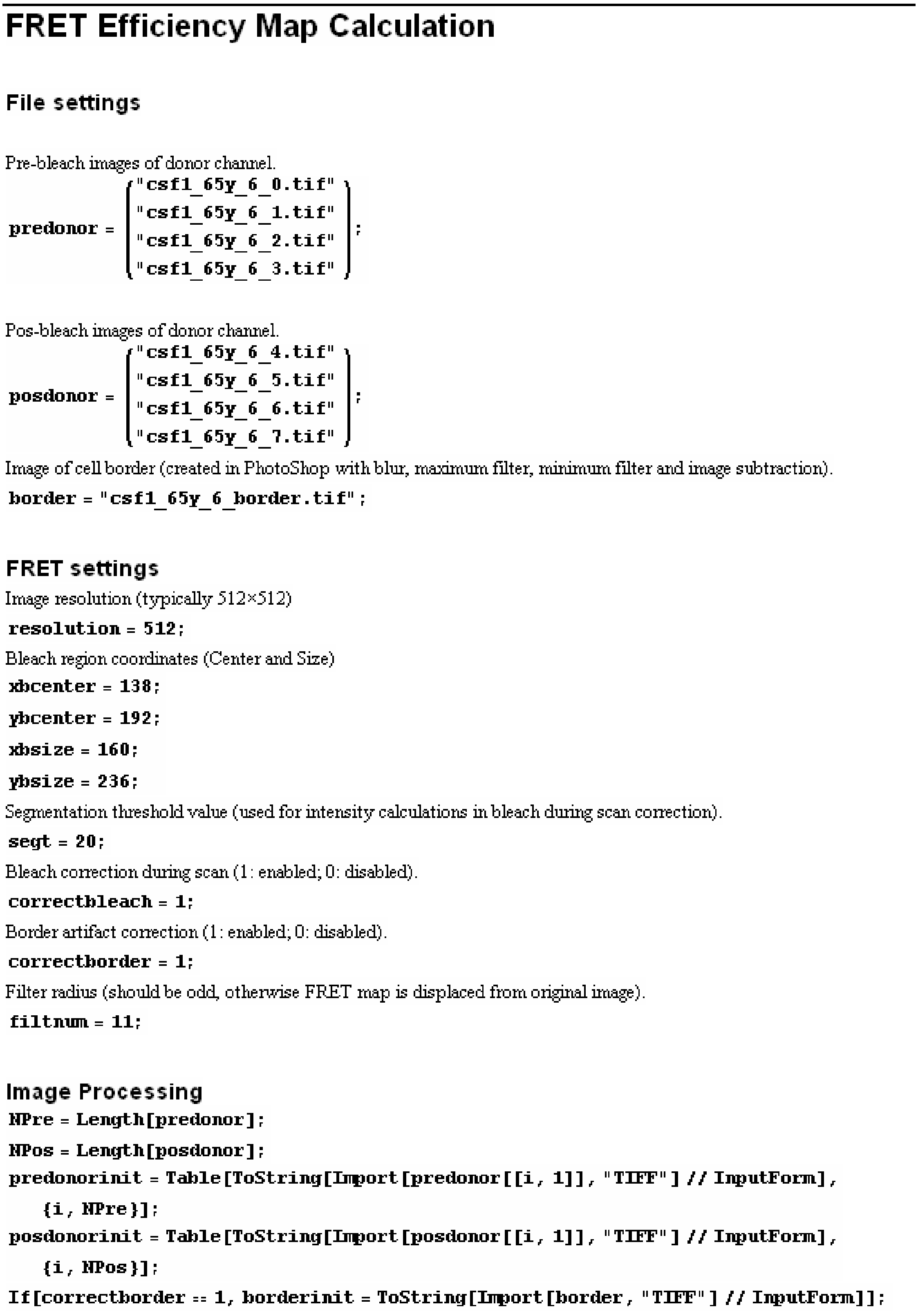

FRET Efficiency Map Calculation

File settings

Pre-bleach images of donor channel.

$$\textbf{predonor} = \begin{pmatrix} \text{"csf1\_65y\_6\_0.tif"} \\ \text{"csf1\_65y\_6\_1.tif"} \\ \text{"csf1\_65y\_6\_2.tif"} \\ \text{"csf1\_65y\_6\_3.tif"} \end{pmatrix};$$

Pos-bleach images of donor channel.

$$\textbf{posdonor} = \begin{pmatrix} \text{"csf1\_65y\_6\_4.tif"} \\ \text{"csf1\_65y\_6\_5.tif"} \\ \text{"csf1\_65y\_6\_6.tif"} \\ \text{"csf1\_65y\_6\_7.tif"} \end{pmatrix};$$

Image of cell border (created in PhotoShop with blur, maximum filter, minimum filter and image subtraction).

```
border = "csf1_65y_6_border.tif";
```

FRET settings

Image resolution (typically 512×512)

```
resolution = 512;
```

Bleach region coordinates (Center and Size)

```
xbcenter = 138;
ybcenter = 192;
xbsize = 160;
ybsize = 236;
```

Segmentation threshold value (used for intensity calculations in bleach during scan correction).

```
segt = 20;
```

Bleach correction during scan (1: enabled; 0: disabled).

```
correctbleach = 1;
```

Border artifact correction (1: enabled; 0: disabled).

```
correctborder = 1;
```

Filter radius (should be odd, otherwise FRET map is displaced from original image).

```
filtnum = 11;
```

Image Processing

```
NPre = Length[predonor];
NPos = Length[posdonor];
predonorinit = Table[ToString[Import[predonor[[i, 1]], "TIFF"] // InputForm],
   {i, NPre}];
posdonorinit = Table[ToString[Import[posdonor[[i, 1]], "TIFF"] // InputForm],
   {i, NPos}];
If[correctborder == 1, borderinit = ToString[Import[border, "TIFF"] // InputForm]];
```

```
predonorconv = Table[
          ToExpression[
    StringInsert[StringInsert[StringReplace[predonorinit[[i]],
       {"Graphics[Raster[" → "",
        ", ColorFunction -> GrayLevel], ImageSize -> {512, 512},
          PlotRange -> {{0, 511}, {1, 512}}, AspectRatio -> Automatic]" → ""}],
      "{", 1], "}", -1]], {i, NPre}];
posdonorconv = Table[
          ToExpression[
    StringInsert[StringInsert[StringReplace[posdonorinit[[i]],
       {"Graphics[Raster[" → "",
        ", ColorFunction -> GrayLevel], ImageSize -> {512, 512},
          PlotRange -> {{0, 511}, {1, 512}}, AspectRatio -> Automatic]" → ""}],
      "{", 1], "}", -1]], {i, NPos}];
If[correctborder == 1,
  borderconv =
   ToExpression[
    StringInsert[
     StringInsert[StringReplace[borderinit,
       {"Graphics[Raster[" → "",
        ", ColorFunction -> GrayLevel], ImageSize -> {512, 512},
          PlotRange -> {{0, 511}, {1, 512}}, AspectRatio -> Automatic]" → ""}],
      "{", 1], "}", -1]]];
preintensdonor = Table[1/2 (Abs[predonorconv[[i, 1]]] + predonorconv[[i, 1]]),
   {i, NPre}];
posintensdonor = Table[1/2 (Abs[posdonorconv[[i, 1]]] + posdonorconv[[i, 1]]),
   {i, NPos}];
predonorinit =.;
posdonorinit =.;
borderinit =.;
```

Calculate bleach region coordinates (x, y, Δx and Δy)

```
If[OddQ[xbsize], xbsize++];
If[OddQ[ybsize], ybsize++];
xbleach = xbcenter - xbsize/2;
ybleach = 512 - ybcenter - ybsize/2;
deltaxbleach = xbsize;
deltaybleach = ybsize;
dilate = 5;
```

Correct for photobleach during scan. All pixels with values lower than background or not inside the bleached region are discarded in the intensity analysis. A threshold segmentation is performed to select the pixels used in the mean intensity calculation.

```
PreMeanIntensity = Table[0, {i, 1, NPre}];
PosMeanIntensity = Table[0, {i, 1, NPos}];
```

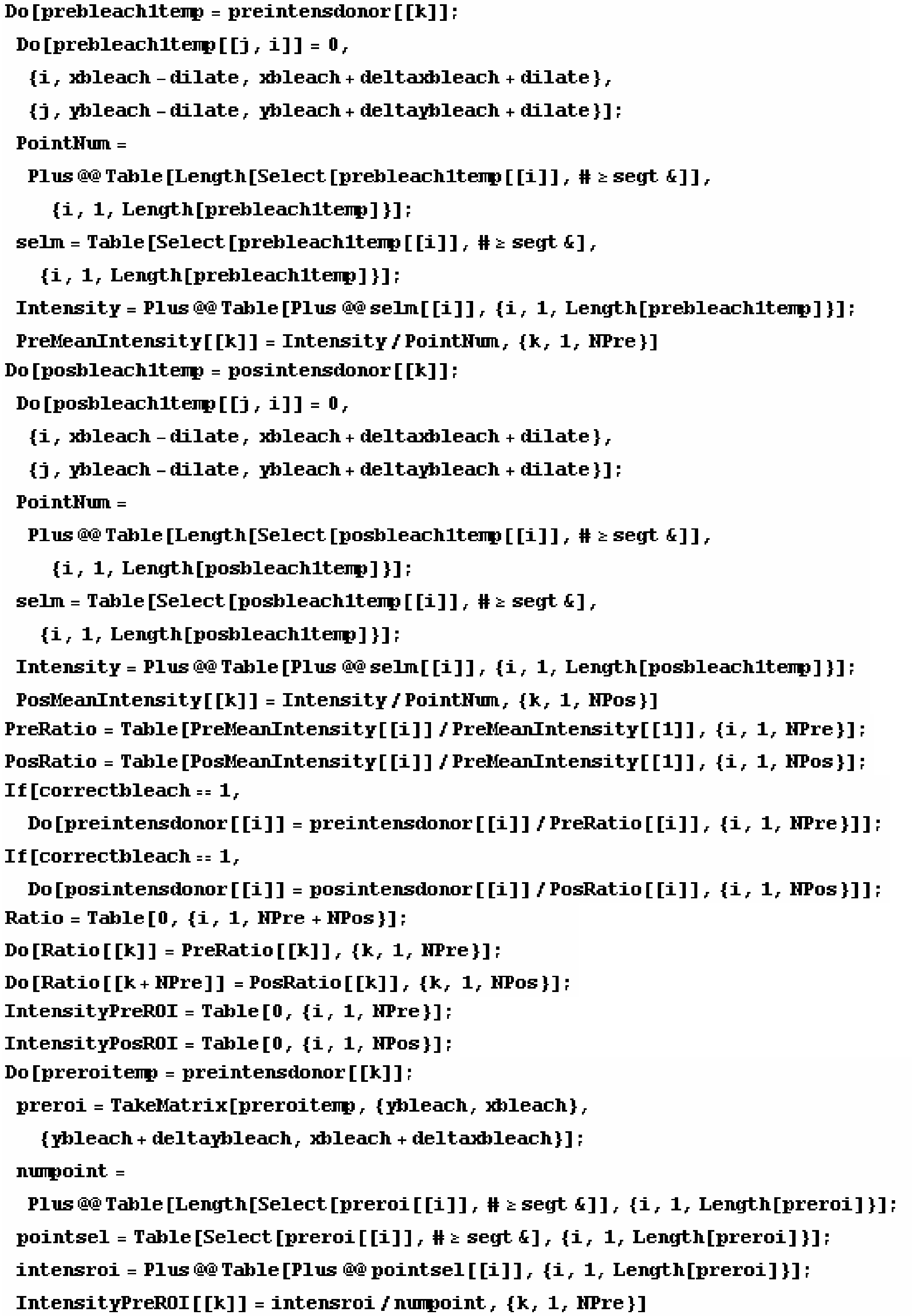

```
Do[prebleach1temp = preintensdonor[[k]];
 Do[prebleach1temp[[j, i]] = 0,
  {i, xbleach - dilate, xbleach + deltaxbleach + dilate},
  {j, ybleach - dilate, ybleach + deltaybleach + dilate}];
 PointNum =
  Plus @@ Table[Length[Select[prebleach1temp[[i]], # ≥ segt &]],
    {i, 1, Length[prebleach1temp]}];
 selm = Table[Select[prebleach1temp[[i]], # ≥ segt &],
   {i, 1, Length[prebleach1temp]}];
 Intensity = Plus @@ Table[Plus @@ selm[[i]], {i, 1, Length[prebleach1temp]}];
 PreMeanIntensity[[k]] = Intensity / PointNum, {k, 1, NPre}]
Do[posbleach1temp = posintensdonor[[k]];
 Do[posbleach1temp[[j, i]] = 0,
  {i, xbleach - dilate, xbleach + deltaxbleach + dilate},
  {j, ybleach - dilate, ybleach + deltaybleach + dilate}];
 PointNum =
  Plus @@ Table[Length[Select[posbleach1temp[[i]], # ≥ segt &]],
    {i, 1, Length[posbleach1temp]}];
 selm = Table[Select[posbleach1temp[[i]], # ≥ segt &],
   {i, 1, Length[posbleach1temp]}];
 Intensity = Plus @@ Table[Plus @@ selm[[i]], {i, 1, Length[posbleach1temp]}];
 PosMeanIntensity[[k]] = Intensity / PointNum, {k, 1, NPos}]
PreRatio = Table[PreMeanIntensity[[i]] / PreMeanIntensity[[1]], {i, 1, NPre}];
PosRatio = Table[PosMeanIntensity[[i]] / PreMeanIntensity[[1]], {i, 1, NPos}];
If[correctbleach == 1,
  Do[preintensdonor[[i]] = preintensdonor[[i]] / PreRatio[[i]], {i, 1, NPre}]];
If[correctbleach == 1,
  Do[posintensdonor[[i]] = posintensdonor[[i]] / PosRatio[[i]], {i, 1, NPos}]];
Ratio = Table[0, {i, 1, NPre + NPos}];
Do[Ratio[[k]] = PreRatio[[k]], {k, 1, NPre}];
Do[Ratio[[k + NPre]] = PosRatio[[k]], {k, 1, NPos}];
IntensityPreROI = Table[0, {i, 1, NPre}];
IntensityPosROI = Table[0, {i, 1, NPos}];
Do[preroitemp = preintensdonor[[k]];
 preroi = TakeMatrix[preroitemp, {ybleach, xbleach},
   {ybleach + deltaybleach, xbleach + deltaxbleach}];
 numpoint =
  Plus @@ Table[Length[Select[preroi[[i]], # ≥ segt &]], {i, 1, Length[preroi]}];
 pointsel = Table[Select[preroi[[i]], # ≥ segt &], {i, 1, Length[preroi]}];
 intensroi = Plus @@ Table[Plus @@ pointsel[[i]], {i, 1, Length[preroi]}];
 IntensityPreROI[[k]] = intensroi / numpoint, {k, 1, NPre}]
```

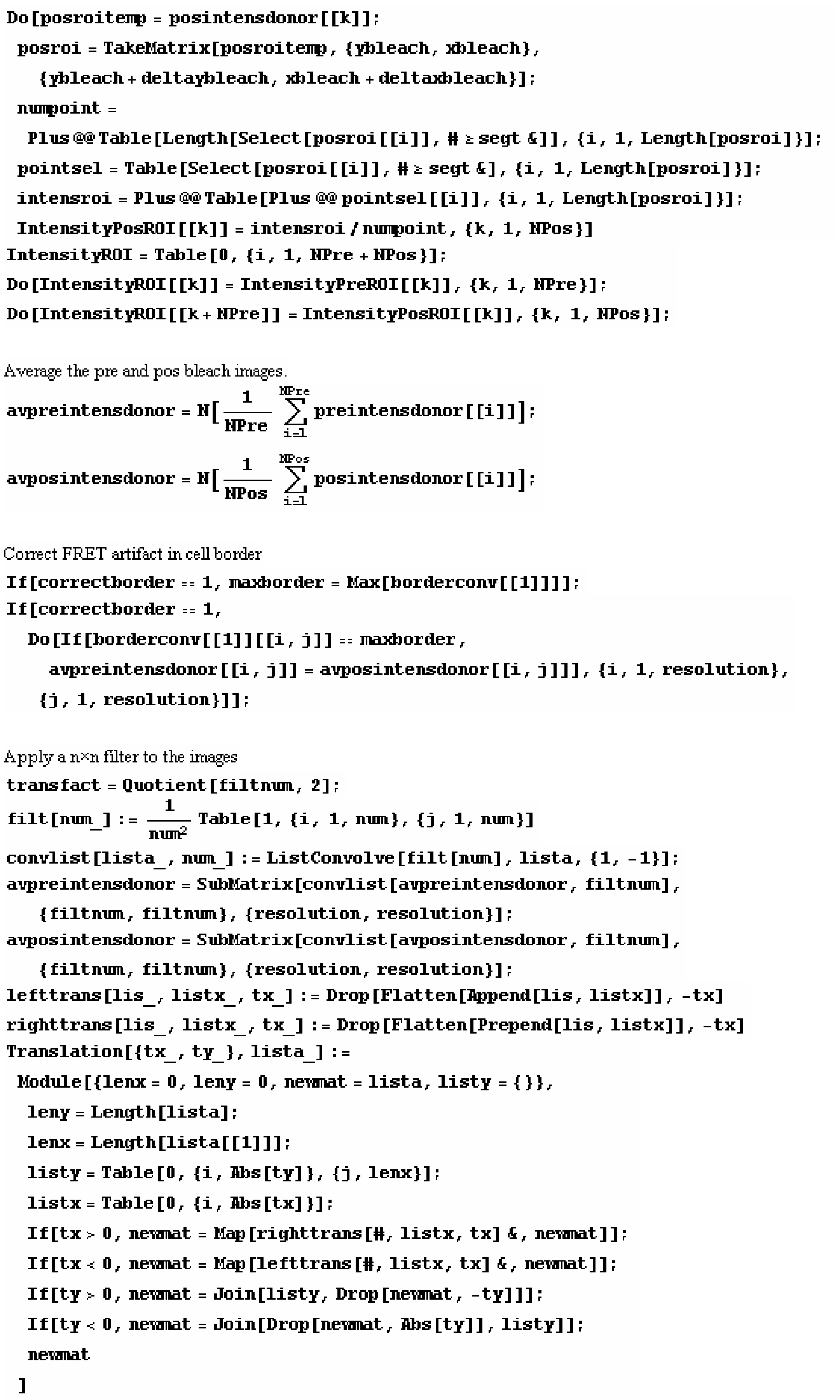

```
Do[posroitemp = posintensdonor[[k]];
 posroi = TakeMatrix[posroitemp, {ybleach, xbleach},
   {ybleach + deltaybleach, xbleach + deltaxbleach}];
 numpoint =
  Plus @@ Table[Length[Select[posroi[[i]], # ≥ segt &]], {i, 1, Length[posroi]}];
 pointsel = Table[Select[posroi[[i]], # ≥ segt &], {i, 1, Length[posroi]}];
 intensroi = Plus @@ Table[Plus @@ pointsel[[i]], {i, 1, Length[posroi]}];
 IntensityPosROI[[k]] = intensroi / numpoint, {k, 1, NPos}]
IntensityROI = Table[0, {i, 1, NPre + NPos}];
Do[IntensityROI[[k]] = IntensityPreROI[[k]], {k, 1, NPre}];
Do[IntensityROI[[k + NPre]] = IntensityPosROI[[k]], {k, 1, NPos}];
```

Average the pre and pos bleach images.

$$\text{avpreintensdonor} = \text{N}\left[\frac{1}{\text{NPre}}\sum_{\text{i}=1}^{\text{NPre}}\text{preintensdonor[[i]]}\right];$$

$$\text{avposintensdonor} = \text{N}\left[\frac{1}{\text{NPos}}\sum_{\text{i}=1}^{\text{NPos}}\text{posintensdonor[[i]]}\right];$$

Correct FRET artifact in cell border

```
If[correctborder == 1, maxborder = Max[borderconv[[1]]]];
If[correctborder == 1,
  Do[If[borderconv[[1]][[i, j]] == maxborder,
    avpreintensdonor[[i, j]] = avposintensdonor[[i, j]]], {i, 1, resolution},
   {j, 1, resolution}]];
```

Apply a n×n filter to the images

```
transfact = Quotient[filtnum, 2];
```

$$\text{filt[num\_]} := \frac{1}{\text{num}^2}\ \text{Table[1, \{i, 1, num\}, \{j, 1, num\}]}$$

```
convlist[lista_, num_] := ListConvolve[filt[num], lista, {1, -1}];
avpreintensdonor = SubMatrix[convlist[avpreintensdonor, filtnum],
   {filtnum, filtnum}, {resolution, resolution}];
avposintensdonor = SubMatrix[convlist[avposintensdonor, filtnum],
   {filtnum, filtnum}, {resolution, resolution}];
lefttrans[lis_, listx_, tx_] := Drop[Flatten[Append[lis, listx]], -tx]
righttrans[lis_, listx_, tx_] := Drop[Flatten[Prepend[lis, listx]], -tx]
Translation[{tx_, ty_}, lista_] :=
 Module[{lenx = 0, leny = 0, newmat = lista, listy = {}},
  leny = Length[lista];
  lenx = Length[lista[[1]]];
  listy = Table[0, {i, Abs[ty]}, {j, lenx}];
  listx = Table[0, {i, Abs[tx]}];
  If[tx > 0, newmat = Map[righttrans[#, listx, tx] &, newmat]];
  If[tx < 0, newmat = Map[lefttrans[#, listx, tx] &, newmat]];
  If[ty > 0, newmat = Join[listy, Drop[newmat, -ty]]];
  If[ty < 0, newmat = Join[Drop[newmat, Abs[ty]], listy]];
  newmat
 ]
```

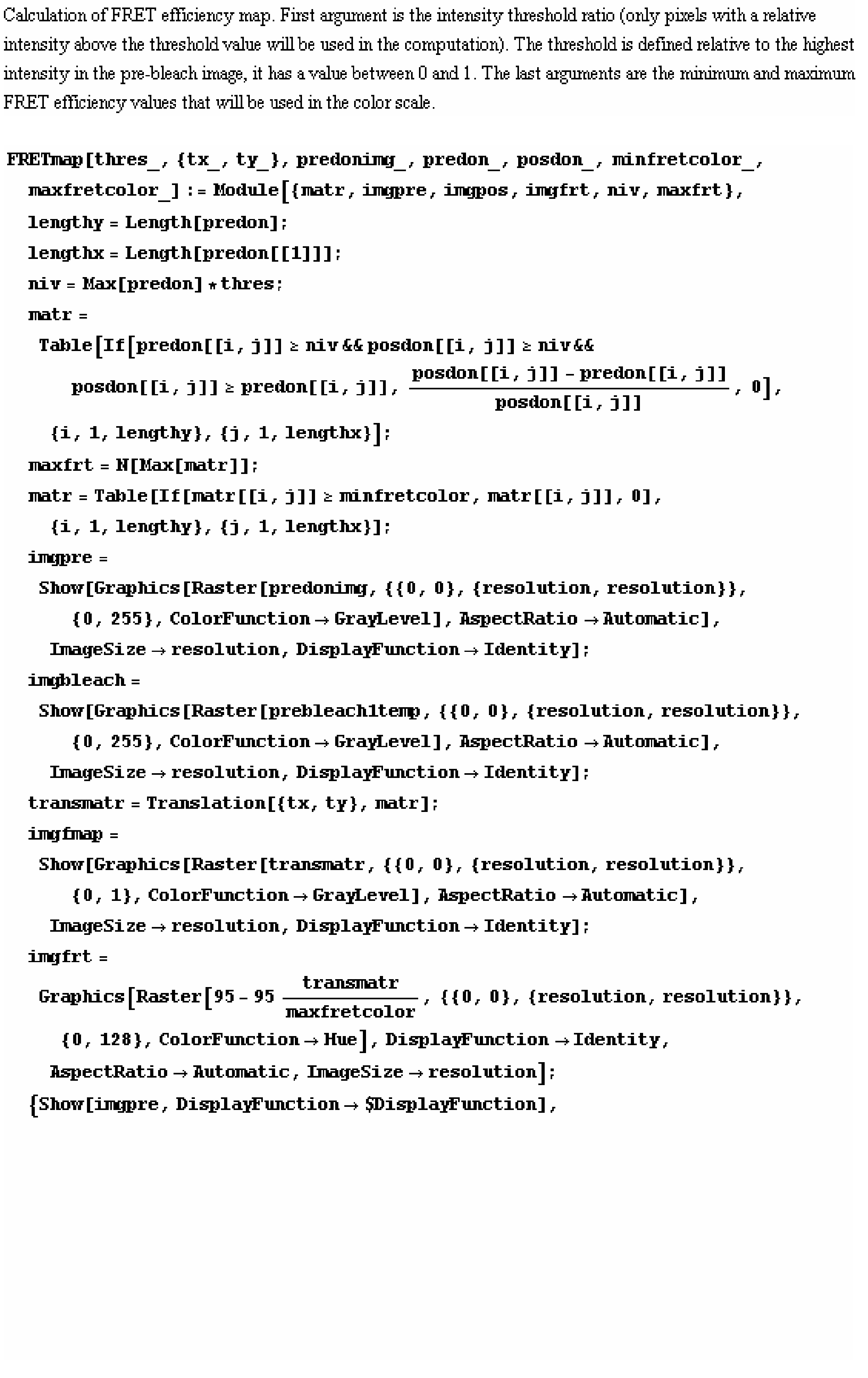

Calculation of FRET efficiency map. First argument is the intensity threshold ratio (only pixels with a relative intensity above the threshold value will be used in the computation). The threshold is defined relative to the highest intensity in the pre-bleach image, it has a value between 0 and 1. The last arguments are the minimum and maximum FRET efficiency values that will be used in the color scale.

```
FRETmap[thres_, {tx_, ty_}, predonimg_, predon_, posdon_, minfretcolor_,
  maxfretcolor_] := Module[{matr, imgpre, imgpos, imgfrt, niv, maxfrt},
  lengthy = Length[predon];
  lengthx = Length[predon[[1]]];
  niv = Max[predon] * thres;
  matr =
   Table[If[predon[[i, j]] ≥ niv && posdon[[i, j]] ≥ niv &&
                                     posdon[[i, j]] - predon[[i, j]]
      posdon[[i, j]] ≥ predon[[i, j]], ─────────────────────────────── , 0],
                                              posdon[[i, j]]
    {i, 1, lengthy}, {j, 1, lengthx}];
  maxfrt = N[Max[matr]];
  matr = Table[If[matr[[i, j]] ≥ minfretcolor, matr[[i, j]], 0],
    {i, 1, lengthy}, {j, 1, lengthx}];
  imgpre =
   Show[Graphics[Raster[predonimg, {{0, 0}, {resolution, resolution}},
      {0, 255}, ColorFunction → GrayLevel], AspectRatio → Automatic],
    ImageSize → resolution, DisplayFunction → Identity];
  imgbleach =
   Show[Graphics[Raster[prebleach1temp, {{0, 0}, {resolution, resolution}},
      {0, 255}, ColorFunction → GrayLevel], AspectRatio → Automatic],
    ImageSize → resolution, DisplayFunction → Identity];
  transmatr = Translation[{tx, ty}, matr];
  imgfmap =
   Show[Graphics[Raster[transmatr, {{0, 0}, {resolution, resolution}},
      {0, 1}, ColorFunction → GrayLevel], AspectRatio → Automatic],
    ImageSize → resolution, DisplayFunction → Identity];
  imgfrt =
                          transmatr
   Graphics[Raster[95 - 95 ────────────── , {{0, 0}, {resolution, resolution}},
                          maxfretcolor
     {0, 128}, ColorFunction → Hue], DisplayFunction → Identity,
    AspectRatio → Automatic, ImageSize → resolution];
  {Show[imgpre, DisplayFunction → $DisplayFunction],
```

FRET Efficiency Map Output

```
FRETmap[.10, {transfact, transfact}, predonorconv[[1, 1]], avpreintensdonor,
 avposintensdonor, 0.01, .3]
```

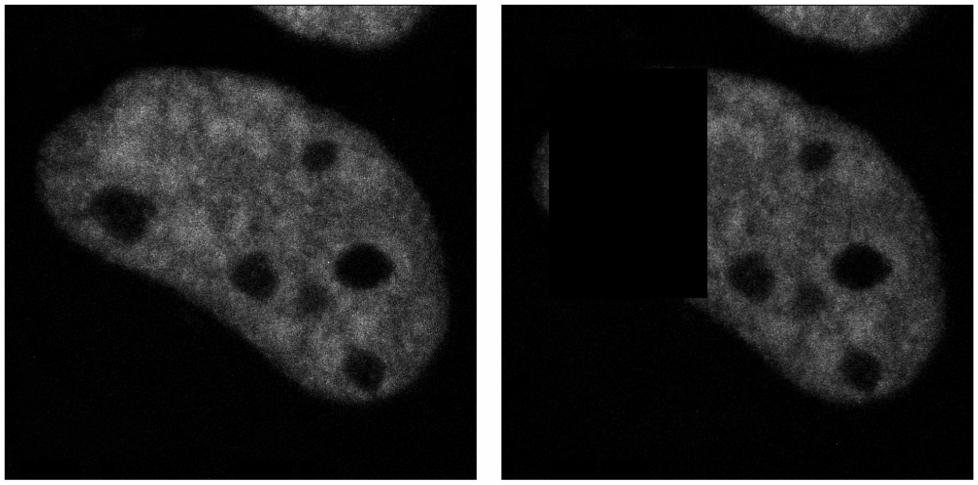

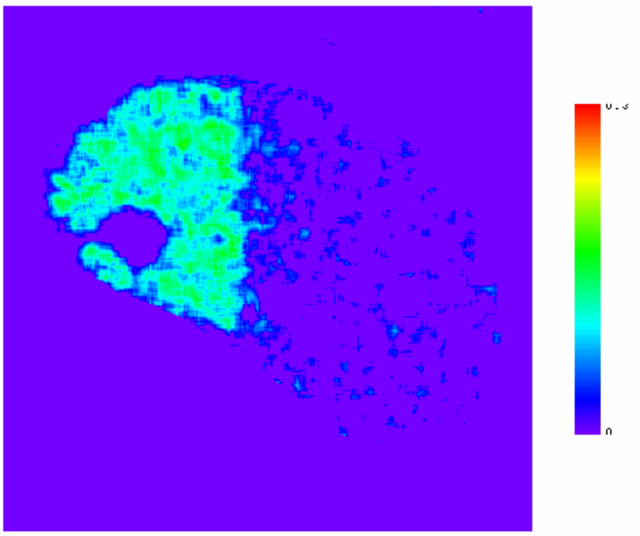

```
{- Graphics -, - Graphics -, - Graphics -, - Graphics -, - Graphics -, 0.181745}
```

```
ListPlot[IntensityROI, PlotJoined → True, PlotStyle → Hue[.7]];
```

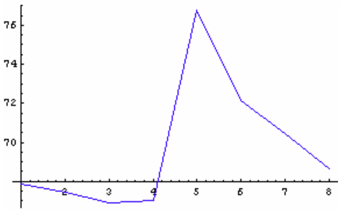

```
ListPlot[Ratio, PlotJoined → True, PlotStyle → Hue[.6]];
```

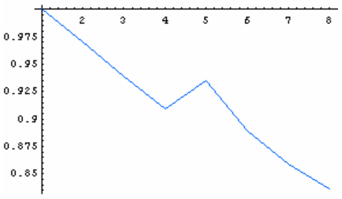

4. Photobleaching experiments and kinetic modeling of mRNA intranuclear mobility

4.1 Abstract

After being released from transcription sites, which are distributed throughout the nucleoplasm, messenger ribonucleoproteins (mRNPs) must reach the nuclear pore complexes (NPCs) in order to be translocated to the cytoplasm. The nature of this transport process has been a matter of debate over the years (Carmo-Fonseca et al., 2002; Politz and Pederson, 2000; Vargas et al., 2005) but an increasing amount of data supports the growing consensus that mRNPs move inside the nucleus by diffusion until they associate physically with components of the NPC (Cole and Scarcelli, 2006). We have developed quantitative photobleaching methods to investigate the mobility of mRNPs within the nucleus of living human cells. We describe how the diffusion coefficients of RNP complexes containing mRNA can be obtained from quantitative FLIP experiments performed on cells expressing GFP-tagged versions of the mRNA-binding proteins PABPN1 and TAP. Our results for mRNP diffusion rates are consistent with recent data obtained with other techniques (Molenaar et al., 2004; Shav-Tal et al., 2004a; Vargas et al., 2005) and furthermore show that, although the movement of mRNPs is reduced upon energy depletion (Calapez et al., 2002), no myosin motors are involved in the travel of export competent mRNPs to the nuclear pores.

4.2 Introduction

In eukaryotes, mRNAs are transcribed in the nucleus and exported to the cytoplasm to be translated into protein. Immediately upon synthesis, nascent transcripts associate with proteins forming ribonucleoprotein (RNP) particles, large dynamic complexes whose protein content evolves throughout the mRNA lifetime (see section 1.3 in Chapter 1). How mRNPs travel from the sites of transcription dispersed throughout the nucleoplasm to the nuclear pore complexes has been a controversial issue over the years (see section 1.3.3 in Chapter 1). Currently, an increasing amount of data supports the idea that macromolecular mobility inside the nucleus is mainly due to Brownian motion (Carmo-Fonseca et al., 2002; Cole and Scarcelli, 2006), which makes it unlikely that any motor-driven transport mechanisms with inherent directionality operate inside the nucleus to move mRNPs to the nuclear pores. However, the nucleus interior is not a uniform fluid medium and nuclear diffusion is greatly impaired by obstructions imposed by macromolecular crowding. Consistent with this view, large macromolecules such as 2 MDa dextrans have been shown to be immobilized within the nucleus (Seksek et al., 1997). In contrast, mRNPs (which are expected to be even larger than 2 MDa) are completely mobile inside the nucleus. However, this mobility is significantly reduced when the cells are depleted of ATP or incubated at a reduced temperature, suggesting that energy consumption is required to counteract obstructions to diffusion (Calapez et al., 2002). It thus seems possible that the mechanisms underlying mRNP movement involve a combination of passive diffusion and energy-dependent reactions.

We have developed a quantitative Fluorescence Loss In Photobleaching (FLIP, see section 1.5.3 in Chapter 1) method to characterize the kinetics of a mixed population of GFP-tagged molecules diffusing at different rates within the cell. This novel methodology can distinguish and estimate the fraction of independent populations of GFP fusion proteins which are bound to mRNP complexes from those that are unbound. In addition, the effective diffusion coefficient of each of these populations can also be estimated with this method. In order to apply this method to the study of mRNP mobility in living cell nuclei, RNP complexes were made fluorescent by transient expression of GFP fused to two distinct mRNA-binding proteins, PABPN1 and TAP.

The nuclear poly(A) binding protein (PABPN1) binds to the growing poly(A) tails formed at the 3'-ends of nearly all eukaryotic mRNAs. PABPN1 cooperates with the cleavage machinery to stimulate the polyadenylation activity of poly(A) polymerase. The cleavage and polyadenylation reactions are thought to be coupled to splicing of the last intron and to occur at the same time or just before transcription termination (see section 1.3.2 in Chapter 1), implying that PABPN1 will bind to nearly terminated and spliced transcripts.

In addition to PABPN1, we aimed at achieving a more specific visualization of mRNAs in transit to the cytoplasm by using GFP fused to the export factor TAP. This protein associates with cellular mRNPs and is thought to promote their export by interacting directly with components of the nuclear pore during NPC translocation (see section 1.3.4 in Chapter 1).

Our results show that both GFP-PABPN1 and GFP-TAP diffuse inside the nucleus essentially as two populations, one with a slower diffusion coefficient of ~ 0.09 $\mu m^2 s^{-1}$ which is common to both proteins and likely corresponds to mRNP-bound particles and another with an effective diffusion coefficient of ~ 8.6 $\mu m^2 s^{-1}$ for GFP-PABPN1 and ~ 4.3 $\mu m^2 s^{-1}$ for GFP-TAP, which presumably corresponds to unbound molecules that may nonetheless interact with other nuclear structures. The diffusion coefficient values we obtain for mRNPs inside the living cell nucleus are consistent with recent estimates obtained by others (Molenaar et al., 2004; Shav-Tal et al., 2004a; Vargas et al., 2005).

Numerous studies have previously reported the presence of actin in the nucleus (reviewed in (Rando et al., 2000)). Furthermore, it was suggested that nuclear actin associates with mRNPs (Percipalle et al., 2002) and participates in the nuclear export of mRNA (Hofmann et al., 2001; Kimura et al., 2000). Among several other proteins, actin interacts with myosins, which are members of a motor protein family that couples ATP hydrolysis to molecular movement. Interestingly, myosins have also been found in the nucleus (Pestic-Dragovich et al., 2000). The interaction between actin and myosin can be blocked by a small molecule termed 2,3-butanedione monoxime (BDM), which acts as a myosin-ATPase inhibitor (Ostap, 2002). BDM has been reported to impair the movement of PML bodies in living cells (Muratani et al., 2002). These data prompted us to determine whether BDM affects the mobility of mRNPs in the nucleus.

The results show that treatment of cells with BDM for 30 minutes significantly increases the diffusion rate of GFP-TAP molecules in the nucleus. The data further indicates that this is not due to a direct effect of the drug on mRNP mobility, but rather a consequence of transcription inhibition. This represents the first demonstration *in vivo* that myosin motors are involved in transcriptional activity by RNA Pol II. In the absence of newly synthesized mRNA there is an increased pool of fast moving nuclear GFP-TAP molecules, which are most likely unbound to mRNPs. The diffusion rate of slow moving GFP-TAP molecules is not altered by BDM, suggesting that the intranuclear movement of TAP-associated mRNPs is independent of myosin motors.

4.3 Materials and Methods

Cell culture, transfections and drug treatment

HeLa cells were cultured as monolayers in Modified Eagle's Medium (MEM) supplemented with 10% fetal calf serum (Gibco-BRL, Paisley, Scotland). For photobleaching experiments, cells were plated and observed in glass bottom chambers (MatTek Corporation, Ashland, MA). For imaging, the medium was changed to D-MEM/F-12 without phenol red supplemented with 15 mM HEPES buffer (Gibco). All GFP fusion constructs were obtained by subcloning into the appropriate pEGFP-C vector (Clontech Laboratories, Palo Alto, CA, USA). The construction and properties of GFP-PABPN1 and GFP-PABPN1dm (Calado and Carmo-Fonseca, 2000; Calado et al., 2000) and of GFP-TAP and GFP-TAP 371-619 (Bachi et al., 2000) have been previously described. The pEGFP-coilin-PABPN1 plasmid was constructed by subcloning the cDNA of coilin into the pEGFP-PABPN1 vector. HeLa subconfluent cells were transiently transfected with FuGENE6 reagent (Roche Biochemicals, Indianapolis, IN) using 1 µg of DNA, and analyzed at 16-24h after transfection.

Drug treatments

Actinomycin D (Sigma Chemical Co., St. Louis, MO) was used at 5 µg/ml from a stock solution of 5 mg/ml in DMSO. DRB (Sigma) was used at 75 µM from a stock solution of 11 mM in ethanol. BDM (Sigma) was used at 40 mM from a 0.5 M stock solution freshly prepared in serum free medium and α-amanitin was used at 20µg/ml from a stock solution of 1mg/ml in PBS.

Confocal microscopy

Live cells were imaged at 37ºC maintained by a heating/cooling frame (LaCon, Staig, Germany) in conjunction with an objective heater (PeCon, Erbach, Germany). Images were acquired on a Zeiss LSM 510 confocal microscope (Carl Zeiss, Jena, Germany) using a PlanApochromat 63x/1.4 objective. EGFP fluorescence was detected using the 488 nm laser line of an Ar laser (25 mW nominal output) and a LP 505 filter. The pinhole aperture was set to 1 Airy unit.

Photobleaching experiments

FRAP and FLIP were performed essentially as described (Braga et al., 2004b; Calapez et al., 2002; Phair and Misteli, 2000). Each FRAP analysis started with three image scans, followed by a single bleach pulse of 37 ms on a spot with a diameter of 25 pixel (0.71 μm radius). A series of 97 single section images (of size 512x50 and pixel width 57 nm) was then collected, with the first image acquired 2 ms after the end of the bleaching process and the other images at 78 ms intervals. For imaging, the laser power was attenuated to 0.1-0.2% of the bleach intensity. For FLIP experiments, cells were repeatedly bleached at intervals of 3.64 s and imaged between bleach pulses. Bleaching was performed by 279 ms bleach pulses on a spot with a diameter of 30 pixels (1.065 μm radius). Repetitive bleach pulses were achieved taking advantage of the trigger interface for LSM 510. An electronic oscillator circuit was built to create pulses with a user defined frequency (see Appendix 4.A). When connected to the LSM 510, it would then trigger the bleaching events. A series of 350 images were collected for each cell with laser power attenuated to 1% of the bleach intensity.

For each FRAP time series, the background and nuclear regions were identified using an implementation of the ICM segmentation algorithm in Mathworks Matlab software. The average fluorescence in the nucleus *T(t)* and the average fluorescence in the bleached region *I(t)* were calculated for each background subtracted image at time *t* after bleaching. FRAP recovery curves were normalized according to (Phair and Misteli, 2000),

$$Irel(t) = \frac{I(t)}{I_0} \frac{T_0}{T(t)}$$

where T_0 is the fluorescence in the nucleus before bleaching and I_0 is the fluorescence in the bleached region before bleaching. This normalization corrects for the loss of fluorescence caused by imaging which was < 5%. Quantitative kinetic analysis of FRAP data was performed as described (Braga et al., 2004b; Calapez et al., 2002).

FLIP sequence images were background subtracted and further processed in ImageJ (http://rsb.info.nih.gov/ij/) using a rigid body registration algorithm to correct for cell displacement during image acquisition. The processed FLIP stack was then re-sampled from 512×512 pixels to 64×64 pixels and imported into a Mathematica 5.0 (Wolfram Research) notebook (see Appendixes 4.C and 4.D).

The nucleus was identified using threshold segmentation and the bleach region coordinates were obtained directly from the LSM files using either a Mathworks Matlab routine or the LSM software itself. Nuclear fluorescence was measured in ring-shaped regions of interest defined at increasing distances from the bleach circular region. For fitting purposes, the fluorescence from the whole nucleus, excluding the bleach region, was used to calculate the normalized fluorescence loss.

Nuclear fluorescence loss from FLIP experiments could then be fitted either to a single exponential with rate constant R or to a nonlinear curve corresponding to the sum of two exponentials,

$$f(t) = p\exp(-R_1 t) + (1-p)\exp(-R_2 t)$$

where p is the proportion of the slower population relative to the total fluorescence, R_1 is the rate constant associated with this slower population and R2 the rate constant of the faster one. The optimal fit for each case was chosen according to its chi-square value. In order to relate the FLIP rate constants with the effective diffusion coefficients for each population, the diffusion equation was solved numerically using a finite difference approach and the real geometry of a nucleus (see Results for details of the implementation). Bleaching parameters were obtained from cells expressing the immobile protein GFP-coilin-PABPN1. The system of ordinary differential equations obtained for each cell geometry was simulated in Mathematica (see Appendix 4.C) and Berkeley Madonna (http://www.berkeleymadonna.com, see Appendix 4.E) and fitted to the data using the later software.

4.4 Results

4.4.1 Estimating the fraction of GFP fusion proteins bound to mRNP complexes by FLIP

To perform FLIP, a region in the nucleus is repeatedly bleached using high laser power intensity while the surrounding area is imaged between each round of bleaching. The loss of fluorescence in the area outside the bleached region is plotted over time, providing information on the rate of displacement of the molecules from that particular site (see section 1.5.3 in Chapter 1). Most theoretical models that have been proposed for FLIP analysis assume that the free or unbound protein moved so fast in the timescale of the experiment that it could be treated as being well-mixed in the nuclear compartment. Hence, diffusion during bleaching was systematically neglected (Phair and Misteli, 2001). However, when performing FLIP experiments using GFP-tagged PABPN1 and TAP we observe that the concentration of the labeled proteins is not the same throughout the nucleus, but rather decreases as the bleach area is approached. Thus, diffusion cannot be neglected and such compartmental modeling approaches that treat the nucleus as a well-mixed compartment are not valid for our case. Instead, FLIP experiments can be used to resolve populations of molecules that are diffusing at different rates. Simulation of a FLIP experiment with freely mobile molecules diffusing at 0.1 $\mu m^2 s^{-1}$ shows that the decline in fluorescence is mainly due to diffusion during each bleach period (Figure 4.1A, B).

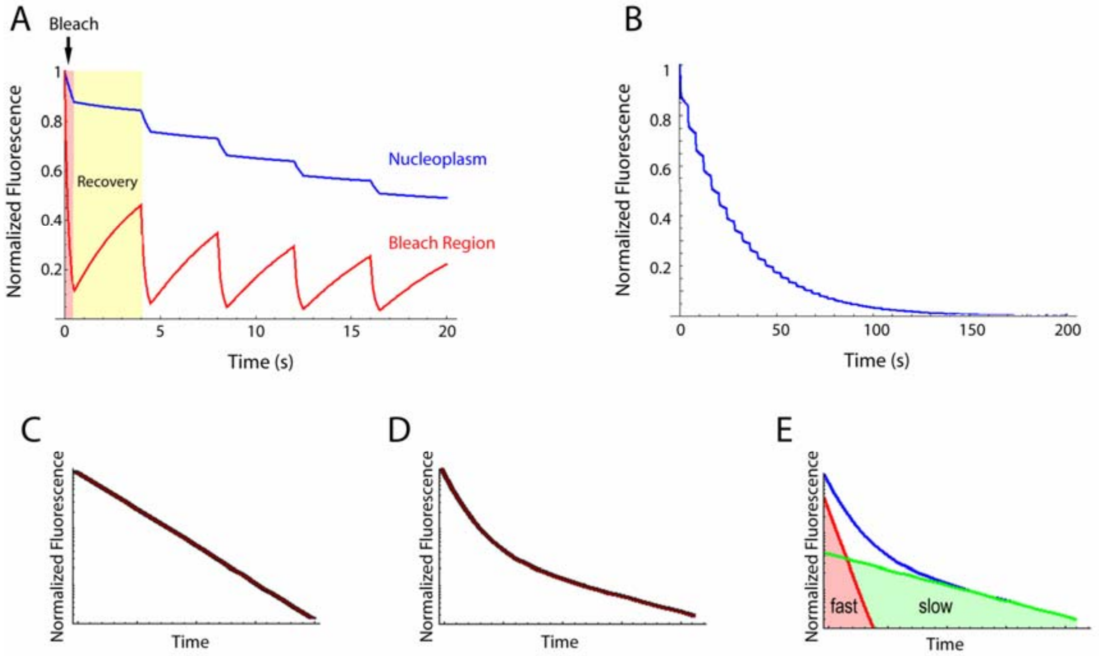

Figure 4.1 – Simulated FLIP experiments (A) A FLIP experiment was simulated for a single population of freely diffusing molecules (D=0.1 $\mu m^2 s^{-1}$). During each bleach there is a fluorescence loss both in the bleached region (**A**, *red line*) and in the unbleached nucleoplasm (**A**, *blue line*). After each bleach (**A**, *Recovery*), the fluorescence increases in the bleached region while it continues to decrease in the unbleached nucleoplasm. Note that the fluorescence loss in the unbleached region is higher during the bleach period than during recovery. **(B)** Fluorescence loss in the unbleached nucleoplasm after prolonged repetitive bleaching. **(C)** Same data as in **B** but plotted in a semi-log graph. **(D, E)** A FLIP experiment was simulated for a mixed population of freely diffusing molecules. We have considered a fraction of slow-moving molecules (representing 30% of the total population) and a fraction of faster molecules moving at a rate ten times higher. **D** shows a semi-log plot of global fluorescence loss in the unbleached region. **E** depicts separately the fluorescence loss for each population of molecules present in the mix.

If there is a single population of GFP fusion molecules diffusing in the nucleoplasm, the plot of fluorescence loss will be an exponential (a straight line when plotted on semi-log graphs, Figure 4.1C). However, if there are two populations, one diffusing faster than the other, loss of fluorescence will be the sum of two exponentials (Figure 4.1D, E). Fitting the FLIP curve to the nonlinear function of two-exponential decay

$$f(t) = p\exp(-R_1 t) + (1-p)\exp(-R_2 t)$$

yields the proportion of fast and slow populations, as well as the rate constants associated with the loss of fluorescence R_1 and R_2. This formula assumes that we are in the presence of two independent populations of molecules that are diffusing in the nucleus. Additional slow phases in FLIP curves may appear due to the import of unbleached molecules from the cytoplasm or release from an intranuclear-bound pool of protein, if these phenomena occur in the timescale of the FLIP experiment.

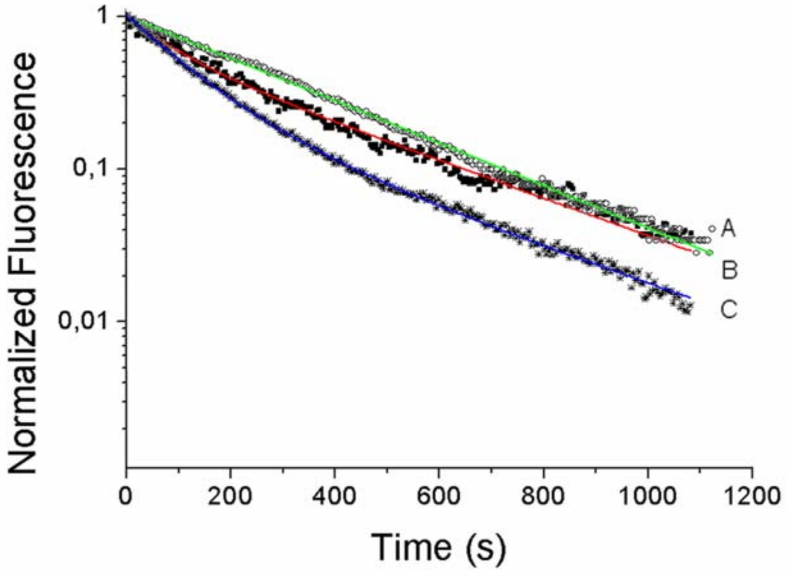

		p	R1	R2	χ2
A	—○—	1	0,00334 ± 8,3823E-6	N/A	0,00012
B	—■—	0,61410 ± 0,03148	0,00280 ± 0,00009	0,01090 ± 0,00085	0,00047
C	—✱—	0,28715 ± 0,01504	0,00264 ± 0,00008	0,00852 ± 0,00014	0,00005

Figure 4.2 – FLIP kinetics of GFP-PABPN1 and GFP-PABPN1dm. Semi-logarithmic plots of nuclear loss of fluorescence in FLIP experiments performed on HeLa cells expressing GFP-PABPN1 (**A** and **B**) and GFP-PABPN1dm (**C**). Fitting functions are plotted in color. In **A**, a single exponential fit shows the existence of a single population of slow moving GFP-PABPN1. (**B**) a cell expressing a higher level of GFP-PABPN1 (higher absolute fluorescence intensity) can be fitted by a nonlinear function of two-exponential decay that reveals the same slow moving population with an abundance of ~ 60% and a faster one with a rate constant three times higher. In **C**, a cell expressing GFP-PABPN1dm was fitted to the same nonlinear function, and the same populations of slow and fast proteins are detected. Contrasting to the situation shown in **B**, the faster population is the most abundant (~ 70%).

Kinetic analysis of FLIP data for cells expressing low levels of GFP-PABPN1 revealed the existence of a single slow-moving population, indicating that the vast majority of the fusion protein is bound to RNA (Figure 4.2). In cells expressing higher levels of GFP-PABPN1, the analysis revealed two populations: one slow (with kinetics similar to that detected in low-level-expressing cells) and one faster (with kinetics similar to the RNA-binding defective mutant). This suggests that the faster population of GFP-fusion molecules represents a pool of free proteins unbound to RNA. In contrast to the results obtained with GFP-PABPN1, FLIP analysis of cells expressing low levels of GFP-TAP shows the presence of a mixed population of slow and fast moving molecules suggesting that approximately 44 % of TAP molecules in the nucleus are not bound to mRNP complexes (Figure 4.3).

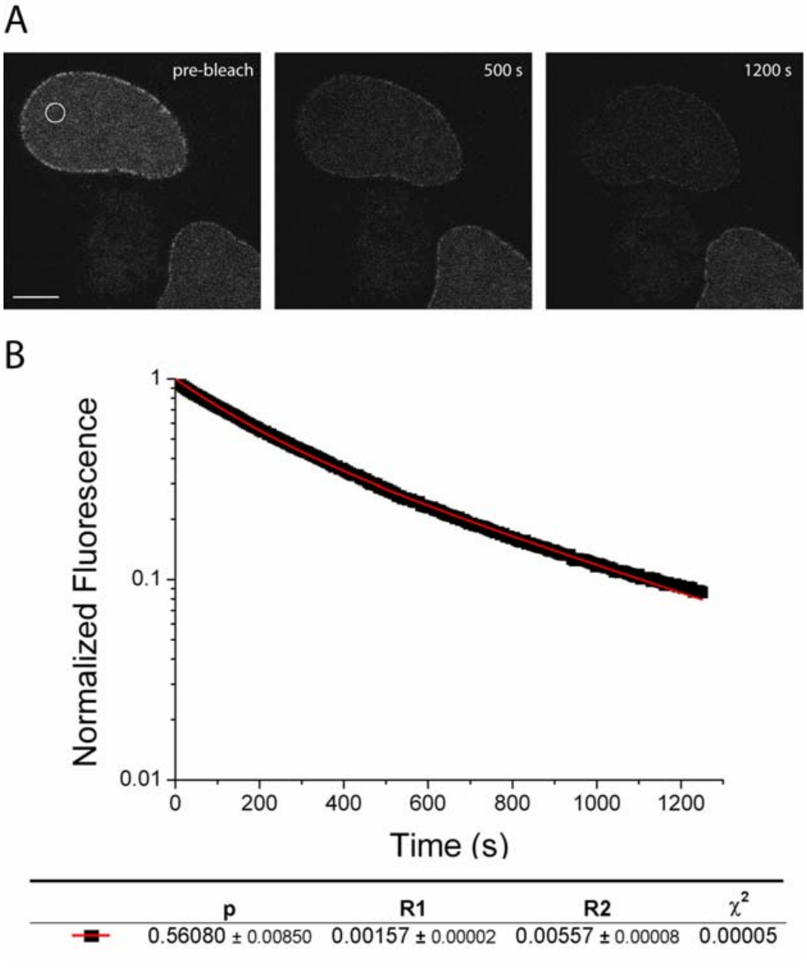

	p	R1	R2	χ^2
■	0.56080 ± 0.00850	0.00157 ± 0.00002	0.00557 ± 0.00008	0.00005

Figure 4.3 – FLIP kinetics of GFP-TAP (A) FLIP sequence of a HeLa cell expressing GFP-TAP. Bleaching was performed every 3.64 s in the area indicated by the white circle and the fluorescence in the bleached region was recorded. An adjacent cell nucleus (bottom right) was used to assess loss of fluorescence due to imaging. Images were taken at the indicated time points. Bar: 5 µm. **(B)** Semi-log plot of nuclear loss of fluorescence and corresponding fitting function (*red line*) for FLIP experiments performed on cells expressing GFP-TAP. The fitting parameters p, R_1 and R_2 are also shown.

Thus, when expressed at a low level, the vast majority of GFP-PABPN1 molecules are incorporated into RNP complexes. Under the same conditions, approximately half of the GFP-TAP molecules roam the nucleus as RNP-unbound protein.

4.4.2 GFP-TAP kinetics is altered by BDM treatment

To determine whether myosin motors are involved in the movement of export-competent mRNAs from the sites of transcription to the nuclear pore complexes, we performed photobleaching experiments in HeLa cells expressing GFP-TAP that were either non-treated or treated with the myosin inhibitor BDM. Only cells containing minimal detectable levels of GFP fluorescence were selected for image acquisition to avoid over-expression of the transfected protein.

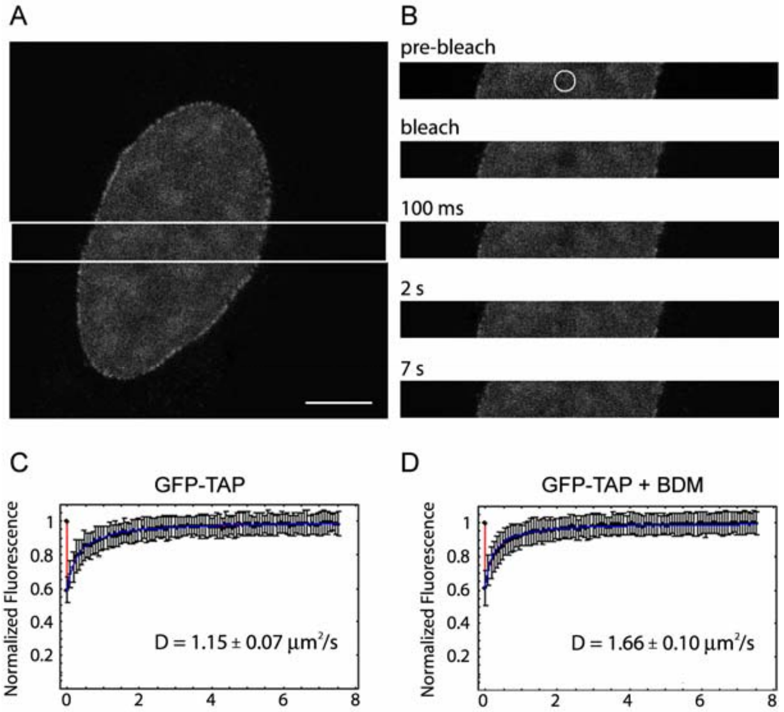

Figure 4.4 – The effective diffusion coefficient of GFP-TAP is higher after BDM treatment (A) HeLa cell expressing GFP-TAP. The white box indicates the region scanned in a FRAP experiment. Bar: 5 µm. **(B)** FRAP sequence of the scanned region depicted in **A**. The images were acquired before and during recovery after photobleaching. The white circle indicates the bleached region **(C, D)** FRAP kinetics of cells expressing GFP-TAP either non-treated (**C**) or treated with BDM for 30 min (**D**). The recovery curves correspond to a pool of three independent experiments, with 10 different cells analyzed per experiment. Error bars represent standard deviations. *D* values represent mean ± standard deviation.

We performed FRAP experiments in HeLa cells expressing GFP-TAP that were wither non-treated or treated with BDM for 30 min. Assuming that mRNP mobility was driven by myosin motors, we expected a reduction in the diffusion coefficient of GFP-TAP. Surprisingly, the results show that the GFP-TAP effective diffusion coefficient increased from 1.15 μm^2/s in control cells to 1.66 μm^2/s after BDM treatment. No immobile fraction was detected in either case (Figure 4.4).

In order to conclude that the diffusion coefficient estimated for GFP-TAP represents a measure of the mobility rate of mRNP complexes in the nucleus, it was crucial to determine the fraction of GFP fusion molecules that is actually bound to mRNPs. We used FLIP to discriminate between GFP-TAP molecules that are bound to mRNPs from those that are unbound in the absence and presence of BDM. Kinetic analysis of FLIP data revealed the existence of two populations of diffusing GFP-TAP in the nucleus. We assume that the slower population corresponds to GFP-tagged molecules associated with mRNP complexes whereas the faster population represents proteins unbound to mRNPs. In both control and BDM-treated cells, we observe two populations of GFP-TAP, with similar rate constants (Figure 4.5).

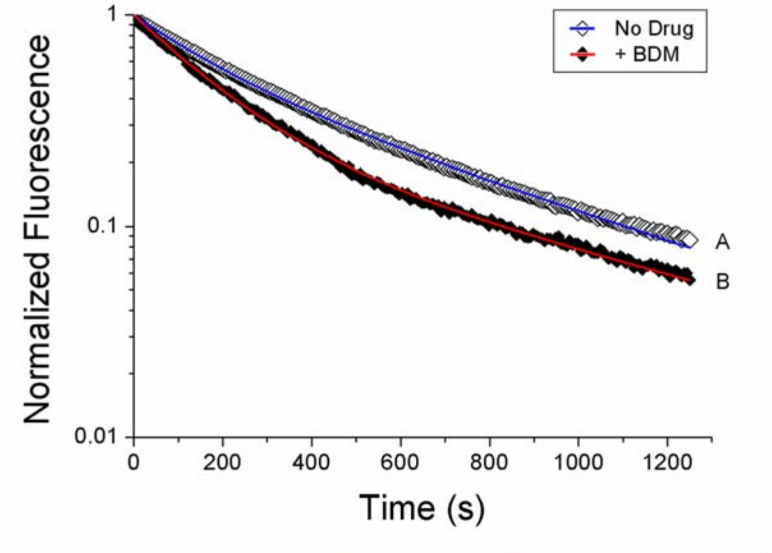

		p	R1 (slow)	R2 (fast)	χ^2
A	◇	0.56080 ± 0.00850	0.00157 ± 0.00002	0.00557 ± 0.00008	0.00005
B	◆	0.26805 ± 0.00600	0.00126 ± 0.00002	0.00576 ± 0.00004	0.00006

Figure 4.5 – FLIP kinetics of GFP-TAP in the presence and absence of BDM. Semi-log plots of nuclear loss of fluorescence in FLIP experiments performed in cells expressing GFP-TAP with no drug treatment and after 30 min of treatment with BDM. Fitting functions are plotted in color. In both cases the fluorescence loss can be fitted by a nonlinear function $F(t) = p\exp(-R_1 t) + (1-p)\exp(-R_2 t)$ that reveals the proportion of fast and slow moving molecules in the nucleus. Note that while the rate constants for the slow and fast populations are similar in control and drug treated cells, the proportion *p* of slow moving molecules decreases from 56% to 27% after BDM treatment.

However, in control cells the slower population represents more than half (approximately 56%) of the total GFP-TAP molecules in the nucleus, whereas after BDM treatment this population is reduced to less than 30%. These results imply that BDM increases the pool of nuclear GFP-TAP molecules unbound to mRNP complexes without interfering with the diffusion rate of TAP-associated mRNPs. Since the mobility rate of non-bound GFP-TAP is significantly higher than that of GFP-TAP associated with mRNPs, the increased proportion of non-bound molecules in the nucleus of BDM-treated cells is most probably responsible for the higher effective diffusion coefficient measured in FRAP experiments.

One possible explanation for the increased pool of nuclear GFP-TAP molecules unbound to mRNPs is that the release of the mRNA from the site of transcription is impaired by BDM and therefore less RNA is available to bind do TAP in the nucleoplasm. The effect of BDM was analyzed on nascent human β-globin transcripts by fluorescence *in situ* hybridization. Contrary to the initial hypothesis that BDM impairs the release of mRNPs from the transcription site, the results showed that BDM alone abolishes detection of β-globin RNA at the site of transcription within 10 min of drug addition (*data not shown*). Very similar time course results are obtained following treatment with the transcription inhibitor DRB, raising the unsuspected possibility that BDM might inhibit mRNA transcription.

The effect of BDM on transcription activity was next studied using an *in situ* method based on the incorporation of 5-fluorine-substituted uridine (FU). When added to the culture medium this uridine analogue is incorporated by the cells, allowing nascent RNA to be detected using antibodies against halogenated UTP (Boisvert et al., 2000). Incubation of cells with FU for 15 min results in labeling of transcription sites both throughout the nucleoplasm and in the nucleolus (*data not shown*). Treatment with DRB, which specifically inhibits transcription of protein-coding genes (Medlin et al., 2003) produces a significant reduction of the labeling in the nucleoplasm, without affecting nucleolar staining. Similar results were obtained when cells were treated with BDM before FU incorporation (*data not shown*). Since DRB blocks specifically elongation of transcription of mRNAs (Medlin et al., 2003), these results suggest that BDM interferes predominantly with the transcriptional activity of RNA Pol II. Biochemical assays indicate that BDM does not seem to have any effect on *in vitro* transcription, suggesting that the effect of BDM on transcription is not a direct effect on RNA Pol II but rather an inhibitory effect that may be dependent on associations of transcription complex with the nuclear structure.

4.4.3 BDM and DRB have similar effects in the kinetics of GFP-TAP

To confirm that the effect induced by BDM on the kinetics of GFP-TAP can be explained by a block in transcriptional activity, photobleaching experiments were further performed in the presence of DRB (Figure 4.6).

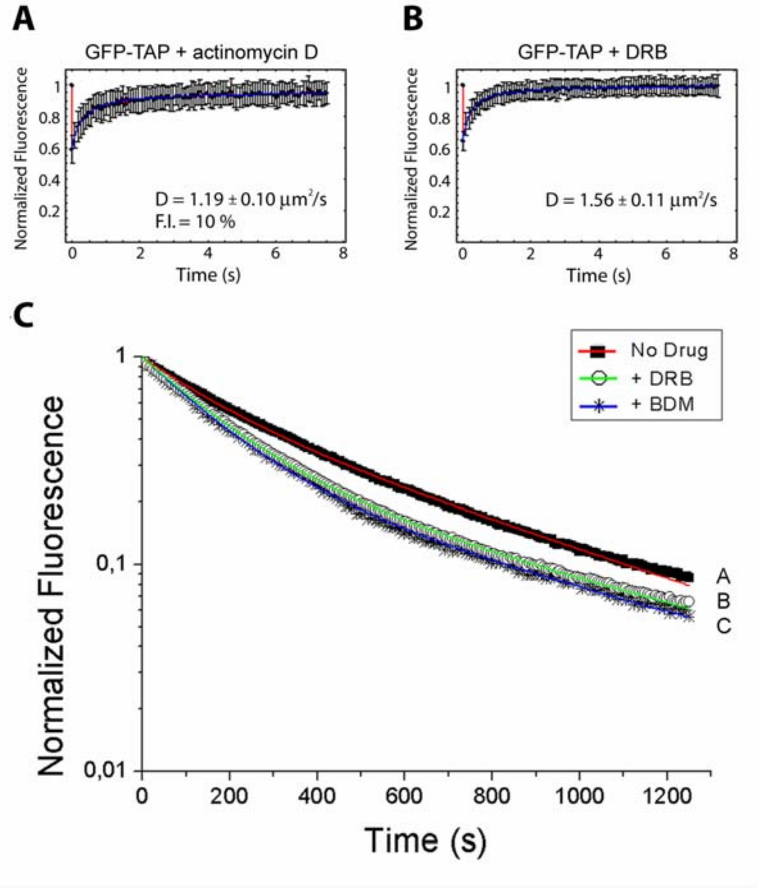

		p	R1 (slow)	R2 (fast)	χ^2
A	■	0.56080 ± 0.00850	0.00157 ± 0.00002	0.00557 ± 0.00008	0.00005
B	○	0.30307 ± 0.00516	0.00129 ± 0.00002	0.00560 ± 0.00004	0.00004
C	✳	0.26805 ± 0.00600	0.00126 ± 0.00002	0.00576 ± 0.00004	0.00006

Figure 4.6 – FRAP and FLIP kinetics of GFP-TAP in the presence of DRB. FRAP recovery curves of Hela cells expressing GFP-TAP that were either non-treated (**A**) or treated with DRB for 30 min (**B**). The recovery curves correspond to a pool of three independent experiments, with 10 different cells analyzed per experiment. Error bars represent standard deviations. *D* values represent mean ± standard deviation. **(C)** Semi-logarithmic plots of nuclear fluorescence in FLIP experiments performed on HeLa cells expressing GFP-TAP. The cells were either non-treated or treated with DRB and BDM for 30 min. Fitting functions are plotted in color. The rate constants R_1 and R_2 for the slow and fast GFP-TAP populations are not significantly altered by any of the two drugs. In addition, the proportion *p* of slow moving molecules is very similar in cells treated with either DRB (30%) or BDM (27%).

The results show that DRB causes an increase in the effective diffusion coefficient of GFP-TAP, similarly to that observed after BDM treatment (Figure 4.4D). In FLIP experiments the effect of DRB was also very similar to that of BDM. In fact, DRB treatment decreased the proportion of slow moving nuclear GFP-TAP molecules from 56% in control cells to approximately 30% as in BDM-treated cells (Figure 4.6C). The rate constants for the slow and fast moving populations of GFP-TAP molecules are similar in non-treated cells and in cells treated with either DRB or BDM, consistent with the view that in all cases the two populations correspond to molecules that are either associated or non-associated with mRNPs, respectively.

To further demonstrate that the BDM and DRB effects on GFP-TAP mobility are mainly caused by an increase of the nuclear pool of molecules that do not associate with mRNPs, additional FRAP experiments were performed on HeLa cells expressing GFP-TAP(371-619), a TAP fragment with impaired ability to bind to mRNA (Bachi et al., 2000) that moves in the nucleus with a significantly higher diffusion rate than the wild type protein (2.91 $\mu m^2 s^{-1}$ versus 1.15 $\mu m^2 s^{-1}$; see (Calapez et al., 2002)).

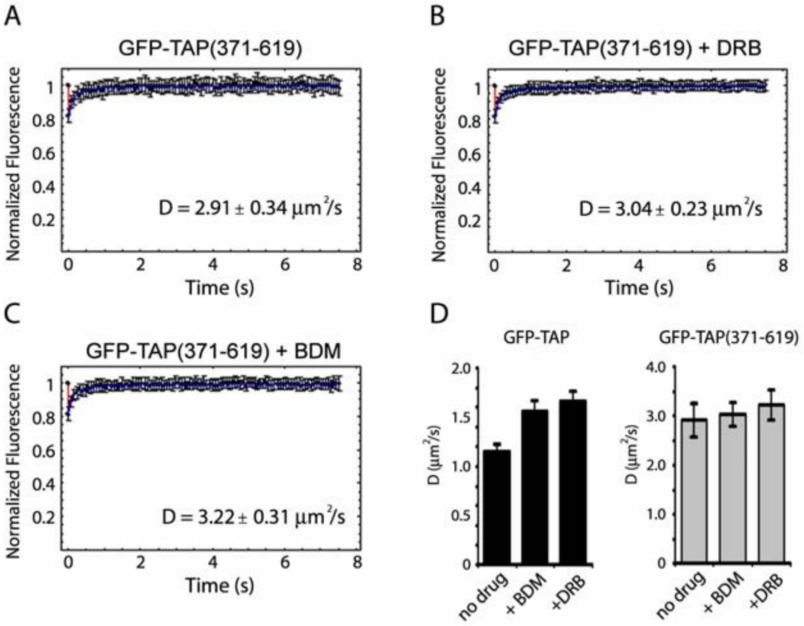

Figure 4.7 – FRAP kinetics of a TAP mutant with impaired ability to bind mRNPs. FRAP experiments were performed on HeLa cells expressing GFP-TAP(371-619). The cells were either non treated (**A**) or treated with DRB (**B**) and BDM (**C**) for 30 min. The recovery curves correspond to a pool of three independent experiments, with 10 different cells analyzed per experiment. Error bars represent standard deviations. *D* values represent mean ± standard deviation. For comparison, the mean effective diffusion coefficients obtained for GFP-TAP and GFP-TAP(371-619) are plotted (**D**). Note that the values of *D* for full length GFP-TAP are significantly higher after DRB or BDM treatment. In contrast, the values of *D* for the mutant protein are not altered by the drugs.

Assuming that BDM and DRB are primarily affecting mRNA synthesis and consequently increasing the proportion of TAP molecules unbound to mRNPs, no effect should be detected on the diffusion rate of a mutant protein that fails to associate with mRNP complexes. According to the prediction, the effective diffusion coefficients of GFP-TAP(371-619) measured by FRAP were similar in HeLa cells that were either non-treated (2.91 $\mu m^2 s^{-1}$), treated with DRB (3.04 $\mu m^2 s^{-1}$) or treated with BDM (3.22 $\mu m^2 s^{-1}$; Figure 4.7).

In conclusion, the data strongly suggests that BDM does not interfere directly with the mobility of mRNP complexes in the nucleus but rather increases the nuclear pool of fast moving TAP molecules due to a block in RNA transcription.

4.4.4 Estimating the effective diffusion coefficients of GFP fusion proteins bound to mRNP complexes by FLIP

As we have shown previously, FLIP experiments can be used to resolve independent populations of molecules that are diffusing at different rates. In our FLIP implementation, if there are two populations of molecules, one diffusing faster than the other, the fluorescence loss can be fitted to a nonlinear curve corresponding to a sum of exponentials (see section 4.4.1 and Materials and Methods). The rate constants of fluorescence loss obtained with this fitting procedure are related to the effective diffusion coefficient of each population of molecules, but they depend also on the size of the cellular compartment where diffusion is occurring and on experimental parameters such as bleaching time and the time interval between each bleach pulse.

In order to determine the effective diffusion coefficient corresponding to each of these rate constants, computer simulations of FLIP experiments were performed using a compartmental modeling approach, a method which has already been used by others to simulate FRAP and Photoactivation experiments (Beaudouin, 2003; Beaudouin et al., 2006). FLIP experiments were modeled by simulating diffusion and repetitive bleaching of fluorescent molecules inside the nucleus. The geometry of the nucleus was taken into account by modeling this cellular compartment as a grid of square elements with a grid step of 0.45 μm. Diffusion was only allowed to occur between nearest neighbors, so that at the border, for instance, diffusion could only occur between adjacent grid cells that are inside the nucleus. Each population of molecules was allowed to diffuse inside the nucleus with a single diffusion coefficient D given by Fick's second law $\partial C(\vec{r},t)/\partial t = D\nabla^2 C(\vec{r},t)$, where $C(\vec{r},t)$ represents the local concentration of fluorescent molecules. This diffusion equation cannot be solved analytically in the complex geometry of the cell nucleus. Instead, we used a finite differences approximation:

$$\frac{\partial C(i,j,t)}{\partial t} = -\frac{D}{g^2}\left[4C(i,j,t) - C(i-1,j,t) - C(i+1,j,t) - C(i,j-1,t) - C(i,j+1,t)\right]$$

where g is the grid step. Using this finite differences approach, the diffusion equation can be written as a system of coupled ordinary differential equations, each one corresponding to an element in the grid that defines the nucleus (Figure 4.8).

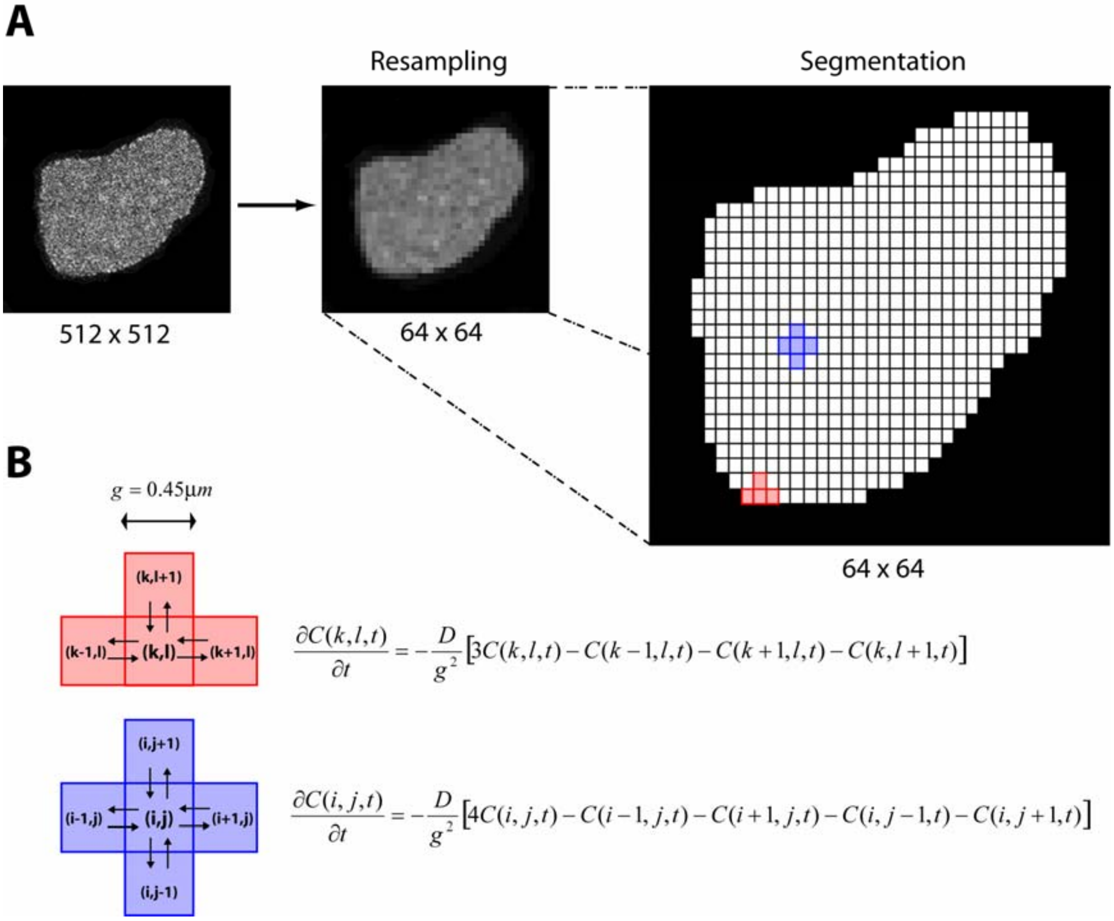

Figure 4.8 – Modeling diffusion in the nucleus with finite differences approximation. (A) A CLSM image of the nucleus with an original size of 512×512 pixels is re-sampled using nearest neighbor interpolation, so that each cell in the grid corresponds to 8 pixels in the original image. Threshold segmentation is then used to define the nuclear grid, with each square element having a fixed size of 0.45×0.45 μm^2. **(B)** The diffusion equation is then approximated in finite differences, resulting in a system of ordinary differential equations, one for each element in the grid. Diffusion is only allowed between nearest neighbors, so the equations will be different depending on the position of each square element. Shown are the equations for a grid element in the interior of the nucleus (*blue squares* in **A**) and another at the border (*red squares* in **A**).

Repetitive bleaching is incorporated into the simulations by adding a bleach term to the diffusion equation in the grid cells that correspond to the bleach region of interest (ROI). Photobleaching is considered a simple irreversible first order reaction (Axelrod et al., 1976a) with rate constant $K_{bleach}(r) = \alpha \cdot I(r)$, which depends on the bleaching intensity $I(r)$ at each position *r*. The concentration of the unbleached fluorophore $C(r,t)$ at position *r* and time *t* is given by

$$dC(r,t)/dt = -K_{bleach}(r) \cdot C(r,t).$$

Hence, for a bleaching pulse that lasts a time interval Δ*T*, the fluorophore concentration immediately after bleaching is given by

$$C(r,\Delta T) = C_0 \exp\left(-K_{bleach}(r) \cdot \Delta T\right)$$

where C_0 is the initial fluorophore concentration. Assuming a Gaussian bleaching intensity profile, we have

$$C(r,\Delta T) = C_0 \exp\left(-\alpha \cdot I_0 \Delta T \exp\left(-\frac{2r^2}{w^2}\right)\right)$$

where I_0 is the bleaching intensity value at $r = 0$ and w is the bleaching radius. Since bleaching is a first order reaction, we have for each bleaching ROI cell

$$dC(i,j,t)/dt = -K^*_{bleach}(i,j) \cdot C(i,j,t)$$

where $K^*_{bleach}(i,j)$ is dependent on the bleaching intensity profile. Its value can be obtained using the approximation

$$K^*_{bleach}(i,j) = \frac{\ln\left(C(i,j,0)/C(i,j,\Delta T)\right)}{\Delta T}$$

The ratio between the concentration before and after bleaching ($C(i,j,0)$ and $C(i,j,\Delta T)$ respectively) for each cell in the bleaching ROI is derived from experimental bleaching parameters obtained from HeLa cells expressing the immobile protein GFP-coilin-PABPN1 (Figure 4.9). Since each cell in the grid corresponds to a square of 8×8 pixels in the CLSM image, the bleaching profile is re-sampled into 8 pixel segments, and the average concentration ratio before and after bleaching is calculated for each segment as

$$\frac{C(i,j,\Delta T)}{C(i,j,0)} = \int_0^R 2\pi \cdot r \exp\left(-\alpha \cdot I_0 \Delta T \exp\left(-2\frac{r^2}{w^2}\right)\right) / \left(\pi \cdot R^2\right) dr$$

where $R = 8$ and both $\alpha . I_0$ and w are obtained by fitting the bleaching profile of GFP-coilin-PABPN1 to a Gaussian bleaching intensity profile (see Appendix 4.B).

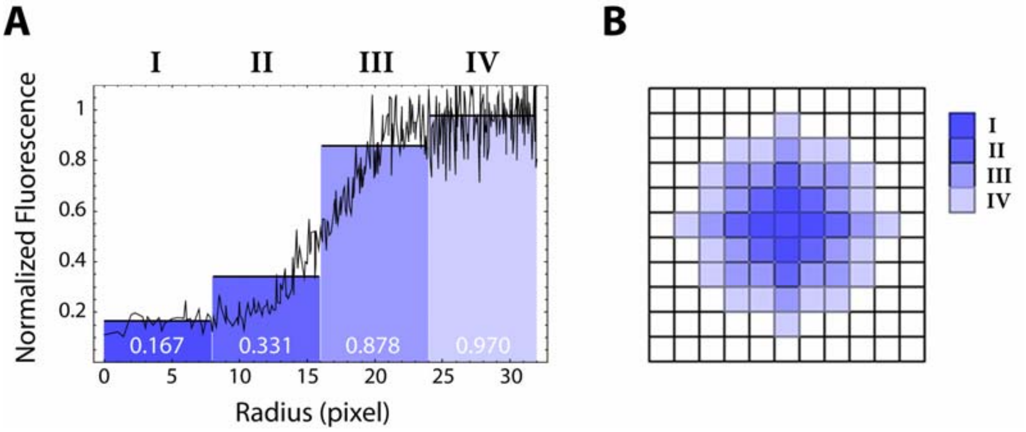

Figure 4.9 – Modeling bleaching in the nuclear grid (A) The experimental bleaching profile obtained for HeLa cells expressing the immobile protein GFP-coilin-PABPN1 is used to derive the bleaching rate constants for each grid cell in the bleach ROI. The average concentration ratio before and after bleaching (*white*) is calculated for 8 pixel segments as a function of the distance to the bleach ROI center. **(B)** The bleaching profile is thus re-sampled in the same way as the cell nucleus, with 4 different bleaching rate constants being attributed to pixels in the grid that correspond to the 8 pixel segments in **A** (*I, II, III, IV*) .

For cells which belong to the bleaching ROI, the ordinary differential equations are thus

$$\frac{\partial C(i,j,t)}{\partial t} = -\frac{D}{g^2}\left[4C(i,j,t) - C(i-1,j,t) - C(i+1,j,t) - C(i,j-1,t) - C(i,j+1,t)\right] - K^*_{bleach}(i,j)C(i,j,t)$$

The initial distribution of fluorescence is taken into account in the initial conditions for the differential equations. Since the FLIP images were acquired in two dimensions in a CLSM and perpendicularly to the optical axis, the compartmental model for FLIP simulations based on finite differences approach was also developed in a two-dimensional approach. The validity of such two-dimensional models for simulating diffusion in a three-dimensional nuclear or cellular volume has been tested by others (Beaudouin et al., 2006). Given the nuclear dimensions and the fact that the bleaching profile is not significantly altered throughout its axial extent in our experimental conditions (Braga et al., 2004a), we consider the 2D model sufficient for fitting purposes, when characterizing protein dynamics occurring in a 3D nucleus.

Thus, given the cell geometry, experimental FLIP parameters such as bleach pulse duration (ΔT) and time interval between bleach pulses (T), the simulations will reproduce a FLIP experiment for a particular cell, for a given diffusion coefficient of the fluorescent protein under study (Figure 4.10 and Appendix 4.C).

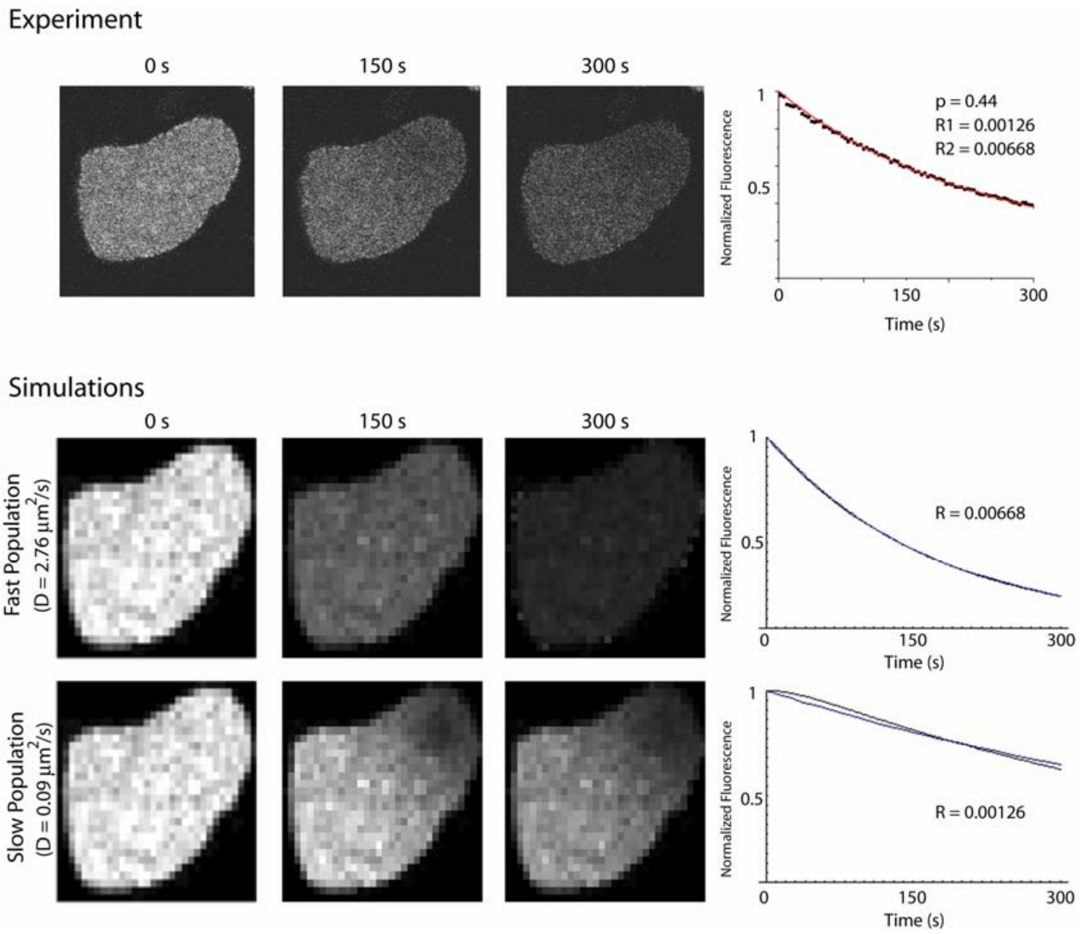

Figure 4.10 – FLIP experiments and simulations results. Single cell FLIP analysis for GFP-TAP revealed the existence of two diffusing populations of molecules, with different rate constants (*R1* and *R2*) and the proportion *p* of each one (*Experiment*). FLIP simulations performed with different effective diffusion coefficients are then used to relate these rate constants with two independent populations diffusing at 0.09 and 3.28 $\mu m^2 s^{-1}$ (*Simulations*).

By simulating FLIP experiments for different diffusion coefficient values it is possible to obtain a FLIP decay curve for a given area in the cell nucleus, which can then be fitted to a single exponential decay. The rate constants thus obtained can then be compared with the experimental two-exponential fit values, allowing the determination of the effective diffusion coefficient for each population (Figure 4.10). However, as it can be seen for the simulated FLIP curve corresponding to the slower diffusion coefficient of 0.09 $\mu m^2 s^{-1}$, fluorescence loss curves in FLIP experiments can deviate from single exponentials when the diffusion coefficient is low. This effect is mainly due to cell geometry, as it is only visible when bleaching is performed away from the nucleus center (Figure 4.11).

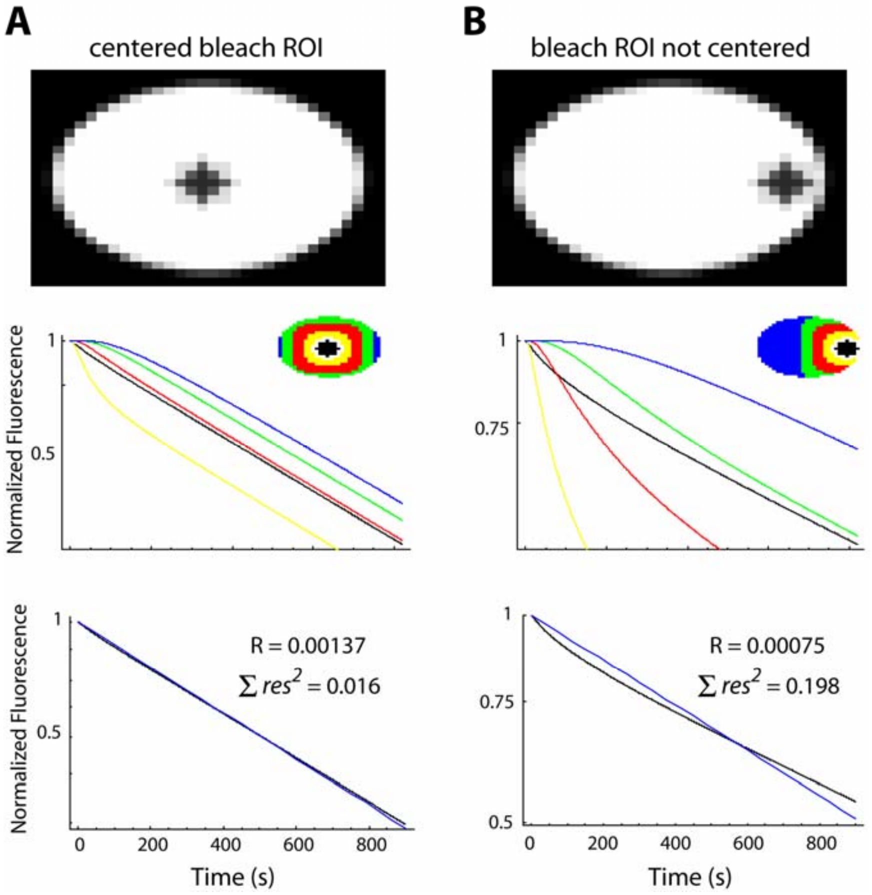

Figure 4.11 – Bleach area positioning alters FLIP decay curves. FLIP simulations performed in an artificial ellipsoid nucleus for a single diffusing population of molecules with a diffusion coefficient of 0.05 $\mu m^2 s^{-1}$. Changing the position of the bleached region from the nucleus center (**A**) to the nuclear periphery (**B**) alters the fluorescence loss curve measured in the whole nucleus (*black line*) to a non-exponential decay (notice the increase in the sum of the square of the fit residues Σres^2) and reduces the rate constant obtained by such non-optimal fit (from 0.00137 to 0.00075). Also shown are the fluorescence loss curves measured in different ring areas at increasing distances from the bleached region (*yellow, red, green* and *blue lines*).

Fitting an exponential function to a FLIP decay curve in the case of low D values is thus only valid if bleaching is performed away from the periphery of the cellular compartment where diffusion is occurring. In order to eliminate this limitation in determining of effective diffusion coefficients from FLIP curves, we fitted the data obtained from FLIP simulations directly to experimental fluorescence loss curves, instead of exponential curves. We thus propose to use a two-step fitting procedure, in which a two-exponential fit to the FLIP curves is first used to assess the existence of more than one population of mobile molecules and to get a first estimate of the proportion *p* of the slower population relative to the total fluorescence. This estimate is then used in the second run of the fitting procedure, where the simulated fluorescence loss obtained for several values of the parameters D_1, D_2 and *p* (where D_1 and D_2 are the diffusion coefficients of each population of molecules) is directly compared with the experimental data, measured in exactly the same way as the simulations (Figure 4.12 and Appendixes 4.D, E).

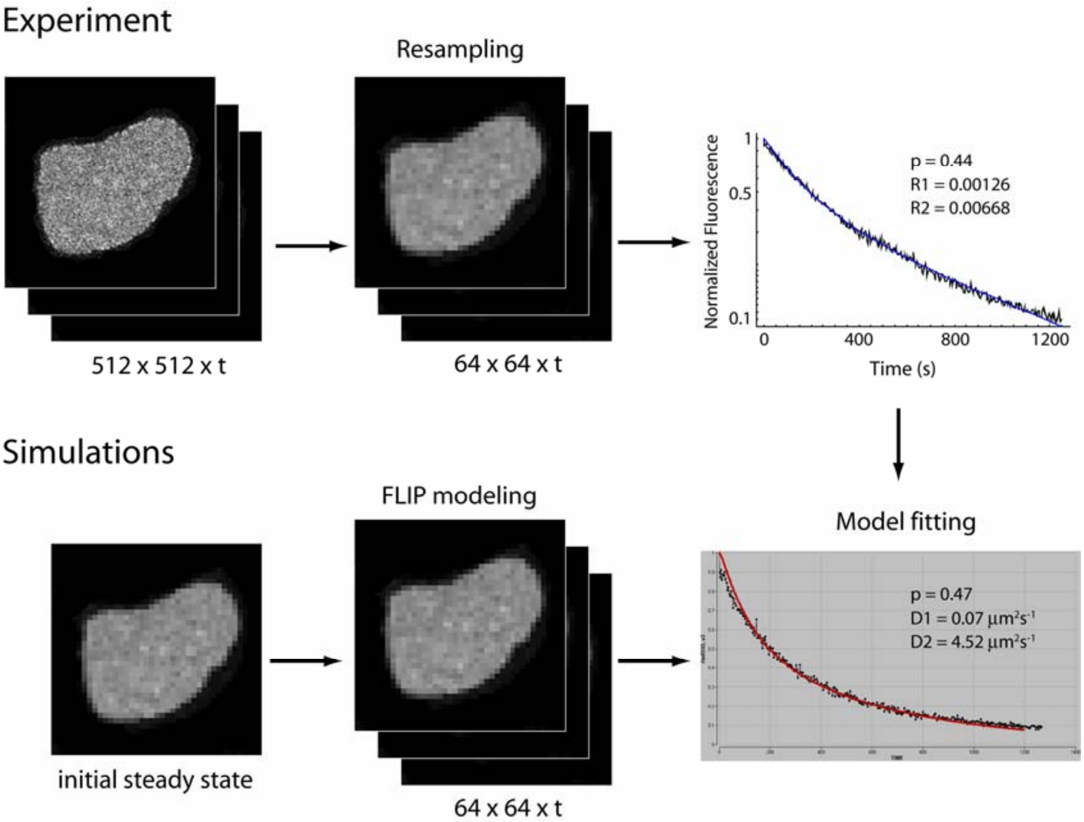

Figure 4.12 – FLIP modeling and fitting to experimental data. Schematic outline of the methodology used to estimate effective diffusion coefficients from FLIP decay curves. The image stack corresponding to a FLIP experiment performed in a HeLa cell (with dimensions *512×512×t* where *t* is the number of time points) is re-sampled in the *x* and *y* dimensions to 64×64 pixels. Fluorescence loss is then measured in a defined region of interest and fitted to a bi-exponential curve (*blue line* in top graph), yielding a first estimate for the proportion *p* of slow moving molecules. The initial steady-state distribution of fluorescence is taken into account in the initial conditions of the FLIP model, which uses a finite difference approach to simulate diffusion and bleaching inside the nuclear area, yielding FLIP decay curves as a function of the diffusion coefficients of each species (*D1* and *D2*) and the proportion *p* of the slower one. Fitting the simulated FLIP curves to the experimental data then allows for the determination of each of these parameters (*red line* in bottom graph).

We next applied this FLIP modeling approach to our experimental data on GFP-TAP and GFP-PABPN1 mobility inside the nucleus. Both proteins are able to bind to mRNA, albeit with different affinities and at distinct steps of mRNA processing (see sections 1.3.2 and 1.3.4 in Chapter 1). In addition, while PABPN1 binds to polyadenylated RNA independently of its export to the cytoplasm, TAP only binds to mRNA transcripts which are to be exported through the nuclear pore complexes. As mentioned in the previous sections, FLIP experiments were performed in cells expressing either GFP-PABPN1 or a point mutant variant of this protein with impaired ability to bind to poly(A)RNA. For TAP, FLIP experiments were performed in cell expressing GFP-TAP either with no drug treatment or treated with the transcription inhibitor DRB or the myosin inhibitor BDM. The results obtained with the FLIP modeling are summarized in table 4.1.

		p	**D_1 ($\mu m^2 s^{-1}$)**	**D_2 ($\mu m^2 s^{-1}$)**
GFP-PABPN1	wt	0.67 ± 0.23	0.11 ± 0.04	7.45 ± 2.72
	dm	0.26 ± 0.04	0.08 ± 0.03	9.67 ± 0.34
	average		*0.09 ± 0.04*	*8.56 ± 2.11*
GFP-TAP	no drug	0.55 ± 0.24	0.08 ± 0.05	4.25 ± 1.90
	+ DRB	0.34 ± 0.14	0.09 ± 0.02	3.80 ± 2.24
	+ BDM	0.35 ± 0.13	0.11 ± 0.04	4.93 ± 1.97
	average		*0.09 ± 0.05*	*4.29 ± 1.99*

Table 4.1 – Quantitative FLIP analysis of the mobility of the RNA binding proteins PABPN1 and TAP. Compartmental modeling of FLIP experiments yielded effective diffusion coefficient values for two independent populations of molecules discernible in the fluorescence loss signal of both GFP-PABPN1 and GFP-TAP. Shown are the average values for the slow (**D_1**) and fast (**D_2**) components of the FLIP curve for GFP-PABPN1 wt, dm and a pool of both (*average*) and GFP-TAP with no drug treatment, with the addition of DRB, BDM and a pool of all the three experiments. The proportion **p** of the slower moving population relative to the total fluorescence is also shown for each case. Each experiment corresponds to data obtained from 4 to 6 different cells for GFP-PABPN1 and from 10 to 15 cells in the case of GFP-TAP. Values represent mean ± standard deviation.

For both GFP-PABPN1 and GFP-TAP it was possible to discern two populations of diffusing molecules from the FLIP curves. Fitting a two-exponential formula to the fluorescence loss in each cell yielded an estimate of the proportion *p* of the slow moving population, as well as two rate constants associated with each population that were similar but nonetheless variable from cell to cell (see Figure 4.2). By integrating the geometry of the nucleus and the position of the bleach area in the FLIP compartmental modeling it was possible to obtain estimates for the diffusion coefficient values of both slow and fast moving populations of tagged molecules for each cell. Remarkably, the diffusion coefficient value of 0.09 $\mu m^2 s^{-1}$ we obtained for the slow moving population, which we believe corresponds to mRNA-bound molecules, is the same in both GFP-PABPN1 and GFP-TAP experiments. Moreover, this value remains unchanged in the FLIP experiments performed with the mutant GFP-PABPN1dm and in cells expressing GFP-TAP treated either with DRB or BDM. The estimates for the diffusion coefficient value of the faster moving population of molecules is different between GFP-PABPN1 (8.56 $\mu m^2 s^{-1}$) and GFP-TAP (4.29 $\mu m^2 s^{-1}$) but nonetheless remains largely unaltered by the introduction of a point mutation in PABPN1 or of drug treatments in GFP-TAP. The differences in the FLIP curves observed experimentally are thus attributed to different proportions of slow and fast moving populations of GFP-tagged molecules present in each cell, rather than being a consequence of changes in the diffusion coefficient of any of them.

Influence of protein-RNA binding affinities on diffusion coefficient estimates

Our FLIP modeling assumes that the fluorescent signal observed in the CLSM results from a mix of two independent populations of molecules (i.e. there is no mixing between the two populations), diffusing at different rates inside a cellular compartment. In order to obtain estimates for the diffusion coefficient of mRNP particles inside the nucleus, we tagged the RNA-binding proteins PABPN1 and TAP with GFP and studied their mobility, assuming that part of the total population of these molecules was bound to mRNA. Under this assumption, the fluorescence loss in FLIP is then a reflection of the dynamics of both mRNA-bound and unbound GFP-tagged PABPN1 and TAP. In order to test to what extent the independence of the two populations was required for the FLIP analysis to be accurate, we incorporated binding and unbinding of tagged molecules to RNA in a reaction-diffusion model of our system (see section 1.6.2 in Chapter 1). For both PABPN1 and TAP, we assumed a binding reaction of the form $F + S \leftrightarrows C$, where F represents the non-bound fluorescent protein, S the non-bound non-fluorescent mRNP particle and C the fluorescent complex formed by the two. We considered the three species to be homogeneously distributed throughout the nucleus and their total amount to be constant during the FLIP experiment. Photobleaching destroys the fluorescence of GFP-tagged molecules, but does not alter the binding kinetics of each protein.

Incorporating binding into the diffusion and repetitive bleaching equations yields the following reaction-diffusion system:

$$\begin{cases} \dfrac{\partial F(\vec{r},t)}{\partial t} = D_2 \nabla^2 F(\vec{r},t) - k_{on} S \cdot F(\vec{r},t) + k_{off} C(\vec{r},t) - \alpha I(\vec{r},t) \\ \dfrac{\partial C(\vec{r},t)}{\partial t} = D_1 \nabla^2 C(\vec{r},t) + k_{on} S \cdot F(\vec{r},t) - k_{off} C(\vec{r},t) - \alpha I(\vec{r},t) \end{cases}$$

where D_1 and D_2 are the diffusion coefficients of the fluorescently RNA-bound and unbound molecules respectively, S is the concentration of the RNA substrate, k_{on} and k_{off} are the on- and off-rates of the binding reaction and $\alpha I(\vec{r},t)$ the bleaching rate constant for a Gaussian laser beam.

The affinity of the unbound fluorescent protein to the RNA substrate is given by the dissociation constant $K_D = k_{off} / k_{on}$, which can be obtained from the concentration of the chemical reagents at equilibrium: $K_D = S_{eq} F_{eq} / C_{eq}$. Thus, a lower value for the dissociation constant reflects a higher affinity of the protein to the RNA substrate.

Because the RNA molecules are not affected by bleaching and we assume the total amount of RNA to remain constant throughout the duration of the FLIP experiment, the concentration S will remain a constant. If p is the percentage of tagged-molecules bound to RNA at any given time, the equilibrium concentration of unbound RNA is given by $S_{eq} = K_D p/(1-p)$ and the term $k_{on}S$ in the reaction-diffusion equations can be substituted by the pseudo-on rate constant $k_{on}^* = k_{off}\, p/(1-p)$.

The reaction-diffusion model was implemented in an ellipsoid nucleus and numerically solved for different values of k_{off} (see Appendix 4.F). Simulated FLIP curves were generated using experimental values for bleaching and image acquisition parameters. Bleaching was performed at the center of the nucleus. The diffusion coefficients of unbound RNA and RNA-binding proteins were set to 0.04 and 20 $\mu m^2 s^{-1}$, respectively. For a single population of molecules diffusing at 0.04 $\mu m^2 s^{-1}$, the fluorescence loss could be fit to a single exponential function with rate constant $R = 0.00120$ (Figure 4.13A). We then modeled FLIP experiments in the presence of the two populations, with the proportion p of unbound RNA-binding proteins at any time point set to 0.6. If there is no binding, i.e. if the two populations are independent, the fluorescence loss resulting from repetitive bleaching can be fitted by a two-exponential function.

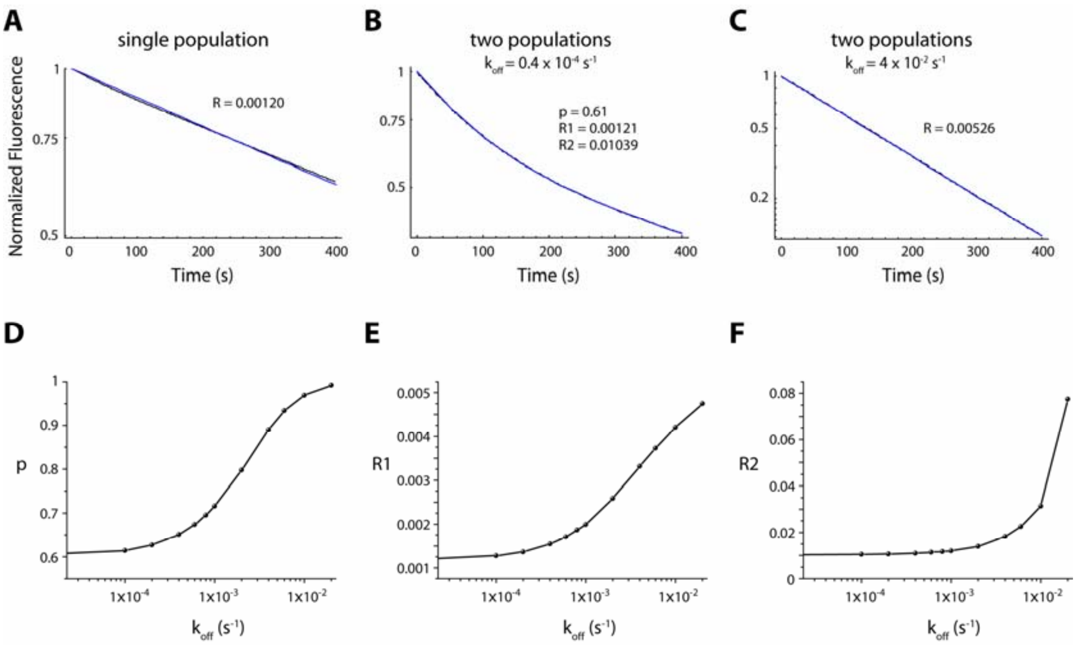

Figure 4.13 – Influence of the binding affinity on FLIP analysis. (A) FLIP simulations performed in an artificial ellipsoid nucleus for a single diffusing population of molecules with a diffusion coefficient of 0.04 $\mu m^2 s^{-1}$ yield a single exponential fit to the fluorescence loss. **(B)** Two diffusing populations with D_1=0.04 $\mu m^2 s^{-1}$ and D_2=20 $\mu m^2 s^{-1}$ which are allowed to bind to each other with high affinity ($k_{off} = 0.4 \times 10^{-4} s^{-1}$) originate a simulated fluorescence loss than can be fitted with a two-exponential function, correctly estimating the proportion *p* of slower, unbound molecules and the rate constants associated with each population. **(C)** The same two diffusing populations simulated in **B** now bind with less affinity to each other ($k_{off} = 4 \times 10^{-2} s^{-1}$), which results in a fluorescence loss curve that is no longer fitted by a two-exponential function and is thus unable to resolve the two populations. **(D)** FLIP curves for two populations diffusing with the same rates as in **A** and **B** (D_1=0.04 $\mu m^2 s^{-1}$, D_2=20 $\mu m^2 s^{-1}$, *p*=0.60) were simulated for varying k_{off} values. For lower values of k_{off}, the percentage *p* of unbound molecules is correctly determined by the FLIP analysis, but with increasing k_{off} the fluorescence loss curve gradually deviates from a two-exponential decay to a single exponential loss of fluorescence **(E**, **F)** The rate constants obtained with two-exponential fits also change with varying k_{off}, as shown in these log-linear plots obtained from simulated FLIP experiments.

If the RNA-binding protein (GFP-PABPN1 or GFP-TAP) binds with very high affinity to the substrate RNA, i.e. for low values of k_{off} that cause the reaction to be nearly irreversible, the fluorescence loss can still be fit by a two-exponential function which correctly yields the proportion *p* of unbound molecules and the rate constants $R1 = 0.00121$ and $R2 = 0.01039$ associated with each population (Figure

4.13B). If we significantly increase the value of k_{off} though, while keeping all the other parameters constant (D_1=0.04 $\mu m^2 s^{-1}$, D_2=20 $\mu m^2 s^{-1}$, p=0.60) then the fluorescence loss in FLIP will no longer be fitted by a two-exponential function, but by a single exponential instead, with a rate constant that is not related with any of the diffusing population of molecules (Figure 4.13C).

The influence of the binding affinity on the fluorescence loss curve in FLIP experiments can be investigated by generating simulated FLIP curves for increasing values of k_{off} (Figures 4.13D, E and F). The results confirm that the two-exponential fit and consequently the FLIP modeling approach can only be applied to determine the fraction and effective diffusion coefficients of two diffusing populations of molecules if any binding reactions between them occur with high affinity. Thus, for k_{off} values that are lower than ~ $0.5\times10^{-3}s^{-1}$, both the proportion p and the effective diffusion coefficients can be determined with a 10% accuracy using the FLIP modeling approach (initial plateau levels in the plots of Figure 4.13D, E and F). As the k_{off} value increases though, the FLIP curve rapidly changes to a single exponential fit, increasing the p estimate until only a single population can be determined (Figure 4.13D), albeit with a concurrently increasing rate constant that reflects binding and diffusion between the two populations, instead of the diffusion coefficient of the slower population (Figure 4.13E). Notably, the rate constant corresponding to the faster population of molecules remains approximately the same as the k_{off} value is increased up to ~ $0.5\times10^{-2}s^{-1}$, before increasing steeply for k_{off} values which correspond to p values higher than 0.9 (Figure 4.13F). This increase in the rate constant value for the faster population might be a consequence of erroneously fitting a two-exponential function to a single-exponential decay, whereas the higher values for the rate constant of the slower population obtained with increasing k_{off} are likely to be a result of an increasingly present “effective diffusion” regime, as the chemical reaction becomes faster than diffusion itself (see section 1.6.2 in Chapter 1).

4.5 Discussion

We have shown in this study how FLIP experiments can be used to discriminate between diffusion rates of mRNP-bound and free GFP-fusion molecules, an information which is not directly obtainable from standard FRAP experiments. Although FRAP can be used to assess mRNP mobility, it does not resolve a mixed population of GFP fusion proteins such as that composed by a fraction of slow-moving molecules bound to mRNP complexes and a fast-moving fraction of unbound molecules. In a system containing a mix of two mobile populations diffusing at different rates, a single diffusion coefficient is estimated by FRAP, which will be lower than the individual diffusion coefficients of each population (Braga et al., 2004b).

The novel FLIP methodology we developed can distinguish and estimate the fraction of independent populations of GFP fusion proteins which are bound to mRNP complexes from those that are unbound, and furthermore estimate the effective diffusion coefficient of each of these populations.

We have used GFP-TAP and GFP-PABPN1 to visualize the mobility of mRNPs within the nucleus of living HeLa cells. While GFP-PABPN1 binds to the poly(A) tails present in nearly all eukaryotic mRNAs, GFP-TAP is expected to bind more specifically to mRNAs which are to be exported to the cytoplasm (see sections 1.3.2 and 1.3.4 in Chapter 1). Our results show that both GFP-PABPN1 and GFP-TAP diffuse inside the nucleus essentially as two populations, one with a slower diffusion coefficient of ~ 0.09 $\mu m^2 s^{-1}$ which is common to both proteins, and another with an effective diffusion coefficient of ~ 8.6 $\mu m^2 s^{-1}$ for GFP-PABPN1 and ~ 4.3 $\mu m^2 s^{-1}$ for GFP-TAP. Notably, the diffusion coefficient of 0.09 $\mu m^2 s^{-1}$ estimated for the slower population present in both GFP-PABPN1 and GFP-TAP experiments is very similar to recent estimates for the diffusion coefficient of mRNPs which were obtained using very distinct experimental approaches (see section 1.3.3 in Chapter 1). Diffusion coefficient values ranging from 0.04 to 0.09 $\mu m^2 s^{-1}$ have been reported for mRNP movement inside the nucleus, using real time single mRNP imaging techniques (Molenaar et al., 2004; Shav-Tal et al., 2004a; Vargas et al., 2005).

The faster populations detected in both GFP-PABPN1 ($D = 8.6$ μm^{2}s^{-1}) and GFP-TAP ($D = 4.3$ μm^{2}s^{-1}) experiments are likely to correspond to unbound pools of protein which nonetheless may interact with other nuclear structures or nuclear proteins. In both cases, the diffusion coefficients obtained with this novel FLIP methodology might reflect different interactions which are likely to occur in a timescale faster than diffusion of the free protein, and will therefore give rise to an effective diffusion regime (see section 1.6.2 in Chapter 1). Based on their molecular weights, GFP-PABPN1 and GFP-TAP would be expected to diffuse inside the nucleus with diffusion coefficient values of ~ 25 and 21 μm^{2}s^{-1}, respectively. However, as both proteins are likely to have multiple interaction partners distinct from mRNP complexes (see sections 1.3.2 and 1.3.4 in Chapter 1) their nuclear mobility rates may be hindered by such binding events. GFP-PABPN1, for instance, is known to associate with nuclear speckles (see section 1.2.2 in Chapter 1). This association occurs in a timescale which is much faster than diffusion itself, as no GFP-PABPN1 accumulation is seen at the speckles when FLIP experiments are performed. In fact, the decay in normalized fluorescence occurs at the same rate in nuclear speckles and nucleoplasmic areas (*data not shown*), similarly to what is observed with the GFP-tagged splicing factors U2AF^{65}, U2AF^{35} and SF1 (see Chapter 2). Thus, although both proteins are expected to interact with a plethora of nuclear partners besides mRNA, the different effective diffusion coefficients obtained for each of them (detected as fast moving populations in the FLIP analysis) indicate that the interactions GFP-TAP is involved in have a more noticeable effect on the overall mobility of the RNA-unbound pool of this protein.

The *in vivo* binding kinetics of GFP-PABPN1 and GFP-TAP to mRNA are not known. Although TAP is able to bind directly to mRNA, adaptor RNA-binding proteins are thought to be required to mediate the interaction between the TAP-p15 heterodimer and mRNA (see section 1.3.4 in Chapter 1) (Dreyfuss et al., 2002; Stutz and Izaurralde, 2003). *In vitro* data for PABPN1 binding to poly(A) molecules in solution estimated the affinity for an isolated binding site as being in the nanomolar range – K_D=2×10^{-9} M and k_{on}=4×10^{8} M^{-1}s^{-1} – (Meyer et al., 2002; Wahle et al., 1993) with detectable, albeit weak cooperativity between adjacent PABPN1 molecules (see section 1.3.2 in Chapter 1) (Meyer et al., 2002). These *in vitro* binding affinities are not consistent with our own FLIP data, which clearly reveals the existence of two different populations of diffusing molecules for both GFP-TAP and GFP-PABPN1, instead of just a single population that would be detected if the binding parameters had values similar to the ones measured *in vitro*. If we expect PABPN1 and TAP to bind to mRNA in a reversible manner with low affinity values, then the existence of two populations in the FLIP analysis is intriguing. *In vivo* binding can therefore be very different from the *in vitro* situation, in which the proteins are isolated from the nuclear environment, and therefore lack their natural partners and may be prevented from establishing the same interactions they undergo *in vivo*. Cooperative binding, presumably involving other protein partners, might indeed increase the affinity of PABPN1 and TAP to mRNA *in vivo*, thereby conferring these proteins the ability to be used as tools for the study of mRNA mobility with FLIP analysis.

We have previously showed that when cells are depleted of ATP or incubated at reduced temperature, the mobility of TAP-associated mRNPs is significantly reduced (Calapez et al., 2002). Here we examined also whether myosin motors mediate the movement of export competent mRNPs in the nucleus. To address this issue we have incubated HeLa cells expressing GFP-TAP with 2,3-butanedione monoxime (BDM), which has been widely used at milimolar concentrations in cell biology experiments as an ATPase inhibitor of the myosin superfamily (Castillo et al., 2002; Ostap, 2002; Ramachandran et al., 2003).

FLIP experiments allowed us to distinguish between the slow moving GFP-TAP bound to mRNP complexes and fast moving GFP-TAP that is not associated with mRNPs. FRAP analysis of cells treated with BDM for 30 minutes shows an increase in the diffusion coefficient of GFP-TAP molecules in the nucleus. However, this does not necessarily reflect a direct effect of the drug on mRNP mobility, since FLIP data reveals that BDM induces a significant increase in the population of fast moving GFP-TAP molecules. Assuming that fast moving GFP-TAP molecules are not bound to mRNPs, the results suggest that BDM decreases the pool of intranuclear mRNPs available for TAP binding. This could be caused either by a defect in assembly of mRNPs competent for TAP recognition or by a block in mRNA synthesis.

Visualization of β-globin mRNA in murine erythroleulemia cells by fluorescence *in situ* hybridization shows that after BDM treatment nascent transcripts are no longer detected in the nucleus, similarly to what is observed following incubation of cells with the transcription inhibitors Actinomycin D, DRB and α-amanitin (Custodio et al., 1999). In further agreement with the view that BDM inhibits mRNA synthesis, the drug causes a general reduction of incorporation of the uridine analog in nucleoplasm without interfering with transcription activity in the nucleus.

We therefore conclude that BDM specifically blocks transcription by RNA Poll II *in vivo*. As a consequence of this effect, the drug reduces the amount of nuclear mRNAs available to recruit TAP. This in turn increases the pool of fast moving GFP-TAP molecules observed in photobleaching experiments.

Supporting the view that an inhibitor of the actin-myosin interaction interferes with transcriptional activity, previous studies have implicated nuclear actin in transcription of cellular and viral genes (Burke et al., 1998; Egly et al., 1984; Scheer et al., 1984) and chromatin remodeling events (Zhao et al., 1998). More recently, a nuclear isoform of myosin I was reported to associate with RNA Pol II and an anti-myosin antibody blocked RNA synthesis *in vitro* (Pestic-Dragovich et al., 2000).

In summary, two major conclusions are derived from this study. First, the results argue that myosin motors are unlikely to mediate transport of mRNP complexes traveling from the sites of transcription to the nuclear pores. Second, we demonstrate for the first time that BDM has an inhibitory effect on transcriptional activity by RNA Pol II *in vivo*. This raises the possibility that the previously reported impairment of PML nuclear body movement induced by BDM (Muratani et al., 2002) may be an indirect effect of transcription inhibition, rather than a direct reflection of myosin-dependent mobility. Further studies are clearly needed to define the molecular mechanisms that mediate energy-dependent mobility within the nucleus.

Appendix 4.A – Electronic oscillator circuit for triggering FLIP bleach events

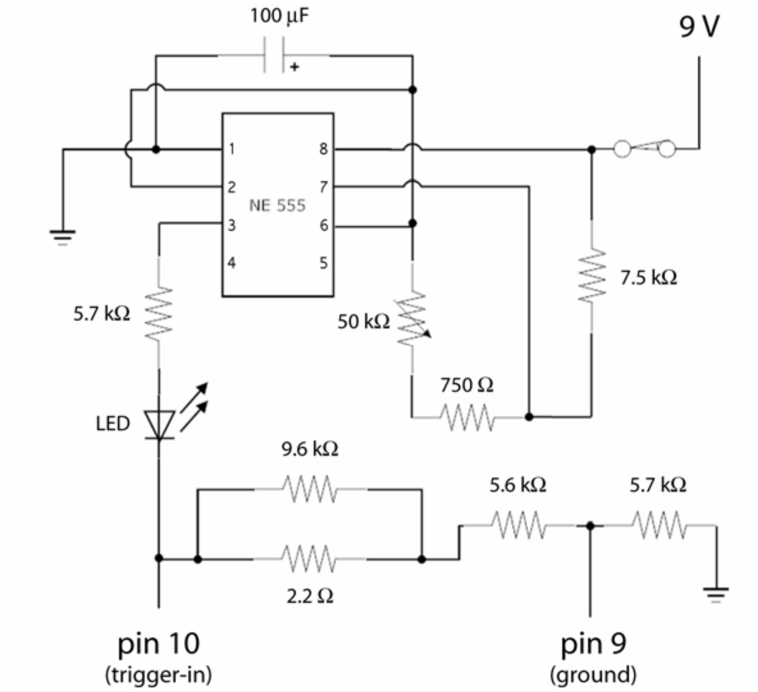

The electronic oscillator circuit was designed to take advantage of the LSM 510 Trigger-in feature to control bleaching events externally, as repetitive bleaching was not performed by version 2.8 of the LSM software. Basically, it consists of a 555 timer integrated circuit (*NE 555*) operating in astable mode, i.e. continually pulsing until power is removed. The frequency of operation of the astable circuit depends on the values of the resistors and capacitor used, and could be changed using the variable 50 kΩ resistor. A light-emitting diode (*LED*) which pulsed with this same frequency was used to check proper functioning of the circuit by simple visual inspection. Upon 9V power supply, the electronic oscillator circuit would thus provide repetitive 5V triggering pulses directly to the trigger interface of the LSM 510, which used pins 10 and 9 as input for the *trigger 1* event that was recognized by the software and used to initiate the bleaching procedure.

Appendix 4.B - Mathematica Notebook for Gaussian bleach intensity profile fitting

---

FLIP Gaussian bleach profile fit

ReadFiles and file formats

```
ReadFiles[lfiles_List] :=
          Map[ReadList[#, Real,
                         RecordSeparators -> {"\n", "\r"},
                         RecordLists -> True] &,
               lfiles];
ReadFiles[form_String] :=
          Map[ReadList[#, Real,
                         RecordSeparators -> {"\n", "\r"},
                         RecordLists -> True] &,
               FileNames[form]];
```

Laser profile (zoom 4)

This is the post-bleach bleaching profile for fixed cells.

```
immob =
  ReadFiles["C:\\Documents and Settings\\joserino\\My Documents\\Ze
     Rino\\FRAP\\Profiles\\prf_z4_d30_i5_o25_25_Sep_2002.prf"];
ListPlot[immob[[1]], PlotJoined -> True, PlotRange → {0, 1.1}, Frame -> True];
```

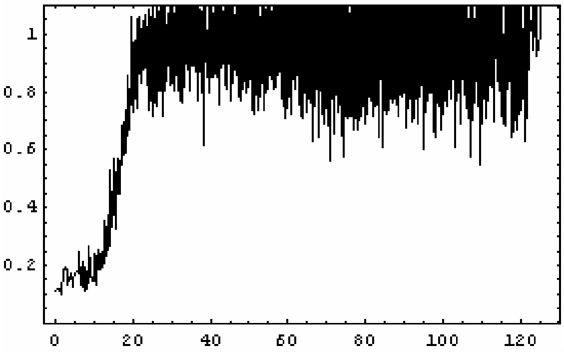

```
resimmob = NonlinearRegress[Map[{#[[1]], #[[2]]} &, immob[[1]]],
  Exp[-K * E^(-2 r^2/w^2)] + c, r, {w, K, c},
  RegressionReport → {BestFitParameters, ParameterCITable}]
{BestFitParameters → {w → 17.3341, K → 3.15102, c → -0.0127795}, ParameterCITable →
        Estimate        Asymptotic SE      CI
  w     17.3341         0.426027           {16.4987, 18.1694}
  K     3.15102         0.245215           {2.67022, 3.63183}            }
  c     -0.0127795      0.00260432         {-0.0178859, -0.00767317}
```

Profile partition:

```
immobzoom = Take[immob[[1]], {1, 337}];

ListPlot[immobzoom, PlotJoined -> True, PlotRange → {0, 1.1}, Frame -> True];
```

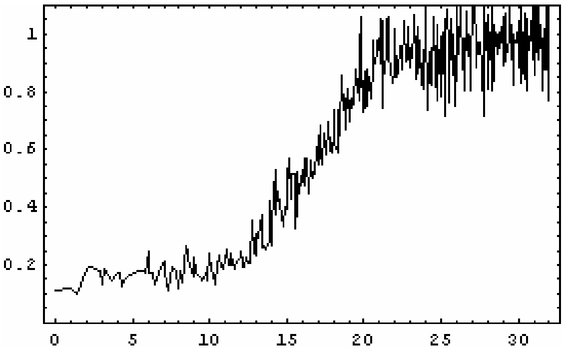

```
immobpart1 = Take[immob[[1]], 30];
ListPlot[immobpart1, PlotJoined -> True, PlotRange → {0, 1.1}, Frame -> True];
```

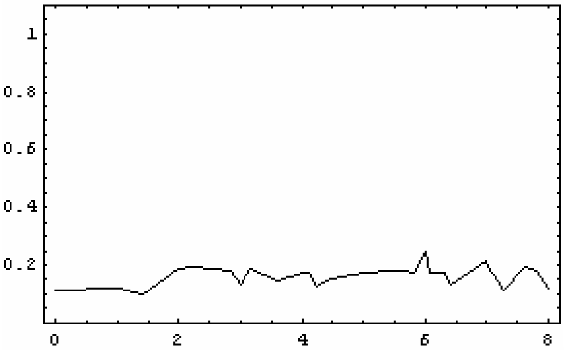

```
resimmob1 = NonlinearRegress[Map[{#[[1]], #[[2]]} &, immobpart1],
  Exp[-K * E^(-2 r^2/w^2)] + c, r, {w, K, c},
  RegressionReport → {BestFitParameters, ParameterCITable}]
{BestFitParameters → {w → 2.04345, K → 0.0717774, c → -0.830863}, ParameterCITable →

        Estimate      Asymptotic SE    CI
  w     2.04345       0.880655         {0.236497, 3.85041}     }
  K     0.0717774     0.0298291        {0.0105731, 0.132982}
  c     -0.830863     0.00599243       {-0.843158, -0.818567}
Show[Plot[(Exp[-K * E^(-2 r^2/w^2)] + c) /. (BestFitParameters /. resimmob1),
  {r, 0, 8}, DisplayFunction → Identity],
 ListPlot[Map[{#[[1]], #[[2]]} &, immobpart1], PlotJoined → True,
  PlotStyle → {RGBColor[1, 0, 0]}, DisplayFunction → Identity],
 PlotRange → {0, 1.5}, DisplayFunction → $DisplayFunction]
```

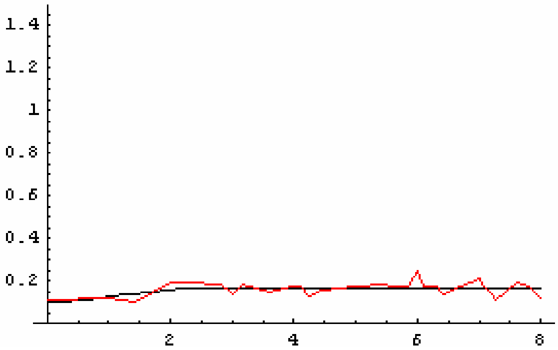

```
- Graphics -
N[∫_0^8 (2 π r (Exp[-K * E^(-2 r^2/w^2)] + c) /. (BestFitParameters /. resimmob1)) dr]
 ---------------------------------------------------------------------------------
                                     π 8^2
```

```
0.166837
immobpart2 = Take[immob[[1]], {30, 98}];
immobpart2[[All, 1]] = immobpart2[[All, 1]] - 8;
ListPlot[immobpart2, PlotJoined -> True, PlotRange → {0, 1.1}, Frame -> True];
```

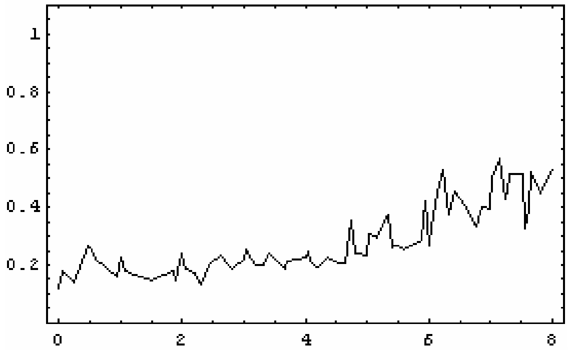

```
resimmob2 = NonlinearRegress[Map[{#[[1]], #[[2]]} &, immobpart2],
  Exp[-K * E^(-2 r^2/w^2)] + c, r, {w, K, c},
  RegressionReport → {BestFitParameters, ParameterCITable}]
{BestFitParameters → {w → 10.5755, K → 2.73979, c → 0.108228}, ParameterCITable →

        Estimate     Asymptotic SE    CI
  w     10.5755      0.838374         {8.90164, 12.2494}       }
  K     2.73979      0.818912         {1.10478, 4.3748}
  c     0.108228     0.0624893        {-0.0165355, 0.232992}
Show[Plot[(Exp[-K * E^(-2 r^2/w^2)] + c) /. (BestFitParameters /. resimmob2),
  {r, 0, 8}, DisplayFunction → Identity],
 ListPlot[Map[{#[[1]], #[[2]]} &, immobpart2], PlotJoined → True,
  PlotStyle → {RGBColor[1, 0, 0]}, DisplayFunction → Identity],
 PlotRange → {0, 1.5}, DisplayFunction → $DisplayFunction]
```

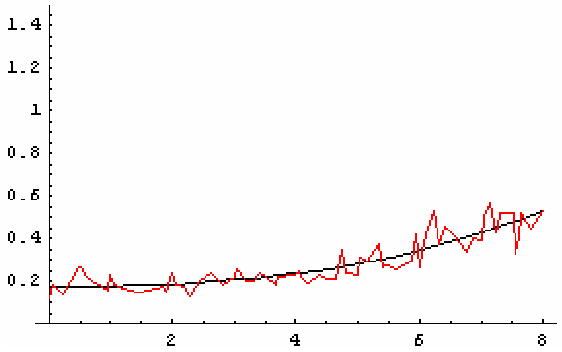

```
- Graphics -
N[Integrate[(2 π r (Exp[-K * E^(-2 r^2/w^2)] + c) /. (BestFitParameters /. resimmob2)), {r, 0, 8}] / (π 8^2)]
0.330901
immobpart3 = Take[immob[[1]], {98, 200}];
immobpart3[[All, 1]] = immobpart3[[All, 1]] - 16;
ListPlot[immobpart3, PlotJoined -> True, PlotRange → {0, 1.1}, Frame -> True];
```

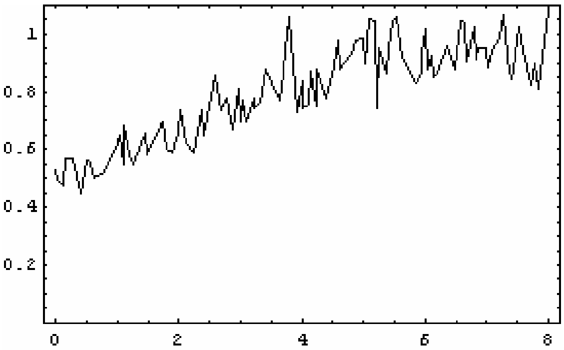

```
resimmob3 = NonlinearRegress[Map[{#[[1]], #[[2]]} &, immobpart3],
  Exp[-K*E^(-2 r^2/w^2)] + c, r, {w, K, c},
  RegressionReport → {BestFitParameters, ParameterCITable}]
{BestFitParameters → {w → 4.28392, K → 0.523989, c → -0.0558284}, ParameterCITable →
        Estimate        Asymptotic SE      CI
  w     4.28392         0.279283           {3.72983, 4.83801}         }
  K     0.523989        0.0337509          {0.457028, 0.590949}
  c     -0.0558284      0.0136157          {-0.0828415, -0.0288154}
Show[Plot[(Exp[-K*E^(-2 r^2/w^2)] + c) /. (BestFitParameters /. resimmob3),
  {r, 0, 8}, DisplayFunction → Identity],
 ListPlot[Map[{#[[1]], #[[2]]} &, immobpart3], PlotJoined → True,
  PlotStyle → {RGBColor[1, 0, 0]}, DisplayFunction → Identity],
 PlotRange → {0, 1.5}, DisplayFunction → $DisplayFunction]
```

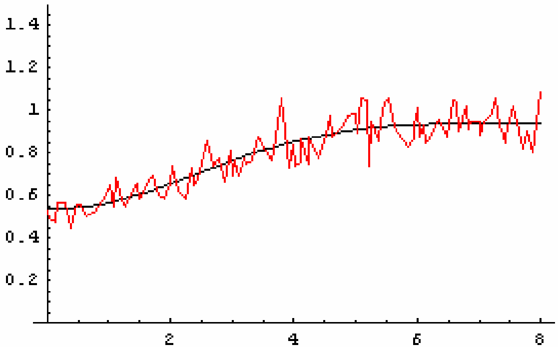

```
- Graphics -
N[∫_0^8 (2 π r (Exp[-K*E^(-2 r^2/w^2)] + c) /. (BestFitParameters /. resimmob3)) dr]
 ─────────────────────────────────────────────────────────────────────────────
                                   π 8^2
0.877914
immobpart4 = Take[immob[[1]], {200, 337}];
immobpart4[[All, 1]] = immobpart4[[All, 1]] - 24;
ListPlot[immobpart4, PlotJoined -> True, PlotRange → {0, 1.1}, Frame -> True];
```

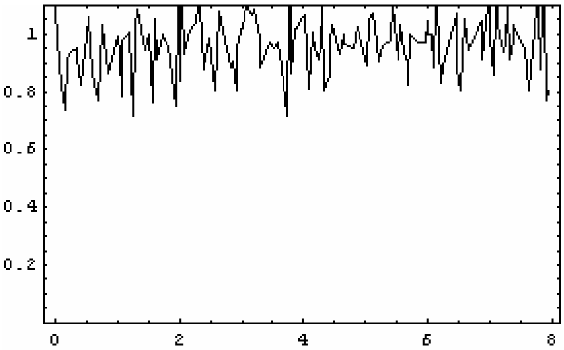

```
resimmob4 = NonlinearRegress[Map[{#[[1]], #[[2]]} &, immobpart4],
  Exp[-K * E^(-2 r^2/w^2)] + c, r, {w, K, c},
  RegressionReport → {BestFitParameters, ParameterCITable}]
```

```
{BestFitParameters → {w → 2.17226, K → 0.058561, c → -0.0276969}, ParameterCITable →

        Estimate       Asymptotic SE     CI
  w     2.17226        1.46373           {-0.722552, 5.06708}
  K     0.058561       0.0317652         {-0.00426086, 0.121383}    }
  c     -0.0276969     0.0107274         {-0.0489124, -0.00648147}
```

```
Show[Plot[(Exp[-K * E^(-2 r^2/w^2)] + c) /. (BestFitParameters /. resimmob4),
  {r, 0, 8}, DisplayFunction → Identity],
 ListPlot[Map[{#[[1]], #[[2]]} &, immobpart4], PlotJoined → True,
  PlotStyle → {RGBColor[1, 0, 0]}, DisplayFunction → Identity],
 PlotRange → {0, 1.5}, DisplayFunction → $DisplayFunction]
```

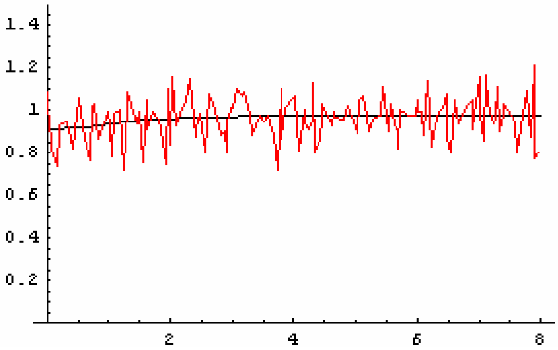

```
- Graphics -
```

$$\frac{\mathrm{N}\left[\int_0^8 \left(2\,\pi\,r\,\left(\mathrm{Exp}\left[-K * E^{-2\frac{r^2}{w^2}}\right] + c\right) \;/.\; (\mathrm{BestFitParameters} \;/.\; \mathrm{resimmob4})\right) dr\right]}{\pi\,8^2}$$

```
0.970175
```

Appendix 4.C - Mathematica Notebook for processing experimental FLIP data

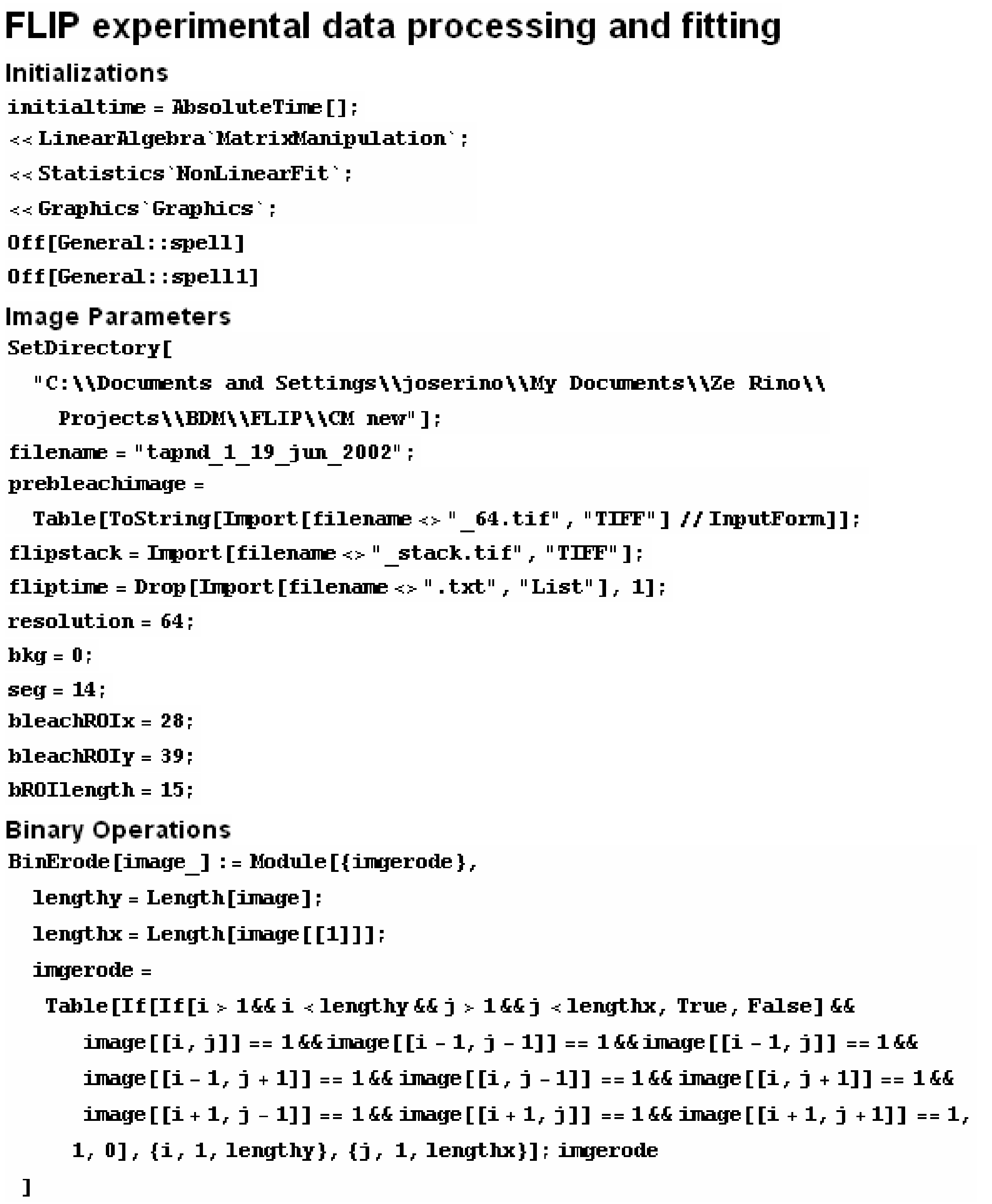

FLIP experimental data processing and fitting

Initializations

```
initialtime = AbsoluteTime[];
<< LinearAlgebra`MatrixManipulation`;
<< Statistics`NonLinearFit`;
<< Graphics`Graphics`;
Off[General::spell]
Off[General::spell1]
```

Image Parameters

```
SetDirectory[
  "C:\\Documents and Settings\\joserino\\My Documents\\Ze Rino\\
    Projects\\BDM\\FLIP\\CM new"];
filename = "tapnd_1_19_jun_2002";
prebleachimage =
  Table[ToString[Import[filename <> "_64.tif", "TIFF"] // InputForm]];
flipstack = Import[filename <> "_stack.tif", "TIFF"];
fliptime = Drop[Import[filename <> ".txt", "List"], 1];
resolution = 64;
bkg = 0;
seg = 14;
bleachROIx = 28;
bleachROIy = 39;
bROIlength = 15;
```

Binary Operations

```
BinErode[image_] := Module[{imgerode},
  lengthy = Length[image];
  lengthx = Length[image[[1]]];
  imgerode =
   Table[If[If[i > 1 && i < lengthy && j > 1 && j < lengthx, True, False] &&
      image[[i, j]] == 1 && image[[i - 1, j - 1]] == 1 && image[[i - 1, j]] == 1 &&
      image[[i - 1, j + 1]] == 1 && image[[i, j - 1]] == 1 && image[[i, j + 1]] == 1 &&
      image[[i + 1, j - 1]] == 1 && image[[i + 1, j]] == 1 && image[[i + 1, j + 1]] == 1,
     1, 0], {i, 1, lengthy}, {j, 1, lengthx}]; imgerode
 ]
```

```
BinDilate[image_] := Module[{imgdilate},
  lengthy = Length[image];
  lengthx = Length[image[[1]]];
  imgdilate =
   Table[If[If[i > 1&& i < lengthy && j > 1&& j < lengthx, True, False] &&
      image[[i, j]] == 0 && image[[i - 1, j - 1]] == 0 && image[[i - 1, j]] == 0 &&
      image[[i - 1, j + 1]] == 0 && image[[i, j - 1]] == 0 && image[[i, j + 1]] == 0 &&
      image[[i + 1, j - 1]] == 0 && image[[i + 1, j]] == 0 && image[[i + 1, j + 1]] == 0,
     0, 1], {i, 1, lengthy}, {j, 1, lengthx}];
  Do[imgdilate[[1, All]] = 0];
  Do[imgdilate[[lengthy, All]] = 0];
  Do[imgdilate[[All, 1]] = 0];
  Do[imgdilate[[All, lengthx]] = 0];
  imgdilate
 ]
```

Image Conversion

```
prebleachimageconv =
  ToExpression[
    StringInsert[StringInsert[StringReplace[prebleachimage,
       {"Graphics[Raster[" → "",
        ", ColorFunction -> GrayLevel], ImageSize -> {64, 64},
           PlotRange -> {{0, 63}, {1, 64}}, AspectRatio -> Automatic]" → ""}],
      "{", 1], "}", -1]][[1]];
flipstackst = Table[ToString[flipstack[[i]] // InputForm],
   {i, 1, Length[flipstack]}];
flipstackconv =
  Table[
   ToExpression[
     StringInsert[StringInsert[StringReplace[flipstackst[[i]],
        {"Graphics[Raster[" → "",
         ", ColorFunction -> GrayLevel], ImageSize -> {64, 64},
            PlotRange -> {{0, 63}, {1, 64}}, AspectRatio -> Automatic]" →
          ""}], "{", 1], "}", -1]][[1]], {i, 1, Length[flipstack]}];
Show[Graphics[Raster[flipstackconv[[10]], {{0, 0}, {64, 64}}, {0, 30},
   ColorFunction → GrayLevel], AspectRatio → Automatic], ImageSize → 256,
 DisplayFunction → $DisplayFunction]
```

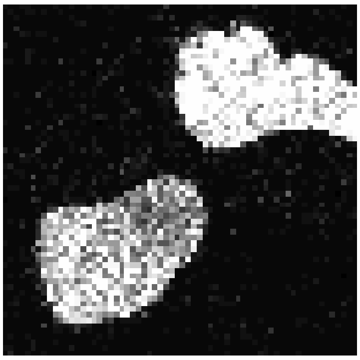

```
- Graphics -
```

Image ROIs

```
prebleachimageback = 1/2 (Abs[prebleachimageconv - bkg] + prebleachimageconv - bkg);
Show[Graphics[Raster[prebleachimageback, {{0, 0}, {resolution, resolution}},
   {0, 30}, ColorFunction → GrayLevel], AspectRatio → Automatic],
 ImageSize → 256, DisplayFunction → $DisplayFunction]
```

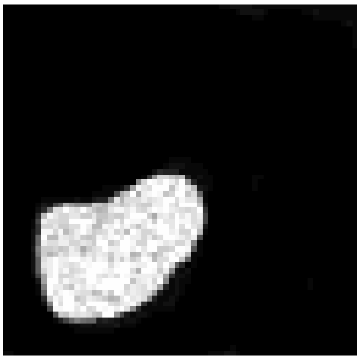

```
- Graphics -
```

```
imageseg =
  Table[Which[prebleachimageback[[i, j]] < seg, 0,
    prebleachimageback[[i, j]] ≥ seg, 1], {i, 1, resolution}, {j, 1, resolution}];
Show[Graphics[Raster[imageseg, {{0, 0}, {resolution, resolution}},
   {0, 1}, ColorFunction → GrayLevel], AspectRatio → Automatic],
 ImageSize → 256, DisplayFunction → $DisplayFunction]
```

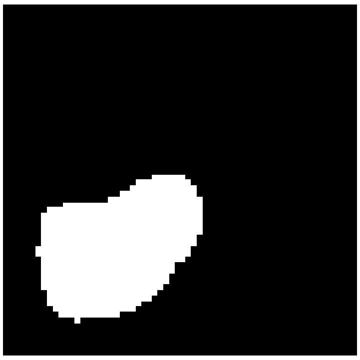

```
- Graphics -
```

Bleach and Measure ROIs Definition

```
bROIx = bleachROIx;
bROIy = resolution - bleachROIy;
bROIimageseg = Table[0, {i, 1, resolution}, {j, 1, resolution},
   {k , 1, bROIlength}];
bROIxilimit = If[bROIx - bROIlength ≥ 1, bROIx - bROIlength, 1];
bROIxslimit = If[bROIx + bROIlength ≤ resolution, bROIx + bROIlength,
   resolution];
bROIyilimit = If[bROIy - bROIlength ≥ 1, bROIy - bROIlength, 1];
bROIyslimit = If[bROIy + bROIlength ≤ resolution, bROIy + bROIlength,
   resolution];
Do[Do[If[Ceiling[√((i - bROIy)^2 + (j - bROIx)^2)] == k && imageseg[[i, j]] == 1,
   bROIimageseg[[i, j, k]] = k, 0], {i, bROIyilimit, bROIyslimit},
  {j, bROIxilimit, bROIxslimit}], {k, 1, bROIlength}]
bROIimageseg[[bROIy, bROIx, 1]] = 1;
imagerois = imageseg + Sum[bROIimageseg[[All, All, k]], {k, 1, bROIlength}];
```

```
Show[Graphics[Raster[imagerois, {{0, 0}, {resolution, resolution}},
    {0, 15}, ColorFunction → GrayLevel], AspectRatio → Automatic],
 ImageSize → 256, DisplayFunction → $DisplayFunction]
```

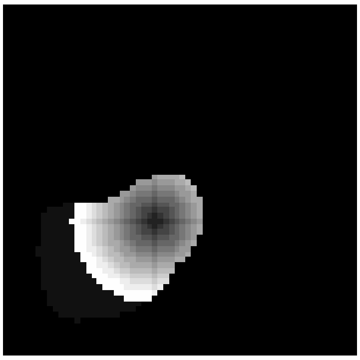

```
- Graphics -
```

```
NROI = Length[Position[imageseg, 1]];
mROIimageseg1 = Table[0, {i, 1, resolution}, {j, 1, resolution}];
Do[If[imagerois[[i, j]] ≥ 6 && imagerois[[i, j]] ≤ 8, mROIimageseg1[[i, j]] = 1],
  {i, 1, resolution}, {j, 1, resolution}];
mROIimageseg2 = Table[0, {i, 1, resolution}, {j, 1, resolution}];
Do[If[imagerois[[i, j]] ≥ 9 && imagerois[[i, j]] ≤ 11, mROIimageseg2[[i, j]] = 1],
  {i, 1, resolution}, {j, 1, resolution}];
mROIimageseg3 = Table[0, {i, 1, resolution}, {j, 1, resolution}];
Do[If[imagerois[[i, j]] ≥ 12 && imagerois[[i, j]] ≤ 14,
   mROIimageseg3[[i, j]] = 1], {i, 1, resolution}, {j, 1, resolution}];
mROIimageseg4 = Table[0, {i, 1, resolution}, {j, 1, resolution}];
Do[If[imagerois[[i, j]] == 1 || imagerois[[i, j]] ≥ 15, mROIimageseg4[[i, j]] = 1],
  {i, 1, resolution}, {j, 1, resolution}];
mROIimagesegT = Table[0, {i, 1, resolution}, {j, 1, resolution}];
Do[If[imagerois[[i, j]] == 1 || imagerois[[i, j]] ≥ 6, mROIimagesegT[[i, j]] = 1],
  {i, 1, resolution}, {j, 1, resolution}];
Show[Graphics[Raster[flipstackconv[[10]] * mROIimageseg4, {{0, 0}, {64, 64}},
    {0, 30}, ColorFunction → GrayLevel], AspectRatio → Automatic],
 ImageSize → 256, DisplayFunction → $DisplayFunction]
```

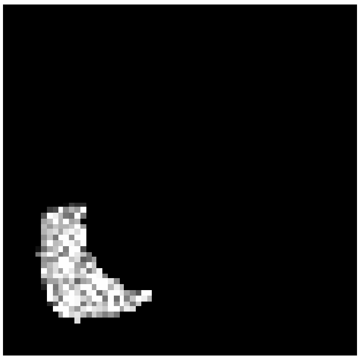

```
- Graphics -
```

Normalized Fluorescence

```
NROI = Length[Position[imageseg, 1]];
```

```
rowmin = Min[Table[Position[imageseg, 1][[i, 1]], {i, 1, NROI}]];
rowmax = Max[Table[Position[imageseg, 1][[i, 1]], {i, 1, NROI}]];
colmin = Min[Table[Position[imageseg, 1][[i, 2]], {i, 1, NROI}]];
colmax = Max[Table[Position[imageseg, 1][[i, 2]], {i, 1, NROI}]];
rowlength = rowmax - rowmin + 1;
collength = colmax - colmin + 1;
cellrois = Table[imagerois[[i, j]], {i, rowmin - 2, rowmax + 1},
   {j, colmin - 2, colmax + 1}];
init = Table[prebleachimageback[[i, j]], {i, rowmin - 2, rowmax + 1},
   {j, colmin - 2, colmax + 1}];
Do[cellrois[[i, 1]] = i - 1, {i, 1, rowlength + 3}]
Do[cellrois[[1, i]] = i - 1, {i, 1, collength + 3}]
Do[init[[i, 1]] = i - 1, {i, 1, rowlength + 3}]
Do[init[[1, i]] = i - 1, {i, 1, collength + 3}]
Show[Graphics[Raster[cellrois, {{0, 0}, {rowlength + 3, collength + 3}},
   {0, 15}, ColorFunction → GrayLevel]], ImageSize → 256,
 DisplayFunction → $DisplayFunction]
```

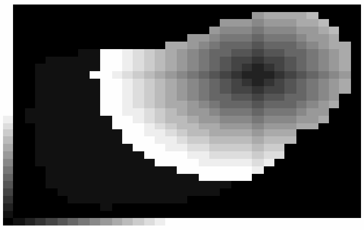

```
- Graphics -
Export[filename <> "_cellrois.csv", cellrois];
Export[filename <> "_init.csv", init];
NmROI1 = Length[Position[mROIimageseg1, 1]];
NmROI2 = Length[Position[mROIimageseg2, 1]];
NmROI3 = Length[Position[mROIimageseg3, 1]];
NmROI4 = Length[Position[mROIimageseg4, 1]];
NmROIT = Length[Position[mROIimagesegT, 1]];
FROI1[i_] :=
    1
  ------
  NmROI1
   Plus @@
    Table[flipstackconv[[i]][[Position[mROIimageseg1,1][[k,1]],Position[mROIimageseg1,1][[k,2]]]],
     {k, 1, NmROI1}]
FROI2[i_] :=
    1
  ------
  NmROI2
   Plus @@
    Table[flipstackconv[[i]][[Position[mROIimageseg2,1][[k,1]],Position[mROIimageseg2,1][[k,2]]]],
     {k, 1, NmROI2}]
FROI3[i_] :=
    1
  ------
  NmROI3
   Plus @@
    Table[flipstackconv[[i]][[Position[mROIimageseg3,1][[k,1]],Position[mROIimageseg3,1][[k,2]]]],
     {k, 1, NmROI3}]
```

```
FROI4[i_] :=
    1
 -------
 NmROI4
  Plus @@
   Table[flipstackconv[[i]][[Position[mROIimageseg4,1][[k,1]],Position[mROIimageseg4,1][[k,2]]]],
    {k, 1, NmROI4}]
FROIT[i_] :=
    1
 -------
 NmROIT
  Plus @@
   Table[flipstackconv[[i]][[Position[mROIimagesegT,1][[k,1]],Position[mROIimagesegT,1][[k,2]]]],
    {k, 1, NmROIT}]
NorFluorescence1 = {};
NorFluorescence2 = {};
NorFluorescence3 = {};
NorFluorescence4 = {};
NorFluorescence5 = {};
                                                FROI1[i]
NorFluorescence1 = Table[{fliptime[[i]], N[ ---------- ]},
                                                FROI1[1]
   {i, 1, Length[fliptime]}];
                                                FROI2[i]
NorFluorescence2 = Table[{fliptime[[i]], N[ ---------- ]},
                                                FROI2[1]
   {i, 1, Length[fliptime]}];
                                                FROI3[i]
NorFluorescence3 = Table[{fliptime[[i]], N[ ---------- ]},
                                                FROI3[1]
   {i, 1, Length[fliptime]}];
                                                FROI4[i]
NorFluorescence4 = Table[{fliptime[[i]], N[ ---------- ]},
                                                FROI4[1]
   {i, 1, Length[fliptime]}];
                                                FROIT[i]
NorFluorescenceT = Table[{fliptime[[i]], N[ ---------- ]},
                                                FROIT[1]
   {i, 1, Length[fliptime]}];
result = Export[filename <> "_mROI1.txt", NorFluorescence1, "CSV"];
result = Export[filename <> "_mROI2.txt", NorFluorescence2, "CSV"];
result = Export[filename <> "_mROI3.txt", NorFluorescence3, "CSV"];
result = Export[filename <> "_mROI4.txt", NorFluorescence4, "CSV"];
result = Export[filename <> "_mROIT.txt", NorFluorescenceT, "CSV"];
```

Fits

```
N[FROIT[1]]
25.345
ListPlot[NorFluorescenceT, PlotJoined → True, PlotRange → {0, 1}];
```

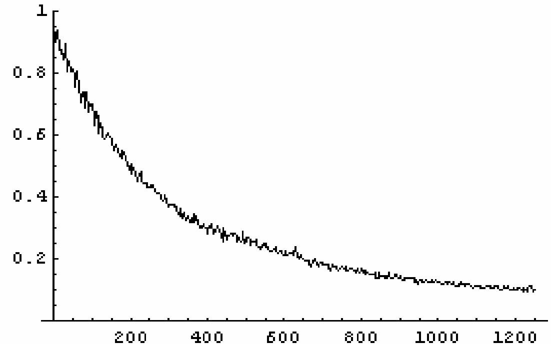

```
Show[ListPlot[NorFluorescenceT, PlotJoined → True, PlotRange → {0, 1},
   PlotStyle → {RGBColor[0, 0, 0]}, DisplayFunction → Identity],
  ListPlot[NorFluorescence1, PlotJoined → True, PlotStyle → {RGBColor[1, 1, 0]},
   DisplayFunction → Identity],
  ListPlot[NorFluorescence2, PlotJoined → True, PlotStyle → {RGBColor[1, 0, 0]},
   DisplayFunction → Identity],
  ListPlot[NorFluorescence3, PlotJoined → True, PlotStyle → {RGBColor[0, 1, 0]},
   DisplayFunction → Identity],
  ListPlot[NorFluorescence4, PlotJoined → True, PlotStyle → {RGBColor[0, 0, 1]},
   DisplayFunction → Identity], DisplayFunction → $DisplayFunction];
```

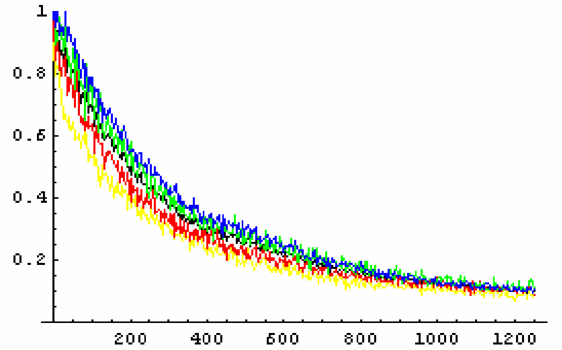

```
Show[LogListPlot[NorFluorescenceT, PlotJoined → True,
   PlotStyle → {RGBColor[0, 0, 0]}, DisplayFunction → Identity],
  LogListPlot[NorFluorescence1, PlotJoined → True,
   PlotStyle → {RGBColor[1, 1, 0]}, DisplayFunction → Identity],
  LogListPlot[NorFluorescence2, PlotJoined → True,
   PlotStyle → {RGBColor[1, 0, 0]}, DisplayFunction → Identity],
  LogListPlot[NorFluorescence3, PlotJoined → True,
   PlotStyle → {RGBColor[0, 1, 0]}, DisplayFunction → Identity],
  LogListPlot[NorFluorescence4, PlotJoined → True,
   PlotStyle → {RGBColor[0, 0, 1]}, DisplayFunction → Identity],
  DisplayFunction → $DisplayFunction];
```

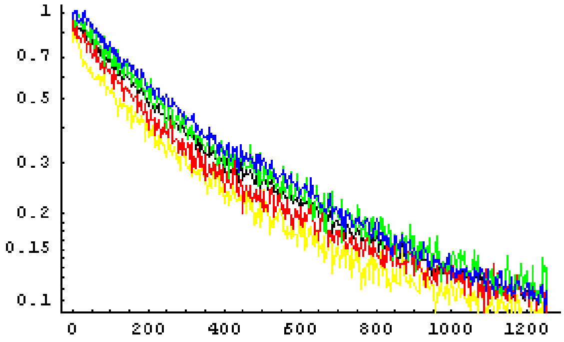

One Exponential

```
FitExp = NonlinearRegress[NorFluorescenceT, e^-R*t, t, {R, .001},
  MaxIterations → 200, Method → QuasiNewton,
  RegressionReport → {BestFitParameters, ParameterCITable, EstimatedVariance}]
```

```
{BestFitParameters → {R → 0.00275802}, ParameterCITable →
        Estimate      Asymptotic SE    CI
  R     0.00275802    0.0000319635     {0.00269515, 0.00282089}',
 EstimatedVariance → 0.00327566}
```

```
Show[LogListPlot[NorFluorescenceT, PlotJoined → True,
  DisplayFunction → Identity],
 LogPlot[e^-R*t /. (BestFitParameters /. FitExp),
  {t, 0, fliptime[[Length[fliptime]]]}, PlotStyle → {RGBColor[0, 0, 1]},
  DisplayFunction → Identity], DisplayFunction → $DisplayFunction]
```

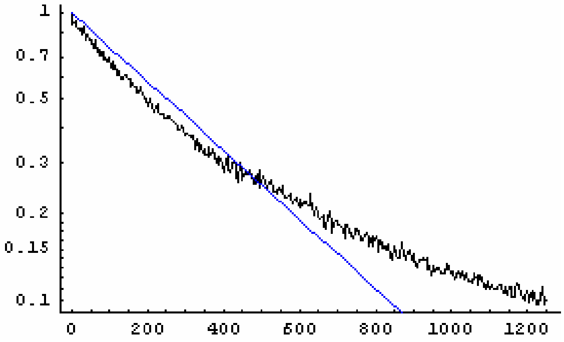

```
- Graphics -
```

Two Exponentials

```
FitTwoExp = NonlinearRegress[NorFluorescenceT, (p * e^-R1*t + (1 - p) * e^-R2*t),
  t, {{p, .4}, {R1, .001}, {R2, .01}}, MaxIterations → 200,
  Method → QuasiNewton,
  RegressionReport → {BestFitParameters, ParameterCITable, EstimatedVariance}]
{BestFitParameters → {p → 0.444345, R1 → 0.00126575, R2 → 0.0066812},
 ParameterCITable →
        Estimate       Asymptotic SE      CI
  p     0.444345       0.0130676          {0.418643, 0.470047}
  R1    0.00126575     0.0000341901       {0.00119851, 0.001333}  ,
  R2    0.0066812      0.000170872        {0.00634513, 0.00701728}

 EstimatedVariance → 0.000183952}
Show[LogListPlot[NorFluorescenceT, PlotJoined → True,
  DisplayFunction → Identity],
 LogPlot[(p * e^-R1*t + (1 - p) * e^-R2*t) /. (BestFitParameters /. FitTwoExp),
  {t, 0, fliptime[[Length[fliptime]]]}, PlotStyle → {RGBColor[0, 0, 1]},
  DisplayFunction → Identity], DisplayFunction → $DisplayFunction]
```

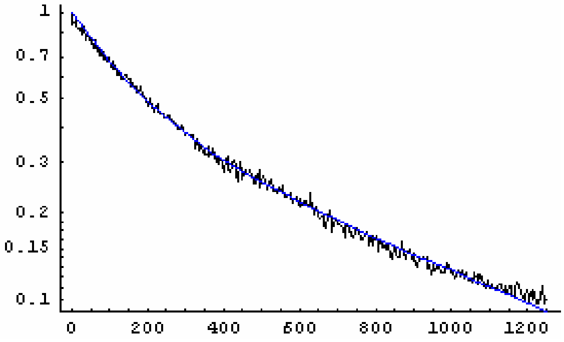

Appendix 4.D - Mathematica Notebook for FLIP simulations

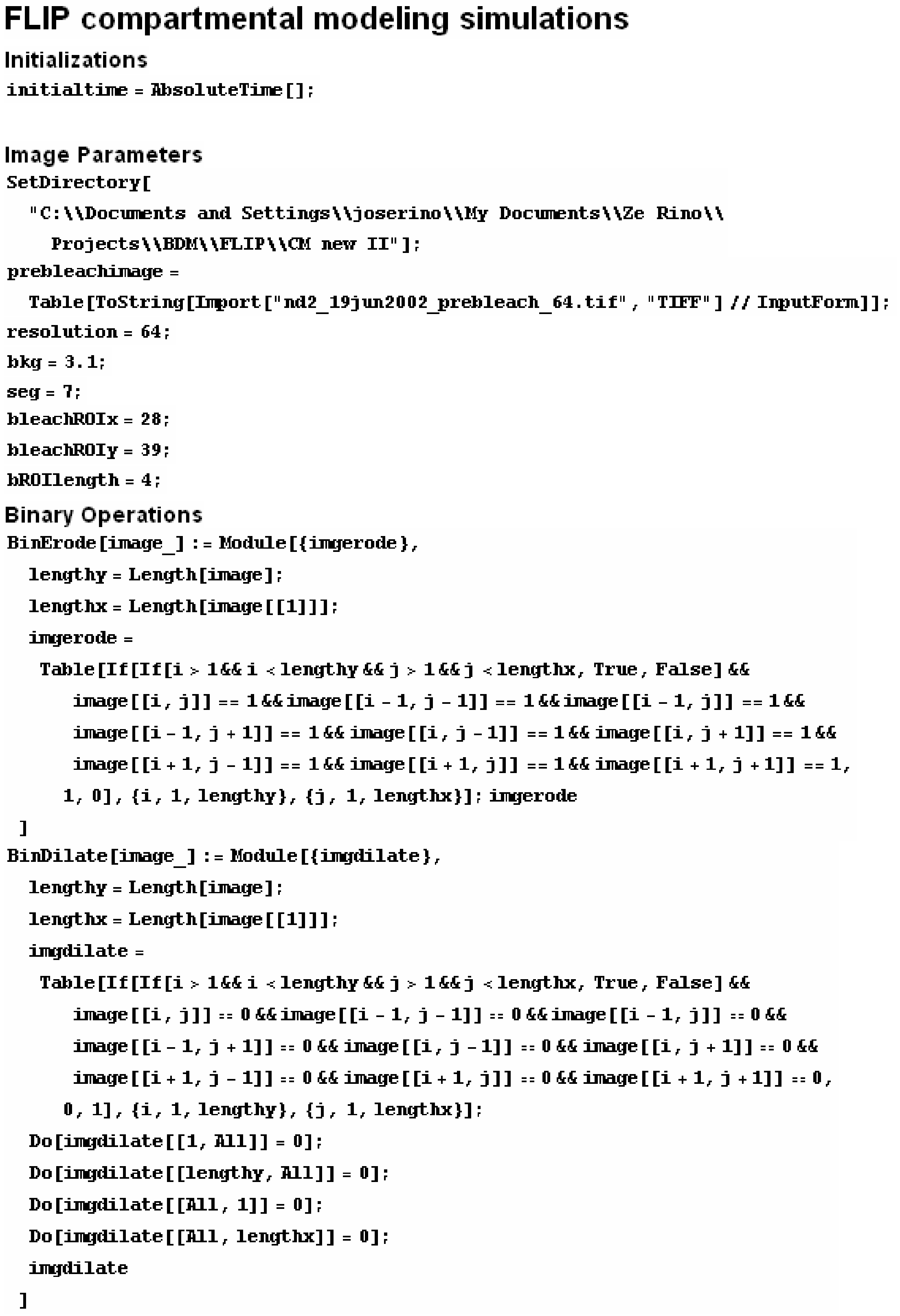

FLIP compartmental modeling simulations

Initializations

```
initialtime = AbsoluteTime[];
```

Image Parameters

```
SetDirectory[
  "C:\\Documents and Settings\\joserino\\My Documents\\Ze Rino\\
    Projects\\BDM\\FLIP\\CM new II"];
prebleachimage =
  Table[ToString[Import["nd2_19jun2002_prebleach_64.tif", "TIFF"] // InputForm]];
resolution = 64;
bkg = 3.1;
seg = 7;
bleachROIx = 28;
bleachROIy = 39;
bROIlength = 4;
```

Binary Operations

```
BinErode[image_] := Module[{imgerode},
  lengthy = Length[image];
  lengthx = Length[image[[1]]];
  imgerode =
   Table[If[If[i > 1&& i < lengthy && j > 1&& j < lengthx, True, False] &&
      image[[i, j]] == 1&& image[[i - 1, j - 1]] == 1&& image[[i - 1, j]] == 1&&
      image[[i - 1, j + 1]] == 1 && image[[i, j - 1]] == 1 && image[[i, j + 1]] == 1&&
      image[[i + 1, j - 1]] == 1 && image[[i + 1, j]] == 1 && image[[i + 1, j + 1]] == 1,
     1, 0], {i, 1, lengthy}, {j, 1, lengthx}]; imgerode
 ]
BinDilate[image_] := Module[{imgdilate},
  lengthy = Length[image];
  lengthx = Length[image[[1]]];
  imgdilate =
   Table[If[If[i > 1&& i < lengthy && j > 1&& j < lengthx, True, False] &&
      image[[i, j]] == 0 && image[[i - 1, j - 1]] == 0 && image[[i - 1, j]] == 0 &&
      image[[i - 1, j + 1]] == 0 && image[[i, j - 1]] == 0 && image[[i, j + 1]] == 0 &&
      image[[i + 1, j - 1]] == 0 && image[[i + 1, j]] == 0 && image[[i + 1, j + 1]] == 0,
     0, 1], {i, 1, lengthy}, {j, 1, lengthx}];
  Do[imgdilate[[1, All]] = 0];
  Do[imgdilate[[lengthy, All]] = 0];
  Do[imgdilate[[All, 1]] = 0];
  Do[imgdilate[[All, lengthx]] = 0];
  imgdilate
 ]
```

Image Conversion

```
prebleachimageconv =
  ToExpression[
    StringInsert[StringInsert[StringReplace[prebleachimage,
       {"Graphics[Raster[" → "",
        ", ColorFunction -> GrayLevel], ImageSize -> {64, 64},
           PlotRange -> {{0, 63}, {1, 64}}, AspectRatio -> Automatic]" → ""}],
      "{", 1], "}", -1]][[1]];
```

Bleach ROIs Definition

```
bROIx = bleachROIx;
bROIy = resolution - bleachROIy;
bROIimageseg = Table[0, {i, 1, resolution}, {j, 1, resolution},
   {k , 1, bROIlength}];
Do[Do[If[Ceiling[√((i - bROIy)^2 + (j - bROIx)^2)] == k, bROIimageseg[[i, j, k]] = 1, 0],
  {i, bROIy - bROIlength, bROIy + bROIlength},
  {j, bROIx - bROIlength, bROIx + bROIlength}], {k, 1, bROIlength}]
bROIimageseg[[bROIy, bROIx, 1]] = 1;
```

Image ROIs

```
prebleachimageback = 1/2 (Abs[prebleachimageconv - bkg] + prebleachimageconv - bkg);
imageseg =
  Table[Which[prebleachimageback[[i, j]] < seg, 0,
    prebleachimageback[[i, j]] ≥ seg, 1], {i, 1, resolution}, {j, 1, resolution}];
Show[Graphics[Raster[prebleachimageback, {{0, 0}, {resolution, resolution}},
   {0, 30}, ColorFunction → GrayLevel], AspectRatio → Automatic],
 ImageSize → 256, DisplayFunction → $DisplayFunction]
imageseg = BinDilate[BinErode[BinErode[BinDilate[imageseg]]]];
Show[Graphics[Raster[imageseg, {{0, 0}, {resolution, resolution}},
   {0, 1}, ColorFunction → GrayLevel], AspectRatio → Automatic],
 ImageSize → 256, DisplayFunction → $DisplayFunction]
```

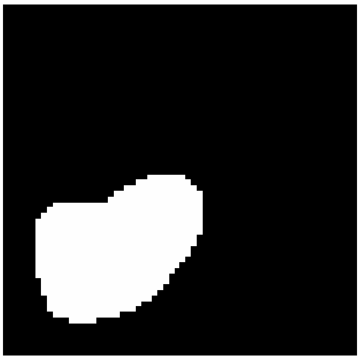

```
Show[
 Graphics[Raster[bROIimageseg[[All, All, 2]], {{0, 0}, {resolution, resolution}},
   {0, 1}, ColorFunction → GrayLevel], AspectRatio → Automatic],
 ImageSize → 256, DisplayFunction → $DisplayFunction]
bROItotal = Sum[bROIimageseg[[All, All, k]], {k, 1, bROIlength}];
mROIimagesegT = imageseg - bROItotal;
Show[Graphics[Raster[mROIimagesegT, {{0, 0}, {resolution, resolution}},
   {0, 1}, ColorFunction → GrayLevel], AspectRatio → Automatic],
 ImageSize → 256, DisplayFunction → $DisplayFunction]
```

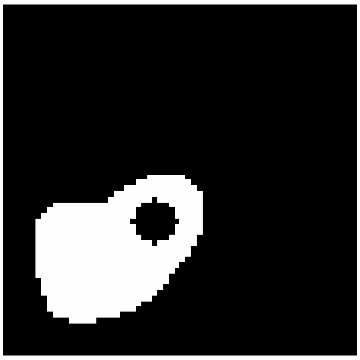

```
- Graphics -
```

FLIP Parameters

```
TFLIP = 3.64;
ATbleach = .279;
               ⎛.1668⎞
bROIRatios =   ⎜.3309⎟;
               ⎜.8779⎟
               ⎝.9702⎠
                                        Log[           1           ]
                                                bROIRatios[[k,1]]
RateConstantBleach[k_] := Table[ ───────────────────────────── ];
                                             ATbleach
                         ⎛0.088⎞
DiffusionCoefficients =  ⎝ 2.76⎠;
```

Compartmental Model Equations

```
Kbleach[t_, TFLIP_, ATbleach_, k_] =
  If[Mod[t, TFLIP] < ATbleach, RateConstantBleach[k], 0];
NROI = Length[Position[imageseg, 1]];
rowmin = Min[Table[Position[imageseg, 1][[i, 1]], {i, 1, NROI}]];
rowmax = Max[Table[Position[imageseg, 1][[i, 1]], {i, 1, NROI}]];
colmin = Min[Table[Position[imageseg, 1][[i, 2]], {i, 1, NROI}]];
colmax = Max[Table[Position[imageseg, 1][[i, 2]], {i, 1, NROI}]];
rowlength = rowmax - rowmin;
collength = colmax - colmin;
cellroi = Table[imageseg[[i, j]], {i, rowmin - 1, rowmax + 1},
   {j, colmin - 1, colmax + 1}];
bleachroi = Table[bROIimageseg[[i, j, k]], {i, rowmin - 1, rowmax + 1},
   {j, colmin - 1, colmax + 1}, {k, 1, bROIlength}];
measureroiT = Table[mROIimagesegT[[i, j]], {i, rowmin - 1, rowmax + 1},
   {j, colmin - 1, colmax + 1}];
sstate = Table[prebleachimageback[[i, j]], {i, rowmin - 1, rowmax + 1},
   {j, colmin - 1, colmax + 1}];
init = Table[prebleachimageback[[i, j]], {i, rowmin - 1, rowmax + 1},
   {j, colmin - 1, colmax + 1}];
Show[Graphics[Raster[measureroiT, {{0, 0}, {rowlength + 3, collength + 3}},
   {0, 1}, ColorFunction → GrayLevel]], ImageSize → 256,
 DisplayFunction → $DisplayFunction]
```

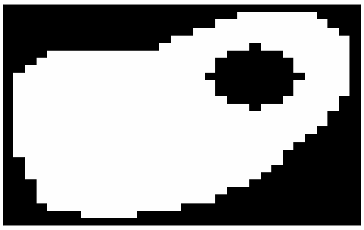

```
- Graphics -
```

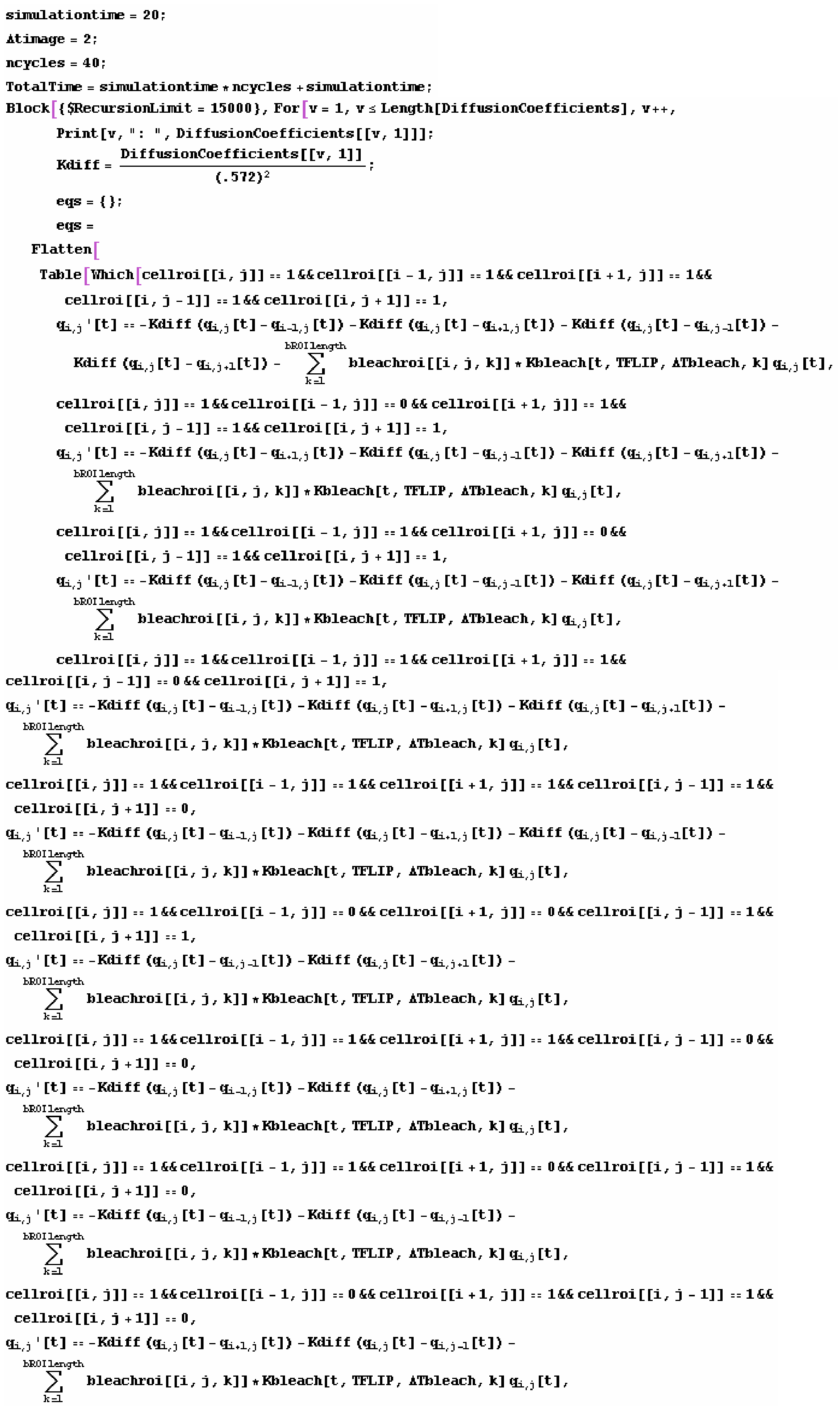

```
simulationtime = 20;
Δtimage = 2;
ncycles = 40;
TotalTime = simulationtime * ncycles + simulationtime;
Block[{$RecursionLimit = 15000}, For[v = 1, v ≤ Length[DiffusionCoefficients], v++,
      Print[v, ": ", DiffusionCoefficients[[v, 1]]];
      Kdiff = DiffusionCoefficients[[v, 1]] / (.572)^2;
      eqs = {};
      eqs =
    Flatten[
     Table[Which[cellroi[[i, j]] == 1 && cellroi[[i - 1, j]] == 1 && cellroi[[i + 1, j]] == 1 &&
        cellroi[[i, j - 1]] == 1 && cellroi[[i, j + 1]] == 1,
      q_{i,j}'[t] == -Kdiff (q_{i,j}[t] - q_{i-1,j}[t]) - Kdiff (q_{i,j}[t] - q_{i+1,j}[t]) - Kdiff (q_{i,j}[t] - q_{i,j-1}[t]) -
        Kdiff (q_{i,j}[t] - q_{i,j+1}[t]) - Sum_{k=1}^{bROIlength} bleachroi[[i, j, k]] * Kbleach[t, TFLIP, ΔTbleach, k] q_{i,j}[t],
      cellroi[[i, j]] == 1 && cellroi[[i - 1, j]] == 0 && cellroi[[i + 1, j]] == 1 &&
       cellroi[[i, j - 1]] == 1 && cellroi[[i, j + 1]] == 1,
      q_{i,j}'[t] == -Kdiff (q_{i,j}[t] - q_{i+1,j}[t]) - Kdiff (q_{i,j}[t] - q_{i,j-1}[t]) - Kdiff (q_{i,j}[t] - q_{i,j+1}[t]) -
        Sum_{k=1}^{bROIlength} bleachroi[[i, j, k]] * Kbleach[t, TFLIP, ΔTbleach, k] q_{i,j}[t],
      cellroi[[i, j]] == 1 && cellroi[[i - 1, j]] == 1 && cellroi[[i + 1, j]] == 0 &&
       cellroi[[i, j - 1]] == 1 && cellroi[[i, j + 1]] == 1,
      q_{i,j}'[t] == -Kdiff (q_{i,j}[t] - q_{i-1,j}[t]) - Kdiff (q_{i,j}[t] - q_{i,j-1}[t]) - Kdiff (q_{i,j}[t] - q_{i,j+1}[t]) -
        Sum_{k=1}^{bROIlength} bleachroi[[i, j, k]] * Kbleach[t, TFLIP, ΔTbleach, k] q_{i,j}[t],
      cellroi[[i, j]] == 1 && cellroi[[i - 1, j]] == 1 && cellroi[[i + 1, j]] == 1 &&
cellroi[[i, j - 1]] == 0 && cellroi[[i, j + 1]] == 1,
q_{i,j}'[t] == -Kdiff (q_{i,j}[t] - q_{i-1,j}[t]) - Kdiff (q_{i,j}[t] - q_{i+1,j}[t]) - Kdiff (q_{i,j}[t] - q_{i,j+1}[t]) -
  Sum_{k=1}^{bROIlength} bleachroi[[i, j, k]] * Kbleach[t, TFLIP, ΔTbleach, k] q_{i,j}[t],
cellroi[[i, j]] == 1 && cellroi[[i - 1, j]] == 1 && cellroi[[i + 1, j]] == 1 && cellroi[[i, j - 1]] == 1 &&
 cellroi[[i, j + 1]] == 0,
q_{i,j}'[t] == -Kdiff (q_{i,j}[t] - q_{i-1,j}[t]) - Kdiff (q_{i,j}[t] - q_{i+1,j}[t]) - Kdiff (q_{i,j}[t] - q_{i,j-1}[t]) -
  Sum_{k=1}^{bROIlength} bleachroi[[i, j, k]] * Kbleach[t, TFLIP, ΔTbleach, k] q_{i,j}[t],
cellroi[[i, j]] == 1 && cellroi[[i - 1, j]] == 0 && cellroi[[i + 1, j]] == 0 && cellroi[[i, j - 1]] == 1 &&
 cellroi[[i, j + 1]] == 1,
q_{i,j}'[t] == -Kdiff (q_{i,j}[t] - q_{i,j-1}[t]) - Kdiff (q_{i,j}[t] - q_{i,j+1}[t]) -
  Sum_{k=1}^{bROIlength} bleachroi[[i, j, k]] * Kbleach[t, TFLIP, ΔTbleach, k] q_{i,j}[t],
cellroi[[i, j]] == 1 && cellroi[[i - 1, j]] == 1 && cellroi[[i + 1, j]] == 1 && cellroi[[i, j - 1]] == 0 &&
 cellroi[[i, j + 1]] == 0,
q_{i,j}'[t] == -Kdiff (q_{i,j}[t] - q_{i-1,j}[t]) - Kdiff (q_{i,j}[t] - q_{i+1,j}[t]) -
  Sum_{k=1}^{bROIlength} bleachroi[[i, j, k]] * Kbleach[t, TFLIP, ΔTbleach, k] q_{i,j}[t],
cellroi[[i, j]] == 1 && cellroi[[i - 1, j]] == 1 && cellroi[[i + 1, j]] == 0 && cellroi[[i, j - 1]] == 1 &&
 cellroi[[i, j + 1]] == 0,
q_{i,j}'[t] == -Kdiff (q_{i,j}[t] - q_{i-1,j}[t]) - Kdiff (q_{i,j}[t] - q_{i,j-1}[t]) -
  Sum_{k=1}^{bROIlength} bleachroi[[i, j, k]] * Kbleach[t, TFLIP, ΔTbleach, k] q_{i,j}[t],
cellroi[[i, j]] == 1 && cellroi[[i - 1, j]] == 0 && cellroi[[i + 1, j]] == 1 && cellroi[[i, j - 1]] == 1 &&
 cellroi[[i, j + 1]] == 0,
q_{i,j}'[t] == -Kdiff (q_{i,j}[t] - q_{i+1,j}[t]) - Kdiff (q_{i,j}[t] - q_{i,j-1}[t]) -
  Sum_{k=1}^{bROIlength} bleachroi[[i, j, k]] * Kbleach[t, TFLIP, ΔTbleach, k] q_{i,j}[t],
```

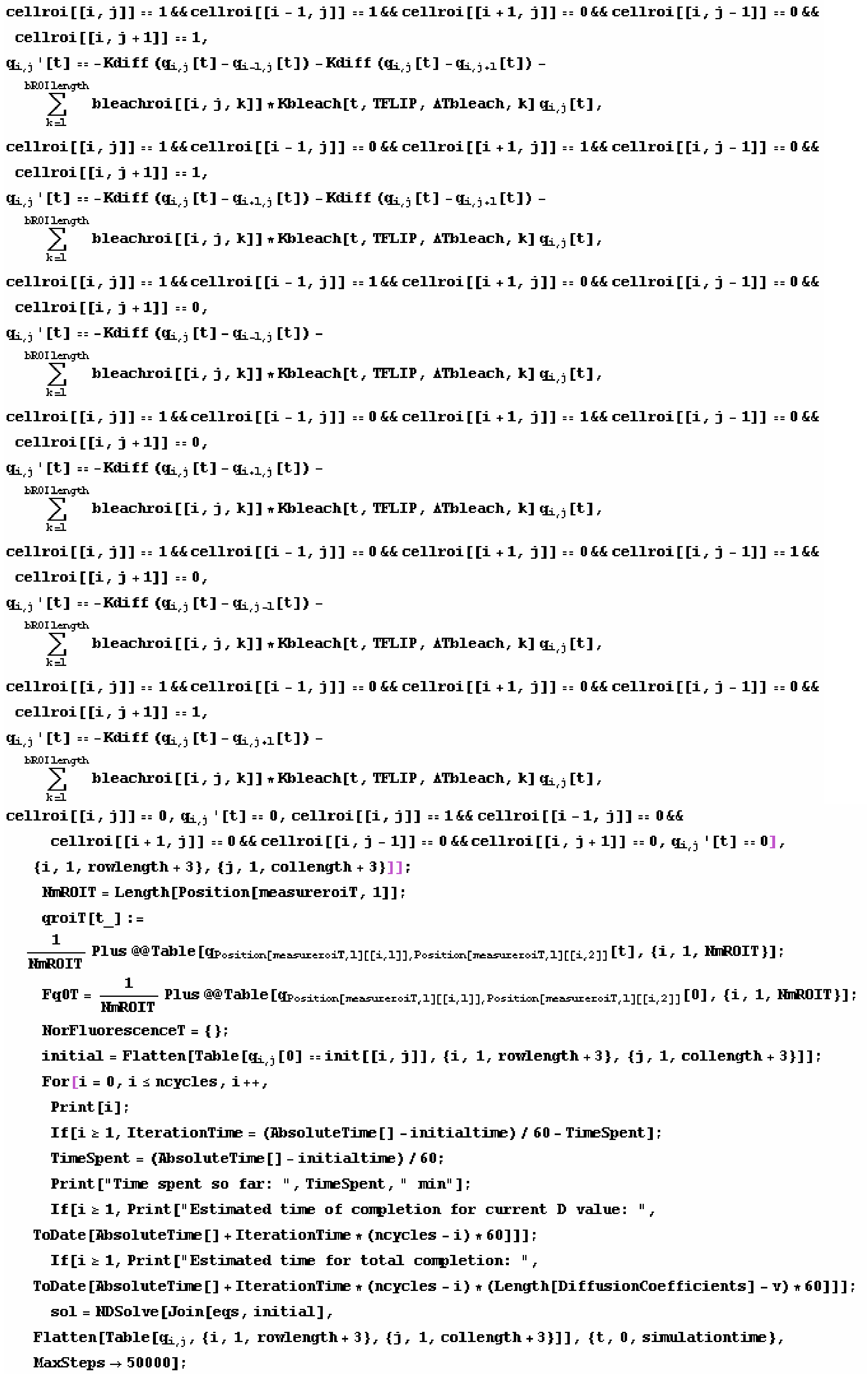

```
cellroi[[i, j]] == 1 && cellroi[[i - 1, j]] == 1 && cellroi[[i + 1, j]] == 0 && cellroi[[i, j - 1]] == 0 &&
 cellroi[[i, j + 1]] == 1,
q_{i,j}'[t] == -Kdiff (q_{i,j}[t] - q_{i-1,j}[t]) - Kdiff (q_{i,j}[t] - q_{i,j+1}[t]) -
  bROIlength
     Σ      bleachroi[[i, j, k]] * Kbleach[t, TFLIP, ΔTbleach, k] q_{i,j}[t],
    k=1
cellroi[[i, j]] == 1 && cellroi[[i - 1, j]] == 0 && cellroi[[i + 1, j]] == 1 && cellroi[[i, j - 1]] == 0 &&
 cellroi[[i, j + 1]] == 1,
q_{i,j}'[t] == -Kdiff (q_{i,j}[t] - q_{i+1,j}[t]) - Kdiff (q_{i,j}[t] - q_{i,j+1}[t]) -
  bROIlength
     Σ      bleachroi[[i, j, k]] * Kbleach[t, TFLIP, ΔTbleach, k] q_{i,j}[t],
    k=1
cellroi[[i, j]] == 1 && cellroi[[i - 1, j]] == 1 && cellroi[[i + 1, j]] == 0 && cellroi[[i, j - 1]] == 0 &&
 cellroi[[i, j + 1]] == 0,
q_{i,j}'[t] == -Kdiff (q_{i,j}[t] - q_{i-1,j}[t]) -
  bROIlength
     Σ      bleachroi[[i, j, k]] * Kbleach[t, TFLIP, ΔTbleach, k] q_{i,j}[t],
    k=1
cellroi[[i, j]] == 1 && cellroi[[i - 1, j]] == 0 && cellroi[[i + 1, j]] == 1 && cellroi[[i, j - 1]] == 0 &&
 cellroi[[i, j + 1]] == 0,
q_{i,j}'[t] == -Kdiff (q_{i,j}[t] - q_{i+1,j}[t]) -
  bROIlength
     Σ      bleachroi[[i, j, k]] * Kbleach[t, TFLIP, ΔTbleach, k] q_{i,j}[t],
    k=1
cellroi[[i, j]] == 1 && cellroi[[i - 1, j]] == 0 && cellroi[[i + 1, j]] == 0 && cellroi[[i, j - 1]] == 1 &&
 cellroi[[i, j + 1]] == 0,
q_{i,j}'[t] == -Kdiff (q_{i,j}[t] - q_{i,j-1}[t]) -
  bROIlength
     Σ      bleachroi[[i, j, k]] * Kbleach[t, TFLIP, ΔTbleach, k] q_{i,j}[t],
    k=1
cellroi[[i, j]] == 1 && cellroi[[i - 1, j]] == 0 && cellroi[[i + 1, j]] == 0 && cellroi[[i, j - 1]] == 0 &&
 cellroi[[i, j + 1]] == 1,
q_{i,j}'[t] == -Kdiff (q_{i,j}[t] - q_{i,j+1}[t]) -
  bROIlength
     Σ      bleachroi[[i, j, k]] * Kbleach[t, TFLIP, ΔTbleach, k] q_{i,j}[t],
    k=1
cellroi[[i, j]] == 0, q_{i,j}'[t] == 0, cellroi[[i, j]] == 1 && cellroi[[i - 1, j]] == 0 &&
     cellroi[[i + 1, j]] == 0 && cellroi[[i, j - 1]] == 0 && cellroi[[i, j + 1]] == 0, q_{i,j}'[t] == 0],
   {i, 1, rowlength + 3}, {j, 1, collength + 3}]];
    NmROIT = Length[Position[measureroiT, 1]];
    qroiT[t_] :=
     1
  ------ Plus @@ Table[q_{Position[measureroiT,1][[i,1]],Position[measureroiT,1][[i,2]]}[t], {i, 1, NmROIT}];
  NmROIT
                1
    Fq0T = -------- Plus @@ Table[q_{Position[measureroiT,1][[i,1]],Position[measureroiT,1][[i,2]]}[0], {i, 1, NmROIT}];
            NmROIT
    NorFluorescenceT = {};
    initial = Flatten[Table[q_{i,j}[0] == init[[i, j]], {i, 1, rowlength + 3}, {j, 1, collength + 3}]];
    For[i = 0, i ≤ ncycles, i++,
     Print[i];
     If[i ≥ 1, IterationTime = (AbsoluteTime[] - initialtime) / 60 - TimeSpent];
     TimeSpent = (AbsoluteTime[] - initialtime) / 60;
     Print["Time spent so far: ", TimeSpent, " min"];
     If[i ≥ 1, Print["Estimated time of completion for current D value: ",
   ToDate[AbsoluteTime[] + IterationTime * (ncycles - i) * 60]]];
     If[i ≥ 1, Print["Estimated time for total completion: ",
   ToDate[AbsoluteTime[] + IterationTime * (ncycles - i) * (Length[DiffusionCoefficients] - v) * 60]]];
     sol = NDSolve[Join[eqs, initial],
   Flatten[Table[q_{i,j}, {i, 1, rowlength + 3}, {j, 1, collength + 3}]], {t, 0, simulationtime},
   MaxSteps → 50000];
```

```
If[i == 0, initFluorescenceT = (Fq0T /. sol)[[1]]];
        If[i == 0,
          NorFluorescenceT = Join[NorFluorescenceT,
        Table[{t, (groiT[t] /. sol)/initFluorescenceT [[1]]}, {t, 0, simulationtime, Δtimage}]],
          NorFluorescenceT = Join[NorFluorescenceT,
        Table[{t + i * simulationtime, (groiT[t] /. sol)/initFluorescenceT [[1]]},
         {t, Δtimage, simulationtime, Δtimage}]]];
        initial = Flatten[Table[q_{i,j}[0] == Evaluate[q_{i,j}[simulationtime] /. sol][[1]],
        {i, 1, rowlength + 3}, {j, 1, collength + 3}]];
    ];
  starttime = 30;
  initialtimeindex = {};
  Do[If[NorFluorescenceT[[i, 1]] ≥ starttime, initialtimeindex = Append[initialtimeindex, i]],
    {i, 1, Length[NorFluorescenceT]}];
  NorFluorescenceT = Drop[NorFluorescenceT, initialtimeindex[[1]] - 1];
  Do[NorFluorescenceT[[i, 1]] = NorFluorescenceT[[i, 1]] - NorFluorescenceT[[1, 1]],
    {i, 2, Length[NorFluorescenceT]}];
  Do[NorFluorescenceT[[i, 2]] = NorFluorescenceT[[i, 2]] / NorFluorescenceT[[1, 2]],
    {i, 2, Length[NorFluorescenceT]}];
  NorFluorescenceT[[1, 1]] = 0;
  NorFluorescenceT[[1, 2]] = 1;
  FitExp = NonlinearRegress[NorFluorescenceT, ⅇ^(-R*t), t, {R, .001}, MaxIterations → 200,
      Method → QuasiNewton,
      RegressionReport → {BestFitParameters, ParameterCITable, EstimatedVariance}];
  Print[DiffusionCoefficients[[v, 1]], " -> ", R /. (BestFitParameters /. FitExp)];
  Show[LogListPlot[NorFluorescenceT, PlotJoined → True, DisplayFunction → Identity],
   LogPlot[ⅇ^(-R*t) /. (BestFitParameters /. FitExp), {t, 0, TotalTime}, PlotStyle → {RGBColor[0, 0, 1]},
    DisplayFunction → Identity], DisplayFunction → $DisplayFunction]]]
```

```
0.088 -> 0.00125958
```

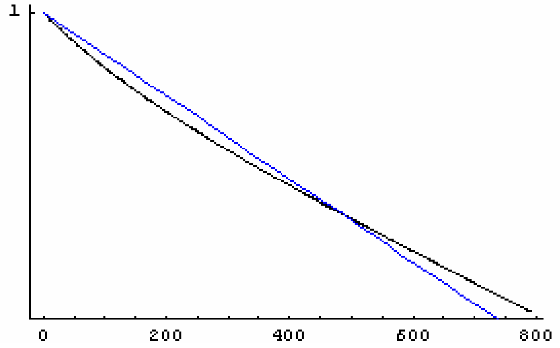

```
2.76 -> 0.00668574
```

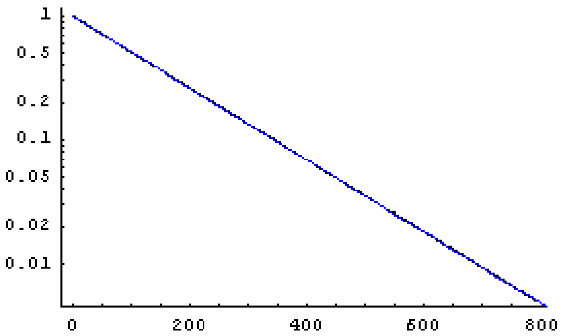

```
TimeSpent = (AbsoluteTime[] - initialtime) / 60
112.411979167
```

Appendix 4.E – Berkeley Madonna code for FLIP simulations

```
METHOD RK4

STARTTIME = 0
STOPTIME=700.0
DT = 0.125

rows = 33
columns = 44

d/dt (qF[2..rows-1,2..columns-1]) = IF (cellroi[i,j]=1 AND cellroi[i-1,j]=1 AND cellroi[i+1,j]=1 AND
cellroi[i,j-1]=1 AND cellroi[i,j+1]=1)
THEN -KdiffF*0.5*(sstateF[i,j]+sstateF[i-1,j])*(qF[i,j]/sstateF[i,j]-qF[i-1,j]/sstateF[i-1,j])-
KdiffF*0.5*(sstateF[i,j]+sstateF[i+1,j])*(qF[i,j]/sstateF[i,j]-qF[i+1,j]/sstateF[i+1,j])-
KdiffF*0.5*(sstateF[i,j]+sstateF[i,j-1])*(qF[i,j]/sstateF[i,j]-qF[i,j-1]/sstateF[i,j-1])-
KdiffF*0.5*(sstateF[i,j]+sstateF[i,j+1])*(qF[i,j]/sstateF[i,j]-qF[i,j+1]/sstateF[i,j+1])-
Kbleach1*(bleach1[i,j]*qF[i,j])-Kbleach2*(bleach2[i,j]*qF[i,j])-Kbleach3*(bleach3[i,j]*qF[i,j])-
Kbleach4*(bleach4[i,j]*qF[i,j])

ELSE IF (cellroi[i,j]=1 AND cellroi[i-1,j]=0 AND cellroi[i+1,j]=1 AND cellroi[i,j-1]=1 AND
cellroi[i,j+1]=1)
THEN -KdiffF*0.5*(sstateF[i,j]+sstateF[i+1,j])*(qF[i,j]/sstateF[i,j]-qF[i+1,j]/sstateF[i+1,j])-
KdiffF*0.5*(sstateF[i,j]+sstateF[i,j-1])*(qF[i,j]/sstateF[i,j]-qF[i,j-1]/sstateF[i,j-1])-
KdiffF*0.5*(sstateF[i,j]+sstateF[i,j+1])*(qF[i,j]/sstateF[i,j]-qF[i,j+1]/sstateF[i,j+1])-
Kbleach1*(bleach1[i,j])*qF[i,j]-Kbleach2*(bleach2[i,j])*qF[i,j]-Kbleach3*(bleach3[i,j])*qF[i,j]-
Kbleach4*(bleach4[i,j]*qF[i,j])

ELSE IF (cellroi[i,j]=1 AND cellroi[i-1,j]=1 AND cellroi[i+1,j]=0 AND cellroi[i,j-1]=1 AND
cellroi[i,j+1]=1)
THEN -KdiffF*0.5*(sstateF[i,j]+sstateF[i-1,j])*(qF[i,j]/sstateF[i,j]-qF[i-1,j]/sstateF[i-1,j])-
KdiffF*0.5*(sstateF[i,j]+sstateF[i,j-1])*(qF[i,j]/sstateF[i,j]-qF[i,j-1]/sstateF[i,j-1])-
KdiffF*0.5*(sstateF[i,j]+sstateF[i,j+1])*(qF[i,j]/sstateF[i,j]-qF[i,j+1]/sstateF[i,j+1])-
Kbleach1*(bleach1[i,j])*qF[i,j]-Kbleach2*(bleach2[i,j])*qF[i,j]-Kbleach3*(bleach3[i,j])*qF[i,j]-
Kbleach4*(bleach4[i,j]*qF[i,j])

ELSE IF (cellroi[i,j]=1 AND cellroi[i-1,j]=1 AND cellroi[i+1,j]=1 AND cellroi[i,j-1]=0 AND
cellroi[i,j+1]=1)
THEN -KdiffF*0.5*(sstateF[i,j]+sstateF[i-1,j])*(qF[i,j]/sstateF[i,j]-qF[i-1,j]/sstateF[i-1,j])-
KdiffF*0.5*(sstateF[i,j]+sstateF[i+1,j])*(qF[i,j]/sstateF[i,j]-qF[i+1,j]/sstateF[i+1,j])-
KdiffF*0.5*(sstateF[i,j]+sstateF[i,j+1])*(qF[i,j]/sstateF[i,j]-qF[i,j+1]/sstateF[i,j+1])-
Kbleach1*(bleach1[i,j])*qF[i,j]-Kbleach2*(bleach2[i,j])*qF[i,j]-Kbleach3*(bleach3[i,j])*qF[i,j]-
Kbleach4*(bleach4[i,j]*qF[i,j])

ELSE IF (cellroi[i,j]=1 AND cellroi[i-1,j]=1 AND cellroi[i+1,j]=1 AND cellroi[i,j-1]=1 AND
cellroi[i,j+1]=0)
THEN -KdiffF*0.5*(sstateF[i,j]+sstateF[i-1,j])*(qF[i,j]/sstateF[i,j]-qF[i-1,j]/sstateF[i-1,j])-
KdiffF*0.5*(sstateF[i,j]+sstateF[i+1,j])*(qF[i,j]/sstateF[i,j]-qF[i+1,j]/sstateF[i+1,j])-
KdiffF*0.5*(sstateF[i,j]+sstateF[i,j-1])*(qF[i,j]/sstateF[i,j]-qF[i,j-1]/sstateF[i,j-1])-
Kbleach1*(bleach1[i,j])*qF[i,j]-Kbleach2*(bleach2[i,j])*qF[i,j]-Kbleach3*(bleach3[i,j])*qF[i,j]-
Kbleach4*(bleach4[i,j]*qF[i,j])

ELSE IF (cellroi[i,j]=1 AND cellroi[i-1,j]=0 AND cellroi[i+1,j]=1 AND cellroi[i,j-1]=0 AND
cellroi[i,j+1]=1)
THEN -KdiffF*0.5*(sstateF[i,j]+sstateF[i+1,j])*(qF[i,j]/sstateF[i,j]-qF[i+1,j]/sstateF[i+1,j])-
KdiffF*0.5*(sstateF[i,j]+sstateF[i,j+1])*(qF[i,j]/sstateF[i,j]-qF[i,j+1]/sstateF[i,j+1])-
Kbleach1*(bleach1[i,j])*qF[i,j]-Kbleach2*(bleach2[i,j])*qF[i,j]-Kbleach3*(bleach3[i,j])*qF[i,j]-
Kbleach4*(bleach4[i,j]*qF[i,j])
```

```
ELSE IF (cellroi[i,j]=1 AND cellroi[i-1,j]=0 AND cellroi[i+1,j]=1 AND cellroi[i,j-1]=1 AND
cellroi[i,j+1]=0)
THEN -KdiffF*0.5*(sstateF[i,j]+sstateF[i+1,j])*(qF[i,j]/sstateF[i,j]-qF[i+1,j]/sstateF[i+1,j])-
KdiffF*0.5*(sstateF[i,j]+sstateF[i,j-1])*(qF[i,j]/sstateF[i,j]-qF[i,j-1]/sstateF[i,j-1])-
Kbleach1*(bleach1[i,j])*qF[i,j]-Kbleach2*(bleach2[i,j])*qF[i,j]-Kbleach3*(bleach3[i,j])*qF[i,j]-
Kbleach4*(bleach4[i,j]*qF[i,j])

ELSE IF (cellroi[i,j]=1 AND cellroi[i-1,j]=1 AND cellroi[i+1,j]=0 AND cellroi[i,j-1]=1 AND
cellroi[i,j+1]=0)
THEN -KdiffF*0.5*(sstateF[i,j]+sstateF[i-1,j])*(qF[i,j]/sstateF[i,j]-qF[i-1,j]/sstateF[i-1,j])-
KdiffF*0.5*(sstateF[i,j]+sstateF[i,j-1])*(qF[i,j]/sstateF[i,j]-qF[i,j-1]/sstateF[i,j-1])-
Kbleach1*(bleach1[i,j])*qF[i,j]-Kbleach2*(bleach2[i,j])*qF[i,j]-Kbleach3*(bleach3[i,j])*qF[i,j]-
Kbleach4*(bleach4[i,j]*qF[i,j])

ELSE IF (cellroi[i,j]=1 AND cellroi[i-1,j]=1 AND cellroi[i+1,j]=0 AND cellroi[i,j-1]=0 AND
cellroi[i,j+1]=1)
THEN -KdiffF*0.5*(sstateF[i,j]+sstateF[i-1,j])*(qF[i,j]/sstateF[i,j]-qF[i-1,j]/sstateF[i-1,j])-
KdiffF*0.5*(sstateF[i,j]+sstateF[i,j+1])*(qF[i,j]/sstateF[i,j]-qF[i,j+1]/sstateF[i,j+1])-
Kbleach1*(bleach1[i,j])*qF[i,j]-Kbleach2*(bleach2[i,j])*qF[i,j]-Kbleach3*(bleach3[i,j])*qF[i,j]-
Kbleach4*(bleach4[i,j]*qF[i,j])

ELSE IF (cellroi[i,j]=1 AND cellroi[i-1,j]=1 AND cellroi[i+1,j]=1 AND cellroi[i,j-1]=0 AND
cellroi[i,j+1]=0)
THEN -KdiffF*0.5*(sstateF[i,j]+sstateF[i-1,j])*(qF[i,j]/sstateF[i,j]-qF[i-1,j]/sstateF[i-1,j])-
KdiffF*0.5*(sstateF[i,j]+sstateF[i+1,j])*(qF[i,j]/sstateF[i,j]-qF[i+1,j]/sstateF[i+1,j])-
Kbleach1*(bleach1[i,j])*qF[i,j]-Kbleach2*(bleach2[i,j])*qF[i,j]-Kbleach3*(bleach3[i,j])*qF[i,j]-
Kbleach4*(bleach4[i,j]*qF[i,j])

ELSE IF (cellroi[i,j]=1 AND cellroi[i-1,j]=0 AND cellroi[i+1,j]=0 AND cellroi[i,j-1]=1 AND
cellroi[i,j+1]=1)
THEN -KdiffF*0.5*(sstateF[i,j]+sstateF[i,j-1])*(qF[i,j]/sstateF[i,j]-qF[i,j-1]/sstateF[i,j-1])-
KdiffF*0.5*(sstateF[i,j]+sstateF[i,j+1])*(qF[i,j]/sstateF[i,j]-qF[i,j+1]/sstateF[i,j+1])-
Kbleach1*(bleach1[i,j])*qF[i,j]-Kbleach2*(bleach2[i,j])*qF[i,j]-Kbleach3*(bleach3[i,j])*qF[i,j]-
Kbleach4*(bleach4[i,j]*qF[i,j])

ELSE IF (cellroi[i,j]=1 AND cellroi[i-1,j]=1 AND cellroi[i+1,j]=0 AND cellroi[i,j-1]=0 AND
cellroi[i,j+1]=0)
THEN -KdiffF*0.5*(sstateF[i,j]+sstateF[i-1,j])*(qF[i,j]/sstateF[i,j]-qF[i-1,j]/sstateF[i-1,j])-
Kbleach1*(bleach1[i,j])*qF[i,j]-Kbleach2*(bleach2[i,j])*qF[i,j]-Kbleach3*(bleach3[i,j])*qF[i,j]-
Kbleach4*(bleach4[i,j]*qF[i,j])

ELSE IF (cellroi[i,j]=1 AND cellroi[i-1,j]=0 AND cellroi[i+1,j]=1 AND cellroi[i,j-1]=0 AND
cellroi[i,j+1]=0)
THEN -KdiffF*0.5*(sstateF[i,j]+sstateF[i+1,j])*(qF[i,j]/sstateF[i,j]-qF[i+1,j]/sstateF[i+1,j])-
Kbleach1*(bleach1[i,j])*qF[i,j]-Kbleach2*(bleach2[i,j])*qF[i,j]-Kbleach3*(bleach3[i,j])*qF[i,j]-
Kbleach4*(bleach4[i,j]*qF[i,j])

ELSE IF (cellroi[i,j]=1 AND cellroi[i-1,j]=0 AND cellroi[i+1,j]=0 AND cellroi[i,j-1]=1 AND
cellroi[i,j+1]=0)
THEN -KdiffF*0.5*(sstateF[i,j]+sstateF[i,j-1])*(qF[i,j]/sstateF[i,j]-qF[i,j-1]/sstateF[i,j-1])-
Kbleach1*(bleach1[i,j])*qF[i,j]-Kbleach2*(bleach2[i,j])*qF[i,j]-Kbleach3*(bleach3[i,j])*qF[i,j]-
Kbleach4*(bleach4[i,j]*qF[i,j])

ELSE IF (cellroi[i,j]=1 AND cellroi[i-1,j]=0 AND cellroi[i+1,j]=0 AND cellroi[i,j-1]=0 AND
cellroi[i,j+1]=1)
THEN -KdiffF*0.5*(sstateF[i,j]+sstateF[i,j+1])*(qF[i,j]/sstateF[i,j]-qF[i,j+1]/sstateF[i,j+1])-
Kbleach1*(bleach1[i,j])*qF[i,j]-Kbleach2*(bleach2[i,j])*qF[i,j]-Kbleach3*(bleach3[i,j])*qF[i,j]-
Kbleach4*(bleach4[i,j]*qF[i,j])

ELSE 0

d/dt (qF[1,1..columns]) = 0
d/dt (qF[1..rows,1]) = 0
```

```
d/dt (qF[rows,1..columns]) = 0
d/dt (qF[1..rows,columns]) = 0

d/dt (qC[2..rows-1,2..columns-1]) = IF (cellroi[i,j]=1 AND cellroi[i-1,j]=1 AND cellroi[i+1,j]=1 AND
cellroi[i,j-1]=1 AND cellroi[i,j+1]=1)
THEN -KdiffC*0.5*(sstateC[i,j]+sstateC[i-1,j])*(qC[i,j]/sstateC[i,j]-qC[i-1,j]/sstateC[i-1,j])-
KdiffC*0.5*(sstateC[i,j]+sstateC[i+1,j])*(qC[i,j]/sstateC[i,j]-qC[i+1,j]/sstateC[i+1,j])-
KdiffC*0.5*(sstateC[i,j]+sstateC[i,j-1])*(qC[i,j]/sstateC[i,j]-qC[i,j-1]/sstateC[i,j-1])-
KdiffC*0.5*(sstateC[i,j]+sstateC[i,j+1])*(qC[i,j]/sstateC[i,j]-qC[i,j+1]/sstateC[i,j+1])-
Kbleach1*(bleach1[i,j]*qC[i,j])-Kbleach2*(bleach2[i,j]*qC[i,j])-Kbleach3*(bleach3[i,j]*qC[i,j])-
Kbleach4*(bleach4[i,j]*qC[i,j])

ELSE IF (cellroi[i,j]=1 AND cellroi[i-1,j]=0 AND cellroi[i+1,j]=1 AND cellroi[i,j-1]=1 AND
cellroi[i,j+1]=1)
THEN -KdiffC*0.5*(sstateC[i,j]+sstateC[i+1,j])*(qC[i,j]/sstateC[i,j]-qC[i+1,j]/sstateC[i+1,j])-
KdiffC*0.5*(sstateC[i,j]+sstateC[i,j-1])*(qC[i,j]/sstateC[i,j]-qC[i,j-1]/sstateC[i,j-1])-
KdiffC*0.5*(sstateC[i,j]+sstateC[i,j+1])*(qC[i,j]/sstateC[i,j]-qC[i,j+1]/sstateC[i,j+1])-
Kbleach1*(bleach1[i,j])*qC[i,j]-Kbleach2*(bleach2[i,j])*qC[i,j]-Kbleach3*(bleach3[i,j])*qC[i,j]-
Kbleach4*(bleach4[i,j]*qC[i,j])

ELSE IF (cellroi[i,j]=1 AND cellroi[i-1,j]=1 AND cellroi[i+1,j]=0 AND cellroi[i,j-1]=1 AND
cellroi[i,j+1]=1)
THEN -KdiffC*0.5*(sstateC[i,j]+sstateC[i-1,j])*(qC[i,j]/sstateC[i,j]-qC[i-1,j]/sstateC[i-1,j])-
KdiffC*0.5*(sstateC[i,j]+sstateC[i,j-1])*(qC[i,j]/sstateC[i,j]-qC[i,j-1]/sstateC[i,j-1])-
KdiffC*0.5*(sstateC[i,j]+sstateC[i,j+1])*(qC[i,j]/sstateC[i,j]-qC[i,j+1]/sstateC[i,j+1])-
Kbleach1*(bleach1[i,j])*qC[i,j]-Kbleach2*(bleach2[i,j])*qC[i,j]-Kbleach3*(bleach3[i,j])*qC[i,j]-
Kbleach4*(bleach4[i,j]*qC[i,j])

ELSE IF (cellroi[i,j]=1 AND cellroi[i-1,j]=1 AND cellroi[i+1,j]=1 AND cellroi[i,j-1]=0 AND
cellroi[i,j+1]=1)
THEN -KdiffC*0.5*(sstateC[i,j]+sstateC[i-1,j])*(qC[i,j]/sstateC[i,j]-qC[i-1,j]/sstateC[i-1,j])-
KdiffC*0.5*(sstateC[i,j]+sstateC[i+1,j])*(qC[i,j]/sstateC[i,j]-qC[i+1,j]/sstateC[i+1,j])-
KdiffC*0.5*(sstateC[i,j]+sstateC[i,j+1])*(qC[i,j]/sstateC[i,j]-qC[i,j+1]/sstateC[i,j+1])-
Kbleach1*(bleach1[i,j])*qC[i,j]-Kbleach2*(bleach2[i,j])*qC[i,j]-Kbleach3*(bleach3[i,j])*qC[i,j]-
Kbleach4*(bleach4[i,j]*qC[i,j])

ELSE IF (cellroi[i,j]=1 AND cellroi[i-1,j]=1 AND cellroi[i+1,j]=1 AND cellroi[i,j-1]=1 AND
cellroi[i,j+1]=0)
THEN -KdiffC*0.5*(sstateC[i,j]+sstateC[i-1,j])*(qC[i,j]/sstateC[i,j]-qC[i-1,j]/sstateC[i-1,j])-
KdiffC*0.5*(sstateC[i,j]+sstateC[i+1,j])*(qC[i,j]/sstateC[i,j]-qC[i+1,j]/sstateC[i+1,j])-
KdiffC*0.5*(sstateC[i,j]+sstateC[i,j-1])*(qC[i,j]/sstateC[i,j]-qC[i,j-1]/sstateC[i,j-1])-
Kbleach1*(bleach1[i,j])*qC[i,j]-Kbleach2*(bleach2[i,j])*qC[i,j]-Kbleach3*(bleach3[i,j])*qC[i,j]-
Kbleach4*(bleach4[i,j]*qC[i,j])

ELSE IF (cellroi[i,j]=1 AND cellroi[i-1,j]=0 AND cellroi[i+1,j]=1 AND cellroi[i,j-1]=0 AND
cellroi[i,j+1]=1)
THEN -KdiffC*0.5*(sstateC[i,j]+sstateC[i+1,j])*(qC[i,j]/sstateC[i,j]-qC[i+1,j]/sstateC[i+1,j])-
KdiffC*0.5*(sstateC[i,j]+sstateC[i,j+1])*(qC[i,j]/sstateC[i,j]-qC[i,j+1]/sstateC[i,j+1])-
Kbleach1*(bleach1[i,j])*qC[i,j]-Kbleach2*(bleach2[i,j])*qC[i,j]-Kbleach3*(bleach3[i,j])*qC[i,j]-
Kbleach4*(bleach4[i,j]*qC[i,j])

ELSE IF (cellroi[i,j]=1 AND cellroi[i-1,j]=0 AND cellroi[i+1,j]=1 AND cellroi[i,j-1]=1 AND
cellroi[i,j+1]=0)
THEN -KdiffC*0.5*(sstateC[i,j]+sstateC[i+1,j])*(qC[i,j]/sstateC[i,j]-qC[i+1,j]/sstateC[i+1,j])-
KdiffC*0.5*(sstateC[i,j]+sstateC[i,j-1])*(qC[i,j]/sstateC[i,j]-qC[i,j-1]/sstateC[i,j-1])-
Kbleach1*(bleach1[i,j])*qC[i,j]-Kbleach2*(bleach2[i,j])*qC[i,j]-Kbleach3*(bleach3[i,j])*qC[i,j]-
Kbleach4*(bleach4[i,j]*qC[i,j])

ELSE IF (cellroi[i,j]=1 AND cellroi[i-1,j]=1 AND cellroi[i+1,j]=0 AND cellroi[i,j-1]=1 AND
cellroi[i,j+1]=0)
THEN -KdiffC*0.5*(sstateC[i,j]+sstateC[i-1,j])*(qC[i,j]/sstateC[i,j]-qC[i-1,j]/sstateC[i-1,j])-
KdiffC*0.5*(sstateC[i,j]+sstateC[i,j-1])*(qC[i,j]/sstateC[i,j]-qC[i,j-1]/sstateC[i,j-1])-
```

```
Kbleach1*(bleach1[i,j])*qC[i,j]-Kbleach2*(bleach2[i,j])*qC[i,j]-Kbleach3*(bleach3[i,j])*qC[i,j]-
Kbleach4*(bleach4[i,j]*qC[i,j])

ELSE IF (cellroi[i,j]=1 AND cellroi[i-1,j]=1 AND cellroi[i+1,j]=0 AND cellroi[i,j-1]=0 AND
cellroi[i,j+1]=1)
THEN -KdiffC*0.5*(sstateC[i,j]+sstateC[i-1,j])*(qC[i,j]/sstateC[i,j]-qC[i-1,j]/sstateC[i-1,j])-
KdiffC*0.5*(sstateC[i,j]+sstateC[i,j+1])*(qC[i,j]/sstateC[i,j]-qC[i,j+1]/sstateC[i,j+1])-
Kbleach1*(bleach1[i,j])*qC[i,j]-Kbleach2*(bleach2[i,j])*qC[i,j]-Kbleach3*(bleach3[i,j])*qC[i,j]-
Kbleach4*(bleach4[i,j]*qC[i,j])

ELSE IF (cellroi[i,j]=1 AND cellroi[i-1,j]=1 AND cellroi[i+1,j]=1 AND cellroi[i,j-1]=0 AND
cellroi[i,j+1]=0)
THEN -KdiffC*0.5*(sstateC[i,j]+sstateC[i-1,j])*(qC[i,j]/sstateC[i,j]-qC[i-1,j]/sstateC[i-1,j])-
KdiffC*0.5*(sstateC[i,j]+sstateC[i+1,j])*(qC[i,j]/sstateC[i,j]-qC[i+1,j]/sstateC[i+1,j])-
Kbleach1*(bleach1[i,j])*qC[i,j]-Kbleach2*(bleach2[i,j])*qC[i,j]-Kbleach3*(bleach3[i,j])*qC[i,j]-
Kbleach4*(bleach4[i,j]*qC[i,j])

ELSE IF (cellroi[i,j]=1 AND cellroi[i-1,j]=0 AND cellroi[i+1,j]=0 AND cellroi[i,j-1]=1 AND
cellroi[i,j+1]=1)
THEN -KdiffC*0.5*(sstateC[i,j]+sstateC[i,j-1])*(qC[i,j]/sstateC[i,j]-qC[i,j-1]/sstateC[i,j-1])-
KdiffC*0.5*(sstateC[i,j]+sstateC[i,j+1])*(qC[i,j]/sstateC[i,j]-qC[i,j+1]/sstateC[i,j+1])-
Kbleach1*(bleach1[i,j])*qC[i,j]-Kbleach2*(bleach2[i,j])*qC[i,j]-Kbleach3*(bleach3[i,j])*qC[i,j]-
Kbleach4*(bleach4[i,j]*qC[i,j])

ELSE IF (cellroi[i,j]=1 AND cellroi[i-1,j]=1 AND cellroi[i+1,j]=0 AND cellroi[i,j-1]=0 AND
cellroi[i,j+1]=0)
THEN -KdiffC*0.5*(sstateC[i,j]+sstateC[i-1,j])*(qC[i,j]/sstateC[i,j]-qC[i-1,j]/sstateC[i-1,j])-
Kbleach1*(bleach1[i,j])*qC[i,j]-Kbleach2*(bleach2[i,j])*qC[i,j]-Kbleach3*(bleach3[i,j])*qC[i,j]-
Kbleach4*(bleach4[i,j]*qC[i,j])

ELSE IF (cellroi[i,j]=1 AND cellroi[i-1,j]=0 AND cellroi[i+1,j]=1 AND cellroi[i,j-1]=0 AND
cellroi[i,j+1]=0)
THEN -KdiffC*0.5*(sstateC[i,j]+sstateC[i+1,j])*(qC[i,j]/sstateC[i,j]-qC[i+1,j]/sstateC[i+1,j])-
Kbleach1*(bleach1[i,j])*qC[i,j]-Kbleach2*(bleach2[i,j])*qC[i,j]-Kbleach3*(bleach3[i,j])*qC[i,j]-
Kbleach4*(bleach4[i,j]*qC[i,j])

ELSE IF (cellroi[i,j]=1 AND cellroi[i-1,j]=0 AND cellroi[i+1,j]=0 AND cellroi[i,j-1]=1 AND
cellroi[i,j+1]=0)
THEN -KdiffC*0.5*(sstateC[i,j]+sstateC[i,j-1])*(qC[i,j]/sstateC[i,j]-qC[i,j-1]/sstateC[i,j-1])-
Kbleach1*(bleach1[i,j])*qC[i,j]-Kbleach2*(bleach2[i,j])*qC[i,j]-Kbleach3*(bleach3[i,j])*qC[i,j]-
Kbleach4*(bleach4[i,j]*qC[i,j])

ELSE IF (cellroi[i,j]=1 AND cellroi[i-1,j]=0 AND cellroi[i+1,j]=0 AND cellroi[i,j-1]=0 AND
cellroi[i,j+1]=1)
THEN -KdiffC*0.5*(sstateC[i,j]+sstateC[i,j+1])*(qC[i,j]/sstateC[i,j]-qC[i,j+1]/sstateC[i,j+1])-
Kbleach1*(bleach1[i,j])*qC[i,j]-Kbleach2*(bleach2[i,j])*qC[i,j]-Kbleach3*(bleach3[i,j])*qC[i,j]-
Kbleach4*(bleach4[i,j]*qC[i,j])

ELSE 0

d/dt (qC[1,1..columns]) = 0
d/dt (qC[1..rows,1]) = 0
d/dt (qC[rows,1..columns]) = 0
d/dt (qC[1..rows,columns]) = 0

s1 = ARRAYSUM(m1[*])/ARRAYSUM(m10[*])
s2 = ARRAYSUM(m2[*])/ARRAYSUM(m20[*])
s3 = ARRAYSUM(m3[*])/ARRAYSUM(m30[*])
s4 = ARRAYSUM(m4[*])/ARRAYSUM(m40[*])
sT = ARRAYSUM(mT[*])/ARRAYSUM(mT0[*])
sstateF[1..rows,1..columns] = #init(i,j) * (1 - pC)
sstateC[1..rows,1..columns] = #init(i,j) * pC
INIT qF[1..rows,1..columns] = #init(i,j) * (1 - pC)
```

```
INIT qC[1..rows,1..columns] = #init(i,j) * pC
cellroi[1..rows,1..columns] = IF (#cellrois(i,j) >= 1) THEN 1 ELSE 0
mroi1[1..rows,1..columns] = IF (#cellrois(i,j) >= 6 AND #cellrois(i,j) <= 8) THEN 1 ELSE 0
mroi2[1..rows,1..columns] = IF (#cellrois(i,j) >= 9 AND #cellrois(i,j) <= 11) THEN 1 ELSE 0
mroi3[1..rows,1..columns] = IF (#cellrois(i,j) >= 12 AND #cellrois(i,j) <= 14) THEN 1 ELSE 0
mroi4[1..rows,1..columns] = IF (#cellrois(i,j) = 1 OR #cellrois(i,j) >= 15) THEN 1 ELSE 0
mroiT[1..rows,1..columns] = IF (#cellrois(i,j) = 1 OR #cellrois(i,j) >= 6) THEN 1 ELSE 0
m1[1..rows,1..columns] = mroi1[i,j] * (qF[i,j] + qC[i,j])
m10[1..rows,1..columns] = mroi1[i,j] * #init(i,j)
m2[1..rows,1..columns] = mroi2[i,j] * (qF[i,j] + qC[i,j])
m20[1..rows,1..columns] = mroi2[i,j] * #init(i,j)
m3[1..rows,1..columns] = mroi3[i,j] * (qF[i,j] + qC[i,j])
m30[1..rows,1..columns] = mroi3[i,j] * #init(i,j)
m4[1..rows,1..columns] = mroi4[i,j] * (qF[i,j] + qC[i,j])
m40[1..rows,1..columns] = mroi4[i,j] * #init(i,j)
mT[1..rows,1..columns] = mroiT[i,j] * (qF[i,j] + qC[i,j])
mT0[1..rows,1..columns] = mroiT[i,j] * #init(i,j)
bleach1[1..rows,1..columns] = IF (#cellrois(i,j) = 2) THEN 1 ELSE 0
bleach2[1..rows,1..columns] = IF (#cellrois(i,j) = 3) THEN 1 ELSE 0
bleach3[1..rows,1..columns] = IF (#cellrois(i,j) = 4) THEN 1 ELSE 0
bleach4[1..rows,1..columns] = IF (#cellrois(i,j) = 5) THEN 1 ELSE 0

DiffF = 5
DiffC = 0.1
pC = 0.7
KdiffF = DiffF / (0.572^2)
KdiffC = DiffC / (0.572^2)
TFLIP = 3.64
deltaTbleach = 0.279
bleachRatios[1] = 0.1668
bleachRatios[2] = 0.3309
bleachRatios[3] = 0.8779
bleachRatios[4] = 0.9702
bleachRate[1..4] = (LOGN(1/bleachRatios[i]))/deltaTbleach
Kbleach1 = IF(MOD(TIME,TFLIP) < deltaTbleach) THEN bleachRATE[1] ELSE 0
Kbleach2 = IF(MOD(TIME,TFLIP) < deltaTbleach) THEN bleachRATE[2] ELSE 0
Kbleach3 = IF(MOD(TIME,TFLIP) < deltaTbleach) THEN bleachRATE[3] ELSE 0
Kbleach4 = IF(MOD(TIME,TFLIP) < deltaTbleach) THEN bleachRATE[4] ELSE 0
```

5. Nuclear transit of an mRNA export protein studied by FLIP and Photoactivation techniques

5.1 Abstract

Inside a living cell, proteins are constantly exchanging between different subcellular compartments. Understanding the life cycle of a particular molecule requires the determination of the time of permanence inside each compartment. We used compartmental analysis and a confocal FLIP variant to study the recovery kinetics of a fluorescent molecule and determine its permanence time in a subcellular compartment. This approach is valid if the exchange rates are slower than the diffusion rates of the molecule inside the compartment and it is specially suited for proteins which shuttle between two compartments but have low steady-state concentrations in one of them. Such is the case of the nuclear export factor TAP, which is barely detectable in the cytoplasm at steady state. Using this novel FLIP variant, we were able to study the role of the different structural domains of TAP in its shuttling activity.

5.2 Introduction

Living cells are extremely dynamic entities, with many of its molecular components exhibiting continuous shuttling activity between several cellular substructures or compartments. Understanding the function and life cycle of such molecules requires the determination of the times of permanence inside the different cellular compartments.

Photobleaching methods such as Fluorescence Recovery After Photobleaching (FRAP, see section 1.5.3 in Chapter 1) have been used previously to study the shuttling activity of proteins between the nucleus and the cytoplasm and determine the permeability of the nuclear envelope (Wei et al., 2003). In such approaches, a large portion, or the entirety of the cellular compartment (i.e. the nucleus or the cytoplasm) is photobleached once, and the recovery to the steady-state situation is recorded over time. If diffusion of the molecule under study (e.g. GFP) inside each of the cellular compartments is faster than translocation through the nuclear pore complexes (NPCs), then both the nucleus and the cytoplasm can be treated as well-mixed compartments (Jacquez, 1996).

However, if the steady-state distribution of the fluorescent protein is such that it is highly concentrated in one of the compartments and virtually absent in the other, then its permanence time cannot be determined using the FRAP technique. In this case, photobleaching one of the compartments a single time would either destroy the vast majority of fluorescent protein in the cell, or have no effect at all in the overall fluorescence loss of the tagged protein.

In order to determine the permanence time of the nuclear export factor TAP, which binds to mRNPs that are to be exported from the nucleus to the cytoplasm, we performed FLIP after photoactivation experiments in living cells expressing PA-GFP-tagged TAP-p15. In this approach, the nuclear pool of protein was photoactivated followed by repeated photobleaching of the compartment where the fluorescent protein concentration is lower (the cytoplasm). We then used a two-compartment model to study the kinetics of shuttling PA-GFP-TAP-p15 and of mutants of TAP with modified cargo-binding and NPC-binding domains. The results thus obtained allowed us to measure the permanence time of TAP-p15 in the nucleus and the kinetic differences that resulted from mutations in the different TAP domains, which are in agreement with previous studies regarding their role in TAP-p15 translocation through the nuclear pore complexes.

5.3 Materials and Methods

Cell culture and transfections

HeLa cells were cultured as monolayers in Modified Eagle's Medium (MEM) supplemented with 10% fetal calf serum (Gibco-BRL, Paisley, Scotland). Cells were plated and observed in glass bottom chambers (MatTek Corporation, Ashland, MA). For imaging the medium was changed to D-MEM/F-12 without phenol red, supplemented with 15 mM HEPES buffer (Gibco).

GFP-TAP, p15 and GFP-TAP-mutants plasmids have been described before (Braun et al., 2002). PA-GFP-TAP and PA-GFP-tagged TAP mutants were made by replacing the coding sequence of EGFP with PA-GFP (Patterson and Lippincott-Schwartz, 2002). HeLa subconfluent cells were transiently co-transfected with 0.5 μg of TAP and p15 plasmid DNA by using FuGENE6 reagent (Roche Biochemicals, Indianapolis, IN) according to the manufacturer's protocol.

Confocal Microscopy and Bleaching Protocols

Live cell microscopy was performed on a confocal microscope (Axiovert 100M with LSM 510 scanning module, Zeiss, Jena, Germany). Images were acquired on the Zeiss confocal microscope using the PlanApochromat 63x/1.4 objective. PA-GFP imaging was performed in multi-tracking mode with a 413/488 dichroic mirror. In one track the native protein was imaged using low intensity levels (~ 5 μW) of the 413 nm line of a Kr laser a LP 430 filter. The second track was used to image photoactivated protein with the 488 nm line of an Ar laser (25 mW nominal output) and a LP 505 filter. Photoactivation was performed with high intensity (~ 1 mW) 413 nm Kr laser line. Cell samples were equilibrated for 15 minutes on a temperature-regulated microscope stage (F25-MP, Julabo, Allentown, USA) at 37 ºC.

FLIP experiments using PA-GFP required the photoactivation of the nuclear pool of protein prior to repetitive bleaching in the cytoplasm. Photoactivation was performed using an 806 ms bleach pulse of the 413 nm Kr laser line at a region of interest (ROI) that coincided with the cell nucleus (~ 350 μm^2 area). Immediately after photoactivation, cells were repeatedly bleached at intervals of ~ 20 s and imaged between bleach pulses.

Bleaching of the photoactivated protein was performed by 15.5 s bleach pulses on a defined ROI that coincided with the cell cytoplasm, excluding a ring area (~ 1.5 μm radius) around the cell nucleus, to prevent nuclear fluorescence bleaching due to minor cell movement during image acquisition. Repetitive bleaching pulses were achieved using a macro for LSM software developed by Gwénaël Rabut at the EMBL (http://www.embl-heidelberg.de/ExternalInfo/ellenberg/homepage/macros.html).

A series of 30 images were collected for each cell with laser power from both lasers (413 nm and 488 nm) attenuated to 1% of the bleaching intensity of each laser. A calibration plot, relating measured fluorescence levels with concentrations of GFP, was done by making serial dilutions of a purified 200 μM EGFP solution in 20mM Tris 7.5, 100mM NaCl, 100mM EDTA (a kind gift from Dr. Konstantin Lukyanov, IBCH, Moscow, Russia). Background fluorescence was estimated by imaging a neutral Tris solution devoid of GFP molecules. The average nuclear concentrations of PA-GFP-TAP in transfected HeLa cells were calculated by measuring average fluorescence in more than 33 cells.

FLIP Image Analysis

The Physiology package of the LSM Image Examiner program (Zeiss, Jena and EMBL, Heidelberg, Germany) was used to create plots of fluorescence intensity versus time in the nuclear and cytoplasmic regions of the cells (using the ROI mean function of the software). The average fluorescence in the nucleus of bleached cells *I(t)* and the average fluorescence in the nucleus of non-bleached cells *N(t)* were calculated for each background subtracted image at time *t*. FLIP curves for bleached cells were then normalized and corrected for loss of fluorescence caused by imaging,

$$I_N(t) = \frac{I(t)}{I_0}\frac{N_0}{N(t)}$$

where N_0 and I_0 are the nuclear fluorescence intensities of non-bleached cells and bleached cells, respectively, before bleaching started. Loss of fluorescence due to imaging in FLIP could reach 20-25 % over the time course of the experience. Data obtained from the plots was fitted to expected theoretical curves using Origin (Microcal Software Inc., Northampton, USA). FLIP experimental data was fitted to $F(t) = e^{-Kt}$, thus obtaining the parameter *K*, from which the permanence time inside the nucleus was estimated by each method (see below). The ratio between the steady-state concentrations in the cytoplasm and nucleus of cells expressing GFP-TAP was calculated by simply dividing nuclear and cytoplasmic background subtracted fluorescence.

FLIP Quantitative Kinetic Analysis

Assuming a linear exchange between compartments, the two-compartment model used to study the exchange of PA-GFP-TAP between the nucleus and the cytoplasm consists of the following set of differential equations:

$$\begin{cases} \dot{C}_N = -\dfrac{K_O A}{V_N} C_N + \dfrac{K_I A}{V_N} C_C \\ \dot{C}_C = \dfrac{K_O A}{V_C} C_N - \dfrac{K_I A}{V_C} C_C - K_b C_C \end{cases}$$

where *A* is the nuclear membrane area, K_O is the outflow rate, K_I is the inflow rate, C_N and C_C are the nuclear and cytoplasmic concentrations of PA-GFP-TAP, respectively and K_b represents the bleaching rate. These equations describe the evolution of the visible part of the system (i.e. unbleached fluorescent molecules), although it should be emphasized that bleaching does not perturb the kinetic steady state. Since only the nuclear fluorescence is photo-activated, the system has the following initial conditions:

$$\begin{cases} C_N(0) = C_{N0} \\ C_C(0) = 0 \end{cases}$$

If $K_b >> K_I > K_0$, that is, if the vast majority of PA-GFP-TAP molecules that leave the nucleus are bleached, then we can assume that there is no influx of protein back to the nucleus, and $K_I \approx 0$. In this case, we have simply

$$\dot{C}_N = -\frac{K_O A}{V_N} C_N$$

And the solution is

$$C_N(t) = C_{N0} e^{-\frac{K_O A}{V_N} t}$$

The number of particles inside this compartment would decay exponentially and the mean permanence time of a particle inside the nucleus would be:

$$\bar{t} = \int_0^{+\infty} t\, e^{-\frac{K_O A}{V_N} t} \Bigg/ \int_0^{+\infty} e^{-\frac{K_O A}{V_N} t} = \frac{V_N}{K_O A}$$

Experimentally, we determine a total nuclear fluorescence decay rate K:

$$K = \frac{K_O A}{V_N}$$

The average time PAGFP-TAP takes to leave the nucleus is then simply:

$$\bar{t}_{out} = \frac{1}{K}$$

Estimation of the number of translocations through the nuclear pore

The number of GFP or PAGFP-TAP translocations through the nuclear pore complex per time unit (N_{trans}) is given by:

$$N_{trans} = \frac{C_0 V_N N_A}{\bar{t}_{out} N_{pores}}$$

where C_0 is the average concentration of protein in the nucleus (which is determined using the calibration plot), V_N is the nuclear volume and N_{pores} is the total number of pores. Note that, in a steady-state situation, the number of molecules that pass through the nuclear pore is the same in both the inward and outward directions.

5.4 Results

The permanence time of shuttling proteins cannot be determined using the FRAP technique if the steady-state levels of fluorescence are such that the vast majority of protein is mostly present in one of the compartments and virtually absent in the other. In order to determine the permanence time inside the nucleus of a protein such as TAP-p15, we used the FLIP technique to repeatedly bleach the cytoplasm, with a bleaching rate constant that ensures the destruction of fluorescence for the vast majority of the exported protein.

This approach uses a two-compartment model to study the kinetics of the shuttling protein. The model is valid if mixing within the nucleus and the cytoplasm is fast, compared with protein exchange between them, i.e. compared to protein translocation through the nuclear pore complexes. If FLIP is performed when the system is at steady state, i.e. when we have fluorescent protein both in the nucleus and in the cytoplasm, then the monitored fluorescence in the FLIP experiment will reflect both export and import of fluorescent protein that was not bleached. In order to look at just one of the processes, it is necessary to photoactivate the fluorescent protein in the compartment where the concentration is higher and perform the repetitive bleaching on the other one. This way, only proteins that are translocated from one compartment to the other will be bleached, and FLIP data will yield the export rate directly (Figure 5.1).

We used the FLIP after photoactivation technique to determine the average permanence time of TAP, a nuclear export factor for mRNA, and of several TAP mutants in the nucleus of living HeLa cells. In FLIP experiments using PA-GFP-TAP, the nuclear pool of protein is photoactivated before repetitive bleaching the cytoplasm with images being acquired between bleaching pulses (Figure 5.1A). Since only the nuclear pool of protein is photoactivated and the bleaching kinetics is much higher than both import and export kinetics (the bleaching process can be considered constant throughout the entire experiment, interrupted only when imaging was performed), the vast majority of molecules exported from the nucleus to the cytoplasm would be immediately bleached. The slow rate-limiting step of nuclear export will then be dominant in the exponential decay of fluorescence and the rate constant K that is measured will be very close to the actual rate constant for export rates of mRNPs bound to PA-GFP-TAP (and mutants).

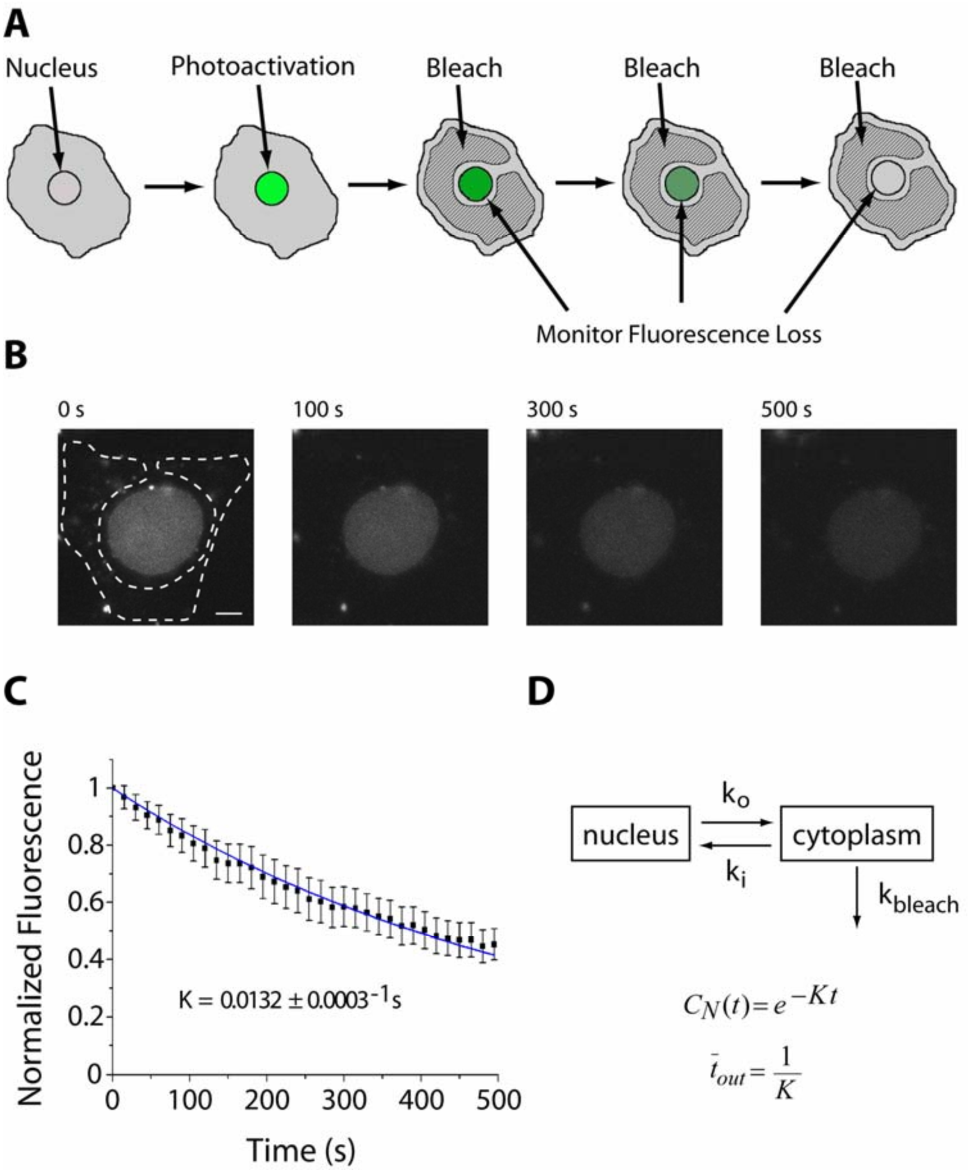

Figure 5.1 – FLIP after photoactivation analysis of cells expressing PA-GFP-TAP **(A)** Diagram illustrating the FLIP after photoactivation technique. **(B)** FLIP sequence of a HeLa cell expressing PA-GFP-TAP. Bleaching was performed in the cytoplasmic area indicated by the dashed lines after photoactivation of the nuclear pool of protein. Nuclear fluorescence was recorded every 20 s. Images were taken at the indicated time points. Bar: 5 µm. **(C)** Plot of nuclear loss of fluorescence caused by cytoplasmic FLIP in HeLa cells expressing PA-GFP-TAP and corresponding best fit to $F(t) = e^{-Kt}$ (*blue line*, see Materials and Methods). Nuclear fluorescence was background subtracted, normalized and corrected for loss of fluorescence due to imaging. The curves correspond to a total number of 33 cells analyzed. Error bars represent standard deviations. **(D)** Two-compartment model for nucleo-cytoplasmic exchange measured with FLIP and corresponding equations. k_{bleach} represents the FLIP bleaching rate constant.

The results obtained for PA-GFP-TAP and mutants are shown in Figure 5.2 and summarized in Table 5.1.

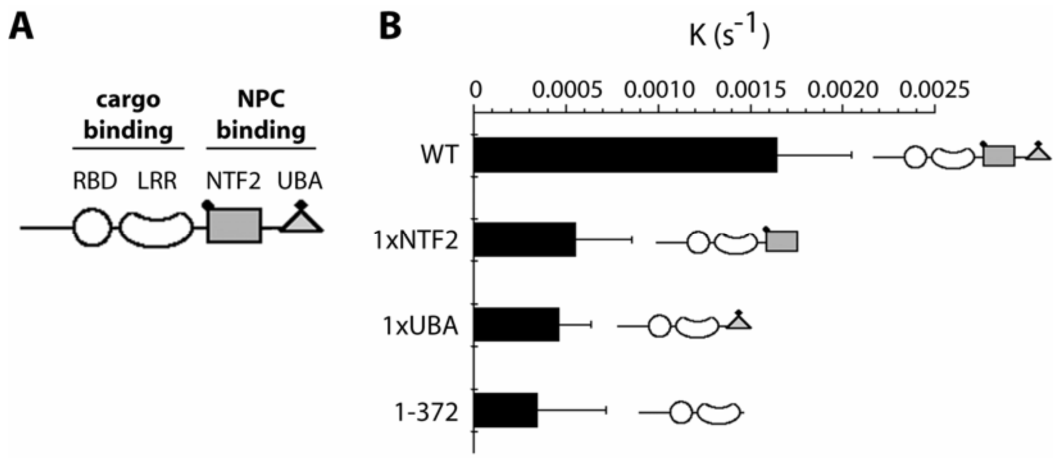

Figure 5.2 – FLIP after photoactivation results for PA-GFP-TAP and mutants **(A)** Structural and functional domains of human TAP. The cargo-binding (residues 1 to 372) consists of an RNP-like RNA-binding domain (RBD) and a leucine rich repeat domain (LRR). The NPC-binding domain (residues 372 to 619) consists of the NTF2-like and UBA-like domains, each of them featuring a nucleoporin binding site. **(B)** Rate constants obtained from cytoplasmic FLIP experiments performed in HeLa cells expressing PA-GFP-TAP and mutants. Values of *K* represent an average for a total number of analyzed cells ranging from 12 (PA-GFP-TAP-1xUBA) to 33 (PA-GFP-TAP). Error bars represent standard deviations.

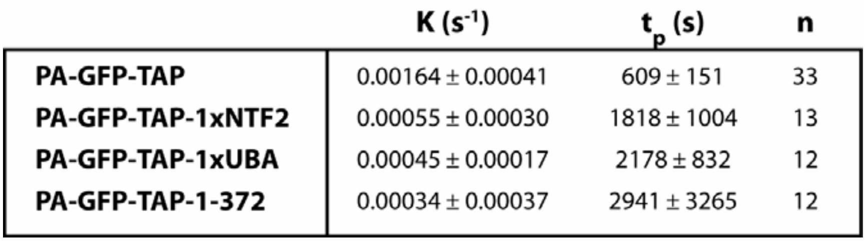

	K (s^{-1})	t_p (s)	n
PA-GFP-TAP	0.00164 ± 0.00041	609 ± 151	33
PA-GFP-TAP-1xNTF2	0.00055 ± 0.00030	1818 ± 1004	13
PA-GFP-TAP-1xUBA	0.00045 ± 0.00017	2178 ± 832	12
PA-GFP-TAP-1-372	0.00034 ± 0.00037	2941 ± 3265	12

Table 5.1 – Rate constants and permanence times obtained from cytoplasmic FLIP after photoactivation experiments performed on HeLa cells expressing wild-type and different mutants of the TAP protein tagged with PA-GFP.

Using the calibration data from EGFP experiments (*data not shown*), and assuming that the data is also valid for photoactivated PA-GFP, we estimated the average concentration of PA-GFP-TAP in the transfected HeLa cells we used to be ~ 12.5 μM (calculated from an average value of photoactivated PA-GFP-TAP fluorescence in the nuclei of 33 cells). Using this value and the average permanence time obtained for PA-GFP-TAP we obtain a value for the mean number of PA-GFP-TAP translocations through the nuclear pore of ~ 4.6 molecules per pore per second (see Materials and Methods). In contrast, the TAP mutant with the slowest export rate constant, PA-GFP-TAP-1-372 (which corresponds to the cargo-binding domains of TAP alone) only has an estimated value of ~ 0.9 molecules per pore per second.

5.5 Discussion

In this chapter, we describe a novel FLIP after Photoactivation technique that can be used to estimate the time of permanence inside a cellular compartment for a given protein that shuttles between two compartments but has a low steady-state concentration in one of them. Using this FLIP method, we found the permanence time of TAP inside the nucleus to be 609 ± 151 s.

The TAP-p15 heterodimer is thought to be the predominant export receptor for cellular mRNAs (Herold et al., 2003). TAP-p15 heterodimers promote the nuclear export of bulk mRNA across nuclear pore complexes by binding to FG-nucleoporin repeats (see section 1.2.1 in Chapter 1) via the NTF2-like and UBA-like domains, both of them being required for efficient transportation across the central channel of the NPC (see section 1.3.4 in Chapter 1).

The permanence time for TAP-p15 inside the nucleus is relatively high. Rather than reflecting an inefficient export process however, this might be instead the result of a very efficient nuclear retention process, which effectively prevents TAP "leakage" into the cytoplasm. Supporting this view is the recent finding of a specific nucleoporin (RanBP2/Nup358) at the cytoplasmic filaments of the NPC that was identified as a major binding site for TAP-p15, restricting its diffusion into the cytoplasm after NPC translocation (Forler et al., 2004). TAP-p15 is thus thought to dissociate from mRNPs and be re-imported to the nucleus immediately after NPC translocation, thereby accounting for the very low steady-state levels of the protein in the cytoplasm and the relatively high nuclear permanence time.

When TAP is mutated and different domains responsible for binding to the NPC are removed, the protein export function is impaired, and we were able to measure the kinetic differences resulting from these mutations. In fact, removal of one of the NPC-binding domains (either NTF2 or UBA) is sufficient to impair the nuclear export of the protein, and these mutants show very similar kinetics to the mutant lacking the entire NPC-binding domain, in agreement with previous results (Braun et al., 2002).

6. Conclusion and Perspectives

All biological phenomena are dynamic: motion is one of the defining characteristics of life. Cells, being the smallest independent units of life, are of course no exception to this rule. They are extremely dynamic entities. But cells (and organisms) also possess another conspicuous quality: an elaborate spatial organization. Cellular architecture is what ultimately differentiates cells from homogeneous soups of the molecules that compose them. How this organization is generated, maintained and reproduced is therefore a key issue to understand the living state. Most of our early knowledge about sub-cellular architecture originated from snapshots of cells frozen in time (having been chemically fixed and stained to be used in conventional electron and light microscopy), and so it is no surprise to find that the interpretations of these images often led to an understanding of cellular architecture as being the result of complex clockwork mechanisms and molecular machines (Kurakin, 2005b). Furthermore, these macromolecular machineries, such as the transcription, splicing and translation apparatus, have traditionally been studied separate from each other and by means of isolating and characterizing their individual components. These reductionist approaches have thus led to a framework of understanding cellular architecture as the result of such clockwork-like mechanisms, often represented in the literature by means of flowcharts and diagrams no different than those used in engineering computers, aircrafts and microscopes (Kurakin, 2005a). The life cycle of mRNA, the molecule that carries the information contained in genes from the nuclear sites of transcription to the ribosomes in the cytoplasm, is a striking example of this, having been represented in charts with the different processing steps of transcription, capping, splicing, cleavage, polyadenylation and export to the cytoplasm connected to each other as if they were consecutive independent events in an assembly line of a cellular factory (Alberts, 1994).

This view is contradicted, however, by a recent accumulation of data which is incompatible with a clockwork perception of cellular organization (Misteli, 2001a; Misteli, 2001b). Novel imaging methods and technology, and in particular those based on *in vivo* fluorescence techniques such as FRAP, FLIP and FRET are now favoring an image of the cell as a dynamic system of interlinked and interdependent macromolecular structures which have been proposed to function under the general principles of stochasticity and self-organization (Misteli, 2001a).

In this thesis, we aimed at developing novel photobleaching methodologies and improving existing ones in order to better characterize molecular motion and interactions inside the living cell. These are of paramount importance in understanding the complex dynamics of the chemical reactions in which the different molecular species are involved inside the cell, often with a high degree of spatio-temporal intermingling between the different chemical pathways. Such is also the case of the extremely complex process of eukaryotic gene expression, which relies on mRNA biogenesis, processing and regulation to convey the genetic information stored in DNA into functional proteins. mRNAs have an intricate, elaborate existence, in the course of which they associate with a vast diversity of proteins forming mRNPs. The protein content of this molecular escort evolves throughout the lifetime of the mRNPs, from the moment the precursor messenger RNA is transcribed in the nucleus until it is finally translated and eventually degraded in the cytoplasm (Moore, 2005).

The methodologies presented in this thesis were applied to the study of different events in the life cycle of mRNPs, from the early processing steps of splicing (focusing on splicing factors dynamics and interactions inside the nucleus), followed by mRNP intranuclear mobility and finally addressing its export through the nuclear pore complexes.

In Chapter 2, different photobleaching techniques (FRAP, FLIP, FRAP-FIM) were employed to probe the nuclear mobility of the GFP-tagged snRNP component SmE and the splicing factors U2AF^{65}, U2AF^{35}, SF1 and SC35. These components of the spliceosome are found distributed throughout the nucleoplasm of living cells, concentrated in nuclear speckles and excluded from nucleoli (see section 1.2.2 in Chapter 1). We studied the recruitment mechanism of splicing factors from the speckles to the sites of transcription, addressing the question of whether there was an active transcription-dependent signal for recruiting SFs to splicing locations. This recruitment signal could manifest itself by an increase in the retention time of SFs at the speckles when transcription is inhibited either by the use of drugs (such as DRB) or by expression of a dominant negative protein that prevented the import of core spliceosome components to the nucleus (spn1Δ1-65). We found that this was not the case. FLIP experiments demonstrated that splicing factors mobility increased when transcription was inhibited, which ruled out the recruitment signal hypothesis. Instead, we propose that SFs are constantly shuttling in and out of the nuclear speckles but they are transiently retained in transcription sites. The recruitment model would thus rely solely on stochastic mechanisms, with splicing factors being allowed to randomly wander through the nucleoplasm, eventually reaching a transcription site and engaging in splicing activity, before resuming their diffusional behavior. Monte-Carlo simulations, where SFs were modeled as random walkers with different probabilities of becoming bound to speckles and transcription sites, were able to explain both the increase in SFs concentration at the speckles and the faster decay rates observed in FLIP experiments. We thus show that the recruitment of splicing factors to the nuclear speckles is independent of the transcriptional state of the cell, as previously proposed by others (Carrero et al., 2006; Misteli, 2001a) and that the levels of SFs in the different nuclear domains are compatible with stochastic models of self-organization.

We have also shown that, although these proteins are highly dynamic inside the nucleus (with FRAP determined diffusion coefficient values ranging from 0.70 to 1.84 $\mu m^2 s^{-1}$ in the nucleoplasm and 0.30 to 1.22 $\mu m^2 s^{-1}$ in the nuclear speckles), their mobility rates are lower than expected, considering their molecular weight and the diffusion coefficient values obtained for exogenous molecules of similar size. This discrepancy in the kinetic behavior was shown to be related with the ability of splicing factors to interact with each other, as the abolition of specific interaction domains restored the mobility of these proteins to values similar to those of exogenous molecules. Splicing factors are known to interact at the spliceosome, and since transcription sites are distributed throughout the nucleoplasm, a general reduction in their FRAP determined diffusion coefficients would be expected as the result of engagement to active spliceosomes conspicuously present in any given nucleoplasmic area.

In order to look at splicing sites more directly, we used cells infected with adenovirus, in which all the transcription (and therefore splicing) machinery is recruited to viral transcription rings. The FRAP determined diffusion coefficients estimated in these viral rings areas were effectively reduced when compared to those of exogenous molecules and binding-impaired mutants. However, the FRAP recovery curves were consistent with an “effective diffusion” behavior, which was also reflected in the inability of FRAP-FIM experiments to determine the residence times of SFs at the viral transcription rings. The binding reactions of the splicing factors we have studied to active spliceosomes thus seem to occur in a timescale that is faster than diffusion itself.

Splicing factors interactions at the spliceosome can account for a reduction in the effective diffusion coefficient that is determined by FRAP in the nucleoplasm, but in the nuclear speckles, which are devoid of active spliceosomes (Cmarko et al., 1999; Misteli and Spector, 1999), the reduced *D* values suggested the formation of large multi-protein complexes distinct of the spliceosome. In Chapter 3 we set out to identify and visualize these interactions using FRET approaches. To this purpose, an improved Acceptor Photobleaching FRET methodology was developed that allowed the spatial mapping of interactions between a donor-tagged and acceptor-tagged fluorescent proteins. With this novel method, we were able to detect interactions between the splicing factors $U2AF^{65}$ and $U2AF^{35}$ as well as $U2AF^{65}$ and SF1 both in the nucleoplasm (where these interactions were already known to occur in active spliceosomes) and in the speckles (where no interactions between these splicing factors had been reported). Importantly, we also detected these interactions when transcription, and therefore splicing, was directly inhibited using DRB. A novel $U2AF^{65}$ self-interaction was also detected using our Acceptor Photobleaching FRET approach and confirmed (as the previous interactions) with FRET-FLIM methods.

The existence of splicing factors complexes where these interactions might occur and which are, as we have shown, distinct from the spliceosome and still present when transcription is inhibited, strongly suggests that the assembly of the "splicing machinery" probably occurs by formation of pre-assembled particles rather than stepwise addition of discrete components. Again, this is highly compatible with self-organization mechanisms where structures or complexes arise spontaneously and stochastically as the result of interactions between their components, which are of a promiscuous and transient nature. Molecular diffusion and the ability to interact and self-interact (in addition to the self-interaction we detected for $U2AF^{65}$, another one has been reported for $U2AF^{35}$ (Chusainow et al., 2005)) might provide the mechanisms necessary for the formation of steady-state structures such as the speckles and the assembly of complex structures such as the dynamic spliceosome. The dynamic instability of self-organizing systems, which are not affected by individual fluctuations in the behavior of its components but show a high degree of plasticity in response to environmental changes, can account, among other things, by the changes in speckles morphology when transcription is inhibited.

Before being translated into protein, the vast majority of properly assembled mRNPs must travel from the sites of transcription to the nuclear pore complexes, in order to be exported to the cytoplasm. The nature of this movement has remained controversial over the years, as proponents of a vectorial motor-driven transport for mRNP claimed that the nucleus is a much too crowded and viscous environment for simple diffusion to be an effective transport mechanism within it. However, the recent accumulation of data provides increasing support for the idea that macromolecular mobility inside the nucleus occurs mainly by Brownian motion, not only for mRNPs (Calapez et al., 2002; Carmo-Fonseca et al., 2002; Molenaar et al., 2004; Politz et al., 2006; Shav-Tal et al., 2004a; Vargas et al., 2005) but also for proteins (Beaudouin et al., 2006; Kruhlak et al., 2000; Partikian et al., 1998) and exogenous molecules that are injected into the cells nuclei (Braga et al., 2004a; Seksek et al., 1997). Nonetheless, nuclear diffusion of large macromolecules appears to be impaired by obstructions imposed by macromolecular crowding (Seksek et al., 1997), which however is not the case of mRNPs. Our own data suggests that energy consumption is required to counteract obstructions to mRNP diffusion (Calapez et al., 2002), in which case a combination of passive diffusion and energy-dependent reactions might be involved in mRNP movement.

In Chapter 4, the intranuclear mobility of mRNPs was studied using a novel quantitative FLIP methodology that allows for the kinetic characterization of a mixed population of GFP-tagged molecules diffusing at different rates within the cell nucleus. We used GFP-PABPN1 and GFP-TAP as markers for mRNP mobility, as both proteins are able to bind mRNA, although at different stages and to different types of mRNA. PABPN1 binds the poly(A) tails of all poly(A)-RNA whereas TAP, together with p15, binds to mRNPs which are to be exported through the nuclear pore complexes. Our results show that both RNA-binding proteins diffuse inside the nucleus essentially as two populations, which we propose to correspond to mRNP-bound and unbound fractions. Using this FLIP analysis on cells expressing GFP-TAP and treated with a myosin inhibitor (BDM), we were able to show that mRNP movement is not dependent on myosin motors, although interestingly, the same does not hold for transcription itself, which we show for the first time to be dependent *in vivo* on the activity of myosin and probably actin, as previously suggested by others using *in vitro* data (Burke et al., 1998; Egly et al., 1984; Pestic-Dragovich et al., 2000; Scheer et al., 1984).

Most significantly, the diffusion coefficient values determined with this FLIP method for the slower populations of both GFP-PABPN1 and GFP-TAP, which we interpret as being mRNP-bound, is the same for both proteins (0.09 ± 0.05 $\mu m^2 s^{-1}$) and is consistent with estimates obtained by others (Molenaar et al., 2004; Shav-Tal et al., 2004a; Vargas et al., 2005). The FLIP determined diffusion coefficients for the RNA-unbound pools of GFP-PABPN1 and GFP-TAP are 8.56 ± 2.11 $\mu m^2 s^{-1}$ and 4.29 ± 1.99 $\mu m^2 s^{-1}$, respectively. Although neither of them corresponds to the expected diffusion coefficient of "freely diffusing" particle inside the nucleus, considering the molecular weight of both GFP-tagged proteins, none of these proteins is expected to interact solely with mRNA. The wide spectrum of interactions between PABPN1 and various proteins involved in mRNA synthesis and transport as been pointed out by others (Bear et al., 2003). PABPN1 also concentrates at nuclear speckles (with binding kinetics that, like that of splicing factors studied in Chapter 2, appear to be faster than diffusion itself) and is able to interact with U2AF^{65} (Tavanez, J.P. *personal communication*). TAP has also been shown to interact with other proteins involved in RNA export (Braun, 2002). We thus interpret the FLIP determined diffusion coefficients of the RNA-unbound GFP-TAP and GFP-PABPN1 has being "effective diffusion coefficients" that reflect the transient, rapid interactions these proteins undergo inside live cells nuclei with partners other than mRNA.

This "effective diffusion" behavior may be universal to all functional proteins roaming the nucleus, as they are expected to interact with their partners while moving inside this cellular compartment. Such stochastic, transient interactions would then be responsible for "slowing down" proteins which would otherwise wander the nucleus at much higher diffusion rates. Inert molecules, on the other hand, should not display this behavior and we believe this to be the case of GFP alone ($D = 33.3 \pm 3.6\ \mu m^2 s^{-1}$) and FITC-labeled dextrans. Binding reactions have therefore a significant effect on the mobility of nuclear proteins, and the same holds for the binding reactions of both GFP-PABPN1 and GFP-TAP to mRNA itself. Whether these proteins are stably bound to mRNPs *in vivo* or otherwise only transiently interact with this complex macromolecule remains unknown. *In vitro* data for PABPN1 binding to poly(A) molecules in solution suggests that the affinity is relatively low – $K_D = 2\times10^{-9}$ M and $k_{on} = 4\times10^{8}\ M^{-1}s^{-1}$ – (Meyer et al., 2002; Wahle et al., 1993). However, as the authors point out, the model which was used to characterize the binding properties of

PABPN1 did not take into account the fact that this protein forms spherical particles on poly(A) (see section 1.3.2 in Chapter 1) and so it is likely that there are also interactions between protein monomers bound at distant sites which were not taken into account. Our FLIP results clearly suggest that both proteins should bind to mRNPs *in vivo* with a relatively high affinity ($k_{off} \leq 1 \times 10^{-3} s^{-1}$). If this was not the case, then the RNA-bound slower population would not be detected in the FLIP analysis (see section 4.4.4 in Chapter 4). *In vivo* binding of PABPN1 and TAP to mRNA can therefore be very different from the *in vitro* situation.

Both PABPN1 and TAP are able to shuttle between the nucleus and the cytoplasm. In a steady state situation though, they are essentially nuclear proteins with very low concentration levels at the cytoplasm. The import of unbleached molecules from the cytoplasm could conceivably lead to the appearance of additional slow phases in FLIP curves, although we do not believe this to be the case for both PABPN1 and TAP as the fraction of slower moving molecules detected by FLIP corresponds to the majority of the fluorescent signal in both cases.

The nucleocytoplasmic exchange of TAP was studied in Chapter 5 with a novel FLIP after Photoactivation methodology that we developed to measure the nuclear permanence time of shuttling proteins with steady-state distributions similar to that of TAP and PABPN1. This approach is valid if the exchange between the nucleus and the cytoplasm is sufficiently slower than protein diffusion inside each of these compartments, and is particularly useful for cases where there the protein is highly concentrated in one of the compartments and virtually absent in the other. In this method, the nuclear pool of protein is first photoactivated and then repeatedly photobleached in the cytoplasm. A two-compartment model is then used to study the kinetics of the shuttling protein.

Using this FLIP after Photoactivation approach, we found the average permanence time of PA-GFP-TAP in the nucleus to be 609 ± 151 s, a value that might reflect the existence of an efficient nuclear retention process that prevents TAP "leakage" into the cytoplasm. This is consistent with recent data that identified a specific protein in the nuclear pore complex that presumably plays an important role in restricting TAP diffusion into the cytoplasm after NPC translocation (Forler et al., 2004). TAP-p15 is thus thought to dissociate from mRNPs and be re-imported to the nucleus immediately after NPC translocation, thereby accounting for the very low steady-state levels of the protein in the cytoplasm and the relatively high nuclear permanence time.

The past few years have been remarkably exciting in providing us with new findings that are revolutionizing the way biologists look at the nucleus. Together with computer modeling approaches, photobleaching techniques are proving to be essential tools in unraveling molecular dynamics and interactions inside the living cell. The cell nucleus, in particular, is increasingly viewed as a highly dynamic entity where simple diffusion, stochasticity and self-organization processes are replacing clockwork precision energy-driven mechanisms as sole responsibles for its elaborate architecture and organization. Taken together, we believe that the results of this work where mRNP biogenesis, its transport inside the nucleus and its export to the cytoplasm have all been addressed have provided valuable contributions to the field.

Notwithstanding the breakthroughs that were made, many more questions remain to be answered. Novel probes and instruments are already available that can be used with the methods presented here. They also open up possibilities for the development of new methodologies that will surely lead to increasingly accurate modeling techniques. We are only beginning to understand how the nucleus components are coordinated in time and space. These are clearly exciting times for a physicist to be working on biology!

References

Aguilera, A. 2005. Cotranscriptional mRNP assembly: from the DNA to the nuclear pore. *Curr Opin Cell Biol*. 17:242-50.

Agutter, P.S. 1994. Models for solid-state transport: messenger RNA movement from nucleus to cytoplasm. *Cell Biol Int*. 18:849-58.

Alberts, B. 1994. Molecular Biology of the Cell, 3rd edition. Garland Publishing, Inc., New York.

Aloy, P., and R.B. Russell. 2006. Structural systems biology: modelling protein interactions. *Nat Rev Mol Cell Biol*. 7:188-97.

Amos, W.B., and J.G. White. 2003. How the confocal laser scanning microscope entered biological research. *Biol Cell*. 95:335-42.

Ando, R., H. Hama, M. Yamamoto-Hino, H. Mizuno, and A. Miyawaki. 2002. An optical marker based on the UV-induced green-to-red photoconversion of a fluorescent protein. *Proc Natl Acad Sci U S A*. 99:12651-6.

Ando, R., H. Mizuno, and A. Miyawaki. 2004. Regulated fast nucleocytoplasmic shuttling observed by reversible protein highlighting. *Science*. 306:1370-3.

Axelrod, D., D.E. Koppel, J. Schlessinger, E. Elson, and W.W. Webb. 1976a. Mobility measurement by analysis of fluorescence photobleaching recovery kinetics. *Biophys J*. 16:1055-69.

Axelrod, D., P. Ravdin, D.E. Koppel, J. Schlessinger, W.W. Webb, E.L. Elson, and T.R. Podleski. 1976b. Lateral motion of fluorescently labeled acetylcholine receptors in membranes of developing muscle fibers. *Proc Natl Acad Sci U S A*. 73:4594-8.

Azubel, M., N. Habib, R. Sperling, and J. Sperling. 2006. Native spliceosomes assemble with pre-mRNA to form supraspliceosomes. *J Mol Biol*. 356:955-66.

Bachi, A., I.C. Braun, J.P. Rodrigues, N. Pante, K. Ribbeck, C. von Kobbe, U. Kutay, M. Wilm, D. Gorlich, M. Carmo-Fonseca, and E. Izaurralde. 2000. The C-terminal domain of TAP interacts with the nuclear pore complex and promotes export of specific CTE-bearing RNA substrates. *Rna*. 6:136-58.

Bacia, K., and P. Schwille. 2003. A dynamic view of cellular processes by in vivo fluorescence auto- and cross-correlation spectroscopy. *Methods*. 29:74-85.

Bain, A.J., R.J. Marsh, D.A. Armoogum, O. Mongin, L. Porres, and M. Blanchard-Desce. 2003. Time-resolved stimulated emission depletion in two-photon excited states. *Biochem Soc Trans*. 31:1047-51.

Baluska, F., D. Volkmann, and P.W. Barlow. 2004. Eukaryotic cells and their cell bodies: Cell Theory revised. *Ann Bot (Lond)*. 94:9-32.

Bastiaens, P.I., I.V. Majoul, P.J. Verveer, H.D. Soling, and T.M. Jovin. 1996. Imaging the intracellular trafficking and state of the AB5 quaternary structure of cholera toxin. *EMBO J*. 15:4246-53.

Bastiaens, P.I., and R. Pepperkok. 2000. Observing proteins in their natural habitat: the living cell. *Trends Biochem Sci*. 25:631-7.

Bear, D.G., N. Fomproix, T. Soop, B. Bjorkroth, S. Masich, and B. Daneholt. 2003. Nuclear poly(A)-binding protein PABPN1 is associated with RNA polymerase II during transcription and accompanies the released transcript to the nuclear pore. *Exp Cell Res*. 286:332-44.

Bear, J., W. Tan, A.S. Zolotukhin, C. Tabernero, E.A. Hudson, and B.K. Felber. 1999. Identification of novel import and export signals of human TAP, the protein that binds to the constitutive transport element of the type D retrovirus mRNAs. *Mol Cell Biol*. 19:6306-17.

Beaudouin, J. 2003. Structural and molecular dynamics of nuclear proteins revealed by fluorescence microscopy. UNIVERSITÉ PARIS 7. 117.

Beaudouin, J., F. Mora-Bermudez, T. Klee, N. Daigle, and J. Ellenberg. 2006. Dissecting the contribution of diffusion and interactions to the mobility of nuclear proteins. *Biophys J*. 90:1878-94.

Belgareh, N., G. Rabut, S.W. Bai, M. van Overbeek, J. Beaudouin, N. Daigle, O.V. Zatsepina, F. Pasteau, V. Labas, M. Fromont-Racine, J. Ellenberg, and V. Doye. 2001. An evolutionarily conserved NPC subcomplex, which redistributes in part to kinetochores in mammalian cells. *J Cell Biol*. 154:1147-60.

Bentley, D.L. 2005. Rules of engagement: co-transcriptional recruitment of pre-mRNA processing factors. *Curr Opin Cell Biol*. 17:251-6.

Berk, D.A., F. Yuan, M. Leunig, and R.K. Jain. 1993. Fluorescence photobleaching with spatial Fourier analysis: measurement of diffusion in light-scattering media. *Biophys J*. 65:2428-36.

Bettinger, B.T., D.M. Gilbert, and D.C. Amberg. 2004. Actin up in the nucleus. *Nat Rev Mol Cell Biol*. 5:410-5.

Bird, G., D.A. Zorio, and D.L. Bentley. 2004. RNA polymerase II carboxy-terminal domain phosphorylation is required for cotranscriptional pre-mRNA splicing and 3'-end formation. *Mol Cell Biol*. 24:8963-9.

Black, D.L. 2003. Mechanisms of alternative pre-messenger RNA splicing. *Annu Rev Biochem*. 72:291-336.

Blencowe, B.J. 2000. Exonic splicing enhancers: mechanism of action, diversity and role in human genetic diseases. *Trends Biochem Sci*. 25:106-10.

Blobel, G. 1985. Gene gating: a hypothesis. *Proc Natl Acad Sci U S A*. 82:8527-9.

Blonk, J.C.G., A. Don, H. Van Aalst, and J.J. Birmingham. 1993. Fluorescence photobleaching recovery in the confocal scanning light microscope. *Journal of Microscopy*. 169:363-374.

Boisvert, F.M., M.J. Hendzel, and D.P. Bazett-Jones. 2000. Promyelocytic leukemia (PML) nuclear bodies are protein structures that do not accumulate RNA. *J Cell Biol*. 148:283-92.

Born, M., and E. Wolf. 1993. Principles of Optics: Electromagnetic Theory of Propagation, Interference and Diffraction of Light. Pergamon Press, Oxford.

Braeckmans, K., L. Peeters, N.N. Sanders, S.C. De Smedt, and J. Demeester. 2003. Three-dimensional fluorescence recovery after photobleaching with the confocal scanning laser microscope. *Biophys J*. 85:2240-52.

Braga, J., J.M. Desterro, and M. Carmo-Fonseca. 2004a. Intracellular macromolecular mobility measured by fluorescence recovery after photobleaching with confocal laser scanning microscopes. *Mol Biol Cell*. 15:4749-60.

Braga, J., J. Rino, and M. Carmo-Fonseca. 2004b. Photobleaching microscopy reveals the dynamics of mRNA-binding proteins inside live cell nuclei. *Prog Mol Subcell Biol*. 35:119-34.

Braun, I.C. 2002. The role of TAP in mRNA export. *In* Département de biologie moléculaire. Vol. PhD. Université de Genève, Genève. 142.

Braun, I.C., A. Herold, M. Rode, E. Conti, and E. Izaurralde. 2001. Overexpression of TAP/p15 heterodimers bypasses nuclear retention and stimulates nuclear mRNA export. *J Biol Chem*. 276:20536-43.

Braun, I.C., A. Herold, M. Rode, and E. Izaurralde. 2002. Nuclear export of mRNA by TAP/NXF1 requires two nucleoporin-binding sites but not p15. *Mol Cell Biol*. 22:5405-18.

Braun, I.C., E. Rohrbach, C. Schmitt, and E. Izaurralde. 1999. TAP binds to the constitutive transport element (CTE) through a novel RNA-binding motif that is sufficient to promote CTE-dependent RNA export from the nucleus. *Embo J*. 18:1953-65.

Bridge, E., D.X. Xia, M. Carmo-Fonseca, B. Cardinali, A.I. Lamond, and U. Pettersson. 1995. Dynamic organization of splicing factors in adenovirus-infected cells. *J Virol*. 69:281-90.

Brown, R. 1828. A brief account of microscopical observations made in the months of June, July and August, 1827, on the particles contained in the pollen of plants; and on the general existence of active molecules in organic and inorganic bodies. *Phil. Mag.*:161-173.

Brown, R. 1833. Observations of the organs and mode of fecundation in Orchideae and Asclepiadeae. *Trans. Linn. Soc. London Botany*. 16:685-720.

Brunger, A., R. Peters, and K. Schulten. 1985. Continuous Fluorescence Microphotolysis to observe lateral diffusion in membranes. Theoretical methods and applications. *Journal of Chemical Physics*. 82:2147-2160.

Bulinski, J.C., D.J. Odde, B.J. Howell, T.D. Salmon, and C.M. Waterman-Storer. 2001. Rapid dynamics of the microtubule binding of ensconsin in vivo. *J Cell Sci*. 114:3885-97.

Buratowski, S. 2005. Connections between mRNA 3' end processing and transcription termination. *Curr Opin Cell Biol*. 17:257-61.

Burke, B., and J. Ellenberg. 2002. Remodelling the walls of the nucleus. *Nat Rev Mol Cell Biol*. 3:487-97.

Burke, E., L. Dupuy, C. Wall, and S. Barik. 1998. Role of cellular actin in the gene expression and morphogenesis of human respiratory syncytial virus. *Virology*. 252:137-48.

Calado, A., and M. Carmo-Fonseca. 2000. Localization of poly(A)-binding protein 2 (PABP2) in nuclear speckles is independent of import into the nucleus and requires binding to poly(A) RNA. *J Cell Sci*. 113 (Pt 12):2309-18.

Calado, A., U. Kutay, U. Kuhn, E. Wahle, and M. Carmo-Fonseca. 2000. Deciphering the cellular pathway for transport of poly(A)-binding protein II. *Rna*. 6:245-56.

Calapez, A., H.M. Pereira, A. Calado, J. Braga, J. Rino, C. Carvalho, J.P. Tavanez, E. Wahle, A.C. Rosa, and M. Carmo-Fonseca. 2002. The intranuclear mobility of messenger RNA binding proteins is ATP dependent and temperature sensitive. *J Cell Biol*. 159:795-805.

Calvo, O., and J.L. Manley. 2003. Strange bedfellows: polyadenylation factors at the promoter. *Genes Dev*. 17:1321-7.

Campbell, R.E., O. Tour, A.E. Palmer, P.A. Steinbach, G.S. Baird, D.A. Zacharias, and R.Y. Tsien. 2002. A monomeric red fluorescent protein. *Proc Natl Acad Sci U S A*. 99:7877-82.

Carlsson, K., and A. Liljeborg. 1997. Confocal fluorescence microscopy using spectral and lifetime information to simultaneously record four-fluorophores with high channel separation. *J. Microsc.*:37-46.

Carmo-Fonseca, M. 2002a. The contribution of nuclear compartmentalization to gene regulation. *Cell*. 108:513-21.

Carmo-Fonseca, M. 2002b. New clues to the function of the Cajal body. *EMBO Rep*. 3:726-7.

Carmo-Fonseca, M. 2002c. Understanding nuclear order. *Trends Biochem Sci*. 27:332-4.

Carmo-Fonseca, M., M. Platani, and J.R. Swedlow. 2002. Macromolecular mobility inside the cell nucleus. *Trends Cell Biol*. 12:491-5.

Carrero, G., E. Crawford, M.J. Hendzel, and G. de Vries. 2004a. Characterizing fluorescence recovery curves for nuclear proteins undergoing binding events. *Bull Math Biol*. 66:1515-45.

Carrero, G., E. Crawford, J. Th'ng, G. de Vries, and M.J. Hendzel. 2004b. Quantification of protein-protein and protein-DNA interactions in vivo, using fluorescence recovery after photobleaching. *Methods Enzymol*. 375:415-42.

Carrero, G., M.J. Hendzel, and G. de Vries. 2006. Modelling the compartmentalization of splicing factors. *J Theor Biol*. 239:298-312.

Carrero, G., D. McDonald, E. Crawford, G. de Vries, and M.J. Hendzel. 2003. Using FRAP and mathematical modeling to determine the in vivo kinetics of nuclear proteins. *Methods*. 29:14-28.

Castillo, A.M., J.L. Reyes, E. Sanchez, R. Mondragon, and I. Meza. 2002. 2,3-butanedione monoxime (BDM), a potent inhibitor of actin-myosin interaction, induces ion and fluid transport in MDCK monolayers. *J Muscle Res Cell Motil*. 23:223-34.

Chakalova, L., E. Debrand, J.A. Mitchell, C.S. Osborne, and P. Fraser. 2005. Replication and transcription: shaping the landscape of the genome. *Nat Rev Genet*. 6:669-77.

Chapman, S., K.J. Oparka, and A.G. Roberts. 2005. New tools for in vivo fluorescence tagging. *Curr Opin Plant Biol*. 8:565-73.

Cheutin, T., A.J. McNairn, T. Jenuwein, D.M. Gilbert, P.B. Singh, and T. Misteli. 2003. Maintenance of stable heterochromatin domains by dynamic HP1 binding. *Science*. 299:721-5.

Chodosh, L.A., A. Fire, M. Samuels, and P.A. Sharp. 1989. 5,6-Dichloro-1-beta-D-ribofuranosylbenzimidazole inhibits transcription elongation by RNA polymerase II in vitro. *J Biol Chem*. 264:2250-7.

Chudakov, D.M., V.V. Belousov, A.G. Zaraisky, V.V. Novoselov, D.B. Staroverov, D.B. Zorov, S. Lukyanov, and K.A. Lukyanov. 2003. Kindling fluorescent proteins for precise in vivo photolabeling. *Nat Biotechnol*. 21:191-4.

Chudakov, D.M., V.V. Verkhusha, D.B. Staroverov, E.A. Souslova, S. Lukyanov, and K.A. Lukyanov. 2004. Photoswitchable cyan fluorescent protein for protein tracking. *Nat Biotechnol*. 22:1435-9.

Chusainow, J., P.M. Ajuh, L. Trinkle-Mulcahy, J.E. Sleeman, J. Ellenberg, and A.I. Lamond. 2005. FRET analyses of the U2AF complex localize the U2AF35/U2AF65 interaction in vivo and reveal a novel self-interaction of U2AF35. *Rna*. 11:1201-14.

Cmarko, D., P.J. Verschure, T.E. Martin, M.E. Dahmus, S. Krause, X.D. Fu, R. van Driel, and S. Fakan. 1999. Ultrastructural analysis of transcription and splicing in the cell nucleus after bromo-UTP microinjection. *Mol Biol Cell*. 10:211-23.

Cody, C.W., D.C. Prasher, W.M. Westler, F.G. Prendergast, and W.W. Ward. 1993. Chemical structure of the hexapeptide chromophore of the Aequorea green-fluorescent protein. *Biochemistry*. 32:1212-8.

Cole, C.N., and J.J. Scarcelli. 2006. Transport of messenger RNA from the nucleus to the cytoplasm. *Curr Opin Cell Biol*. 18:299-306.

Cole, N.B., C.L. Smith, N. Sciaky, M. Terasaki, M. Edidin, and J. Lippincott-Schwartz. 1996. Diffusional mobility of Golgi proteins in membranes of living cells. *Science*. 273:797-801.

Conchello, J.A., and J.W. Lichtman. 2005. Optical sectioning microscopy. *Nat Methods*. 2:920-31.

Cone, R.A. 1972. Rotational diffusion of rhodopsin in the visual receptor membrane. *Nat New Biol*. 236:39-43.

Cooper, G.M. 2000. The Cell: a molecular approach, 2nd edition. Sinauer Associates, Sunderland.

Crank, J. 1975. The mathematics of Diffusion. Clarendon Press, Oxford.

Cremer, T., and C. Cremer. 2001. Chromosome territories, nuclear architecture and gene regulation in mammalian cells. *Nat Rev Genet*. 2:292-301.

Cremer, T., M. Cremer, S. Dietzel, S. Muller, I. Solovei, and S. Fakan. 2006. Chromosome territories - a functional nuclear landscape. *Curr Opin Cell Biol*. 18:307-16.

Cubitt, A.B., R. Heim, S.R. Adams, A.E. Boyd, L.A. Gross, and R.Y. Tsien. 1995. Understanding, improving and using green fluorescent proteins. *Trends Biochem Sci*. 20:448-55.

Custodio, N., and M. Carmo-Fonseca. 2001. Quality control of gene expression in the nucleus. *J Cell Mol Med*. 5:267-75.

Custodio, N., M. Carmo-Fonseca, F. Geraghty, H.S. Pereira, F. Grosveld, and M. Antoniou. 1999. Inefficient processing impairs release of RNA from the site of transcription. *Embo J*. 18:2855-66.

Custodio, N., C. Carvalho, I. Condado, M. Antoniou, B.J. Blencowe, and M. Carmo-Fonseca. 2004. In vivo recruitment of exon junction complex proteins to transcription sites in mammalian cell nuclei. *Rna*. 10:622-33.

D'Angelo, M.A., and M.W. Hetzer. 2006. The role of the nuclear envelope in cellular organization. *Cell Mol Life Sci*. 63:316-32.

Daneholt, B. 1999. Pre-mRNP particles: From gene to nuclear pore. *Curr Biol*. 9:R412-5.

Das, R., K. Dufu, B. Romney, M. Feldt, M. Elenko, and R. Reed. 2006. Functional coupling of RNAP II transcription to spliceosome assembly. *Genes Dev*. 20:1100-9.

Davis, I., and D. Ish-Horowicz. 1991. Apical localization of pair-rule transcripts requires 3' sequences and limits protein diffusion in the Drosophila blastoderm embryo. *Cell*. 67:927-40.

Day, R.N. 1998. Visualization of Pit-1 transcription factor interactions in the living cell nucleus by fluorescence resonance energy transfer microscopy. *Mol Endocrinol*. 12:1410-9.

Deryusheva, S., and J.G. Gall. 2004. Dynamics of coilin in Cajal bodies of the Xenopus germinal vesicle. *Proc Natl Acad Sci U S A*. 101:4810-4.

Desterro, J.M., L.P. Keegan, M. Lafarga, M.T. Berciano, M. O'Connell, and M. Carmo-Fonseca. 2003. Dynamic association of RNA-editing enzymes with the nucleolus. *J Cell Sci*. 116:1805-18.

Dirks, R.W., K.C. Daniel, and A.K. Raap. 1995. RNAs radiate from gene to cytoplasm as revealed by fluorescence in situ hybridization. *J Cell Sci*. 108 (Pt 7):2565-72.

Donnert, G., J. Keller, R. Medda, M.A. Andrei, S.O. Rizzoli, R. Luhrmann, R. Jahn, C. Eggeling, and S.W. Hell. 2006. Macromolecular-scale resolution in biological fluorescence microscopy. *Proc Natl Acad Sci U S A*. 103:11440-5.

Doudna, J.A., and V.L. Rath. 2002. Structure and function of the eukaryotic ribosome: the next frontier. *Cell*. 109:153-6.

Dreyfuss, G., V.N. Kim, and N. Kataoka. 2002. Messenger-RNA-binding proteins and the messages they carry. *Nat Rev Mol Cell Biol*. 3:195-205.

Dundr, M., M.D. Hebert, T.S. Karpova, D. Stanek, H. Xu, K.B. Shpargel, U.T. Meier, K.M. Neugebauer, A.G. Matera, and T. Misteli. 2004. In vivo kinetics of Cajal body components. *J Cell Biol*. 164:831-42.

Dundr, M., U. Hoffmann-Rohrer, Q. Hu, I. Grummt, L.I. Rothblum, R.D. Phair, and T. Misteli. 2002. A kinetic framework for a mammalian RNA polymerase in vivo. *Science*. 298:1623-6.

Dworetzky, S.I., and C.M. Feldherr. 1988. Translocation of RNA-coated gold particles through the nuclear pores of oocytes. *J Cell Biol*. 106:575-84.

Dyba, M., S. Jakobs, and S.W. Hell. 2003. Immunofluorescence stimulated emission depletion microscopy. *Nat Biotechnol*. 21:1303-4.

Edidin, M., Y. Zagyansky, and T.J. Lardner. 1976. Measurement of membrane protein lateral diffusion in single cells. *Science*. 191:466-8.

Egly, J.M., N.G. Miyamoto, V. Moncollin, and P. Chambon. 1984. Is actin a transcription initiation factor for RNA polymerase B? *Embo J*. 3:2363-71.

Egyhazi, E. 1975. Inhibition of Balbiani ring RNA synthesis at the initiation level. *Proc Natl Acad Sci U S A*. 72:947-50.

Eils, R., D. Gerlich, W. Tvarusko, D.L. Spector, and T. Misteli. 2000. Quantitative imaging of pre-mRNA splicing factors in living cells. *Mol Biol Cell*. 11:413-8.

Einstein, A. 1956. Investigations on the theory of the brownian movement. Dover Publications, Inc., New York.

Eldridge, C.A., E.L. Elson, and W.W. Webb. 1980. Fluorescence photobleaching recovery measurements of surface lateral mobilities on normal and SV40-transformed mouse fibroblasts. *Biochemistry*. 19:2075-9.

Ellenberg, J., E.D. Siggia, J.E. Moreira, C.L. Smith, J.F. Presley, H.J. Worman, and J. Lippincott-Schwartz. 1997. Nuclear membrane dynamics and reassembly in living cells: targeting of an inner nuclear membrane protein in interphase and mitosis. *J Cell Biol*. 138:1193-206.

Elson, E., and D. Magde. 1974. Fluorescence correlation spectroscopy. I. Conceptual basis and theory. *Biopolymers*. 13:1.

Elson, E.L. 2004. Quick tour of fluorescence correlation spectroscopy from its inception. *J Biomed Opt*. 9:857-64.

Erkmann, J.A., and U. Kutay. 2004. Nuclear export of mRNA: from the site of transcription to the cytoplasm. *Exp Cell Res*. 296:12-20.

Fakan, S. 1994. Perichromatin fibrils are in situ forms of nascent transcripts. *Trends Cell Biol*. 4:86-90.

Femino, A.M., F.S. Fay, K. Fogarty, and R.H. Singer. 1998. Visualization of single RNA transcripts in situ. *Science*. 280:585-90.

Festenstein, R., S.N. Pagakis, K. Hiragami, D. Lyon, A. Verreault, B. Sekkali, and D. Kioussis. 2003. Modulation of heterochromatin protein 1 dynamics in primary Mammalian cells. *Science*. 299:719-21.

Fong, N., and D.L. Bentley. 2001. Capping, splicing, and 3' processing are independently stimulated by RNA polymerase II: different functions for different segments of the CTD. *Genes Dev*. 15:1783-95.

Fong, Y.W., and Q. Zhou. 2001. Stimulatory effect of splicing factors on transcriptional elongation. *Nature*. 414:929-33.

Forler, D., G. Rabut, F.D. Ciccarelli, A. Herold, T. Kocher, R. Niggeweg, P. Bork, J. Ellenberg, and E. Izaurralde. 2004. RanBP2/Nup358 provides a major binding site for NXF1-p15 dimers at the nuclear pore complex and functions in nuclear mRNA export. *Mol Cell Biol*. 24:1155-67.

Foster, H.A., and J.M. Bridger. 2005. The genome and the nucleus: a marriage made by evolution. Genome organisation and nuclear architecture. *Chromosoma*. 114:212-29.

Fribourg, S., I.C. Braun, E. Izaurralde, and E. Conti. 2001. Structural basis for the recognition of a nucleoporin FG repeat by the NTF2-like domain of the TAP/p15 mRNA nuclear export factor. *Mol Cell*. 8:645-56.

Fried, H., and U. Kutay. 2003. Nucleocytoplasmic transport: taking an inventory. *Cell Mol Life Sci*. 60:1659-88.

Furger, A., J.M. O'Sullivan, A. Binnie, B.A. Lee, and N.J. Proudfoot. 2002. Promoter proximal splice sites enhance transcription. *Genes Dev*. 16:2792-9.

Gadella, T.W.J., and T.M. Jovin. 1995. Oligomerization of epidermal growth factor receptors on A431 cells studied by time-resolved fluorescence imaging microscopy. A stereochemical model for tyrosine kinase receptor activation. *J Cell Biol*. 129:1543-58.

Gama-Carvalho, M., R.D. Krauss, L. Chiang, J. Valcarcel, M.R. Green, and M. Carmo-Fonseca. 1997. Targeting of U2AF65 to sites of active splicing in the nucleus. *J Cell Biol*. 137:975-87.

Gatfield, D., and E. Izaurralde. 2002. REF1/Aly and the additional exon junction complex proteins are dispensable for nuclear mRNA export. *J Cell Biol*. 159:579-88.

Gerdes, H.H., and C. Kaether. 1996. Green fluorescent protein: applications in cell biology. *FEBS Lett*. 389:44-7.

Gialitakis, M., A. Kretsovali, C. Spilianakis, L. Kravariti, J. Mages, R. Hoffmann, A.K. Hatzopoulos, and J. Papamatheakis. 2006. Coordinated changes of histone modifications and HDAC mobilization regulate the induction of MHC class II genes by Trichostatin A. *Nucleic Acids Res*. 34:765-72.

Gilmartin, G.M. 2005. Eukaryotic mRNA 3' processing: a common means to different ends. *Genes Dev*. 19:2517-21.

Goodwin, J.S., and A.K. Kenworthy. 2005. Photobleaching approaches to investigate diffusional mobility and trafficking of Ras in living cells. *Methods*. 37:154-64.

Gordon, G.W., G. Berry, X.H. Liang, B. Levine, and B. Herman. 1998. Quantitative fluorescence resonance energy transfer measurements using fluorescence microscopy. *Biophys J*. 74:2702-13.

Gorisch, S.M., P. Lichter, and K. Rippe. 2005. Mobility of multi-subunit complexes in the nucleus: accessibility and dynamics of chromatin subcompartments. *Histochem Cell Biol*. 123:217-28.

Gorlich, D., and U. Kutay. 1999. Transport between the cell nucleus and the cytoplasm. *Annu Rev Cell Dev Biol*. 15:607-60.

Gornemann, J., K.M. Kotovic, K. Hujer, and K.M. Neugebauer. 2005. Cotranscriptional spliceosome assembly occurs in a stepwise fashion and requires the cap binding complex. *Mol Cell*. 19:53-63.

Gosch, M., and R. Rigler. 2005. Fluorescence correlation spectroscopy of molecular motions and kinetics. *Adv Drug Deliv Rev*. 57:169-90.

Grant, R.P., D. Neuhaus, and M. Stewart. 2003. Structural basis for the interaction between the Tap/NXF1 UBA domain and FG nucleoporins at 1A resolution. *J Mol Biol*. 326:849-58.

Gruenbaum, Y., A. Margalit, R.D. Goldman, D.K. Shumaker, and K.L. Wilson. 2005. The nuclear lamina comes of age. *Nat Rev Mol Cell Biol*. 6:21-31.

Gurskaya, N.G., V.V. Verkhusha, A.S. Shcheglov, D.B. Staroverov, T.V. Chepurnykh, A.F. Fradkov, S. Lukyanov, and K.A. Lukyanov. 2006. Engineering of a monomeric green-to-red photoactivatable fluorescent protein induced by blue light. *Nat Biotechnol*. 24:461-5.

Guth, S., T.O. Tange, E. Kellenberger, and J. Valcarcel. 2001. Dual function for U2AF(35) in AG-dependent pre-mRNA splicing. *Mol Cell Biol*. 21:7673-81.

Handwerger, K.E., and J.G. Gall. 2006. Subnuclear organelles: new insights into form and function. *Trends Cell Biol*. 16:19-26.

Handwerger, K.E., C. Murphy, and J.G. Gall. 2003. Steady-state dynamics of Cajal body components in the Xenopus germinal vesicle. *J Cell Biol*. 160:495-504.

Harrer, M., H. Luhrs, M. Bustin, U. Scheer, and R. Hock. 2004. Dynamic interaction of HMGA1a proteins with chromatin. *J Cell Sci*. 117:3459-71.

Heim, R., A.B. Cubitt, and R.Y. Tsien. 1995. Improved green fluorescence. *Nature*. 373:663-4.

Heim, R., and R.Y. Tsien. 1996. Engineering green fluorescent protein for improved brightness, longer wavelengths and fluorescence resonance energy transfer. *Curr Biol*. 6:178-82.

Hell, S.W., G. Reiner, C. Cremer, and E.H.K. Stelzer. 1993. Aberrations in confocal fluorescence microscopy induced by mismatches in refractive index. *Journal of Microscopy*. 169:391-405.

Hell, S.W., and J. Wichmann. 1994. Breaking the diffraction resolution limit by stimulated emission. *Opt. Lett.*:780-782.

Helmchen, F., and W. Denk. 2005. Deep tissue two-photon microscopy. *Nat Methods*. 2:932-40.

Hendzel, M.J., F. Boisvert, and D.P. Bazett-Jones. 1999. Direct visualization of a protein nuclear architecture. *Mol Biol Cell*. 10:2051-62.

Herold, A., T. Klymenko, and E. Izaurralde. 2001. NXF1/p15 heterodimers are essential for mRNA nuclear export in Drosophila. *Rna*. 7:1768-80.

Herold, A., M. Suyama, J.P. Rodrigues, I.C. Braun, U. Kutay, M. Carmo-Fonseca, P. Bork, and E. Izaurralde. 2000. TAP (NXF1) belongs to a multigene family of putative RNA export factors with a conserved modular architecture. *Mol Cell Biol*. 20:8996-9008.

Herold, A., L. Teixeira, and E. Izaurralde. 2003. Genome-wide analysis of nuclear mRNA export pathways in Drosophila. *Embo J*. 22:2472-83.

Hertel, K.J., and B.R. Graveley. 2005. RS domains contact the pre-mRNA throughout spliceosome assembly. *Trends Biochem Sci*. 30:115-8.

Hofmann, W., B. Reichart, A. Ewald, E. Muller, I. Schmitt, R.H. Stauber, F. Lottspeich, B.M. Jockusch, U. Scheer, J. Hauber, and M.C. Dabauvalle. 2001. Cofactor requirements for nuclear export of Rev response element (RRE)- and constitutive transport element (CTE)-containing retroviral RNAs. An unexpected role for actin. *J Cell Biol*. 152:895-910.

Holmer, L., and H.J. Worman. 2001. Inner nuclear membrane proteins: functions and targeting. *Cell Mol Life Sci*. 58:1741-7.

Houtsmuller, A.B. 2005. Fluorescence recovery after photobleaching: application to nuclear proteins. *Adv Biochem Eng Biotechnol*. 95:177-99.

Houtsmuller, A.B., S. Rademakers, A.L. Nigg, D. Hoogstraten, J.H. Hoeijmakers, and W. Vermeulen. 1999. Action of DNA repair endonuclease ERCC1/XPF in living cells. *Science*. 284:958-61.

Houtsmuller, A.B., and W. Vermeulen. 2001. Macromolecular dynamics in living cell nuclei revealed by fluorescence redistribution after photobleaching. *Histochem Cell Biol*. 115:13-21.

Howard, M., and K. Kruse. 2005. Cellular organization by self-organization: mechanisms and models for Min protein dynamics. *J Cell Biol*. 168:533-6.

Howell, J.L., and R. Truant. 2002. Live-cell nucleocytoplasmic protein shuttle assay utilizing laser confocal microscopy and FRAP. *Biotechniques*. 32:80-2, 84, 86-7.

Huang, Y., R. Gattoni, J. Stevenin, and J.A. Steitz. 2003. SR splicing factors serve as adapter proteins for TAP-dependent mRNA export. *Mol Cell*. 11:837-43.

Huber, J., U. Cronshagen, M. Kadokura, C. Marshallsay, T. Wada, M. Sekine, and R. Luhrmann. 1998. Snurportin1, an m3G-cap-specific nuclear import receptor with a novel domain structure. *Embo J*. 17:4114-26.

Huber, J., A. Dickmanns, and R. Luhrmann. 2002. The importin-beta binding domain of snurportin1 is responsible for the Ran- and energy-independent nuclear import of spliceosomal U snRNPs in vitro. *J Cell Biol*. 156:467-79.

Iborra, F.J., D.A. Jackson, and P.R. Cook. 2001. Coupled transcription and translation within nuclei of mammalian cells. *Science*. 293:1139-42.

Iborra, F.J., A. Pombo, D.A. Jackson, and P.R. Cook. 1996. Active RNA polymerases are localized within discrete transcription "factories' in human nuclei. *J Cell Sci*. 109 (Pt 6):1427-36.

Izaurralde, E. 2001. Friedrich Miescher Prize awardee lecture review. A conserved family of nuclear export receptors mediates the exit of messenger RNA to the cytoplasm. *Cell Mol Life Sci*. 58:1105-12.

Izaurralde, E. 2002. A novel family of nuclear transport receptors mediates the export of messenger RNA to the cytoplasm. *Eur J Cell Biol*. 81:577-84.

Jackson, D.A., F.J. Iborra, E.M. Manders, and P.R. Cook. 1998. Numbers and organization of RNA polymerases, nascent transcripts, and transcription units in HeLa nuclei. *Mol Biol Cell*. 9:1523-36.

Jacobson, K., Z. Derzko, E.S. Wu, Y. Hou, and G. Poste. 1976. Measurement of the lateral mobility of cell surface components in single, living cells by fluorescence recovery after photobleaching. *J Supramol Struct*. 5:565(417)-576(428).

Jacquez, J.A. 1996. Compartmental Analysis in Biology and Medicine. BioMedware, Ann Arbor, MI.

Janicki, S.M., T. Tsukamoto, S.E. Salghetti, W.P. Tansey, R. Sachidanandam, K.V. Prasanth, T. Ried, Y. Shav-Tal, E. Bertrand, R.H. Singer, and D.L. Spector. 2004. From silencing to gene expression: real-time analysis in single cells. *Cell*. 116:683-98.

Jonkman, J.E., and E.H.K. Stelzer. 2002. Resolution and Constrast in Confocal and Two-Photon Microscopy. *In* Confocal and Two-Photon Microscopy: Foundations, Applications and Advances. A. Diaspro, editor. Wiley-Liss, Inc., New York.

Jonkman, J.E., J. Swoger, H. Kress, A. Rohrbach, and E.H. Stelzer. 2003. Resolution in optical microscopy. *Methods Enzymol*. 360:416-46.

Kalnina, Z., P. Zayakin, K. Silina, and A. Line. 2005. Alterations of pre-mRNA splicing in cancer. *Genes Chromosomes Cancer*. 42:342-57.

Kang, Y., H.P. Bogerd, J. Yang, and B.R. Cullen. 1999. Analysis of the RNA binding specificity of the human tap protein, a constitutive transport element-specific nuclear RNA export factor. *Virology*. 262:200-9.

Kang, Y., and B.R. Cullen. 1999. The human Tap protein is a nuclear mRNA export factor that contains novel RNA-binding and nucleocytoplasmic transport sequences. *Genes Dev*. 13:1126-39.

Karpova, T.S., C.T. Baumann, L. He, X. Wu, A. Grammer, P. Lipsky, G.L. Hager, and J.G. McNally. 2003. Fluorescence resonance energy transfer from cyan to yellow fluorescent protein detected by acceptor photobleaching using confocal microscopy and a single laser. *J Microsc*. 209:56-70.

Kaufman, E.N., and R.K. Jain. 1990. Quantification of transport and binding parameters using fluorescence recovery after photobleaching. Potential for in vivo applications. *Biophys J*. 58:873-85.

Kaufman, E.N., and R.K. Jain. 1991. Measurement of mass transport and reaction parameters in bulk solution using photobleaching. Reaction limited binding regime. *Biophys J*. 60:596-610.

Keller, R.W., U. Kuhn, M. Aragon, L. Bornikova, E. Wahle, and D.G. Bear. 2000. The nuclear poly(A) binding protein, PABP2, forms an oligomeric particle covering the length of the poly(A) tail. *J Mol Biol*. 297:569-83.

Keminer, O., and R. Peters. 1999. Permeability of single nuclear pores. *Biophys J*. 77:217-28.

Kent, O.A., A. Reayi, L. Foong, K.A. Chilibeck, and A.M. MacMillan. 2003. Structuring of the 3' splice site by U2AF65. *J Biol Chem*. 278:50572-7.

Kenworthy, A.K. 2001. Imaging protein-protein interactions using fluorescence resonance energy transfer microscopy. *Methods*. 24:289-96.

Kerwitz, Y., U. Kuhn, H. Lilie, A. Knoth, T. Scheuermann, H. Friedrich, E. Schwarz, and E. Wahle. 2003. Stimulation of poly(A) polymerase through a direct interaction with the nuclear poly(A) binding protein allosterically regulated by RNA. *Embo J*. 22:3705-14.

Kim, V.N., J. Yong, N. Kataoka, L. Abel, M.D. Diem, and G. Dreyfuss. 2001. The Y14 protein communicates to the cytoplasm the position of exon-exon junctions. *Embo J*. 20:2062-8.

Kimura, H., and P.R. Cook. 2001. Kinetics of core histones in living human cells: little exchange of H3 and H4 and some rapid exchange of H2B. *J Cell Biol*. 153:1341-53.

Kimura, H., K. Sugaya, and P.R. Cook. 2002. The transcription cycle of RNA polymerase II in living cells. *J Cell Biol*. 159:777-82.

Kimura, T., I. Hashimoto, A. Yamamoto, M. Nishikawa, and J.I. Fujisawa. 2000. Rev-dependent association of the intron-containing HIV-1 gag mRNA with the nuclear actin bundles and the inhibition of its nucleocytoplasmic transport by latrunculin-B. *Genes Cells*. 5:289-307.

Kiss, T. 2004. Biogenesis of small nuclear RNPs. *J Cell Sci*. 117:5949-51.

Klar, T.A., S. Jakobs, M. Dyba, A. Egner, and S.W. Hell. 2000. Fluorescence microscopy with diffraction resolution barrier broken by stimulated emission. *Proc Natl Acad Sci U S A*. 97:8206-10.

Kloc, M., N.R. Zearfoss, and L.D. Etkin. 2002. Mechanisms of subcellular mRNA localization. *Cell*. 108:533-44.

Klonis, N., M. Rug, I. Harper, M. Wickham, A. Cowman, and L. Tilley. 2002. Fluorescence photobleaching analysis for the study of cellular dynamics. *Eur Biophys J*. 31:36-51.

Koppel, D.E. 1979. Fluorescence redistribution after photobleaching. A new multipoint analysis of membrane translational dynamics. *Biophys J*. 28:281-91.

Koppel, D.E., and M.P. Sheetz. 1983. A localized pattern photobleaching method for the concurrent analysis of rapid and slow diffusion processes. *Biophys J*. 43:175-81.

Kornblihtt, A.R. 2005. Promoter usage and alternative splicing. *Curr Opin Cell Biol*. 17:262-8.

Kornblihtt, A.R. 2006. Chromatin, transcript elongation and alternative splicing. *Nat Struct Mol Biol*. 13:5-7.

Kornblihtt, A.R., M. de la Mata, J.P. Fededa, M.J. Munoz, and G. Nogues. 2004. Multiple links between transcription and splicing. *Rna*. 10:1489-98.

Koster, M., T. Frahm, and H. Hauser. 2005. Nucleocytoplasmic shuttling revealed by FRAP and FLIP technologies. *Curr Opin Biotechnol*. 16:28-34.

Kramer, A. 1996. The structure and function of proteins involved in mammalian pre-mRNA splicing. *Annu Rev Biochem*. 65:367-409.

Kruhlak, M.J., M.A. Lever, W. Fischle, E. Verdin, D.P. Bazett-Jones, and M.J. Hendzel. 2000. Reduced mobility of the alternate splicing factor (ASF) through the nucleoplasm and steady state speckle compartments. *J Cell Biol*. 150:41-51.

Kubitscheck, U., D. Grunwald, A. Hoekstra, D. Rohleder, T. Kues, J.P. Siebrasse, and R. Peters. 2005. Nuclear transport of single molecules: dwell times at the nuclear pore complex. *J Cell Biol*. 168:233-43.

Kubitscheck, U., P. Wedekind, and R. Peters. 1994. Lateral diffusion measurement at high spatial resolution by scanning microphotolysis in a confocal microscope. *Biophys J*. 67:948-56.

Kubitscheck, U., P. Wedekind, and R. Peters. 1998. Three-dimensional diffusion measurements by scanning microphotolysis. *Journal of Microscopy*. 192:126-138.

Kuhn, U., A. Nemeth, S. Meyer, and E. Wahle. 2003. The RNA binding domains of the nuclear poly(A)-binding protein. *J Biol Chem*. 278:16916-25.

Kuhn, U., and E. Wahle. 2004. Structure and function of poly(A) binding proteins. *Biochim Biophys Acta*. 1678:67-84.

Kurakin, A. 2005a. Self-organization versus Watchmaker: stochastic dynamics of cellular organization. *Biol Chem*. 386:247-54.

Kurakin, A. 2005b. Stochastic cell. *IUBMB Life*. 57:59-63.

Kuthan, H. 2005. Temporal fluctuation of nuclear pore complex localization by single diffusing mRNP complexes. *J Theor Biol*. 236:256-62.

Lall, S., H. Francis-Lang, A. Flament, A. Norvell, T. Schupbach, and D. Ish-Horowicz. 1999. Squid hnRNP protein promotes apical cytoplasmic transport and localization of Drosophila pair-rule transcripts. *Cell*. 98:171-80.

Lamond, A.I., and D.L. Spector. 2003. Nuclear speckles: a model for nuclear organelles. *Nat Rev Mol Cell Biol*. 4:605-12.

Lander, E.S., L.M. Linton, B. Birren, C. Nusbaum, M.C. Zody, J. Baldwin, K. Devon, K. Dewar, M. Doyle, W. FitzHugh, R. Funke, D. Gage, K. Harris, A. Heaford, J. Howland, L. Kann, J. Lehoczky, R. LeVine, P. McEwan, K. McKernan, J. Meldrim, J.P. Mesirov, C. Miranda, W. Morris, J. Naylor, C. Raymond, M. Rosetti, R. Santos, A. Sheridan, C. Sougnez, N. Stange-Thomann, N. Stojanovic, A. Subramanian, D. Wyman, J. Rogers, J. Sulston, R. Ainscough, S. Beck, D. Bentley, J. Burton, C. Clee, N. Carter, A. Coulson, R. Deadman, P. Deloukas, A. Dunham, I. Dunham, R. Durbin, L. French, D. Grafham, S. Gregory, T. Hubbard, S. Humphray, A. Hunt, M. Jones, C. Lloyd, A. McMurray, L. Matthews, S. Mercer, S. Milne, J.C. Mullikin, A. Mungall, R.

Plumb, M. Ross, R. Shownkeen, S. Sims, R.H. Waterston, R.K. Wilson, L.W. Hillier, J.D. McPherson, M.A. Marra, E.R. Mardis, L.A. Fulton, A.T. Chinwalla, K.H. Pepin, W.R. Gish, S.L. Chissoe, M.C. Wendl, K.D. Delehaunty, T.L. Miner, A. Delehaunty, J.B. Kramer, L.L. Cook, R.S. Fulton, D.L. Johnson, P.J. Minx, S.W. Clifton, T. Hawkins, E. Branscomb, P. Predki, P. Richardson, S. Wenning, T. Slezak, N. Doggett, J.F. Cheng, A. Olsen, S. Lucas, C. Elkin, E. Uberbacher, M. Frazier, et al. 2001. Initial sequencing and analysis of the human genome. *Nature*. 409:860-921.

Lang, I., M. Scholz, and R. Peters. 1986. Molecular mobility and nucleocytoplasmic flux in hepatoma cells. *J Cell Biol*. 102:1183-90.

Lawrence, J.B., R.H. Singer, and L.M. Marselle. 1989. Highly localized tracks of specific transcripts within interphase nuclei visualized by in situ hybridization. *Cell*. 57:493-502.

Le Hir, H., D. Gatfield, E. Izaurralde, and M.J. Moore. 2001. The exon-exon junction complex provides a binding platform for factors involved in mRNA export and nonsense-mediated mRNA decay. *Embo J*. 20:4987-97.

Lele, T.P., and D.E. Ingber. 2006. A mathematical model to determine molecular kinetic rate constants under non-steady state conditions using fluorescence recovery after photobleaching (FRAP). *Biophys Chem*. 120:32-5.

Levesque, L., B. Guzik, T. Guan, J. Coyle, B.E. Black, D. Rekosh, M.L. Hammarskjold, and B.M. Paschal. 2001. RNA export mediated by tap involves NXT1-dependent interactions with the nuclear pore complex. *J Biol Chem*. 276:44953-62.

Lichtman, J.W., and J.A. Conchello. 2005. Fluorescence microscopy. *Nat Methods*. 2:910-9.

Liker, E., E. Fernandez, E. Izaurralde, and E. Conti. 2000. The structure of the mRNA export factor TAP reveals a cis arrangement of a non-canonical RNP domain and an LRR domain. *Embo J*. 19:5587-98.

Lippincott-Schwartz, J., N. Altan-Bonnet, and G.H. Patterson. 2003. Photobleaching and photoactivation: following protein dynamics in living cells. *Nat Cell Biol*. Suppl:S7-14.

Lippincott-Schwartz, J., and G.H. Patterson. 2003. Development and use of fluorescent protein markers in living cells. *Science*. 300:87-91.

Lippincott-Schwartz, J., E. Snapp, and A. Kenworthy. 2001. Studying protein dynamics in living cells. *Nat Rev Mol Cell Biol*. 2:444-56.

Lippincott-Schwartz, J., and K.J. Zaal. 2000. Cell cycle maintenance and biogenesis of the Golgi complex. *Histochem Cell Biol*. 114:93-103.

Liu, S., R. Rauhut, H.P. Vornlocher, and R. Luhrmann. 2006. The network of protein-protein interactions within the human U4/U6.U5 tri-snRNP. *Rna*. 12:1418-30.

Liu, X.L., Y. Shen, E.J. Chen, and Z.H. Zhai. 2000. Nuclear assembly of purified Crythecodinium cohnii chromosomes in cell-free extracts of Xenopus laevis eggs. *Cell Res*. 10:127-37.

Lodish, H., A. Berk, P. Matsudaira, C.A. Kaiser, M. Krieger, M.P. Scott, S.L. Zipursky, and J. Darnell. 2003. Molecular Cell Biology - Fifth Edition. W. H. Freeman and Company, New York.

Lukyanov, K.A., D.M. Chudakov, S. Lukyanov, and V.V. Verkhusha. 2005. Innovation: Photoactivatable fluorescent proteins. *Nat Rev Mol Cell Biol*. 6:885-91.

Macara, I.G. 2001. Transport into and out of the nucleus. *Microbiol Mol Biol Rev*. 65:570-94, table of contents.

Mangus, D.A., M.C. Evans, and A. Jacobson. 2003. Poly(A)-binding proteins: multifunctional scaffolds for the post-transcriptional control of gene expression. *Genome Biol*. 4:223.

Maniatis, T., and R. Reed. 2002. An extensive network of coupling among gene expression machines. *Nature*. 416:499-506.

Mans, B.J., V. Anantharaman, L. Aravind, and E.V. Koonin. 2004. Comparative genomics, evolution and origins of the nuclear envelope and nuclear pore complex. *Cell Cycle*. 3:1612-37.

Maquat, L.E. 2005. Nonsense-mediated mRNA decay in mammals. *J Cell Sci*. 118:1773-6.

Marco, S., T. Boudier, C. Messaoudi, and J.L. Rigaud. 2004. Electron tomography of biological samples. *Biochemistry (Mosc)*. 69:1219-25.

Marshall, W.F., A. Straight, J.F. Marko, J. Swedlow, A. Dernburg, A. Belmont, A.W. Murray, D.A. Agard, and J.W. Sedat. 1997. Interphase chromosomes undergo constrained diffusional motion in living cells. *Curr Biol*. 7:930-9.

Martin, W., and E.V. Koonin. 2006. Introns and the origin of nucleus-cytosol compartmentalization. *Nature*. 440:41-5.

Matz, M.V., A.F. Fradkov, Y.A. Labas, A.P. Savitsky, A.G. Zaraisky, M.L. Markelov, and S.A. Lukyanov. 1999. Fluorescent proteins from nonbioluminescent Anthozoa species. *Nat Biotechnol*. 17:969-73.

Maul, G.G., and L. Deaven. 1977. Quantitative determination of nuclear pore complexes in cycling cells with differing DNA content. *J Cell Biol*. 73:748-60.

Mazzarello, P. 1999. A unifying concept: the history of cell theory. *Nat Cell Biol*. 1:E13-5.

McDonald, D., G. Carrero, C. Andrin, G. de Vries, and M.J. Hendzel. 2006. Nucleoplasmic beta-actin exists in a dynamic equilibrium between low-mobility polymeric species and rapidly diffusing populations. *J Cell Biol*. 172:541-52.

Medlin, J.E., P. Uguen, A. Taylor, D.L. Bentley, and S. Murphy. 2003. The C-terminal domain of pol II and a DRB-sensitive kinase are required for 3' processing of U2 snRNA. *Embo J*. 22:925-34.

Melcak, I., S. Cermanova, K. Jirsova, K. Koberna, J. Malinsky, and I. Raska. 2000. Nuclear pre-mRNA compartmentalization: trafficking of released transcripts to splicing factor reservoirs. *Mol Biol Cell*. 11:497-510.

Meyer, S., C. Urbanke, and E. Wahle. 2002. Equilibrium studies on the association of the nuclear poly(A) binding protein with poly(A) of different lengths. *Biochemistry*. 41:6082-9.

Minsky, M. 1988. Memoir on inventing the confocal scanning microscope. *Scanning*:128-138.

Misteli, T. 2000. Cell biology of transcription and pre-mRNA splicing: nuclear architecture meets nuclear function. *J Cell Sci*. 113 (Pt 11):1841-9.

Misteli, T. 2001a. The concept of self-organization in cellular architecture. *J Cell Biol*. 155:181-5.

Misteli, T. 2001b. Protein dynamics: implications for nuclear architecture and gene expression. *Science*. 291:843-7.

Misteli, T. 2005. Concepts in nuclear architecture. *Bioessays*. 27:477-87.

Misteli, T., J.F. Caceres, and D.L. Spector. 1997. The dynamics of a pre-mRNA splicing factor in living cells. *Nature*. 387:523-7.

Misteli, T., and D.L. Spector. 1998. The cellular organization of gene expression. *Curr Opin Cell Biol*. 10:323-31.

Misteli, T., and D.L. Spector. 1999. RNA polymerase II targets pre-mRNA splicing factors to transcription sites in vivo. *Mol Cell*. 3:697-705.

Moir, R.D., M. Yoon, S. Khuon, and R.D. Goldman. 2000. Nuclear lamins A and B1: different pathways of assembly during nuclear envelope formation in living cells. *J Cell Biol*. 151:1155-68.

Molenaar, C., A. Abdulle, A. Gena, H.J. Tanke, and R.W. Dirks. 2004. Poly(A)+ RNAs roam the cell nucleus and pass through speckle domains in transcriptionally active and inactive cells. *J Cell Biol*. 165:191-202.

Moore, M.J. 2005. From birth to death: the complex lives of eukaryotic mRNAs. *Science*. 309:1514-8.

Muratani, M., D. Gerlich, S.M. Janicki, M. Gebhard, R. Eils, and D.L. Spector. 2002. Metabolic-energy-dependent movement of PML bodies within the mammalian cell nucleus. *Nat Cell Biol*. 4:106-10.

Nagy, P., G. Vamosi, A. Bodnar, S.J. Lockett, and J. Szollosi. 1998. Intensity-based energy transfer measurements in digital imaging microscopy. *Eur Biophys J*. 27:377-89.

Narayanan, U., J.K. Ospina, M.R. Frey, M.D. Hebert, and A.G. Matera. 2002. SMN, the spinal muscular atrophy protein, forms a pre-import snRNP complex with snurportin1 and importin beta. *Hum Mol Genet*. 11:1785-95.

Neugebauer, K.M. 2002. On the importance of being co-transcriptional. *J Cell Sci*. 115:3865-71.

Neugebauer, K.M. 2006. Please hold--the next available exon will be right with you. *Nat Struct Mol Biol*. 13:385-6.

Nickerson, J. 2001. Experimental observations of a nuclear matrix. *J Cell Sci*. 114:463-74.

Nilsen, T.W. 2003. The spliceosome: the most complex macromolecular machine in the cell? *Bioessays*. 25:1147-9.

Nissim-Rafinia, M., and B. Kerem. 2005. The splicing machinery is a genetic modifier of disease severity. *Trends Genet*. 21:480-3.

O'Keefe, R.T., A. Mayeda, C.L. Sadowski, A.R. Krainer, and D.L. Spector. 1994. Disruption of pre-mRNA splicing in vivo results in reorganization of splicing factors. *J Cell Biol*. 124:249-60.

Ogg, S.C., and A.I. Lamond. 2002. Cajal bodies and coilin--moving towards function. *J Cell Biol*. 159:17-21.

Oida, T., Y. Sako, and A. Kusumi. 1993. Fluorescence lifetime imaging microscopy (flimscopy). Methodology development and application to studies of endosome fusion in single cells. *Biophys J*. 64:676-85.

Olson, M.O., M. Dundr, and A. Szebeni. 2000. The nucleolus: an old factory with unexpected capabilities. *Trends Cell Biol*. 10:189-96.

Ormo, M., A.B. Cubitt, K. Kallio, L.A. Gross, R.Y. Tsien, and S.J. Remington. 1996. Crystal structure of the Aequorea victoria green fluorescent protein. *Science*. 273:1392-5.

Orphanides, G., and D. Reinberg. 2002. A unified theory of gene expression. *Cell*. 108:439-51.

Osborne, C.S., L. Chakalova, K.E. Brown, D. Carter, A. Horton, E. Debrand, B. Goyenechea, J.A. Mitchell, S. Lopes, W. Reik, and P. Fraser. 2004. Active genes dynamically colocalize to shared sites of ongoing transcription. *Nat Genet*. 36:1065-71.

Ostap, E.M. 2002. 2,3-Butanedione monoxime (BDM) as a myosin inhibitor. *J Muscle Res Cell Motil*. 23:305-8.

Pacheco, T.R., M.B. Coelho, J.M. Desterro, I. Mollet, and M. Carmo-Fonseca. 2006. In vivo requirement of the small subunit of U2AF for recognition of a weak 3' splice site. *Mol Cell Biol*.

Pacheco, T.R., A.Q. Gomes, N.L. Barbosa-Morais, V. Benes, W. Ansorge, M. Wollerton, C.W. Smith, J. Valcarcel, and M. Carmo-Fonseca. 2004. Diversity of vertebrate splicing factor U2AF35: identification of alternatively spliced U2AF1 mRNAS. *J Biol Chem*. 279:27039-49.

Pante, N. 2004. Nuclear pore complex structure: unplugged and dynamic pores. *Dev Cell*. 7:780-1.

Partikian, A., B. Olveczky, R. Swaminathan, Y. Li, and A.S. Verkman. 1998. Rapid diffusion of green fluorescent protein in the mitochondrial matrix. *J Cell Biol*. 140:821-9.

Patterson, G.H. 2004. A new harvest of fluorescent proteins. *Nat Biotechnol*. 22:1524-5.

Patterson, G.H., and J. Lippincott-Schwartz. 2002. A photoactivatable GFP for selective photolabeling of proteins and cells. *Science*. 297:1873-7.

Pederson, T. 2000. Half a century of "the nuclear matrix". *Mol Biol Cell*. 11:799-805.

Pederson, T. 2002. Dynamics and genome-centricity of interchromatin domains in the nucleus. *Nat Cell Biol*. 4:E287-91.

Pederson, T., and U. Aebi. 2002. Actin in the nucleus: what form and what for? *J Struct Biol*. 140:3-9.

Percipalle, P., A. Jonsson, D. Nashchekin, C. Karlsson, T. Bergman, A. Guialis, and B. Daneholt. 2002. Nuclear actin is associated with a specific subset of hnRNP A/B-type proteins. *Nucleic Acids Res*. 30:1725-34.

Pestic-Dragovich, L., L. Stojiljkovic, A.A. Philimonenko, G. Nowak, Y. Ke, R.E. Settlage, J. Shabanowitz, D.F. Hunt, P. Hozak, and P. de Lanerolle. 2000. A myosin I isoform in the nucleus. *Science*. 290:337-41.

Peters, R. 2005. Translocation through the nuclear pore complex: selectivity and speed by reduction-of-dimensionality. *Traffic*. 6:421-7.

Peters, R., A. Brunger, and K. Schulten. 1981. Continuous fluorescence microphotolysis: A sensitive method for study of diffusion processes in single cells. *Proc Natl Acad Sci U S A*. 78:962-966.

Peters, R., and U. Kubitscheck. 1999. Scanning microphotolysis: three-dimensional diffusion measurement and optical single-transporter recording. *Methods*. 18:508-17.

Peters, R., J. Peters, K.H. Tews, and W. Bahr. 1974. A microfluorimetric study of translational diffusion in erythrocyte membranes. *Biochim Biophys Acta*. 367:282-94.

Phair, R.D., S.A. Gorski, and T. Misteli. 2004a. Measurement of dynamic protein binding to chromatin in vivo, using photobleaching microscopy. *Methods Enzymol*. 375:393-414.

Phair, R.D., and T. Misteli. 2000. High mobility of proteins in the mammalian cell nucleus. *Nature*. 404:604-9.

Phair, R.D., and T. Misteli. 2001. Kinetic modelling approaches to in vivo imaging. *Nat Rev Mol Cell Biol*. 2:898-907.

Phair, R.D., P. Scaffidi, C. Elbi, J. Vecerova, A. Dey, K. Ozato, D.T. Brown, G. Hager, M. Bustin, and T. Misteli. 2004b. Global nature of dynamic protein-chromatin interactions in vivo: three-dimensional genome scanning and dynamic interaction networks of chromatin proteins. *Mol Cell Biol*. 24:6393-402.

Platani, M., I. Goldberg, A.I. Lamond, and J.R. Swedlow. 2002. Cajal body dynamics and association with chromatin are ATP-dependent. *Nat Cell Biol*. 4:502-8.

Politz, J.C., E.S. Browne, D.E. Wolf, and T. Pederson. 1998. Intranuclear diffusion and hybridization state of oligonucleotides measured by fluorescence correlation spectroscopy in living cells. *Proc Natl Acad Sci U S A*. 95:6043-8.

Politz, J.C., and T. Pederson. 2000. Review: movement of mRNA from transcription site to nuclear pores. *J Struct Biol*. 129:252-7.

Politz, J.C., R.A. Tuft, T. Pederson, and R.H. Singer. 1999. Movement of nuclear poly(A) RNA throughout the interchromatin space in living cells. *Curr Biol*. 9:285-91.

Politz, J.C., R.A. Tuft, K.V. Prasanth, N. Baudendistel, K.E. Fogarty, L.M. Lifshitz, J. Langowski, D.L. Spector, and T. Pederson. 2006. Rapid, diffusional shuttling of poly(A) RNA between nuclear speckles and the nucleoplasm. *Mol Biol Cell*. 17:1239-49.

Pollok, B.A., and R. Heim. 1999. Using GFP in FRET-based applications. *Trends Cell Biol*. 9:57-60.

Poo, M., and R.A. Cone. 1973. Lateral diffusion of rhodopsin in the visual receptor membrane. *J Supramol Struct*. 1:354.

Prasher, D.C., V.K. Eckenrode, W.W. Ward, F.G. Prendergast, and M.J. Cormier. 1992. Primary structure of the Aequorea victoria green-fluorescent protein. *Gene*. 111:229-33.

Presley, J.F., N.B. Cole, T.A. Schroer, K. Hirschberg, K.J. Zaal, and J. Lippincott-Schwartz. 1997. ER-to-Golgi transport visualized in living cells. *Nature*. 389:81-5.

Proudfoot, N. 2004. New perspectives on connecting messenger RNA 3' end formation to transcription. *Curr Opin Cell Biol*. 16:272-8.

Proudfoot, N., and J. O'Sullivan. 2002. Polyadenylation: a tail of two complexes. *Curr Biol*. 12:R855-7.

Proudfoot, N.J., A. Furger, and M.J. Dye. 2002. Integrating mRNA processing with transcription. *Cell*. 108:501-12.

Rabut, G., V. Doye, and J. Ellenberg. 2004a. Mapping the dynamic organization of the nuclear pore complex inside single living cells. *Nat Cell Biol*. 6:1114-21.

Rabut, G., P. Lenart, and J. Ellenberg. 2004b. Dynamics of nuclear pore complex organization through the cell cycle. *Curr Opin Cell Biol*. 16:314-21.

Rademakers, S., M. Volker, D. Hoogstraten, A.L. Nigg, M.J. Mone, A.A. Van Zeeland, J.H. Hoeijmakers, A.B. Houtsmuller, and W. Vermeulen. 2003. Xeroderma pigmentosum group A protein loads as a separate factor onto DNA lesions. *Mol Cell Biol*. 23:5755-67.

Ramachandran, I., M. Terry, and M.B. Ferrari. 2003. Skeletal muscle myosin cross-bridge cycling is necessary for myofibrillogenesis. *Cell Motil Cytoskeleton*. 55:61-72.

Rando, O.J., K. Zhao, and G.R. Crabtree. 2000. Searching for a function for nuclear actin. *Trends Cell Biol*. 10:92-7.

Reid, B.G., and G.C. Flynn. 1997. Chromophore formation in green fluorescent protein. *Biochemistry*. 36:6786-91.

Ribbeck, K., and D. Gorlich. 2001. Kinetic analysis of translocation through nuclear pore complexes. *Embo J*. 20:1320-30.

Ribbeck, K., and D. Gorlich. 2002. The permeability barrier of nuclear pore complexes appears to operate via hydrophobic exclusion. *Embo J*. 21:2664-71.

Rizzo, M.A., G.H. Springer, B. Granada, and D.W. Piston. 2004. An improved cyan fluorescent protein variant useful for FRET. *Nat Biotechnol*. 22:445-9.

Rodrigues, J.P., M. Rode, D. Gatfield, B.J. Blencowe, M. Carmo-Fonseca, and E. Izaurralde. 2001. REF proteins mediate the export of spliced and unspliced mRNAs from the nucleus. *Proc Natl Acad Sci U S A*. 98:1030-5.

Rosonina, E., J.Y. Ip, J.A. Calarco, M.A. Bakowski, A. Emili, S. McCracken, P. Tucker, C.J. Ingles, and B.J. Blencowe. 2005. Role for PSF in mediating transcriptional activator-dependent stimulation of pre-mRNA processing in vivo. *Mol Cell Biol*. 25:6734-46.

Roy, S.W., and W. Gilbert. 2006. The evolution of spliceosomal introns: patterns, puzzles and progress. *Nat Rev Genet*. 7:211-21.

Saitoh, N., C.S. Spahr, S.D. Patterson, P. Bubulya, A.F. Neuwald, and D.L. Spector. 2004. Proteomic analysis of interchromatin granule clusters. *Mol Biol Cell*. 15:3876-90.

Sanchez-Alvarez, M., A.C. Goldstrohm, M.A. Garcia-Blanco, and C. Sune. 2006. Human transcription elongation factor CA150 localizes to splicing factor-rich nuclear speckles and assembles transcription and splicing components into complexes through its amino and carboxyl regions. *Mol Cell Biol*. 26:4998-5014.

Sanders, R., A. Draaijer, H.C. Gerritsen, P.M. Houpt, and Y.K. Levine. 1995. Quantitative pH imaging in cells using confocal fluorescence lifetime imaging microscopy. *Anal Biochem*. 227:302-8.

Sanford, J.R., and J.F. Caceres. 2004. Pre-mRNA splicing: life at the centre of the central dogma. *J Cell Sci*. 117:6261-3.

Saxton, M.J. 1994. Anomalous diffusion due to obstacles: a Monte Carlo study. *Biophys J*. 66:394-401.

Saxton, M.J. 1996. Anomalous diffusion due to binding: a Monte Carlo study. *Biophys J*. 70:1250-62.

Saxton, M.J. 2001. Anomalous subdiffusion in fluorescence photobleaching recovery: a Monte Carlo study. *Biophys J*. 81:2226-40.

Scheer, U., H. Hinssen, W.W. Franke, and B.M. Jockusch. 1984. Microinjection of actin-binding proteins and actin antibodies demonstrates involvement of nuclear actin in transcription of lampbrush chromosomes. *Cell*. 39:111-22.

Schleiden, M.J. 1838. Beiträge zur Phytogenesis. *J. Arch. Anat. Physiol. Wiss. Med.*:137-176.

Schmid, J.A., and H. Neumeier. 2005. Evolutions in science triggered by green fluorescent protein (GFP). *Chembiochem*. 6:1149-56.

Schwann, T. 1839. Mikroskopische Untersuchungen über die Übereinstimmung in der Struktur und dem Wachstum der Tiere und Pflanzen. Sander'schen Buchhandlung, Berlin.

Schwille, P. 2001. Fluorescence correlation spectroscopy and its potential for intracellular applications. *Cell Biochem Biophys*. 34:383-408.

Schwille, P., U. Haupts, S. Maiti, and W.W. Webb. 1999. Molecular dynamics in living cells observed by fluorescence correlation spectroscopy with one- and two-photon excitation. *Biophys J*. 77:2251-65.

Schwille, P., and E. Haustein. 2000. Fluorescence Correlation Spectroscopy.

Seksek, O., J. Biwersi, and A.S. Verkman. 1997. Translational diffusion of macromolecule-sized solutes in cytoplasm and nucleus. *J Cell Biol*. 138:131-42.

Selenko, P., G. Gregorovic, R. Sprangers, G. Stier, Z. Rhani, A. Kramer, and M. Sattler. 2003. Structural basis for the molecular recognition between human splicing factors U2AF65 and SF1/mBBP. *Mol Cell*. 11:965-76.

Selvin, P.R. 2000. The renaissance of fluorescence resonance energy transfer. *Nat Struct Biol*. 7:730-4.

Shaner, N.C., R.E. Campbell, P.A. Steinbach, B.N. Giepmans, A.E. Palmer, and R.Y. Tsien. 2004. Improved monomeric red, orange and yellow fluorescent proteins derived from Discosoma sp. red fluorescent protein. *Nat Biotechnol*. 22:1567-72.

Shaner, N.C., P.A. Steinbach, and R.Y. Tsien. 2005. A guide to choosing fluorescent proteins. *Nat Methods*. 2:905-9.

Shatkin, A.J., and J.L. Manley. 2000. The ends of the affair: capping and polyadenylation. *Nat Struct Biol*. 7:838-42.

Shav-Tal, Y., J. Blechman, X. Darzacq, C. Montagna, B.T. Dye, J.G. Patton, R.H. Singer, and D. Zipori. 2005. Dynamic sorting of nuclear components into distinct nucleolar caps during transcriptional inhibition. *Mol Biol Cell*. 16:2395-413.

Shav-Tal, Y., X. Darzacq, S.M. Shenoy, D. Fusco, S.M. Janicki, D.L. Spector, and R.H. Singer. 2004a. Dynamics of single mRNPs in nuclei of living cells. *Science*. 304:1797-800.

Shav-Tal, Y., R.H. Singer, and X. Darzacq. 2004b. Imaging gene expression in single living cells. *Nat Rev Mol Cell Biol*. 5:855-61.

Shen, H., and M.R. Green. 2004. A pathway of sequential arginine-serine-rich domain-splicing signal interactions during mammalian spliceosome assembly. *Mol Cell*. 16:363-73.

Shimomura, O., F.H. Johnson, and Y. Saiga. 1962. Extraction, purification and properties of aequorin, a bioluminescent protein from the luminous hydromedusan, Aequorea. *J Cell Comp Physiol*. 59:223-39.

Shin, C., and J.L. Manley. 2004. Cell signalling and the control of pre-mRNA splicing. *Nat Rev Mol Cell Biol*. 5:727-38.

Singh, O.P., B. Bjorkroth, S. Masich, L. Wieslander, and B. Daneholt. 1999. The intranuclear movement of Balbiani ring premessenger ribonucleoprotein particles. *Exp Cell Res*. 251:135-46.

Sleeman, J.E., L. Trinkle-Mulcahy, A.R. Prescott, S.C. Ogg, and A.I. Lamond. 2003. Cajal body proteins SMN and Coilin show differential dynamic behaviour in vivo. *J Cell Sci*. 116:2039-50.

Smith, B.A., and H.M. McConnell. 1978. Determination of molecular motion in membranes using periodic pattern photobleaching. *Proc Natl Acad Sci U S A*. 75:2759-63.

Soller, M. 2006. Pre-messenger RNA processing and its regulation: a genomic perspective. *Cell Mol Life Sci*. 63:796-819.

Soumpasis, D.M. 1983. Theoretical analysis of fluorescence photobleaching recovery experiments. *Biophys J*. 41:95-7.

Spector, D.L. 1993. Macromolecular domains within the cell nucleus. *Annu Rev Cell Biol*. 9:265-315.

Spector, D.L. 2001. Nuclear domains. *J Cell Sci*. 114:2891-3.

Sprague, B.L., and J.G. McNally. 2005. FRAP analysis of binding: proper and fitting. *Trends Cell Biol*. 15:84-91.

Sprague, B.L., F. Muller, R.L. Pego, P.M. Bungay, D.A. Stavreva, and J.G. McNally. 2006. Analysis of binding at a single spatially localized cluster of binding sites by fluorescence recovery after photobleaching. *Biophys J.* 91:1169-91.

Sprague, B.L., R.L. Pego, D.A. Stavreva, and J.G. McNally. 2004. Analysis of binding reactions by fluorescence recovery after photobleaching. *Biophys J.* 86:3473-95.

Squire, A., and P.I. Bastiaens. 1999. Three dimensional image restoration in fluorescence lifetime imaging microscopy. *J Microsc.* 193:36-49.

Stanek, D., and K.M. Neugebauer. 2006. The Cajal body: a meeting place for spliceosomal snRNPs in the nuclear maze. *Chromosoma*.

Stelzer, E.H. 1998. Contrast, resolution, pixelation, dynamic range and signal-to-noise ratio: fundamental limits to resolution in fluorescence light microscopy. *Journal of Microscopy*. 189:15-24.

Stelzer, E.H.K. 1995. The Intermediate Optical System of Laser-Scanning Confocal Microscopes. *In* Handbook of Biological Confocal Microscopy. J.B. Pawley, editor. Plenum Press, New York.

Stevens, S.W., D.E. Ryan, H.Y. Ge, R.E. Moore, M.K. Young, T.D. Lee, and J. Abelson. 2002. Composition and functional characterization of the yeast spliceosomal penta-snRNP. *Mol Cell.* 9:31-44.

Stoffler, D., B. Fahrenkrog, and U. Aebi. 1999. The nuclear pore complex: from molecular architecture to functional dynamics. *Curr Opin Cell Biol.* 11:391-401.

Stoffler, D., B. Feja, B. Fahrenkrog, J. Walz, D. Typke, and U. Aebi. 2003. Cryo-electron tomography provides novel insights into nuclear pore architecture: implications for nucleocytoplasmic transport. *J Mol Biol.* 328:119-30.

Stokes, G.G. 1852. On the change of refrangibility of light. *Phil. Trans. R. Soc. London*:463-562.

Stutz, F., and E. Izaurralde. 2003. The interplay of nuclear mRNP assembly, mRNA surveillance and export. *Trends Cell Biol.* 13:319-27.

Sunn, K.L., J.A. Eisman, E.M. Gardiner, and D.A. Jans. 2005. FRAP analysis of nucleocytoplasmic dynamics of the vitamin D receptor splice variant VDRB1: preferential targeting to nuclear speckles. *Biochem J.* 388:509-14.

Suntharalingam, M., and S.R. Wente. 2003. Peering through the pore: nuclear pore complex structure, assembly, and function. *Dev Cell.* 4:775-89.

Suyama, M., T. Doerks, I.C. Braun, M. Sattler, E. Izaurralde, and P. Bork. 2000. Prediction of structural domains of TAP reveals details of its interaction with p15 and nucleoporins. *EMBO Rep.* 1:53-8.

Tardiff, D.F., and M. Rosbash. 2006. Arrested yeast splicing complexes indicate stepwise snRNP recruitment during in vivo spliceosome assembly. *Rna*.

Tavanez, J.P., P. Calado, J. Braga, M. Lafarga, and M. Carmo-Fonseca. 2005. In vivo aggregation properties of the nuclear poly(A)-binding protein PABPN1. *Rna.* 11:752-62.

Truong, K., and M. Ikura. 2001. The use of FRET imaging microscopy to detect protein-protein interactions and protein conformational changes in vivo. *Curr Opin Struct Biol.* 11:573-8.

Tsay, T.T., and K.A. Jacobson. 1991. Spatial Fourier analysis of video photobleaching measurements. Principles and optimization. *Biophys J.* 60:360-8.

Tseng, Y., J.S. Lee, T.P. Kole, I. Jiang, and D. Wirtz. 2004. Micro-organization and visco-elasticity of the interphase nucleus revealed by particle nanotracking. *J Cell Sci.* 117:2159-67.

Tsien, R.Y. 1998. The green fluorescent protein. *Annu Rev Biochem*. 67:509-44.

Tsien, R.Y. 1999. Rosy dawn for fluorescent proteins. *Nat Biotechnol*. 17:956-7.

Tsien, R.Y. 2005. Building and breeding molecules to spy on cells and tumors. *FEBS Lett*. 579:927-32.

Vagner, S., C. Vagner, and I.W. Mattaj. 2000. The carboxyl terminus of vertebrate poly(A) polymerase interacts with U2AF 65 to couple 3'-end processing and splicing. *Genes Dev*. 14:403-13.

Valadkhan, S. 2005. snRNAs as the catalysts of pre-mRNA splicing. *Curr Opin Chem Biol*. 9:603-8.

van Munster, E.B., and T.W. Gadella. 2005. Fluorescence lifetime imaging microscopy (FLIM). *Adv Biochem Eng Biotechnol*. 95:143-75.

van Munster, E.B., and T.W. Gadella, Jr. 2004a. phiFLIM: a new method to avoid aliasing in frequency-domain fluorescence lifetime imaging microscopy. *J Microsc*. 213:29-38.

van Munster, E.B., and T.W. Gadella, Jr. 2004b. Suppression of photobleaching-induced artifacts in frequency-domain FLIM by permutation of the recording order. *Cytometry A*. 58:185-94.

Vandromme, M., C. Gauthier-Rouviere, N. Lamb, and A. Fernandez. 1996. Regulation of transcription factor localization: fine-tuning of gene expression. *Trends Biochem Sci*. 21:59-64.

Vargas, D.Y., A. Raj, S.A. Marras, F.R. Kramer, and S. Tyagi. 2005. Mechanism of mRNA transport in the nucleus. *Proc Natl Acad Sci U S A*. 102:17008-13.

Vellai, T., and G. Vida. 1999. The origin of eukaryotes: the difference between prokaryotic and eukaryotic cells. *Proc Biol Sci*. 266:1571-7.

Verkhusha, V.V., and A. Sorkin. 2005. Conversion of the monomeric red fluorescent protein into a photoactivatable probe. *Chem Biol*. 12:279-85.

Vermeer, J.E., E.B. Van Munster, N.O. Vischer, and T.W. Gadella, Jr. 2004. Probing plasma membrane microdomains in cowpea protoplasts using lipidated GFP-fusion proteins and multimode FRET microscopy. *J Microsc*. 214:190-200.

Verschure, P.J., I. Van Der Kraan, J.M. Enserink, M.J. Mone, E.M. Manders, and R. Van Driel. 2002. Large-scale chromatin organization and the localization of proteins involved in gene expression in human cells. *J Histochem Cytochem*. 50:1303-12.

Verschure, P.J., I. van der Kraan, E.M. Manders, D. Hoogstraten, A.B. Houtsmuller, and R. van Driel. 2003. Condensed chromatin domains in the mammalian nucleus are accessible to large macromolecules. *EMBO Rep*. 4:861-6.

Verschure, P.J., I. van Der Kraan, E.M. Manders, and R. van Driel. 1999. Spatial relationship between transcription sites and chromosome territories. *J Cell Biol*. 147:13-24.

Visa, N., F. Puvion-Dutilleul, J.P. Bachellerie, and E. Puvion. 1993. Intranuclear distribution of U1 and U2 snRNAs visualized by high resolution in situ hybridization: revelation of a novel compartment containing U1 but not U2 snRNA in HeLa cells. *Eur J Cell Biol*. 60:308-21.

Visser, A.E., F. Jaunin, S. Fakan, and J.A. Aten. 2000. High resolution analysis of interphase chromosome domains. *J Cell Sci*. 113 (Pt 14):2585-93.

Voss, T.C., I.A. Demarco, and R.N. Day. 2005. Quantitative imaging of protein interactions in the cell nucleus. *Biotechniques*. 38:413-24.

Wachsmuth, M., W. Waldeck, and J. Langowski. 2000. Anomalous diffusion of fluorescent probes inside living cell nuclei investigated by spatially-resolved fluorescence correlation spectroscopy. *J Mol Biol*. 298:677-89.

Wachsmuth, M., T. Weidemann, G. Muller, U.W. Hoffmann-Rohrer, T.A. Knoch, W. Waldeck, and J. Langowski. 2003. Analyzing intracellular binding and diffusion with continuous fluorescence photobleaching. *Biophys J*. 84:3353-63.

Wahle, E., A. Lustig, P. Jeno, and P. Maurer. 1993. Mammalian poly(A)-binding protein II. Physical properties and binding to polynucleotides. *J Biol Chem*. 268:2937-45.

Wallrabe, H., and A. Periasamy. 2005. Imaging protein molecules using FRET and FLIM microscopy. *Curr Opin Biotechnol*. 16:19-27.

Wang, E., C.M. Babbey, and K.W. Dunn. 2005. Performance comparison between the high-speed Yokogawa spinning disc confocal system and single-point scanning confocal systems. *J Microsc*. 218:148-59.

Wansink, D.G., W. Schul, I. van der Kraan, B. van Steensel, R. van Driel, and L. de Jong. 1993. Fluorescent labeling of nascent RNA reveals transcription by RNA polymerase II in domains scattered throughout the nucleus. *J Cell Biol*. 122:283-93.

Wei, X., V.G. Henke, C. Strubing, E.B. Brown, and D.E. Clapham. 2003. Real-time imaging of nuclear permeation by EGFP in single intact cells. *Biophys J*. 84:1317-27.

Weiner, A.M. 2005. E Pluribus Unum: 3' end formation of polyadenylated mRNAs, histone mRNAs, and U snRNAs. *Mol Cell*. 20:168-70.

Weis, K. 2003. Regulating access to the genome: nucleocytoplasmic transport throughout the cell cycle. *Cell*. 112:441-51.

Weiss, M., and T. Nilsson. 2004. In a mirror dimly: tracing the movements of molecules in living cells. *Trends Cell Biol*. 14:267-73.

Wetterberg, I., J. Zhao, S. Masich, L. Wieslander, and U. Skoglund. 2001. In situ transcription and splicing in the Balbiani ring 3 gene. *Embo J*. 20:2564-74.

White, J., and E. Stelzer. 1999. Photobleaching GFP reveals protein dynamics inside live cells. *Trends in Cell Biology*. 9.

Wiegand, H.L., G.A. Coburn, Y. Zeng, Y. Kang, H.P. Bogerd, and B.R. Cullen. 2002. Formation of Tap/NXT1 heterodimers activates Tap-dependent nuclear mRNA export by enhancing recruitment to nuclear pore complexes. *Mol Cell Biol*. 22:245-56.

Will, C.L., and R. Luhrmann. 2001. Spliceosomal UsnRNP biogenesis, structure and function. *Curr Opin Cell Biol*. 13:290-301.

Willig, K.I., R.R. Kellner, R. Medda, B. Hein, S. Jakobs, and S.W. Hell. 2006. Nanoscale resolution in GFP-based microscopy. *Nat Methods*. 3:721-3.

Wilson, K.L. 2000. The nuclear envelope, muscular dystrophy and gene expression. *Trends Cell Biol*. 10:125-9.

Wouters, F.S., and P.I. Bastiaens. 1999. Fluorescence lifetime imaging of receptor tyrosine kinase activity in cells. *Curr Biol*. 9:1127-30.

Wouters, F.S., P.I. Bastiaens, K.W. Wirtz, and T.M. Jovin. 1998. FRET microscopy demonstrates molecular association of non-specific lipid transfer protein (nsL-TP) with fatty acid oxidation enzymes in peroxisomes. *Embo J*. 17:7179-89.

Wouters, F.S., P.J. Verveer, and P.I. Bastiaens. 2001. Imaging biochemistry inside cells. *Trends Cell Biol*. 11:203-11.

Woychik, N.A., and M. Hampsey. 2002. The RNA polymerase II machinery: structure illuminates function. *Cell*. 108:453-63.

Wu, E.S., K. Jacobson, F. Szoka, and A. Portis, Jr. 1978. Lateral diffusion of a hydrophobic peptide, N-4-nitrobenz-2-oxa-1,3-diazole gramicidin S, in phospholipid multibilayers. *Biochemistry*. 17:5543-50.

Xia, Z., and Y. Liu. 2001. Reliable and global measurement of fluorescence resonance energy transfer using fluorescence microscopes. *Biophys J*. 81:2395-402.

Xiao, S.H., and J.L. Manley. 1998. Phosphorylation-dephosphorylation differentially affects activities of splicing factor ASF/SF2. *Embo J*. 17:6359-67.

Yamaguchi, Y., T. Wada, and H. Handa. 1998. Interplay between positive and negative elongation factors: drawing a new view of DRB. *Genes Cells*. 3:9-15.

Yoneda, Y. 2000. Nucleocytoplasmic protein traffic and its significance to cell function. *Genes Cells*. 5:777-87.

Yong, J., T.J. Golembe, D.J. Battle, L. Pellizzoni, and G. Dreyfuss. 2004a. snRNAs contain specific SMN-binding domains that are essential for snRNP assembly. *Mol Cell Biol*. 24:2747-56.

Yong, J., L. Wan, and G. Dreyfuss. 2004b. Why do cells need an assembly machine for RNA-protein complexes? *Trends Cell Biol*. 14:226-32.

Yuste, R. 2005. Fluorescence microscopy today. *Nat Methods*. 2:902-4.

Zachar, Z., J. Kramer, I.P. Mims, and P.M. Bingham. 1993. Evidence for channeled diffusion of pre-mRNAs during nuclear RNA transport in metazoans. *J Cell Biol*. 121:729-42.

Zapata-Hommer, O., and O. Griesbeck. 2003. Efficiently folding and circularly permuted variants of the Sapphire mutant of GFP. *BMC Biotechnol*. 3:5.

Zhang, J., R.E. Campbell, A.Y. Ting, and R.Y. Tsien. 2002. Creating new fluorescent probes for cell biology. *Nat Rev Mol Cell Biol*. 3:906-18.

Zhang, M., P.D. Zamore, M. Carmo-Fonseca, A.I. Lamond, and M.R. Green. 1992. Cloning and intracellular localization of the U2 small nuclear ribonucleoprotein auxiliary factor small subunit. *Proc Natl Acad Sci U S A*. 89:8769-73.

Zhao, K., W. Wang, O.J. Rando, Y. Xue, K. Swiderek, A. Kuo, and G.R. Crabtree. 1998. Rapid and phosphoinositol-dependent binding of the SWI/SNF-like BAF complex to chromatin after T lymphocyte receptor signaling. *Cell*. 95:625-36.

Zorio, D.A., and D.L. Bentley. 2004. The link between mRNA processing and transcription: communication works both ways. *Exp Cell Res*. 296:91-7.